

2015

# A sparsity-based framework for resolution enhancement in optical fault analysis of integrated circuits

---

<https://hdl.handle.net/2144/15189>

*Downloaded from DSpace Repository, DSpace Institution's institutional repository*

BOSTON UNIVERSITY  
COLLEGE OF ENGINEERING

Dissertation

**A SPARSITY-BASED FRAMEWORK FOR RESOLUTION  
ENHANCEMENT IN OPTICAL FAULT ANALYSIS OF  
INTEGRATED CIRCUITS**

by

**T. BERKİN ÇİLİNGİROĞLU**

B.S., Koç University, 2006

M.S., Koç University, 2008

Submitted in partial fulfillment of the  
requirements for the degree of  
Doctor of Philosophy

2015

© 2015 by  
T. BERKİN ÇİLİNGİROĞLU  
All rights reserved

## Approved by

First Reader

---

M. Selim Ünlü, PhD  
Professor of Electrical and Computer Engineering  
Professor of Biomedical Engineering

Second Reader

---

W. Clem Karl, PhD  
Professor of Electrical and Computer Engineering  
Professor of Biomedical Engineering

Third Reader

---

Janusz Konrad, PhD  
Professor of Electrical and Computer Engineering

Fourth Reader

---

Bennett B. Goldberg, PhD  
Professor of Physics  
Professor of Biomedical Engineering

Fifth Reader

---

Ajay Joshi, PhD  
Assistant Professor of Electrical and Computer Engineering



## Acknowledgments

Over the course of my PhD studies I have been very privileged to be advised by multiple faculty members. They each exposed me to new ideas and viewpoints, and continued to guide me through the years. I want to thank Prof. Selim Unlu for his full support and for trusting me with all the projects he assigned. He has not only been a supervisor but also a good friend. I want to thank Prof. W. Clem Karl for his continuous suggestions and insightful questions which pushed me to think more and advance my research. I want to thank Prof. Janusz Konrad for being on my side and for showing his full support since my first research year at Boston University. I am grateful for his critiques as well as his encouragement through positive feedback. I want to thank Prof. Bennett Goldberg for exposing me to new viewpoints and his insightful comments. I want to thank both Prof. Selim Unlu and Prof. Bennett Goldberg for giving me the opportunity to work on a multidisciplinary project, which broadened my knowledge and skills. I want to thank Prof. Ajay Joshi for being available when I needed further approval and critique on my work and for sharing his enthusiasm for research with me. I want to thank Dr. Hakan Koklu, I learned a lot from him when I started my PhD thesis project. I have also worked with Aydan Uyar, Dr. Ahmet Tuysuzoglu and Dr. Abdulkadir Yurt, and I thank them for valuable discussions and collaboration. I also want to thank other co-workers for discussions and their contributions, Dr. Helen Fawcett, Dr. Euan Ramsay, Dr. Yang Lu, Mahmoud Zangeneh, Dr. Michael Grogan, Kyle Vigil.

My PhD experience would not have been the same without the warm atmosphere of ISS and OCN Labs. Thanks to my friends at Boston University, I have cheerful and fun memories from my PhD years: Ajay, Ahmet, Alex, Amanda, Anne, Ayca, Aydan, Birant, Bryan, Carlos, Cem, Cristina, Darin, Dave, Delarem, Elif, Emir, Emre, Erhan, George, Gilberto, Hakan, Huseyin, Ivana, Joe, Karen, Ke, Kirill, Limor, Margo,

Niloofar, Ozgur, Phil, Santosh, Sarah, Sonal, Sunmin Theodora, Xiriu, Ye, and Zach. I want to thank Limor for being a great officemate and for her suggestions and her help when I was writing my dissertation and was preparing my defense presentation. Ayca and Emre have always been good friends and great examples, they inspired me through their work and accomplishments.

Last but not least, I want to thank my loving family. I am grateful for their continuous support and love. My parents, Nesim and Haluk, always believed in me and showed their support for me to reach my goals. My brother, Berk, has always been a source of love and joy. My parents-in-law, Zeynep and Mutlu, have always encouraged me and showed their support. I would like to thank my husband, Murat. I cannot imagine a life abroad without him. Him being on my side was the biggest support.

I would also like to acknowledge the funding agency. The material in this dissertation is based upon work supported by the Intelligence Advanced Research Projects Activity (IARPA) via Air Force Research Laboratory (AFRL) contract number: FA8650-11-C- 7102.

I dedicate this dissertation to my family.

# **A SPARSITY-BASED FRAMEWORK FOR RESOLUTION ENHANCEMENT IN OPTICAL FAULT ANALYSIS OF INTEGRATED CIRCUITS**

**T. BERKİN ÇİLİNGİROĞLU**

Boston University, College of Engineering, 2015

Major Professors: M. Selim Ünlü, PhD  
Professor of Electrical and Computer Engineering  
Professor of Biomedical Engineering

W. Clem Karl, PhD  
Professor of Electrical and Computer Engineering  
Professor of Biomedical Engineering

## **ABSTRACT**

The increasing density and smaller length scales in integrated circuits (ICs) create resolution challenges for optical failure analysis techniques. Due to flip-chip bonding and dense metal layers on the front side, optical analysis of ICs is restricted to backside imaging through the silicon substrate, which limits the spatial resolution due to the minimum wavelength of transmission and refraction at the planar interface. The state-of-the-art backside analysis approach is to use aplanatic solid immersion lenses in order to achieve the highest possible numerical aperture of the imaging system. Signal processing algorithms are essential to complement the optical microscopy efforts to increase resolution through hardware modifications in order to meet the resolution requirements of new IC technologies.

The focus of this thesis is the development of sparsity-based image reconstruction

techniques to improve resolution of static IC images and dynamic optical measurements of device activity. A physics-based observation model is exploited in order to take advantage of polarization diversity in high numerical aperture systems. Multiple-polarization observation data are combined to produce a single enhanced image with higher resolution. In the static IC image case, two sparsity paradigms are considered. The first approach, referred to as analysis-based sparsity, creates enhanced resolution imagery by solving a linear inverse problem while enforcing sparsity through non-quadratic regularization functionals appropriate to IC features. The second approach, termed synthesis-based sparsity, is based on sparse representations with respect to overcomplete dictionaries. The domain of IC imaging is particularly suitable for the application of overcomplete dictionaries because the images are highly structured; they contain predictable building blocks derivable from the corresponding computer-aided design layouts. This structure provides a strong and natural a-priori dictionary for image reconstruction. In the dynamic case, an extension of the synthesis-based sparsity paradigm is formulated. Spatial regions of active areas with the same behavior over time or over frequency are coupled by an overcomplete dictionary consisting of space-time or space-frequency blocks. This extended dictionary enables resolution improvement through sparse representation of dynamic measurements. Additionally, extensions to darkfield subsurface microscopy of ICs and focus determination based on image stacks are provided. The resolution improvement ability of the proposed methods has been validated on both simulated and experimental data.

# Contents

<b>1</b>	<b>Introduction</b>	<b>1</b>
1.1	Contributions . . . . .	3
1.2	Thesis organization . . . . .	5
<b>2</b>	<b>Background</b>	<b>7</b>
2.1	Linear inverse problems and regularization . . . . .	7
2.1.1	Tikhonov Regularization . . . . .	8
2.1.2	Non-quadratic regularization . . . . .	9
2.1.3	Dictionary-based sparse regularization . . . . .	11
2.2	Backside optical fault analysis techniques . . . . .	12
2.2.1	Laser voltage probing . . . . .	13
2.2.2	Laser voltage imaging . . . . .	16
2.3	Applanatic solid immersion lens microscopy for integrated circuit imaging and its optical model . . . . .	17
2.3.1	Applanatic solid immersion lenses for integrated circuit imaging	17
2.3.2	Optical model for confocal applanatic solid immersion lens microscopy of integrated circuits . . . . .	20
<b>3</b>	<b>Model of a point spread function for a subsurface aSIL imaging system</b>	<b>31</b>
3.1	Linear observation model . . . . .	32
3.2	Modeling of the PSF . . . . .	32
3.2.1	PSF as the reflection of a tightly focused spot . . . . .	33

3.2.2	Green's function approach for PSF modeling . . . . .	35
3.3	Conclusion . . . . .	37
<b>4</b>	<b>Analysis-based sparse image reconstruction framework for integrated circuit imaging based on polarization diversity</b>	<b>40</b>
4.1	Proposed framework . . . . .	41
4.1.1	Regularized image reconstruction framework for resolution enhanced IC imaging . . . . .	41
4.1.2	Solution to the optimization problem . . . . .	42
4.2	Simulated-data experiments . . . . .	45
4.3	Real-data experiments . . . . .	51
4.4	Comparison of different boundary condition settings . . . . .	61
4.4.1	Mirroring the boundary pixels . . . . .	62
4.4.2	Reconstructing a cropped image . . . . .	62
4.4.3	Modifying the forward model . . . . .	63
4.4.4	Reconstruction results with different boundary condition settings	64
4.5	Conclusions . . . . .	64
<b>5</b>	<b>Dictionary-based image reconstruction for resolution enhancement in integrated circuit imaging</b>	<b>67</b>
5.1	Dictionary-based image reconstruction framework for IC imaging . . .	68
5.1.1	Observation model . . . . .	68
5.1.2	Sparse representation framework for resolution-enhanced IC imaging . . . . .	69
5.1.3	Construction of dictionaries . . . . .	70
5.2	Experimental results . . . . .	72
5.2.1	Comparison of sparse reconstruction approaches through simulated data . . . . .	72

5.2.2	Reconstruction results for aSIL microscopy data . . . . .	74
5.3	Initialization of dictionary-based $\ell_{1/2}$ -regularization . . . . .	88
5.4	Conclusions . . . . .	89
<b>6</b>	<b>Imaging active integrated circuits with 3D dictionaries for laser volt- age imaging</b>	<b>95</b>
6.1	Sparse representation framework for multiple-harmonics LVI . . . . .	97
6.1.1	Frequency-domain sparse representation . . . . .	98
6.1.2	Time-domain sparse representation . . . . .	99
6.2	Constructions of dictionaries . . . . .	100
6.3	Simulated-data experiments . . . . .	102
6.3.1	Comparison of space-frequency representation and space-time representation results . . . . .	151
6.4	Conclusion . . . . .	158
<b>7</b>	<b>Application of resolution enhancement techniques to dark-field sub- surface microscopy of integrated circuits</b>	<b>159</b>
7.1	Dark-field subsurface microscopy for integrated circuits . . . . .	160
7.2	Image reconstruction framework . . . . .	161
7.2.1	PSF Estimation and Observation Model . . . . .	163
7.2.2	Image reconstruction based on non-quadratic regularization . . . . .	164
7.2.3	Dictionary-based image reconstruction . . . . .	165
7.3	Experimental results . . . . .	166
7.4	Conclusions . . . . .	168
<b>8</b>	<b>Focus determination for high NA subsurface imaging of integrated circuits</b>	<b>173</b>
8.1	Focus identification . . . . .	173
8.2	Preliminary focus identification experiment . . . . .	175

8.3	Conclusion . . . . .	179
<b>9</b>	<b>Conclusions</b>	<b>180</b>
9.1	Summary and conclusions . . . . .	180
9.2	Topics for future research . . . . .	182
	<b>References</b>	<b>185</b>



# List of Figures

1·1	Optical measurements of (a) a properly-functioning die and (b) a faulty die . . . . .	2
2·1	Behavior of $l_p$ -norm for $p = 0.5, 1, 2$ . . . . .	10
2·2	Cross sectional diagram of a MOSFET (a) off-state, (b)linear operating regime , (c)saturation regime. . . . .	14
2·3	Experimental configuration for LVP and LVI measurements . . . . .	15
2·4	Data collected from an active inverter chain (a) LSM image and LVI image: (b) amplitude modulation image (c) amplitude phase map . .	17
2·5	Light focusing in (a) a conventional-surface optical microscope, (b) a liquid-immersion lens microscope, (c) a solid-immersion lens microscope, (d) a subsurface microscope and (e) an applanatic solid-immersion (aSIL) lens microscope. . . . .	19
2·6	Focusing on an interface in an aSIL microscope . . . . .	23
2·7	Investigation of the reflected image of a focused spot . . . . .	26
2·8	Schematic of the problem of far-field field propagation with Green's function in aSIL microscope . . . . .	29
3·1	Simulated theoretical PSF for linearly-polarized input light (a) in $x$ direction (b) in $y$ direction . . . . .	34
3·2	Cross sections from the simulated PSF for linearly-polarized input light in $x$ direction . . . . .	35

3.3	Experimental observation images under polarization in (a) $x$ direction and (b) $y$ direction. . . . .	35
3.4	Experimental observation images of aluminum structures under polarization in (a) $x$ direction and (b) $y$ direction. . . . .	36
3.5	Simulated PSFs with linearly-polarized input light in the $y$ direction for aluminum objects (a) $\alpha = 2^3$ , (b) $\alpha = 2.5^3$ , (c) $\alpha = 3^3$ , and for polysilicon objects (d) $\alpha = 2^3$ , (e) $\alpha = 2.5^3$ , (f) $\alpha = 3^3$ . . . . .	38
3.6	Comparison of PSF cross sections for different values of $\alpha$ for aluminum objects (a) horizontal cross section, (b) vertical cross section, and for polysilicon objects (c) horizontal cross section, (d) vertical cross section. . . . .	39
3.7	Comparison of PSF ( $\alpha = 2.75^3$ ) cross section and data cross section: (a) experimental aSIL image, (b) cross section from experimental data along the green line, (c) PSF cross section blue for horizontal and red for vertical. . . . .	39
4.1	(a) Simulated object image and observed images under polarization in (b) $x$ direction and (c) $y$ direction. . . . .	45
4.2	Image reconstruction results on simulated data with no regularization: (a) only from an observation image under $x$ -polarized light, (b) only from an observation image under $y$ -polarized light, (c) from observation images under both $x$ - and $y$ -polarized light. . . . .	46
4.3	Regularized image reconstruction results on simulated data with=: (a) only from an observation image under $x$ -polarized light for $\lambda_1 = 0.0025$ $\lambda_2 = 0.0002$ , (b) only from an observation image under $y$ -polarized light for $\lambda_1 = 0.0025$ $\lambda_2 = 0.0002$ , (c) from observation images under both $x$ - and $y$ -polarized light for $\lambda_1 = 0.005$ $\lambda_2 = 0.0004$ . . . . .	47

4.4	MSE between reconstructed images and underlying object image . . .	48
4.5	The resolution target phantom . . . . .	49
4.6	Simulated observation images of the resolution phantom of Fig. 4.5 for $x$ -polarized input light (a) SNR=16dB, (c) SNR=20dB, (e) SNR=25dB, (g) SNR=30dB, and for $y$ -polarized input light (b) SNR=16dB, (d) SNR=20dB, (f) SNR=25dB, (h) SNR=30dB . . . . .	50
4.7	Results of regularized image reconstruction combining both polariza- tion data (a) SNR=16dB $\lambda_1 = 0.0025$ $\lambda_2 = 0.005$ , (b) SNR=20dB $\lambda_1 = 0.0005$ $\lambda_2 = 0.005$ , (c) SNR=25dB $\lambda_1 = 0.00025$ $\lambda_2 = 0.00025$ , (d) SNR=30dB $\lambda_1 = 0.00025$ $\lambda_2 = 0.005$ . . . . .	52
4.8	MSE between underlying object image and reconstructed images from observation data with different levels of noise . . . . .	52
4.9	Experimental observation images under polarization in (a) $x$ direction and (b) $y$ direction. . . . .	53
4.10	Regularized image reconstruction results on experimental data (a) only from an observation image under $x$ -polarized light for $\lambda_1 = 0.75$ $\lambda_2 =$ $0.5$ , (b) only from an observation image under $y$ -polarized light for $\lambda_1 = 0.5$ $\lambda_2 = 0.35$ , (c) from observation images under both $x$ - and $y$ -polarized light for $\lambda_1 = 1$ $\lambda_2 = 0.5$ . . . . .	54
4.11	Cross sections from the observation data and reconstructed images: (a) horizontal (b) vertical . . . . .	55
4.12	Simulated theoretical PSF for circularly-polarized input light source. .	56
4.13	Experimental observation images . . . . .	56
4.14	Regularized image reconstruction results (a) $\lambda_1 = 0.1$ , $\lambda_2 = 0.01$ , (b) $\lambda_1 = 0.1$ , $\lambda_2 = 0.01$ . . . . .	57

4.15	SEM images for lines resolution target with (a) 282nm (b) 252nm (c) 224nm separation . . . . .	58
4.16	Observation data of resolution target of aluminum lines with 282nm pitch (a) $x$ -polarized input light (b) $y$ -polarized input light, (c) regularized reconstruction results for $\lambda_1 = 0.0005$ , $\lambda_2 = 0.05$ . . . . .	58
4.17	Observation data of resolution target of aluminum lines with 252nm pitch (a) $x$ -polarized input light (b) $y$ -polarized input light, (c) regularized reconstruction results for $\lambda_1 = 0.0005$ , $\lambda_2 = 0.05$ . . . . .	59
4.18	Observation data of resolution target of aluminum lines with 224nm pitch (a) $x$ -polarized input light (b) $y$ -polarized input light, (c) regularized reconstruction results for $\lambda_1 = 0.00005$ , $\lambda_2 = 0.001$ . . . . .	59
4.19	Cross sections from the observation and reconstructions for aluminum lines with 284nm separation (a) horizontal, (b) vertical. . . . .	60
4.20	Cross sections from the observation and reconstructions for aluminum lines with 252nm separation (a) horizontal, (b) vertical. . . . .	60
4.21	Cross sections from the observation and reconstructions for aluminum lines with 224nm separation (a) horizontal, (b) vertical. . . . .	61
4.22	(a)observation (b)observation after mirror-image padding . . . . .	62
4.23	Diagram showing modification of the forward model . . . . .	63
4.24	Image reconstruction results on simulated data comparing different boundary condition settings: (a) mirroring the boundary pixels for $\lambda_1 = 0.5$ , $\lambda_2 = 0.75$ , (b) reconstructing a cropped center area for $\lambda_1 = 0.375$ , $\lambda_2 = 0.59$ , (c) modifying the forward model for $\lambda_1 = 0.0025$ , $\lambda_2 = 0.001$ . . . . .	64

4.25	Image reconstruction results on experimental data comparing different boundary condition settings: (a) mirroring the boundary pixels for $\lambda_1 = 1.25$ , $\lambda_2 = 0.75$ , (b) reconstructing a cropped center area for $\lambda_1 = 1$ , $\lambda_2 = 0.25$ , (c) modifying the forward model for $\lambda_1 = 1$ , $\lambda_2 = 0.5$ . . . . .	65
4.26	MSE between reconstructed images and underlying object image with different boundary condition settings. . . . .	65
5.1	CAD layout example . . . . .	71
5.2	Design example . . . . .	71
5.3	Dictionary elements for the design example from Fig. 5.2 . . . . .	72
5.4	Phantoms for resolution structures used in simulated experiments (a) Phantom 1 (b) Phantom 2 . . . . .	74
5.5	Simulated observation images for Phantom 1 for $x$ -polarized input light: (a) SNR=10dB, (c) SNR=16dB, (e) SNR=20dB, (g) SNR=25dB, and for $y$ -polarized input light : (b) SNR=10dB, (d) SNR=16dB, (f) SNR=20dB, (h) SNR=25dB. . . . .	75
5.6	Simulated observation images for Phantom 2 for $x$ -polarized input light: (a) SNR=10dB, (c) SNR=16dB, (e) SNR=20dB, (g) SNR=25dB, and for $y$ -polarized input light: (b) SNR=10dB, (d) SNR=16dB, (f) SNR=20dB, (h) SNR=25dB. . . . .	76
5.7	Sparse image reconstruction results for Phantom 1, non-quadratic regularization (a) SNR=10dB (d) SNR=16dB (g) SNR=20dB (j) SNR=25dB, dictionary-based $\ell_1$ -regularization (b) SNR=10dB (e) SNR=16dB (h) SNR=20dB (k) SNR=25dB, dictionary-based $\ell_{1/2}$ -regularization (c) SNR=10dB (f) SNR=16dB (i) SNR=20dB (l) SNR=25dB . . . . .	77

5·8	Sparse image reconstruction results for Phantom 2, non-quadratic regularization (a) SNR=10dB (d) SNR=16dB (g) SNR=20dB (j) SNR=25dB, dictionary-based $\ell_1$ -regularization (b) SNR=10dB (e) SNR=16dB (h) SNR=20dB (k) SNR=25dB, dictionary-based $\ell_{1/2}$ -regularization (c) SNR=10dB (f) SNR=16dB (i) SNR=20dB (l) SNR=25dB . . . . .	78
5·9	MSE plot for reconstructions of Phantom 1 . . . . .	79
5·10	MSE plot for reconstructions of Phantom 2 . . . . .	79
5·11	(a) CNN structure design and SEM images for lines resolution targets with (b) 282nm (c) 252nm (d) 224nm line separation. . . . .	80
5·12	CNN-shaped polysilicon resolution target observation data with (a) $x$ -polarized input light (b) $y$ -polarized input . . . . .	81
5·13	CNN-shaped polysilicon resolution target reconstruction results with (a) non-quadratic regularization (b) dictionary-based $\ell_1$ -regularization (c) dictionary-based $\ell_{1/2}$ -regularization. . . . .	82
5·14	Cross sections from the observation and reconstructions for CNN-shaped polysilicon resolution target (a) horizontal (b) vertical . . . . .	83
5·15	Observation data of resolution target of aluminum lines with 282nm pitch (a) $x$ -polarized input light (b) $y$ -polarized input light . . . . .	84
5·16	Observation data of resolution target of aluminum lines with 252nm pitch (a) $x$ -polarized input light (b) $y$ -polarized input light . . . . .	84
5·17	Observation data of resolution target of aluminum lines with 224nm pitch (a) $x$ -polarized input light (b) $y$ -polarized input light . . . . .	85
5·18	Reconstruction results of the resolution target of aluminum lines with 282nm separation (a) non-quadratic regularization, (b) dictionary-based $\ell_1$ -regularization, (c) dictionary-based $\ell_{1/2}$ -regularization. . . . .	85

5.19	Reconstruction results of the resolution target of aluminum lines with 252nm separation (a) non-quadratic regularization, (b) dictionary-based $\ell_1$ -regularization, (c) dictionary-based $\ell_{1/2}$ -regularization. . . . .	86
5.20	Reconstruction results of the resolution target of aluminum lines with 224nm separation (a) non-quadratic regularization, (b) dictionary-based $\ell_1$ -regularization, (c) dictionary-based $\ell_{1/2}$ -regularization. . . . .	86
5.21	Cross sections from observation data and reconstructions for aluminum lines resolution target for 282nm pitch (a) horizontal (b) vertical . . .	87
5.22	Cross sections from observation data and reconstructions for aluminum lines resolution target for 252nm pitch (a) horizontal (b) vertical . . .	87
5.23	Cross sections from observation data and reconstructions for aluminum lines resolution target for 224nm pitch (a) horizontal (b) vertical . . .	88
5.24	$\ell_{1/2}$ -regularization reconstruction results of Phantom 2 observations with different initializations: "all ones" initialization (a) 10 dB (c) 16 dB (e) 20 dB (g) 25 dB, initialization with the result of $\ell_1$ -regularization (b) 10 dB (d) 16 dB (f) 20 dB (h) 25 dB. . . . .	90
5.25	$\ell_{1/2}$ -regularization reconstruction results of Phantom 1 observations with different initializations: "all ones" initialization (a) 10 dB (c) 16 dB (e) 20 dB (g) 25 dB, initialization with the result of $\ell_1$ -regularization (b) 10 dB (d) 16 dB (f) 20 dB (h) 25 dB . . . . .	91
5.26	Comparison of MSE values for reconstructions from Phantom 1 observations for a single realization . . . . .	92
5.27	Comparison of MSE values for reconstructions from Phantom 2 observations for a single realization . . . . .	92

5.28	$l_{1/2}$ -regularization reconstruction results of $282nm$ separation lines data with different initializations: (a) all ones initialization (b) initialization with the result of $l_1$ -regularization . . . . .	93
5.29	$l_{1/2}$ -regularization reconstruction results of $252nm$ separation lines data with different initializations: (a) all ones initialization (b) initialization with the result of $l_1$ -regularization . . . . .	93
5.30	$l_{1/2}$ -regularization reconstruction results of $224nm$ separation lines data with different initializations: (a) all ones initialization (b) initialization with the result of $l_1$ -regularization . . . . .	94
6.1	CAD layout of an inverter . . . . .	100
6.2	Active regions of the inverter, red: n-gate, dark green: p-gate, light green: n-drain, blue: p-drain . . . . .	101
6.3	A rectangular pulse . . . . .	102
6.4	Amplitude of modulation for all scan positions at time $t = 0.02$ ; colored dots mark scan position of the time plots: green p-type drain, blue p-type gate, purple n-type drain, pink n-type gate . . . . .	103
6.5	Amplitude of modulation for all scan positions at time $t = 0.07$ . . .	103
6.6	Modulations over time at single scan position, (a) p-type drain, (b) p-type gate, (c) n-type drain, (d) n-type gate. . . . .	104
6.7	(a) Amplitude and (b) phase of the 1st harmonic for linearly-polarized input light in $x$ -direction. . . . .	105
6.8	(a) Amplitude and (b) Phase of the 2nd harmonic for linearly-polarized input light in $x$ -direction. . . . .	106
6.9	(a) Amplitude and (b) phase of the 3rd harmonic for linearly-polarized input light in $x$ -direction. . . . .	107



6·10	(a) Amplitude and (b) phase of the 4th harmonic for linearly-polarized input light in $x$ -direction. . . . .	108
6·11	(a) Amplitude and (b) phase of the 5th harmonic for linearly-polarized input light in $x$ -direction. . . . .	109
6·12	(a) Amplitude and (b) phase of the 1st harmonic for linearly-polarized input light in $y$ -direction. . . . .	110
6·13	(a) Amplitude and (b) phase of the 2nd harmonic for linearly-polarized input light in $y$ -direction. . . . .	111
6·14	(a) Amplitude and (b) phase of the 3rd harmonic for linearly-polarized input light in $y$ -direction . . . . .	112
6·15	(a) Amplitude and (b) phase of the 4th harmonic for linearly-polarized input light in $y$ -direction . . . . .	113
6·16	(a) Amplitude and (b) phase of the 5th harmonic for linearly-polarized input light in $y$ -direction . . . . .	114
6·17	(a) Amplitude and (b) phase of the 1st harmonic of the reconstruction result of space-frequency sparse representation using all 5 harmonics. Phase values corresponding to amplitudes lower than 1 are set to 0. .	116
6·18	(a) Amplitude and (b) phase of the 2nd harmonic of the reconstruction result of space-frequency sparse representation using all 5 harmonics. Phase values corresponding to amplitudes lower than 1 are set to 0. .	117
6·19	(a) Amplitude and (b) phase of the 3rd harmonic of the reconstruction result of space-frequency sparse representation using all 5 harmonics. Phase values corresponding to amplitudes lower than 1 are set to 0. .	118
6·20	(a) Amplitude and (b) phase of the 4th harmonic of the reconstruction result of space-frequency sparse representation using all 5 harmonics. Phase values corresponding to amplitudes lower than 1 are set to 0. .	119

6·21	(a) Amplitude and (b) phase of the 5th harmonic of the reconstruction result of space-frequency sparse representation using all 5 harmonics. Phase values corresponding to amplitudes lower than 1 are set to 0. .	120
6·22	(a) Amplitude and (b) phase of the 1st harmonic of the reconstruction result of space-frequency sparse representation using 3 harmonics. Phase values corresponding to amplitudes lower than 1 are set to 0. .	121
6·23	(a) Amplitude and (b) phase of the 2nd harmonic of the reconstruction result of space-frequency sparse representation using 3 harmonics. Phase values corresponding to amplitudes lower than 1 are set to 0. .	122
6·24	(a) Amplitude and (b) phase of the 3rd harmonic of the reconstruction result of space-frequency sparse representation using 3 harmonics. Phase values corresponding to amplitudes lower than 1 are set to 0. .	123
6·25	(a) Amplitude and (b) phase of the 1st harmonic of the reconstruction result of space-frequency sparse representation using only 1st harmonic. Phase values corresponding to amplitudes lower than 1 are set to 0. .	124
6·26	(a) Amplitude and (b) phase of the 1st harmonic of the ground truth	125
6·27	(a) Amplitude and (b) phase of the 2nd harmonic of the ground truth	126
6·28	(a) Amplitude and (b) phase of the 3rd harmonic of the ground truth	127
6·29	(a) Amplitude and (b) phase of the 4th harmonic of the ground truth	128
6·30	(a) Amplitude and (b) phase of the 5th harmonic of the ground truth	129
6·31	Comparison of the vertical cross sections of the amplitude of the first harmonic: (a) p-type transistor, (b) n-type transistor. The cross sections for all 5 harmonics reconstruction and only 3 harmonics reconstruction overlap. . . . .	130
6·32	The MSE for the first harmonic of the reconstructions . . . . .	130

6.33	Amplitude of observed modulation (Fourier series expansion of 5 harmonics) in all scan positions for $x$ -polarized input light (a) at time point $t = 0.02$ (a) at time point $t = 0.07$ . . . . .	132
6.34	Amplitude of the observed modulation (Fourier series expansion of 5 harmonics) at all scan positions for $y$ -polarized input light (a) at time $t = 0.02$ , (b) at time $t = 0.07$ . . . . .	133
6.35	Amplitude of the observed modulation (Fourier series expansion of 3 harmonics) at all scan positions for $x$ -polarized input light (a) at time $t = 0.02$ , (b) at time $t = 0.07$ . . . . .	134
6.36	Amplitude of the observed modulation (Fourier series expansion of 3 harmonics) at all scan positions for $y$ -polarized input light (a) at time $t = 0.02$ , (b) at time $t = 0.07$ . . . . .	135
6.37	Amplitude of the observed modulation (Fourier series expansion of 1 harmonic) at all scan positions for $x$ -polarized input light (a) at time $t = 0.02$ , (b) at time $t = 0.07$ . . . . .	136
6.38	Amplitude of the observed modulation (Fourier series expansion of 1 harmonic) at all scan positions for $y$ -polarized input light (a) at time $t = 0.02$ , (b) at time $t = 0.07$ . . . . .	137
6.39	Observed modulations (Fourier series expansion of 5 harmonics) over time at a single scan position: (a) p-type drain, (b) p-type gate, (c) n-type drain, (d) n-type gate for $x$ -polarized input light. . . . .	138
6.40	Observed modulations (Fourier series expansion of 5 harmonics) over time at a single scan position: (a) p-type drain, (b) p-type gate, (c) n-type drain, (d) n-type gate for $y$ -polarized input light. . . . .	139

6.41	Observed modulations (Fourier series expansion of 3 harmonics) over time at a single scan position: (a) p-type drain, (b) p-type gate, (c) n-type drain, (d) n-type gate for $x$ -polarized input light. . . . .	140
6.42	Observed modulations (Fourier series expansion of 3 harmonics) over time at a single scan position: (a) p-type drain, (b) p-type gate, (c) n-type drain, (d) n-type gate for $y$ -polarized input light. . . . .	141
6.43	Observed modulations (Fourier series expansion of 1 harmonic) over time at a single scan position: (a) p-type drain, (b) p-type gate, (c) n-type drain, (d) n-type gate for $x$ -polarized input light. . . . .	142
6.44	Observed modulations (Fourier series expansion of 1 harmonic) over time at a single scan position: (a) p-type drain, (b) p-type gate, (c) n-type drain, (d) n-type gate for $y$ -polarized input light. . . . .	143
6.45	Amplitude of the reconstructed modulation (using all 5 harmonics) for all scan positions (a) at time $t = 0.02$ (b) at time $t = 0.07$ . . . . .	144
6.46	Reconstructed modulation (using all 5 harmonics) over time at a single scan position: (a) p-type drain, (b) p-type gate, (c) n-type drain, (d) n-type gate. . . . .	145
6.47	Amplitude of the reconstructed modulation (using only first 3 harmonics) for all scan positions (a) at time $t = 0.02$ , (b) at time $t = 0.07$ . . . . .	146
6.48	Reconstructed modulation (using only first 3 harmonics) over time at a single scan position: (a) p-type drain, (b) p-type gate, (c) n-type drain, (d) n-type gate. . . . .	147
6.49	Amplitude of the reconstructed modulation (using only first harmonic) for all scan positions (a) at time $t = 0.02$ , (b) at time $t = 0.07$ . . . . .	148

6.50	Reconstructed modulation (using only first harmonic) over time at a single scan position: (a) p-type drain, (b) p-type gate, (c) n-type drain, (d) n-type gate. . . . .	149
6.51	Comparison of vertical cross sections of all scan positions data at time point $t = 0.02$ (a) from p-type transistor (b) from n-type transistor. The cross sections for all 5 harmonics reconstruction and only 3 harmonics reconstruction almost overlap. . . . .	150
6.52	The mean MSE for the reconstruction amplitude at all scan positions at time point $t = 0.02$ and $t = 0.07$ . . . . .	150
6.53	Comparison of amplitudes of the reconstructed modulation for all scan positions at time $t = 0.02$ (a) space-time representation (b) space-frequency representation . . . . .	152
6.54	Comparison of amplitudes of the reconstructed modulation for all scan positions at time $t = 0.07$ (a) space-time representation (b) space-frequency representation . . . . .	153
6.55	Comparison of the reconstructed modulations over time at a single scan position: (a) p-type drain, (b) p-type gate, (c) n-type drain, (d) n-type gate. . . . .	154
6.56	Comparison of vertical cross sections of all scan positions at time $t = 0.02$ : (a) p-type transistor, (b) n-type transistor. . . . .	155
6.57	True cluster labels for the underlying modulation . . . . .	155
6.58	Cluster labels of LVI data under linearly-polarized light in $x$ -direction: (a) 5 harmonics (c) 3 harmonics (e) 1 harmonic, under linearly-polarized light in $y$ -direction: (b) 5 harmonics (d) 3 harmonics (f) 1 harmonic .	156

6.59	Cluster labels for sparse space-time representation: (a) 5 harmonics (c) 3 harmonics (e) 1 harmonic, sparse space-frequency representation: (b) 5 harmonics (d) 3 harmonics (f) 1 harmonic. . . . .	157
6.60	Comparison of localization accuracy . . . . .	158
7.1	Confocal microscope setup. (Collimated beam from 1310nm laser; GM galvanometric mirror; LP linear polarizer; QWP quarter-wave plate; aSIL aplanatic solid immersion lens; pinhole is 10nm . . . . .	161
7.2	(a) Metal lines separated by 252nm, 282nm on a resolution target, imaged using 1310nm circular polarization without linear polarizer in the return path. (b) The same set of metal lines imaged with a linear polarizer and quarter wave plate in place. (c) The intensity profile corresponding to dashed lines in (a) and (b). The dashed line is for circularly-polarized illumination, and the solid line is for the case of linear polarizer and quarter wave plate inserted (b). . . . .	162
7.3	Locations of cross sections used to estimate the LSF of the system. .	163
7.4	(a) SEM image of metal aluminum lines separated by 252nm (right) and 224nm (left), and fabricated on a double-side polished silicon wafer, (b) dark-field subsurface microscopy image. . . . .	166
7.5	(a) Average of cross sections from the center of lines and a least-squares spline approximation to this average (b) The estimated LSF which is the derivative of the least-squares spline approximation and the airy disk fit to this estimated LSF . . . . .	167
7.6	The estimated PSF of the system . . . . .	168
7.7	252nm spacing vertical lines: (a) observation, (b) image reconstruc- tion result based on non-quadratic regularization, (c) dictionary-based image reconstruction result. . . . .	169

7.8	224nm spacing vertical lines: (a) observation, (b) image reconstruction result based on non-quadratic regularization, (c) dictionary-based image reconstruction result. . . . .	170
7.9	224nm spacing horizontal lines: (a) observation, (b) image reconstruction result based on non-quadratic regularization, (c) dictionary-based image reconstruction result. . . . .	171
8.1	Examples of experimental observation data under linearly polarized input light with polarization in $x$ -direction with longitudinal focus point label: (a) 1, (b) 7, (c) 10, (d) 22, (e) 28, (f) 30. . . . .	175
8.2	Examples of experimental observation data under linearly polarized input light with polarization in $y$ -direction with longitudinal focus point label: (a) 1, (b) 7, (c) 10, (d) 22, (e) 28, (f) 30. . . . .	176
8.3	Examples of PSFs under linearly-polarized input light with polarization in the $x$ -direction with longitudinal focus point $z_0 =$ (a) $-340 \mu m$ , (b) $-280 \mu m$ , (c) $-240 \mu m$ , (d) $-180 \mu m$ , (e) $-140 \mu m$ , (f) $-100 \mu m$ , (g) $-60 \mu m$ , (h) $-20 \mu m$ , (i) $0 \mu m$ , (j) $15 \mu m$ , (k) $25 \mu m$ , (l) $55 \mu m$ . . . .	178
8.4	Estimated longitudinal focus point vs experimental data $z$ label. . . .	179

## List of Abbreviations

aSIL	.....	aplanatic Solid Immersion Lens
ASR	.....	Angular Spectrum Representation
BS	.....	Beam Splitter
CAD	.....	Computer-aided Design
CG	.....	Conjugate Gradient
DUT	.....	Device Under Test
FA	.....	Failure Analysis
FDTD	.....	Finite Difference Time Domain
FEM	.....	Finite Element Method
FT	.....	Fourier Transform
FWHM	.....	Full Width at Half Maximum
GRS	.....	Gaussian Reference Sphere
LSF	.....	Line Spread Function
LVI	.....	Laser Voltage Imaging
LVP	.....	Laser Voltage Probing
MOM	.....	Method of Moments
MOSFET	.....	Metal-Oxide-Semiconductor Field-Effect Transistor
MSE	.....	Mean Square Error
NA	.....	Numerical Aperture
OBIC	.....	Optical Beam Induced Current Imaging
OBIRCH	.....	Optical Beam Induced Resistance Change
PEM	.....	Photon Emission Microscopy
PSF	.....	Point Spread Function
SEM	.....	Scanning Electron Microscope
SNR	.....	Signal-to-Noise Ratio
TIVA	.....	Thermally Induced Voltage Alteration



## Chapter 1

# Introduction

Integrated circuit (IC) failure analysis (FA) is the investigation of failure mechanisms during manufacturing process of semiconductor devices. This analysis is crucial to increase the fabrication yield and thus the profit of IC industry. Therefore, it is essential for FA methods to meet the quality requirements in semiconductor device manufacturing. Optical FA is an example of non-invasive fault analysis where optical images of static IC components or dynamic optical measurements of device activity are obtained. Optical techniques for defect detection are limited to backside analysis methods through the silicon substrate because opaque metal interconnect layers and flip-chip bonding obscure the front (Goldstein et al., 1993; Serrels et al., 2008). The rapid decrease in dimensions of IC features necessitates the use of higher resolution optical FA techniques. The highest resolution in backside optical FA was achieved by using applanatic solid immersion lenses (aSILs) thanks to their high numerical aperture (NA) capabilities (Ippolito et al., 2001; Serrels et al., 2008; Köklü et al., 2009). The optical microscopy efforts for increasing resolution of backside optical FA systems continue through hardware modifications, such as the use of radially polarized light for illumination (Yurt et al., 2014a) and the use of apodization masks (Vigil et al., 2014), but they are not enough to meet the requirements of new ICs with smaller and denser components. Therefore, there is a need for model-based signal processing approaches to increase resolution. This thesis focuses on the development of sparse reconstruction methods to increase resolution of optical images of static IC compo-

nents and dynamic optical measurements of device activity. Fig. 1.1 (Liao et al., 2010) shows examples of optical FA data. The gray scale image of static IC components is overlaid with the optical measurement of device activity shown in yellow and green. Yellow corresponds to operation at data frequency and green corresponds to operation at clock frequency. Fig. 1.1a shows data from a properly functioning device whereas Fig. 1.1b shows data from a faulty device where faulty regions are marked. The optical measurements of device activity have higher intensities around the faulty regions.

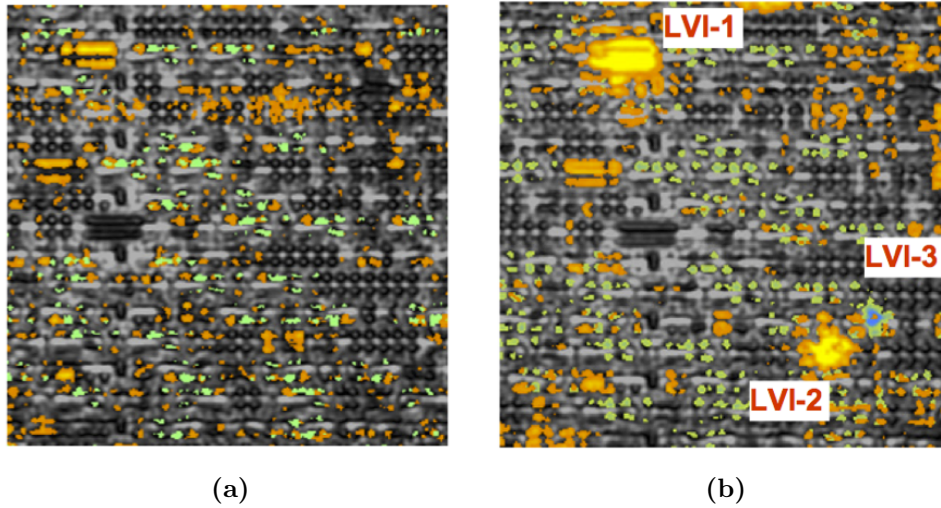


**Figure 1.1:** Optical measurements of (a) a properly-functioning die and (b) a faulty die

In high NA systems, properties of focused light near dielectric interfaces cannot be explained by scalar optics theory thus requiring full vectorial analysis of fields (Richards and Wolf, 1959; Köklü et al., 2009). One such property is that spatial resolution improvement in selected directions can be obtained by changing the polarization direction of linearly polarized illumination (Köklü et al., 2009; Serrels et al., 2008). For an arbitrarily-shaped material object, the response of the high NA system is nonlinear and the modeling of such a system requires vectorial analysis where light

is treated as an electromagnetic field (Török et al., 2008; Chen et al., 2012).

## 1.1 Contributions

The first contribution of this thesis is the development of approximate linear time-invariant (LTI) point spread functions (PSF) that is appropriate for high-NA optical systems. The goal is to use the PSF in a linear inverse problem formulation to increase the resolution of the optical FA data. We propose a PSF model which accounts for the change in system response for different material objects and their different sizes, and which respects the underlying physics.

The second contribution of this thesis is a novel analysis-based sparsifying image reconstruction framework which benefits from polarization diversity of high NA optical systems. In an analysis-based sparsity paradigm an analysis operator is applied to the underlying signal and the sparsity is enforced on the analysis coefficients (Chen et al., 2001; Cetin et al., 2014). When linearly polarized light is used, altering the polarization direction enables the collection of optical images with varying spatial resolution in different directions. A single image with higher resolution can be obtained through an image reconstruction framework which combines a set of images taken with linearly polarized light in various polarization directions. Additionally, this framework benefits from prior knowledge about features in ICs by incorporating non-quadratic regularization functionals in the image reconstruction framework. These non-quadratic regularization functionals enforce the sharpness of edges in the reconstructed image and enable the recovery of small scatterers. A non-quadratic regularization for resolution improvement in optical systems has been proposed in (Gazit et al., 2009) but it has not been used for high NA optical systems where we can benefit from polarization diversity.

The third contribution of this thesis is a synthesis-based sparsity paradigm using

overcomplete dictionaries for IC imaging. In a synthesis-based sparsity paradigm, the underlying signal is represented by an overcomplete dictionary and the sparsity is imposed on the representation coefficients (Chen et al., 2001; Cetin et al., 2014). The domain of IC imaging is particularly suitable for the application of overcomplete dictionaries in an image reconstruction framework because the images are highly structured, containing predictable building blocks derivable from the corresponding computer-aided design (CAD) layouts. This structure provides a strong and natural a-priori dictionary for scene reconstruction.

The fourth contribution of this thesis is the use of space-time and space-frequency dictionaries for dynamic imaging. These methods are an extension of 2D dictionary representation to 3D. Space-time or space-frequency dictionaries are used to represent optical measurements of device activity. Laser voltage imaging (LVI) is an optical FA technique which produces images of active regions operating at a specific frequency. We propose a framework where amplitude and phase images at multiple frequencies can be collected and combined through space-time or space-frequency dictionary-based sparse representation in order to obtain high-resolution images of device activity. The proposed 3D dictionaries couple the spatial regions of active areas with same signature over time or over frequency through space-time or space-frequency dictionary elements.

The fifth contribution of this thesis is a new focus determination method for high-NA subsurface imaging. The shape and support of the spot created by the focused laser light in high-NA systems change when the focus is varied in longitudinal direction near a dielectric interface (Koklu and Unlu, 2009). The proposed focus determination method uses this property to determine the focus point of the focus stack and find the best focus.

## 1.2 Thesis organization

In Chapter 2, we first review linear inversion problems and different regularization approaches for linear inversion problems. We also present a review of backside optical FA methods, aSIL microscopy and the optical model of aSIL microscopy. Mathematical expressions for different components of aSIL microscopy are given in Section 2.3.2.

In Chapter 3, a PSF model is developed to be used in linear inverse problems where the nonlinear optical system is approximated by a linear convolution with the developed PSF. The PSF model accounts for the vectorial properties of high NA systems as well as the dependence of the system response to the material and the size of the object.

In Chapter 4, we present an analysis-based sparse image reconstruction framework using non-quadratic regularization functionals. This framework benefits from polarization diversity of high-NA systems and provides image enhancement and resolution improvement for images obtained using such systems.

In Chapter 5, we introduce an overcomplete dictionary-based sparse scene representation for IC images and formulate a synthesis-based sparse reconstruction framework to improve resolution of IC images.

In Chapter 6, we extend the dictionary-based representation to space-time and space-frequency in order to apply the synthesis-based sparse reconstruction framework to optical measurements of device activity.

In Chapter 7, an application of the proposed reconstruction framework to dark-field subsurface imaging microscopy is presented. Additionally, a method in order to estimate the PSF of the darkfield subsurface imaging microscopy system from observation data is proposed.

In Chapter 8, a focus determination method for high NA subsurface imaging is proposed.

Finally, Chapter 9 includes summary and conclusions of this thesis and gives pointers for future research directions.

## Chapter 2

# Background

### 2.1 Linear inverse problems and regularization

In this dissertation, inversion techniques are used to provide resolution improvement for IC fault detection. This section provides background information on inversion methods. Conventional inversion techniques and their shortcomings are described in order to motivate advanced inversion methods.

A linear inverse problem (Karl, 2000; Demoment, 1989) can be defined as the problem of finding an estimate  $\hat{\mathbf{f}}$  of an unknown underlying object  $\mathbf{f}$  from perturbed observations  $\mathbf{g}$  given a linear observation model  $H$ . The observation model can be formulated as follows:

$$\mathbf{g} = H\mathbf{f} + \mathbf{w}, \quad (2.1)$$

where  $\mathbf{w}$  is the measurement noise. The three main difficulties in such a problem are non-uniqueness of the solution, non-existence of a solution and the ill-conditionedness of the observation matrix  $H$ . The solution is not unique when the nullspace of  $H$  is not empty. If a solution does not exist,  $\mathbf{g}$  does not lie in the range space of  $H$ . When  $H$  is ill-conditioned, small perturbations in  $\mathbf{g}$  might cause drastic changes in the estimate of  $\mathbf{f}$ .

A solution to the problem in (2.1) can be found through least-squares:

$$\hat{\mathbf{f}}_{\text{ls}} = \arg \min_{\mathbf{f}} \| H\mathbf{f} - \mathbf{g} \|_2^2, \quad (2.2)$$

where  $\| \cdot \|_2$  denotes the  $l_2$  norm. The least-squares solution satisfies the normal equations:

$$H^T H \hat{\mathbf{f}}_{ls} = H^T \mathbf{g}. \quad (2.3)$$

The solution found this way, called generalized solution, is the minimum norm solution. The minimum norm solution solves problems resulting from non existence and non uniqueness of a solution. However, if  $H$  is ill-conditioned, small perturbations in  $\mathbf{g}$  can still result in drastic changes in a generalized solution. This instability can be solved through regularization. Another benefit of regularization is that it enables incorporation of prior information about the unknown object  $\mathbf{f}$  into the problem formulation. Hence, the solution will both satisfy the observations and the *a priori* features.

### 2.1.1 Tikhonov Regularization

Tikhonov regularization (Tikhonov, 1963), one of the most common regularization methods, addresses the ill-conditionedness by augmenting the least-squares cost function with a regularization term, for example:

$$\hat{\mathbf{f}}_{\text{tik}} = \arg \min_{\mathbf{f}} \| H\mathbf{f} - \mathbf{g} \|_2^2 + \lambda \| L\mathbf{f} \|_2^2, \quad (2.4)$$

where  $\lambda$  is the regularization parameter,  $L$  is a matrix. The matrix  $L$  can be an identity matrix giving preference to solutions with smaller norms or it can be a highpass operator enforcing smoothness if the underlying object  $\mathbf{f}$  is mostly continuous. The regularization parameter  $\lambda$  adjusts the trade-off between the regularization term and the first term called the data fidelity term. In other words, it adjusts how much prior information will be enforced and how much the solution will fit to the observations.



Tikhonov solution of (2.4) satisfies the following normal equations:

$$(H^T H + \lambda L^T L) \hat{\mathbf{f}}_{\text{tik}} = H^T \mathbf{g}. \quad (2.5)$$

### 2.1.2 Non-quadratic regularization

The non-quadratic regularization is an example of analysis-based sparsity approach. The regularization term in Tikhonov regularization is quadratic in  $\mathbf{f}$ , and leads to normal equations which are linear in  $\mathbf{f}$ . Therefore, it has a straightforward and computationally efficient solution which only requires linear processing. However, it has limitations in the type of features it can recover in  $\mathbf{f}$ . Mainly, Tikhonov regularization is limited in recovering the high frequency components in  $\mathbf{f}$ . Nonetheless, if we use non-quadratic regularization terms, we could incorporate prior information which will allow recovery of high frequency information (Karl, 2000). A non-quadratic regularization problem has the following form:

$$\hat{\mathbf{f}} = \arg \min_{\mathbf{f}} \| H\mathbf{f} - \mathbf{g} \|_2^2 + \lambda J_{\text{reg}}(\mathbf{f}), \quad (2.6)$$

where  $J_{\text{reg}}(\mathbf{f})$  is the non-quadratic regularization term. Examples of non-quadratic regularization include total variation regularization and  $\ell_p$ -norm regularization with  $0 < p \leq 1$ .

Total variation regularization helps preserving edges in the estimated  $\mathbf{f}$  and results in piecewise constant regions (Ring, 2000; Vogel and Oman, 1998). The regularization term for total variation is given by:

$$J_{\text{reg}}(\mathbf{f}) = \| D\mathbf{f} \|_1, \quad (2.7)$$

where  $D$  is a gradient operator. This edge preserving behavior can be explained by the sparsity-enforcing property of the  $\ell_p$ -norm with  $0 < p \leq 1$ . By enforcing sparsity of the gradient, it enforces sparsity of the edges and this results in piecewise continuous

regions.

$\ell_p$ -norm regularization choose  $J_{reg}$  as follows:

$$J_{reg}(\mathbf{f}) = \|\mathbf{f}\|_p^p, \quad (2.8)$$

One of the characteristics of this non-quadratic regularizer is that it does not penalize large values in the estimated  $\mathbf{f}$  as much as the standard quadratic  $\ell_2$  penalty does (Karl, 2000). This behavior can be seen in Fig. 2.1, where values of  $\|f\|_p^p$  are plotted for  $p = \{0.5, 1, 2\}$ . This shows that when  $\|f\|_p^p$  is a regularization term in a minimization problem, large values of  $f$  are penalized less when  $p$  gets smaller. Donoho et. al. (Donoho et al., 1992) show that  $\ell_p$ -norms do not penalize large amplitudes as much and they force the amplitudes in the estimate of  $f$  below certain threshold to zero. Therefore, they enforce sparse solutions with concentrated energy. This behavior helps recovering strong small scatterers and high-frequency information.

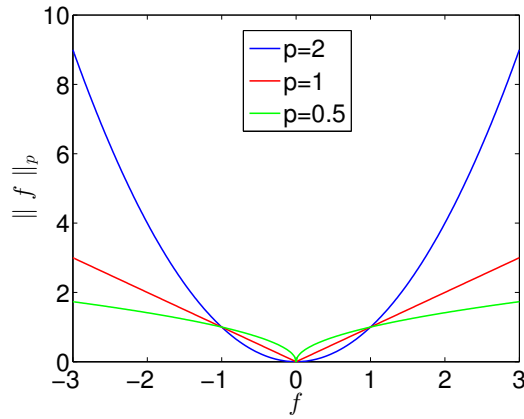


**Figure 2.1:** Behavior of  $\ell_p$ -norm for  $p = 0.5, 1, 2$

One approach in non-quadratic regularization is to use combinations of  $\ell_p$  regularization functionals combining total variation regularization term with  $\ell_p$ -regularization term which enhances small scatterers:

$$\hat{\mathbf{f}} = \arg \min_{\mathbf{f}} \|\mathbf{H}\mathbf{f} - \mathbf{g}\|_2^2 + \lambda_1 \|\mathbf{D}\mathbf{f}\|_p^p + \lambda_2 \|\mathbf{f}\|_p^p, \quad (2.9)$$

where  $\lambda_1$  and  $\lambda_2$  are regularization parameters. The second term in Eq. 2.9 favors sparsity in the edge field of the reconstructed image and the third term favors the sparsity in the reconstructed image. This type of regularization, which enforces both piecewise continuous regions with sharp edges and point-like small scatterers, has been successfully applied to synthetic aperture radar imaging (Çetin and Karl, 2001) and to ultrasound imaging (Tuysuzoglu et al., 2012). In Chapter 4, we propose an image reconstruction framework for IC imaging which is based on this type of non-quadratic regularization.

### 2.1.3 Dictionary-based sparse regularization

The dictionary-based sparse regularization is an example of synthesis-based sparsity approach. If the underlying image is not sparse in data acquisition domain but it can be sparsely represented in another domain, an overcomplete dictionary-based representation can be used to sparsely represent the underlying image:

$$\mathbf{f} = \Phi \boldsymbol{\eta}, \quad (2.10)$$

where  $\Phi$  is the appropriate overcomplete dictionary and  $\boldsymbol{\eta}$  is the vector of representation coefficients. Then, the dictionary-based sparse regularization problem can be expressed as follows:

$$\hat{\boldsymbol{\eta}} = \arg \min_{\boldsymbol{\eta}} J(\boldsymbol{\eta}) = \| H\Phi \boldsymbol{\eta} - \mathbf{g} \|_2^2 + \lambda \| \boldsymbol{\eta} \|_p^p. \quad (2.11)$$

Sparse signal representation based on overcomplete dictionaries is a well-studied topic in the image reconstruction literature. However, the way the overcomplete dictionaries are built differs according to the application domain. One approach is to use a set of training images in order to learn the overcomplete dictionary and then an image reconstruction framework is formulated where the underlying image is

represented as a sparse linear combination of the elements of the learned dictionary (Aharon et al., 2006; Elad and Aharon, 2006; Donoho et al., 2006). In another approach, a predetermined overcomplete dictionary can be built to sparsely represent the scene being imaged, such as a wavelet-based dictionary (Starck et al., 2005; Donoho and Johnstone, 1994), a point- and region-based dictionary or a shape-based dictionary (Samadi et al., 2009). In Chapter 5, we propose a predetermined overcomplete dictionary-based image reconstruction framework for IC imaging. The predetermined dictionary that we are using in Chapter 5 is an adaptation of shape- and region-based dictionary approach that exploits the structure of ICs and prior information about their dimensions.

## 2.2 Backside optical fault analysis techniques

Gordon E. Moore predicted the rapid decrease in IC dimensions (Moore, 1998) and this decrease continues as predicted. The miniaturization of ICs happens in stages because new dimensions require new design rules, changing the fabrication techniques and necessitating modifications in the manufacturing plants. These new stages are referred to as new process nodes. New potential failure reasons appear with new fabrication techniques requiring advanced failure analysis (FA) methods. FA is the technical field of inspecting the failure mechanisms during the manufacturing process of semiconductor devices. The success of this field affects the fabrication yield which is the proportion of operational circuits to the total number of fabricated circuits. Therefore, since the profit of the IC industry heavily depends on yield, it is critical that FA techniques meet the standards required by new process nodes.

FA techniques can be classified into following categories: electrical test, optical imaging/analysis, physical techniques, electron beam imaging/analysis, ion beam techniques, scanning probe techniques. Electrical tests are used to detect faults in

an IC and an effective test circuit design can narrow down the fault area. The other techniques are used to find and localize the defect. Examples of physical techniques are mechanical or ion beam cutting, layer removal and deprocessing to expose deeper layers of an IC and cross sectioning to view a slice of an IC (Soden and Anderson, 1993). The issue with these techniques is that they cannot be used to analyze ICs while they are active. Examples of techniques which were used to measure waveforms from the front side are electrical beam probing and e-beam probing. However, due to the increase in density of opaque metal interconnect layers and due to flip-chip bonding in ICs, access to internal nodes from the front-side became limited (Goldstein et al., 1993). Therefore, backside analysis techniques have been developed to measure waveforms of devices through the silicon substrate. Examples of backside optical fault analysis techniques are optical-beam-induced resistance change (Nikawa et al., 1999), thermally-induced voltage alteration (TIVA) (Cole and Soden, 1994), optical-beam-induced current imaging (OBIC) (Xu and Denk, 1999), laser voltage probing (LVP) (Kolachina, 2011), laser voltage imaging (Ng et al., 2010) and photon emission microscopy (PEM) (Chim, 2000). Besides FA through electrical, thermal and photo remission response data, it is also very critical to acquire high-resolution optical images of ICs taken from the backside because these reflection images are required for the lateral registration of fault analysis data to the circuit layout. In this dissertation, we focus on resolution improvement and image enhancement of these reflection images as well as resolution improvement and timing behavior analysis of LVI data. In the following subsections, we review LVP and LVI FA techniques.

### **2.2.1 Laser voltage probing**

Laser Voltage Probing (LVP) is a backside optical measurement technique of device activity at a specific location on the ICs. LVP measurements are time-domain measurements of the modulation in the operating device. LVP was first developed as a

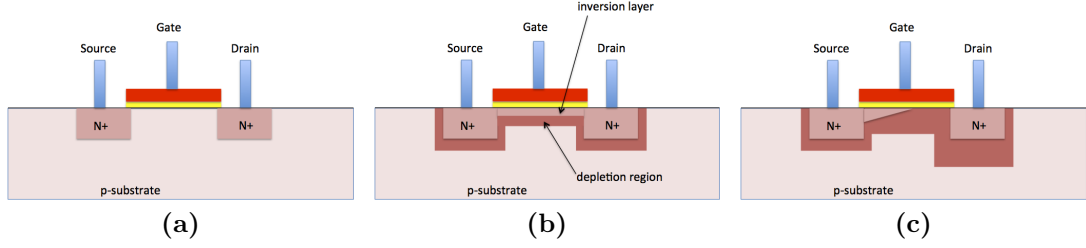


**Figure 2-2:** Cross sectional diagram of a MOSFET (a) off-state, (b)linear operating regime , (c)saturation regime.

noninvasive probing technique by Henrich et. al. (Henrich et al., 1986). Kindereit et. al. quantitatively investigated laser beam modulation in electrically-active devices and explained the origin of the modulation in the laser beam reflected from the active device (Kindereit et al., 2008; Kindereit et al., 2007; Kindereit, 2009). Fig. 2-2 shows a cross-sectional diagram of a metal-oxide-semiconductor field-effect transistor (MOSFET) in the off-state, the linear operating regime and the saturation regime. When the transistor is driven with a pulse, it is switching between these states. If the input is fast enough, the time in which the transistor operates in the saturation regime is very short. In the linear operating and the saturation regimes, there are extra layers called inversion layer and depletion region. These layers are formed because the free carrier densities are changed as a result of the applied voltage. This change in free carrier densities causes a change in the refractive index  $n$  and in the absorption coefficient  $\alpha$ , modeled by the following equations (Soref and Bennett, 1987; Bruce et al., 1999)

$$\Delta n = -\frac{\lambda^2 q^2}{8\pi^2 c_0^2 \epsilon_0 n_0} \left[ \frac{\Delta N_e}{m_e} + \frac{\Delta N_h}{m_h} \right] \quad (2.12)$$

$$\Delta \alpha = \frac{\lambda^2 q^3}{4\pi^2 c_0^3 \epsilon_0 n_0} \left[ \frac{\Delta N_e}{m_e^2 \mu_e} + \frac{\Delta N_h}{m_h^2 \mu_h} \right] \quad (2.13)$$

where  $\Delta n$  and  $\Delta \alpha$  are changes in refractive index and absorption coefficient,  $n_0$  is the index of un-doped silicon,  $q$  is the electron charge,  $\lambda$  is the wavelength,  $\epsilon_0$  is the permittivity of free space,  $c_0$  is the speed of light in vacuum,  $\mu$  is the mobility,  $m$  is

the effective mass and  $\Delta N$  is the change in charge carrier densities.

When a laser is focused on one specific position in these regions while the transistor is switching, there is a change in the reflected light because of the change in refractive index and in absorption coefficient. Therefore, when the transistor is driven by a rectangular pulse, we observe a modulation in the reflected light correlated with the voltage change in the rectangular pulse. LVP is a technique to measure these modulations. Fig. 2.3, adapted from (Kindereit et al., 2008), shows the setup for collecting LVP measurements. The laser is focused on the device under test (DUT). The laser beam reflected from the active device ( $R(x, y, t)$ ) is converted to electrical signal ( $R_n(x, y, t)$ ) by a detector. The reflected light can be expressed as  $R(x, y, t) = R_0(x, y) + \Delta R(x, y, t)$ , where  $R_0(x, y)$  is the reflection from the static parts and  $\Delta R(x, y, t)$  is the modulating part of the reflected light coming from the active regions. LVP measurements ( $LVP(x, y, t)$ ) are time domain measurements of the RF part of the signal which are observed by an oscilloscope.

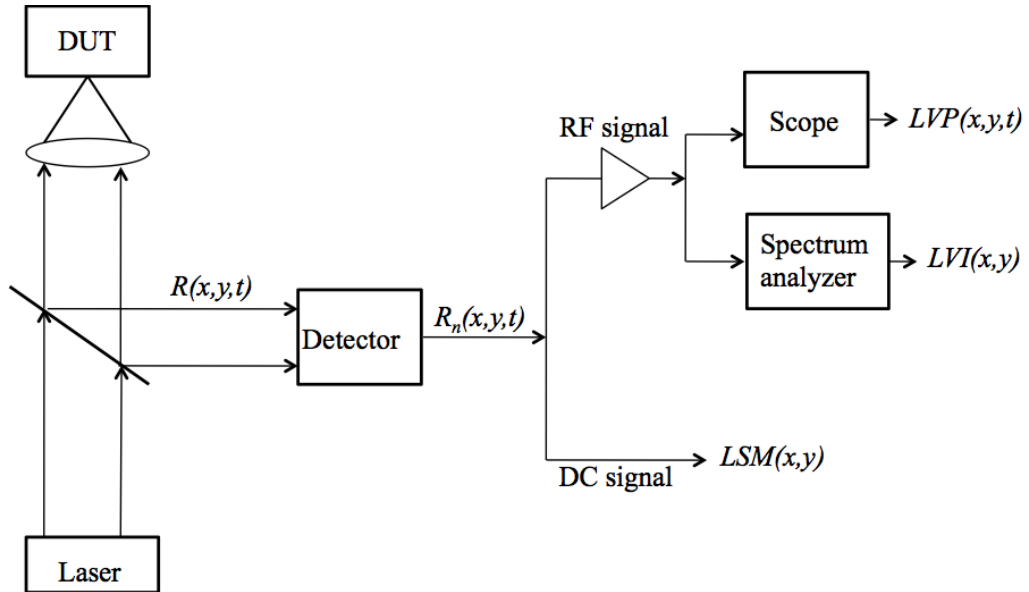


**Figure 2.3:** Experimental configuration for LVP and LVI measurements

### 2.2.2 Laser voltage imaging

One main problem for LVP measurements is the noise level. The change  $\Delta R$  is very small, 600 parts per million, compared to  $R_0$  and the variance of the noise is correlated with the amplitude of  $R$ . Therefore, the modulation can only be observed after averaging multiple times making the LVP measurements time consuming, taking a few minutes per waveform. Therefore, another measurement technique, called Laser Voltage Imaging (LVI) has been developed (Ng et al., 2010).

$$\begin{aligned}
 F(x, y, w) &= \|FT\{R_n(x, y, t)\}\|, \\
 LVI(x, y) &= F(x, y, w_c), \\
 LSM(x, y) &= F(x, y, 0),
 \end{aligned}
 \tag{2.14}$$

where  $FT\{.\}$  denotes fourier transform (FT),  $w_c$  is the operating frequency of the device which is driven by a periodic rectangular pulse,  $LVI(x, y)$ , is the LVI measurement. Thus, LVI measurement records the amplitude and the phase at a specific frequency in the frequency domain. Since the noise is distributed across all frequencies, it is filtered when only looking at single frequency enabling faster data acquisition for LVI than for LVP. Therefore, the laser can be raster-scanned in order to produce amplitude modulation images. Additionally, the DC part of the signal obtained at the detector is also recorded for each  $(x, y)$  location producing an aligned optical image of the device,  $LSM(x, y)$ . It is also possible to use lock-in amplifiers instead of a spectrum analyzer in order to record the phase data to produce amplitude phase maps (Yurt et al., 2012). Examples of LSM data, amplitude modulation image and amplitude phase map are shown in Fig. 2.4. These measurements are taken from an active inverter chain in a  $32nm$  process node technology device.



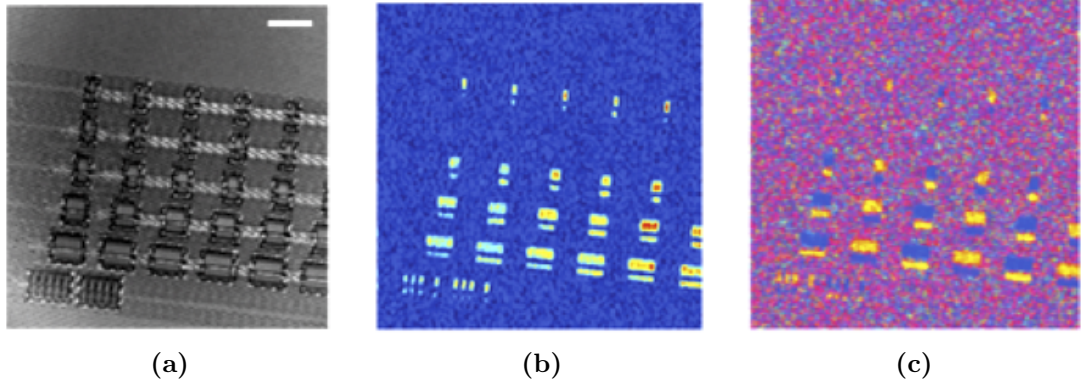


**Figure 2.4:** Data collected from an active inverter chain (a) LSM image and LVI image: (b) amplitude modulation image (c) amplitude phase map

## 2.3 Applanatic solid immersion lens microscopy for integrated circuit imaging and its optical model

Back-side fault isolation and failure analysis through the silicon substrate became more significant for optical inspection of ICs with increasing component density and use of metal interconnect layers (Serrels et al., 2008). In order to overcome resolution limitations of imaging through the silicon substrate, applanatic solid immersion lenses (aSILs) with effective numerical apertures (NA) approaching the index of the substrate ( $NA \simeq 3.5$ ) are required (Köklü et al., 2009). In this dissertation, the focus of the resolution improvement techniques is on the optical fault analysis devices which use aSILs. In this section, necessary background on aSIL microscopy of ICs and how such an optical system can be modeled are presented.

### 2.3.1 Applanatic solid immersion lenses for integrated circuit imaging

The fundamental diffraction limit that defines the lateral spatial resolution in optical microscopy is the Abbe limit (Abbe, 1873). It is given by:  $\frac{\lambda_0}{2NA}$ , where  $\lambda_0$  is the free-space wavelength of light and  $NA$  is the numerical aperture defined as  $NA =$

$n \sin \theta_{max}$  in terms of refractive index  $n$  of the medium and collection angle  $\theta_{max}$ . The collection angle is the maximum angle of light collected from the structures of interest. Based on the Abbe limit, there are two ways of improving the resolution of an optical system. The first is increasing the NA of the optical system and the second is decreasing the wavelength of the light source. When imaging through silicon, there is a limit for decreasing the wavelength, because silicon is an absorptive medium for a range of wavelengths. The bandgap of silicon limits the light that can be used for imaging to wavelengths larger than  $1\mu m$ . Therefore, an applanatic solid immersion lens (aSIL) has been used as a method of increasing the resolution of the IC imaging system (Ippolito et al., 2001) by increasing NA. The aSIL replaces the surrounding medium. Therefore, new surrounding medium has a higher refractive index and the NA of the optical system can be increased.

An immersion technique can be used to increase the NA of the optical system if the structures that are imaged are located on a surface as in Fig. 2.5(a). When an immersion technique is employed, the structures of interest are either immersed in a liquid medium, as in Fig. 2.5(b) or in a solid medium as in Fig. 2.5(c). The main structures of interest in an IC are the transistors and they are fabricated right on the silicon surface at the interface between silicon and silicon dioxide. Other structures of interest are metal interconnects; they are fabricated in the silicon dioxide medium. There may be up to 10 layers of metal interconnects in modern ICs and their depths depend on which metal layer they correspond to. Therefore, we need immersion techniques for subsurface imaging. When the structures that are imaged are buried in a solid, it is not trivial to maximize the NA of the system because the collection angle is limited. This can be seen in Fig. 2.5(d). An aSIL, shown in Fig. 2.5(e) has been used to increase resolution of the optical systems for backside subsurface imaging of ICs by increasing the NA of the system to  $NA_{aSIL} = n^2 NA_{obj}$  (Ippolito

et al., 2001).  $NA_{obj}$  is the NA of the objective and  $n$  is the refractive index of the immersion medium.

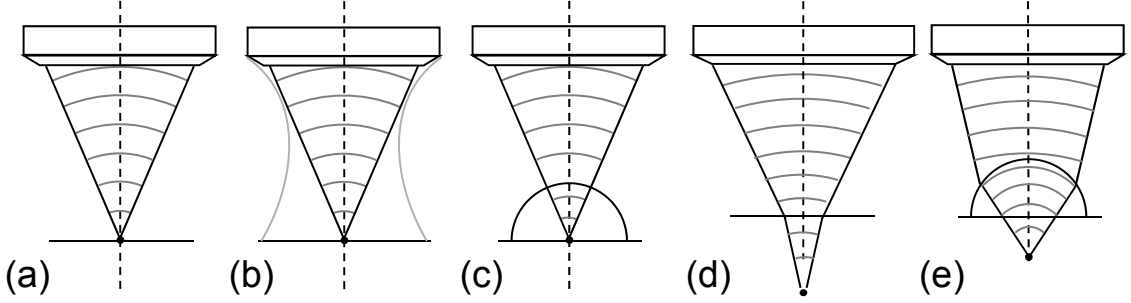


**Figure 2.5:** Light focusing in (a) a conventional-surface optical microscope, (b) a liquid-immersion lens microscope, (c) a solid-immersion lens microscope, (d) a subsurface microscope and (e) an applanatic solid-immersion (aSIL) lens microscope.

The aSIL microscopy became the state of the art technique for backside optical analysis of ICs since it provides the highest NA and best resolution. It has been shown in (Richards and Wolf, 1959) that when linearly-polarized light is focused with a high-NA lens, the focal-plane intensity distribution is highly asymmetric. Using this asymmetry property, spatial resolution improvement in selected directions has been shown through the use of linearly-polarized light in aSIL backside IC imaging (Serrels et al., 2008; Köklü et al., 2009). When linearly-polarized light is used, altering the polarization direction enables the collection of optical images with varying spatial resolution in different directions. One of the contributions of this thesis is a novel image reconstruction algorithm that produces a single image, with improved resolution, from on a set of images taken with linearly-polarized light in various polarization directions. Further improvement of spatial resolution in aSIL IC imaging has been shown through the use of radially polarized light for illumination (Yurt et al., 2014a) and the use of apodization masks (Vigil et al., 2014).

### 2.3.2 Optical model for confocal applanatic solid immersion lens microscopy of integrated circuits

In high-NA optical systems, the properties of focused polarized light and the properties of the observed images cannot be explained using scalar optics; a full vectorial analysis of fields is needed (Richards and Wolf, 1959; Török et al., 2008; Foreman and Török, 2011; Chen et al., 2012). In this section, we review vectorial analysis techniques required to model different components of high-NA optical systems. Later in this dissertation, these techniques are used to model a point spread function (PSF) for the aSIL confocal microscope used in IC analysis experiments. This PSF is incorporated into the proposed advanced inversion techniques in order to provide resolution improvement and image enhancement to the IC analysis data.

The imaging model of a high-NA system has three main components. The first component is the calculation of the focused light near the object of interest, the second component is the calculation of the scattered light, which is the interaction between the focused light and the object of interest. The final component is the far-field propagation of the scattered light to the image plane. There are different approaches in the literature which studies these different components. An expression for focused light when the object of interest is in a layered media is given in (Török et al., 2008). The focused light for an aSIL microscope is derived in (Chen et al., 2012). In order to calculate the scattered light, we need an electromagnetic analysis of fields and for that we need solutions for Maxwell's equations. However, there are analytical solutions for Maxwell equations for only a small set of objects. Therefore, we need rigorous numerical methods, such as the Finite Difference Time Domain (FDTD) method (Yee, 1966), the Finite Element Method (FEM) (Jin, 2014), or the Method of Moments (MOM) (Pocklington, 1897) in order to calculate the scattered field for an arbitrary shaped object. There are two main methods proposed in the literature to propagate

the scattered light to the far-field. The first method was proposed especially for layered media and is based on decomposing an arbitrary field into a superposition of magnetic-dipole waves (Munro and Török, 2007). The second method uses a Green's function formulation in order to calculate the far field propagation of the scattered field. In (Hu et al., 2011), a Green's function of an aSIL microscope for imaging structures buried inside a medium is presented. However, structures of interest in ICs, such as gates, metal layers, are located near the interface of the silicon substrate and the oxide layer. The Green's function in (Hu et al., 2011) is extended in (Yurt et al., 2014b) in order to image structures near an interface in an aSIL microscope.

In this dissertation, we use the Green's function approach for far-field propagation. The electric field at the detector plane of an aSIL microscope can be expressed as:

$$\mathbf{E}_{det} = \overleftrightarrow{\mathbf{G}}_{aSIL}(r, \theta_{aSIL}, \phi) * \mathbf{E}_{scat}(r, \theta_{aSIL}, \phi) + \mathbf{E}_{Ref}(r, \theta_{aSIL}, \phi), \quad (2.15)$$

where  $\mathbf{E}_{det}$  is the field at the detector plane,  $\overleftrightarrow{\mathbf{G}}_{aSIL}$  is the Green's function for aSIL for imaging structures at an interface,  $\mathbf{E}_{scat}$  is the scattered field calculated with numerical analysis,  $\mathbf{E}_{Ref}$  is the reflected field from the interface,  $\theta_{aSIL}$ ,  $\phi$  and  $r$  are the polar coordinates with respect to aSIL. Then, the confocal image of the object can be calculated by integrating the intensity, which is the magnitude of the electric field, at the detector at each scan position. In order to calculate the reflected field,  $\mathbf{E}_{Ref}$ , and the focused field,  $\mathbf{E}_{foc}$ , used in calculation of the scattered field, a mathematical technique called angular spectrum representation (ASR) (Novotny and Hecht, 2006) is required. In the following subsections, we will first give necessary background on ASR. Then, we will review the focused field, the reflected field and the Green's function for aSIL microscopes.

### Angular spectrum representation

Angular spectrum representation (ASR) is a mathematical method to calculate the propagation and the focusing of optical fields in homogeneous media (Novotny and Hecht, 2006). It is very useful for describing laser beam propagation and light focusing. Given an electric field  $\mathbf{E}(\mathbf{r})$  at any point  $\mathbf{r} = (x, y, z)$  in space, ASR can be used to represent the field on a plane at constant  $z$  as a superposition of plane waves and evanescent waves. This representation is given in the following equation:

$$\mathbf{E}(x, y, z) = \iint_{-\infty}^{+\infty} \hat{\mathbf{E}}(k_x, k_y; 0) e^{i[k_x x + k_y y \pm k_z z]} dk_x dk_y, \quad (2.16)$$

where  $k_x, k_y, k_z$  are the spatial frequencies. For a certain spatial frequency pair  $(k_x, k_y)$ , the plane wave and evanescent wave components are as follows:

$$\text{Plane waves: } e^{i[k_x x + k_y y]} e^{\pm i|k_z|z}, \quad k_x^2 + k_y^2 \leq k^2 \quad (2.17)$$

$$\text{Evanescent waves: } e^{i[k_x x + k_y y]} e^{-|k_z||z|}, \quad k_x^2 + k_y^2 > k^2. \quad (2.18)$$

The plane wave components are oscillating functions in  $z$  and the evanescent waves have an exponential decay along the  $z$ -axis. In the following subsections, ASR is used to calculate focused fields at the object plane and detector plane.

### Focused field in aSIL microscopes

In this section, the focusing of a paraxial optical field by an aplanatic lens is studied. The refraction of a ray at an aplanatic lens can be explained by two rules; the sine condition and the intensity law. The focusing in an aplanatic system is shown in Fig. 2-6 which is adapted from representation of the aplanatic system in (Chen et al., 2012). The sine law defines the Gaussian reference sphere (GRS) as the sphere with radius equal to focal length  $f$ , where the incident rays parallel to the optical axis

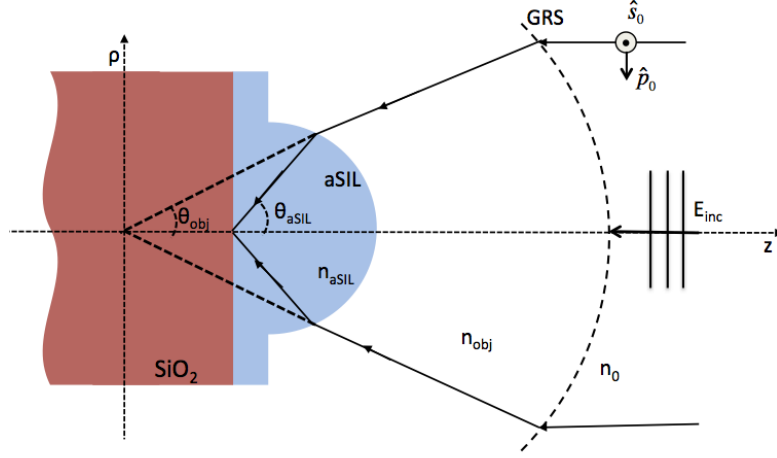


**Figure 2-6:** Focusing on an interface in an aSIL microscope

refract. Unit vectors for  $s$ - and  $p$ - polarized fields in the medium before the objective lens are denoted by  $\hat{\mathbf{s}}_0$  and  $\hat{\mathbf{p}}_0$ . They can be expressed in spherical and cartesian coordinates as follows:

$$\hat{\mathbf{s}}_0 = -\hat{\boldsymbol{\phi}} = \sin\phi\hat{\mathbf{x}} - \cos\phi\hat{\mathbf{y}}, \quad (2.19)$$

$$\hat{\mathbf{p}}_0 = \hat{\boldsymbol{\rho}} = \cos\phi\hat{\mathbf{x}} + \sin\phi\hat{\mathbf{y}}. \quad (2.20)$$

The total electric field after refracting at GRS can be expressed as:

$$\mathbf{E}_\infty = [t_{obj}^s[\mathbf{E}_{inc} \cdot \hat{\mathbf{s}}_0]\hat{\mathbf{s}}_{obj} + t_{obj}^p[\mathbf{E}_{inc} \cdot \hat{\mathbf{p}}_0]\hat{\mathbf{p}}_{obj}] \sqrt{\frac{n_0}{n_{obj}}} \sqrt{\cos\theta_{obj}}, \quad (2.21)$$

where  $\mathbf{E}_{inc}$  is the incident electric field and  $\hat{\mathbf{s}}_{obj}$  and  $\hat{\mathbf{p}}_{obj}$  denote unit vectors for  $s$ - and  $p$ - polarized fields in the medium after the objective lens. They can be expressed as:

$$\hat{\mathbf{s}}_{obj} = -\hat{\boldsymbol{\phi}} = \sin\phi\hat{\mathbf{x}} - \cos\phi\hat{\mathbf{y}}, \quad (2.22)$$

$$\hat{\mathbf{p}}_{obj} = -\hat{\boldsymbol{\theta}}_1 = -\cos\theta_1\cos\phi\hat{\mathbf{x}} - \cos\theta_1\sin\phi\hat{\mathbf{y}} + \sin\theta_1\hat{\mathbf{z}}, \quad (2.23)$$

where  $\theta_1 = \pi - \theta_{obj}$  and  $\theta_{obj}$  is the angle that the wave vector of the refracted ray makes with the  $z$ -axis.  $t_{obj}^s$  and  $t_{obj}^p$  are the transmission coefficients of the lens for the  $s$ - and  $p$ - polarized field components. We assume that they are equal to 1. The term  $\sqrt{\frac{n_0}{n_{obj}}} \sqrt{\cos \theta_{obj}}$  comes from intensity law to satisfy energy conservation,  $n_0$  and  $n_{obj}$  are the refractive indices of the mediums on each side of the reference sphere and in this system they are equal.

After transmission from the aSIL, the electric field can be expressed as:

$$\mathbf{E}'_{\infty} = [t_{sil}^s [\mathbf{E}_{inc} \cdot \hat{\mathbf{s}}_0] \hat{\mathbf{s}}_{sil} + t_{sil}^p [\mathbf{E}_{inc} \cdot \hat{\mathbf{p}}_0] \hat{\mathbf{p}}_{sil}] \sqrt{\cos \theta_{obj}}, \quad (2.24)$$

where  $t_{sil}^s$  and  $t_{sil}^p$  are the transmission coefficients for aSIL and  $\hat{\mathbf{s}}_{sil}$  and  $\hat{\mathbf{p}}_{sil}$  are unit vectors for  $s$ - and  $p$ - polarized fields after aSIL. They are given in the following equations:

$$\hat{\mathbf{s}}_{sil} = -\hat{\phi} = \sin \phi \hat{\mathbf{x}} - \cos \phi \hat{\mathbf{y}}, \quad (2.25)$$

$$\hat{\mathbf{p}}_{sil} = \cos \theta_{sil} \cos \phi \hat{\mathbf{x}} + \cos \theta_{sil} \sin \phi \hat{\mathbf{y}} + \sin \theta_{sil} \hat{\mathbf{z}}, \quad (2.26)$$

$$t_{sil}^s = \frac{2n_{obj} \cos \theta_{sil}}{n_{obj} \cos \theta_{sil} + n_{sil} \cos \theta_{obj}}, \quad (2.27)$$

$$t_{sil}^p = \frac{2n_{obj} \cos \theta_{sil}}{n_{obj} \cos \theta_{obj} + n_{sil} \cos \theta_{sil}}, \quad (2.28)$$

where  $\theta_{sil} = \sin^{-1}(n_{sil} \sin \theta_{obj} / n_{obj})$  is the angle rays inside the aSIL make with the  $z$ -axis.

Then, we can use the ASR equation given in Eq. 2.16 to calculate the field near the focus.

$$\mathbf{E}_{foc}(\mathbf{r}_{sil}) = \frac{ire^{-ik_{sil}r}}{2\pi} \iint_{(k_{x_{sil}}^2 + k_{y_{sil}}^2 \leq k^2)} \mathbf{E}'_{\infty}(k_{x_{sil}}, k_{y_{sil}}) e^{i\mathbf{k}_{sil} \cdot \mathbf{r}_{sil}} \frac{1}{k_{z_{sil}}} dk_{x_{sil}} dk_{y_{sil}}, \quad (2.29)$$

where  $k_{x_{sil}}, k_{y_{sil}}, k_{z_{sil}}$  are the spatial frequencies.

If  $k_{x_{sil}}, k_{y_{sil}}, k_{z_{sil}}$  are represented in spherical coordinates, the field near the focus



is given by,

$$\mathbf{E}_{foc}(\rho_{sil}, \theta_{sil}, z_{sil}) = \frac{ik_{sil}f_{obj}e^{-ik_{obj}f_{obj}}}{2\pi} \int_0^{\theta_{max}} \int_0^{2\pi} \mathbf{E}_{\infty}(\theta_{sil}, \phi_{sil}) e^{ik_{sil}z_{sil} \cos \theta_{sil}} e^{ik_{sil}\rho_{sil} \sin \theta_{sil} \cos(\phi - \phi_{sil})} \sin \theta_{sil} d\phi_{sil} d\theta_{sil}. \quad (2.30)$$

This formulation is sufficient to represent the field near the focus for a linearly-polarized incident light with arbitrary polarization direction. The linearly-polarized incident field in  $x - y$  plane with arbitrary polarization direction can be expressed as:

$$\mathbf{E}_{inc} = E_{inc} \begin{bmatrix} \cos \Delta \\ \sin \Delta \\ 0 \end{bmatrix}, \quad (2.31)$$

where  $\Delta$  is the polarization angle and  $E_{inc}$  is the amplitude profile of the incoming laser beam. For an incoming laser beam of first Hermite Gaussian mode, the amplitude profile can be expressed as follows:

$$E_{inc} = E_o f_w(\theta_{obj}) = E_o e^{-f^2 \sin^2 \theta_{obj} / w_0^2}. \quad (2.32)$$

A detailed procedure to calculate mathematically the integral over  $\phi$  is given in (Novotny and Hecht, 2006). After integration and change of variables a final expression for the focused field of a linearly-polarized incoming light with arbitrary polarization in aSIL microscope can be obtained. This final expression for  $\mathbf{E}_{foc}$  (Chen et al., 2012) is given by:

$$\mathbf{E}_{foc} = -\frac{ik_{sil}f_{obj}e^{-ik_{obj}f_{obj}}}{2} E_0 \begin{bmatrix} \cos \Delta (I_0^L + I_2^L \cos 2\phi_{sil}) + \sin \Delta I_2^L \sin 2\phi_{sil} \\ \cos \Delta I_2^L \sin 2\phi_{sil} + \sin \Delta (I_0^L - I_2^L \cos 2\phi_{sil}) \\ 2iI_1^L (\cos \Delta \cos \phi_{sil} + \sin \Delta \sin \phi_{sil}) \end{bmatrix}, \quad (2.33)$$

where

$$I_m^L = \int_0^{\theta_{obj}^{max}} (\cos\theta_{obj})^3 / 2 \tan\theta_{sil} J_m(k_{sil}\rho_{sil}\sin\theta_{sil}) T_m^L e^{-ik_{sil}z_{sil}\cos\theta_{sil}} d\theta_{obj}, \quad (2.34)$$

$$T_0^L = t_{sil}^s + t_{sil}^p \cos\theta_{sil}, \quad (2.35)$$

$$T_1^L = t_{sil}^p \sin\theta_{sil}, \quad (2.36)$$

$$T_2^L = t_{sil}^s - t_{sil}^p \cos\theta_{sil}, \quad (2.37)$$

$J_m(\cdot)$  is the first-kind Bessel function of order  $m$  and  $\theta_{obj}^{max}$  is the maximum collection angle of the objective lens.

### Reflected image of a focused spot in aSIL microscopes

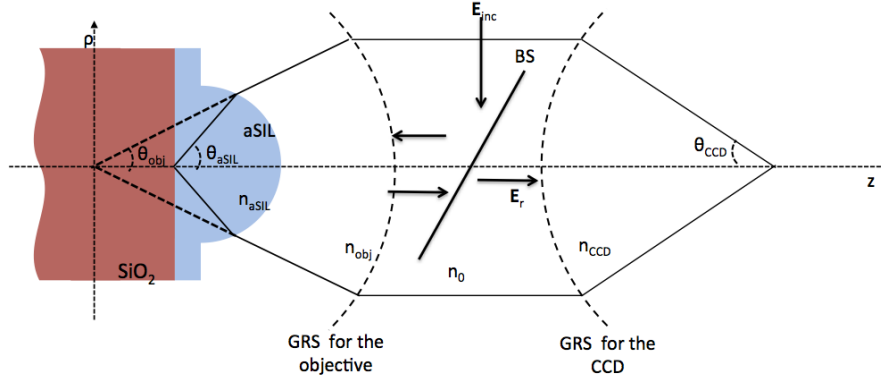


**Figure 2.7:** Investigation of the reflected image of a focused spot

In this section, the formulation to calculate the reflected image of a focused spot of a linearly-polarized beam focused at an interface between two dielectric media is presented. The system configuration is shown in Fig. 2.8. A linearly-polarized beam is reflected by a beam splitter (BS) and focused by an aSIL system on the interface of silicon and silicon dioxide. The reflected light from the interface collected by the aSIL system is transmitted through the beam splitter and refocused by a second lens.

The calculations for the reflected light follow the same procedure as in previous

section. The expressions are the same up to Eq. 2.24. After transmission from the aSIL, the field propagates to the interface and then is reflected from the interface. The reflected field can be expressed as:

$$\mathbf{E}_{\infty}'' = e^{-2ik_{z_{sil}}z_0} [t_{sil}^s r_{int}^s [\mathbf{E}_{inc} \cdot \hat{\mathbf{s}}_0] \hat{\mathbf{s}}_{sil} + t_{sil}^p r_{int}^p [\mathbf{E}_{inc} \cdot \hat{\mathbf{p}}_0] \hat{\mathbf{p}}_{sil}] \sqrt{\cos \theta_{obj}}, \quad (2.38)$$

where  $r_{int}^p$  and  $r_{int}^s$  are the fresnel reflection coefficients of the interface for  $p$ - and  $s$ -polarizations,  $z_0$  is the longitudinal distance of the interface to the focus point. Since the field is reflected and the propagation direction is inverted in  $z$  axis, the expression for unit vectors for  $s$ - and  $p$ - polarized fields has changed:

$$\hat{\mathbf{s}}_{sil} = \hat{\boldsymbol{\phi}} = -\sin\phi \hat{\mathbf{x}} + \cos\phi \hat{\mathbf{y}}, \quad (2.39)$$

$$\hat{\mathbf{p}}_{sil} = \cos\theta_{sil} \cos\phi \hat{\mathbf{x}} + \cos\theta_{sil} \sin\phi \hat{\mathbf{y}} + \sin\theta_{sil} \hat{\mathbf{z}}. \quad (2.40)$$

After transmission from aSIL the field can be expressed as:

$$\mathbf{E}_{\infty}''' = e^{-2ik_{z_{sil}}z_0} [t_{sil}^s r_{int}^s t_{sil2}^s [\mathbf{E}_{inc} \cdot \hat{\mathbf{s}}_0] \hat{\mathbf{s}}_{obj} + t_{sil}^p r_{int}^p t_{sil2}^p [\mathbf{E}_{inc} \cdot \hat{\mathbf{p}}_0] \hat{\mathbf{p}}_{obj}] \sqrt{\cos \theta_{obj}}, \quad (2.41)$$

where  $t_{sil2}^s$  and  $t_{sil2}^p$  are the transmission coefficients for the aSIL for the new direction. Next, the field is refracted at the objective, transmitted through BS and then refracted at the second lens. The field after refracting at the second lens is given by:

$$\mathbf{E}_{\infty}'''' = e^{-2ik_{z_{sil}}z_0} [t_{sil}^s r_{int}^s t_{sil2}^s [\mathbf{E}_{inc} \cdot \hat{\mathbf{s}}_0] \hat{\mathbf{s}}_{ccd} + t_{sil}^p r_{int}^p t_{sil2}^p [\mathbf{E}_{inc} \cdot \hat{\mathbf{p}}_0] \hat{\mathbf{p}}_{ccd}] \sqrt{\cos \theta_{ccd}} \sqrt{\frac{n_0}{n_{ccd}}}, \quad (2.42)$$

where

$$\hat{\mathbf{s}}_{ccd} = -\hat{\boldsymbol{\phi}}_{ccd} = \sin\phi_{ccd} \hat{\mathbf{x}} - \cos\phi_{ccd} \hat{\mathbf{y}}, \quad (2.43)$$

$$\hat{\mathbf{p}}_{ccd} = -\hat{\boldsymbol{\theta}}_{ccd} = -\cos\theta_{ccd} \cos\phi_{ccd} \hat{\mathbf{x}} - \cos\theta_{ccd} \sin\phi_{ccd} \hat{\mathbf{y}} + \sin\theta_{ccd} \hat{\mathbf{z}}, \quad (2.44)$$

$n_{ccd}$  is the refractive index of the medium at the detector, and  $\theta_{ccd}$  is the collection

angle of the second lens. Following the procedure in the previous section where we used the Eq. 2.16 in order to calculate the focused field at the applanatic point, we can use the same equation in order to calculate the reflected field,  $\mathbf{E}_{Ref}$ , at the focus of the second lens. The derived equation is as follows:

$$\mathbf{E}_{Ref} = \frac{ik_{ccd}f_{obj}^2 e^{-ik_{ccd}f_{ccd}}}{2f_{ccd}} E_0 \begin{bmatrix} \cos\Delta(I_0^R - I_2^R \cos 2\phi_{ccd}) - \sin\Delta I_2^R \sin 2\phi_{ccd} \\ -\cos\Delta I_2^R \sin 2\phi_{ccd} + \sin\Delta(I_0^R + I_2^R \cos 2\phi_{ccd}) \\ iI_1^R(\cos\Delta \cos\phi_{ccd} + \sin\Delta \sin\phi_{ccd}) \end{bmatrix}, \quad (2.45)$$

where

$$I_m^R = \int_0^{\theta_{obj}^{max}} f_w(\theta_{obj}) \frac{\cos\theta_{obj}}{\cos\theta_{ccd}} \sin\theta_{obj} J_m(k_{ccd}\rho_{ccd}\sin\theta_{ccd}) T_m^R e^{i(k_{ccd}z\cos\theta_{ccd} - 2k_{sil}\cos\theta_{sil}z_0)} d\theta_{obj}, \quad (2.46)$$

$$T_0^R = t_{sil}^p r_{int}^p t_{sil2}^p \cos\theta_{ccd} - t_{sil}^s r_{int}^s t_{sil2}^s, \quad (2.47)$$

$$T_1^R = t_{sil}^p r_{int}^p t_{sil2}^p \sin\theta_{ccd}, \quad (2.48)$$

$$T_2^R = t_{sil}^p r_{int}^p t_{sil2}^p \cos\theta_{ccd} + t_{sil}^s r_{int}^s t_{sil2}^s. \quad (2.49)$$

$E_{Ref}$  will be used in the following chapters for PSF calculations to be used in inversion techniques for resolution improvement.

### Green's function of an aSIL microscope for imaging objects at an interface

The goal of this section is to review dyadic Green's function of an aSIL microscope to investigate the high-NA far-field imaging of buried objects beyond an interface. The schematic illustration of the problem is given in Fig. 2.8. A dipolar object with an electrical dipole moment  $\boldsymbol{\mu}$  is located in the silicon dioxide medium that has a lower refractive index ( $n_{ox}$ ) than the silicon immersion medium ( $n_{sil}$ ). The electromagnetic solution to the problem of propagating this dipole moment to the CCD plane can be

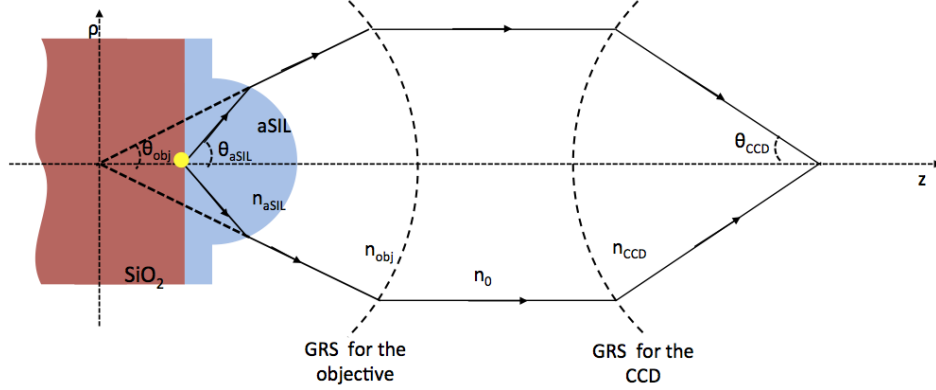


**Figure 2.8:** Schematic of the problem of far-field field propagation with Green's function in aSIL microscope

formulated using the Green's function formalism:

$$\mathbf{E}(\mathbf{r}) = \omega^2 \mu_0 \overleftrightarrow{\mathbf{G}}_{aSIL}(\mathbf{r}; \mathbf{r}_d) \cdot \boldsymbol{\mu}, \quad (2.50)$$

where  $\omega$  is the oscillation frequency of the light,  $\mu_0$  is the vacuum permeability,  $\mathbf{r}_d$  is the location of the dipole object,  $\mathbf{r}$  is the propagation location at the detector plane and  $\overleftrightarrow{\mathbf{G}}_{aSIL}$  is the Green's function for aSIL microscope accounting for the planar dielectric interface. The Green's function satisfying the homogenous space solution is given in (Novotny and Hecht, 2006). However, since objects of interest in ICs are located beyond an interface, the Green's function in (Novotny and Hecht, 2006) needs to be modified. The Green's function for aSIL microscope (Yurt et al., 2014b) accounting for the planar dielectric interface is given in the following equation:

$$\overleftrightarrow{\mathbf{G}}_{aSIL} = -\frac{ik_{ccd}f_{obj}}{8\pi f_{ccd}} \sqrt{\frac{n_{obj}}{n_{ccd}}} e^{i(k_{ccd}f_{ccd} + k_{obj}f_{obj})} \begin{bmatrix} I_0 + I_{21} & I_{22} & -2iI_{11} \\ I_{22} & I_0 - I_{21} & -2iI_{12} \\ 0 & 0 & 0 \end{bmatrix}, \quad (2.51)$$

where

$$\begin{aligned}
I_0 &= \int_0^{\theta_{obj}^{max}} \sin\theta_{obj} \sqrt{\cos\theta_{obj}} \frac{n_{sil}}{n_{obj}} (t_{sil2}^s \frac{k_{z_{sil}}}{k_{z_{ox}}} t_{ox}^s + t_{sil2}^p \frac{n_{sil}}{n_{ox}} t_{ox}^p \cos\theta_{sil}) J_0(\rho) e^{-iz} d\theta_{obj}, \\
I_{11} &= \int_0^{\theta_{obj}^{max}} \sin\theta_{obj} \sqrt{\cos\theta_{obj}} \frac{n_{sil}}{n_{obj}} (t_{sil2}^p \frac{n_{sil} k_{z_{sil}}}{n_{ox} k_{ox}} t_{ox}^p \sin\theta_{sil}) J_1(\rho) e^{-iz} \cos\varphi d\theta_{obj}, \\
I_{12} &= \int_0^{\theta_{obj}^{max}} \sin\theta_{obj} \sqrt{\cos\theta_{obj}} \frac{n_{sil}}{n_{obj}} (t_{sil2}^p \frac{n_{sil} k_{z_{sil}}}{n_{ox} k_{ox}} t_{ox}^p \sin\theta_{sil}) J_1(\rho) e^{-iz} \sin\varphi d\theta_{obj}, \\
I_{21} &= \int_0^{\theta_{obj}^{max}} \sin\theta_{obj} \sqrt{\cos\theta_{obj}} \frac{n_{sil}}{n_{obj}} (t_{sil2}^s \frac{k_{z_{sil}}}{k_{z_{ox}}} t_{ox}^s - t_{sil2}^p \frac{n_{sil}}{n_{ox}} t_{ox}^p \cos\theta_{sil}) J_0(\rho) e^{-iz} \cos 2\varphi d\theta_{obj}, \\
I_{21} &= \int_0^{\theta_{obj}^{max}} \sin\theta_{obj} \sqrt{\cos\theta_{obj}} \frac{n_{sil}}{n_{obj}} (t_{sil2}^s \frac{k_{z_{sil}}}{k_{z_{ox}}} t_{ox}^s - t_{sil2}^p \frac{n_{sil}}{n_{ox}} t_{ox}^p \cos\theta_{sil}) J_0(\rho) e^{-iz} \sin 2\varphi d\theta_{obj},
\end{aligned} \tag{2.52}$$

$$\rho = \sqrt{x^2 + y^2},$$

$$\varphi = \tan^{-1}(y/x),$$

$$x = -(k_{ccd} \sin\theta_{ccd} x_{ccd} + k_{sil} \sin\theta_{sil} x_d), \tag{2.53}$$

$$y = -(k_{ccd} \sin\theta_{ccd} x_{ccd} + k_{sil} \sin\theta_{sil} y_d),$$

$$z = d(k_{z_{ox}} - k_{z_{sil}}) - \left( k_{ccd} \cos\theta_{ccd} z_{ccd} + k_{ox} \sqrt{1 - \left( \frac{k_{sil}}{k_{ox}} \right)^2 \sin^2\theta_{sil} z_d} \right)$$

$k$  is the wave number in the scone lens space,  $f_{ccd}$  is the focal length of the second lens,  $n_{ccd}$  is the refractive index of the second lens medium. A detailed explanation for the derivation of Green's function for structures buried in single medium can be found in (Hu et al., 2011).

## Chapter 3

# Model of a point spread function for a subsurface aSIL imaging system

In high-NA optical systems, multiple observations can be obtained by changing the polarization direction of the linearly-polarized input light source. Each of the observations acquired by linearly-polarized light with different polarization directions provides more detail in one specific direction of spatial image coordinates while under-resolving in other directions. This is due to the fact that linearly-polarized light employed as the input source in high-NA systems results in a PSF that has an elliptical rather than circularly-symmetric support. In order to explain these properties and to have an accurate observation model, full vectorial analysis of fields is required. This model can be divided into three components where we first calculate the focused light near the object of interest, then use rigorous numerical methods to calculate the scattered light resulting from the interaction between the focused light and the object of interest, and then propagate the scattered field to the far field. In Section 2.3.2, a review of these components is presented and an expression for the electric field at the detector is given in Eq. 2.15. This is a nonlinear observation model and we need rigorous numerical analysis methods, such as FDTD to calculate the scattered field for an arbitrarily-shaped object. For a confocal system, the object is raster scanned and for each focus position, the field at the detector is calculated using the Eq. 2.15 and then the intensity for each scan position is calculated by integrating over the detector region. The image of an arbitrary object can be calculated by using this

procedure. FDTD is a computationally intensive method and the confocal system requires the use of the FDTD solver for each scan position. In the following chapters we propose image reconstruction techniques for resolution improvement in high-NA systems. Incorporating this computationally-intensive procedure into a reconstruction framework would significantly increase the computation time. Therefore, we need an approximate linear model which relates the intensity of the object with the collected image intensity. In this chapter, we introduce such a linear model in Section 3.1 and we explain how a PSF for this linear model can be modeled in Section 3.2.

### 3.1 Linear observation model

We approximate the nonlinear optical system with a linear convolutional forward model relating the intensity of the object to the collected image intensity as follows:

$$g^j(x, y) = h^j(x, y) * f(x, y), \quad (3.1)$$

where  $g^j(x, y)$  is the observed intensity under linearly-polarized light in direction  $j$ ,  $f(x, y)$  is the reflectivity of the underlying object,  $*$  denotes the convolution operation, and  $h^j(x, y)$  is the PSF of the optical system having linearly-polarized light in direction  $j$  as the incident light source.

We have used two different approaches in order to model the PSF. The following section explains the details for these two different approaches.

### 3.2 Modeling of the PSF

The PSF of a system can be modeled as the intensity of the electric field at the detector plane as a result of a point source, in other words as a result of a very small object. In Section 2.3.2, the electric field at the detector plane of an aSIL microscope is expressed in Eq. 2.15. This equation expresses the electric field at the



detector plane in terms of the scattered field  $\mathbf{E}_{scat}$ , the interaction of the object with the focused light, and the reflected field  $\mathbf{E}_{Ref}$ , the light reflecting from the interface the object is located on. The first approach uses the fact that the intensity of the scattered field is very small compared to reflected field from the dielectric interface for a point source. For this reason, it models the PSF only in terms of the reflected field. However, this approach ignores the dependence of the PSF of an assumed linear model on material properties of the object and on the size of the object. For large objects and for some materials, a simple model based only on the reflected field is sufficient, but for smaller structures and materials such as metal, a more accurate complex model considering the effect of the scattered field is required. Therefore, we introduce the second approach which models the PSF in terms of both the scattered field and the reflected field. This approach introduces a parameter which models the dependence of the PSF on the size of objects. The following subsections explain these two approaches in detail and present simulated PSFs.

### 3.2.1 PSF as the reflection of a tightly focused spot

The first approach for modeling the PSF only considers the light reflected from the interface that the structures are located on, it ignores the scattered field of the point source. This model is useful for large structures and for materials for which interference between the scattered field and the reflected field is not dominant. In this model, the first term in in Eq. 2.15 is ignored. Hence, we can express the electric field at the detector plane only in terms of the reflected field:

$$\mathbf{E}_{det}(x, y) = \mathbf{E}_{Ref}(x, y). \quad (3.2)$$

The PSF of the system can be calculated as the magnitude of the reflected field:

$$h(x, y) = \|\mathbf{E}_{Ref}(x, y)\|^2. \quad (3.3)$$

Therefore, the PSF becomes the image of a tightly focused beam. The details of calculating the reflected light of a linearly-polarized incident beam are given in Section 2.3.2. This PSF does not include effects coming from the material properties of the structures. However, it still accounts for vectorial properties resulting from the interaction of polarized light with the dielectric interface. The PSF of an aSIL system with linearly polarized input light using this approach, given in Eq. 2.45, is shown in Fig. 3.1. It can be seen from the figure that it has an elliptical support providing higher resolution in one axis than the other. When the polarization angle of the linearly polarized input light is changed, the PSF rotates following the polarization angle. Cross sections for the PSF in Fig. 3.1a are shown in Fig. 3.2. In Fig. 3.3, the observation data for a polysilicon object at the silicon-silicon dioxide interface are given. The horizontal and vertical structures have different resolution and the elliptical support of the PSF explains the dependence of resolution on the orientation of the lines.

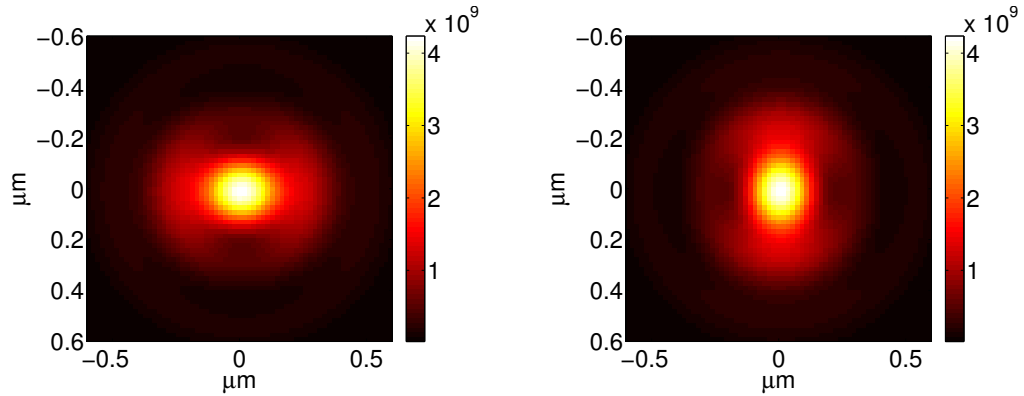


**Figure 3.1:** Simulated theoretical PSF for linearly-polarized input light (a) in  $x$  direction (b) in  $y$  direction

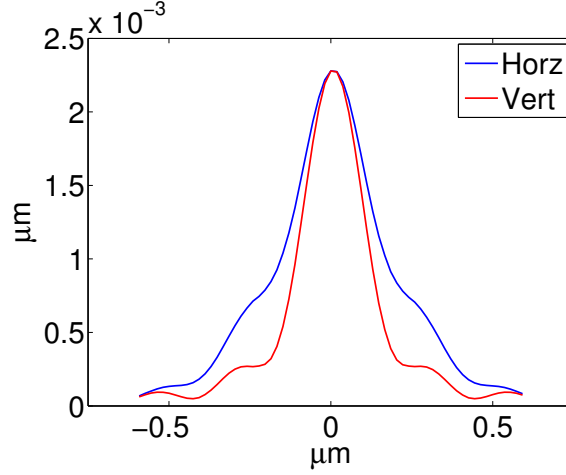


**Figure 3-2:** Cross sections from the simulated PSF for linearly-polarized input light in  $x$  direction

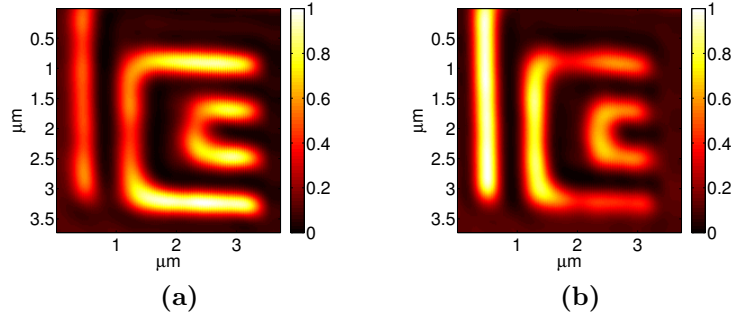


**Figure 3-3:** Experimental observation images under polarization in (a)  $x$  direction and (b)  $y$  direction.

### 3.2.2 Green's function approach for PSF modeling

When structures of interest are much smaller than the focused beam and they are made of materials such as metals, a more accurate PSF is required to efficiently model the optical system. Therefore, we propose a second approach which is based on a nonlinear optical model. According to Eq. 2.15, there is an interference between the reflected field and the far field propagation of scattered field. The first approach in Section 3.2.1 ignores the phase effects as a result of this interference. Especially when structures of interest are made of materials such as metals, these interference

effects are more dominant. In Fig. 3.4, observation data are shown for objects of interest that are made of aluminum. We observe a black outline effect where there is an apparent dip in the intensity at the edges of the structures. This observation data shows the requirement for a more accurate model.

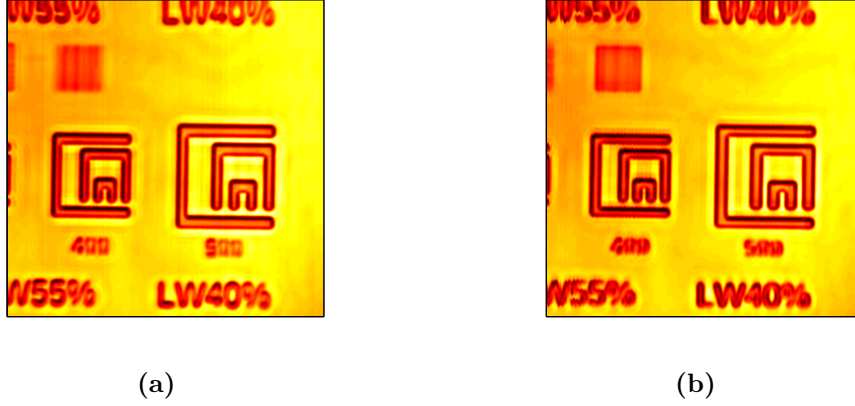


**Figure 3.4:** Experimental observation images of aluminum structures under polarization in (a)  $x$  direction and (b)  $y$  direction.

In order to improve the PSF model, we propose a second approach which is based on the following nonlinear optical model:

$$h(x, y) = \|\alpha * \overleftrightarrow{G}_{aSL}(x, y; x', y') * \vec{E}_{scat}(x', y') + \vec{E}_{Ref}(x, y)\| - \|\vec{E}_{Ref}(x, y)\|^2, \quad (3.4)$$

where  $\alpha$  is a coefficient which accounts for the increase in the scattered field as the size of the objects is increased,  $x$  and  $y$  are coordinates in image plane and  $x'$  and  $y'$  are coordinates in object plane. In order to simulate the PSF of the system, a spherical scatterer with a radius of 25 nm is assumed to be placed near the interface where the objects of interest are located. Then, the PSF of the system is calculated using the scattered field of this spherical object obtained with FDTD solver and the formulation given in Eq. 3.4. When the size of objects of interest increase, the amplitude of  $E_{scat}$  gets larger. Rather than performing a full simulation for each case, we introduce the term  $\alpha$  in Eq. 3.4 to adjust

the PSF depending on the size of object of interest and still use the LTI model. We can change the term  $\alpha$  depending on the size of the objects of interest.

There are two types of samples we are studying, the first one has aluminum resolution structures fabricated on silicon, therefore located on a silicon-air interface. The second one has polysilicon structures located on a silicon-to-silicon dioxide interface. Therefore, we simulated two different PSFs. A spherical particle of radius 25 nm made of the material of interest is placed on the corresponding interface and the image is calculated using Eq. 3.4. Fig. 3-5 shows images of PSFs of objects made of polysilicon and aluminum for different values of  $\alpha$  and in Fig. 3-6 cross sections are plotted to show how the PSF changes when  $\alpha$  is changed. We observe that the PSF for an aluminum object has a higher dependence on the size of the particle whereas the PSF for a polysilicon structure does not change as much when  $\alpha$  is increased. Fig. 3-7 compares the cross sections from the simulated PSF and a cross section along the green line in Fig. 3-7a. The structure in the shape of 2 is made of aluminum and placed at the interface of silicon and air. The cross section is along a line which is thin compared to PSF and can be considered as a line response. Therefore, the PSF is consistent with this experimental data cross section. They have similar shapes and they both show similar dips caused by interference effects.

### 3.3 Conclusion

In this Chapter, we proposed two approaches to model the PSF for high-NA aSIL subsurface imaging. Our goal is to use this PSF for image reconstruction in the following chapters in order to provide image enhancement and resolution improvement to high-NA aSIL imaging of ICs. Both of these PSF models use vectorial optics to account for polarization effects in high-NA subsurface imaging. The Green's function approach extends the first approach in order to provide a more accurate model suitable

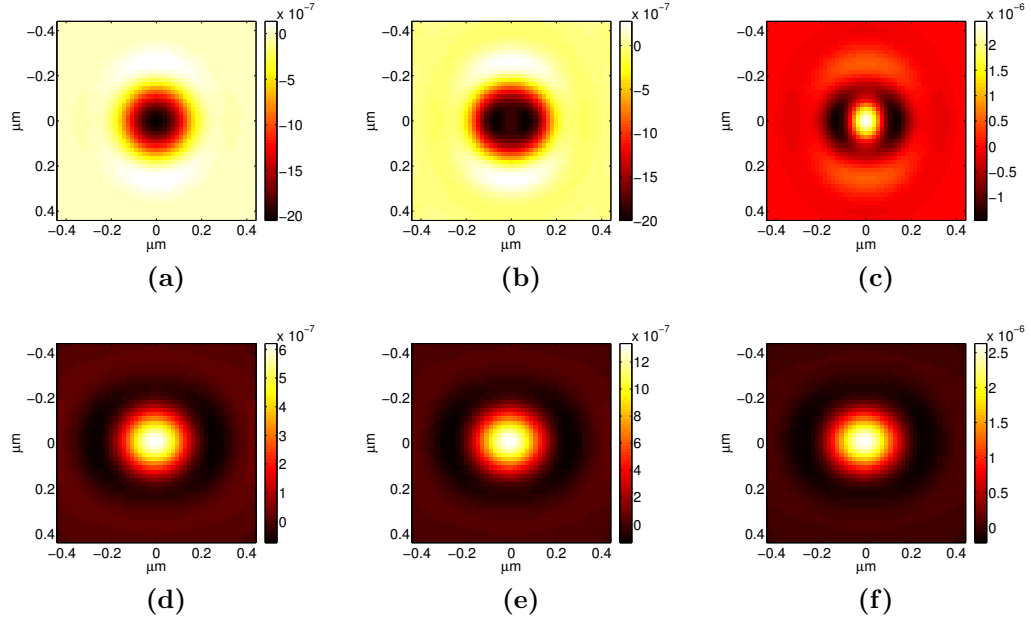


**Figure 3.5:** Simulated PSFs with linearly-polarized input light in the  $y$  direction for aluminum objects (a)  $\alpha = 2^3$ , (b)  $\alpha = 2.5^3$ , (c)  $\alpha = 3^3$ , and for polysilicon objects (d)  $\alpha = 2^3$ , (e)  $\alpha = 2.5^3$ , (f)  $\alpha = 3^3$ .

for a wider range of materials. It also models the dependence of the PSF on the size and the material of the object of interest.

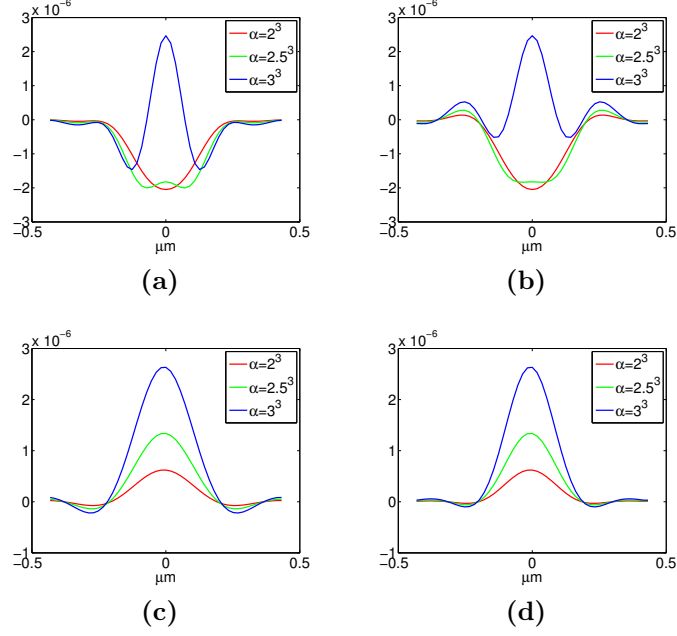


**Figure 3-6:** Comparison of PSF cross sections for different values of  $\alpha$  for aluminum objects (a) horizontal cross section, (b) vertical cross section, and for polysilicon objects (c) horizontal cross section, (d) vertical cross section.

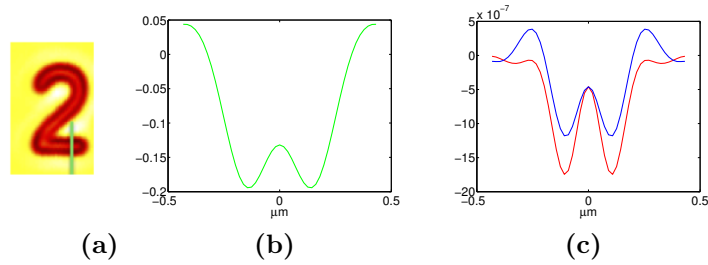


**Figure 3-7:** Comparison of PSF ( $\alpha = 2.75^3$ ) cross section and data cross section: (a) experimental aSIL image, (b) cross section from experimental data along the green line, (c) PSF cross section blue for horizontal and red for vertical.

## Chapter 4

# Analysis-based sparse image reconstruction framework for integrated circuit imaging based on polarization diversity

In this chapter, our goal is to benefit from the properties of polarized light in high-NA systems and the sample being imaged in order to improve resolution of collected aSIL IC images. We propose an analysis-based sparsity paradigm which combines multiple data under linearly-polarized light with different polarization directions. Altering the polarization direction of linearly-polarized input light in high-NA systems enables the collection of optical images with varying spatial resolution in different directions. We propose a novel image reconstruction algorithm that produces a single image, with improved resolution, from a set of images taken using linearly-polarized light with different polarization directions. Features in ICs are composed of lines and rectangular structures and some structures are much smaller than the PSF, this results in piecewise-constant regions and also in images with small scatterers. Therefore, we use non-quadratic regularization functionals which preserve the edges of the underlying features thus enabling recovery of small scatters.

This chapter is organized as follows. In Section 4.1, we provide details of the proposed framework, including the assumed forward model, and describe the proposed reconstruction method. In Section 4.2, we present reconstruction results for simulated



data obtained using the assumed forward model. In Section 4.3, we present results for experimental aSIL data acquired with linearly-polarized and also with circularly-polarized light. Section 4.4 presents a discussion on how reconstruction performance is affected when the boundary conditions are modified. In Section 4.5, we draw conclusions from our work.

## 4.1 Proposed framework

### 4.1.1 Regularized image reconstruction framework for resolution enhanced IC imaging

The goal of the proposed image reconstruction framework is to take advantage of high-resolution orientations in different polarizations (decreased PSF support) and produce a single higher-resolution image. Image reconstruction should also take into account the fact that the underlying features have smooth, homogeneous regions and small scatterers. This prior knowledge about the underlying object can be incorporated in the reconstruction by employing non-quadratic functionals in regularization as explained in Section 2.1.2. The regularized reconstruction can be formulated as the following optimization problem:

$$\hat{f} = \arg \min_f J(f), \quad (4.1)$$

$$J(f) = \sum_{j=1}^N \| h^j(x, y) * f(x, y) - g^j(x, y) \|_2^2 + \lambda_1 \| \nabla f(x, y) \|_1 + \lambda_2 \| f(x, y) \|_1, \quad (4.2)$$

where  $N$  is the total number of acquired images,  $h^j$  is the PSF in polarization direction  $j$ ,  $g^j$  is the observation,  $f$  is the underlying object reflectivity, and  $\lambda_1$  and  $\lambda_2$  are regularization parameters. The first term in Eq. 4.2 is the data fidelity term matching the observed noisy image to the unknown image of the underlying object  $f$ , while the second and third terms are regularizers that favor sparsity in the edge field of the

reconstructed image and the sparsity in the reconstructed image, respectively. Such a linear combination of terms has been used successfully in other application domains (Çetin and Karl, 2001; Tuysuzoglu et al., 2012).

In practice, the data we collect is discretized in spatial coordinates on a uniformly spaced grid and Eq. 4.2 becomes:

$$J(\mathbf{f}) = \sum_{j=1}^N \|H^j \mathbf{f} - \mathbf{g}^j\|_2^2 + \lambda_1 \|D\mathbf{f}\|_1 + \lambda_2 \|\mathbf{f}\|_1, \quad (4.3)$$

where  $\mathbf{g}$  is the vectorized discrete observation data,  $\mathbf{f}$  is the discrete underlying object image,  $H^j$  is the Toeplitz matrix that implements convolution as a matrix operation, and  $D$  is the discrete approximation to the gradient operator that computes first-order image differences in the horizontal and vertical directions. The  $\ell_1$ -norm employed in the 2<sup>nd</sup> and 3<sup>rd</sup> terms of Eq. 4.3 is non-differentiable in the vicinity of 0. Therefore, we use the following smooth approximation to the  $\ell_1$ -norm:

$$\|\mathbf{f}\|_1 \approx \sum_{i=1}^K (|(\mathbf{f})_i|^2 + \beta)^{1/2} \quad (4.4)$$

where  $\beta > 0$  is a small constant,  $K$  is the length of the vector  $\mathbf{f}$ , and  $(\mathbf{f})_i$  is the  $i$ th element of  $\mathbf{f}$ . Using this approximation, the cost function in Eq. 4.3 becomes:

$$\tilde{J}(\mathbf{f}) = \sum_{j=1}^N \|H^j \mathbf{f} - \mathbf{g}^j\|_2^2 + \lambda_1 \sum_{i=1}^M (|(D\mathbf{f})_i|^2 + \beta)^{1/2} + \lambda_2 \sum_{i=1}^K (|(\mathbf{f})_i|^2 + \beta)^{1/2} \quad (4.5)$$

#### 4.1.2 Solution to the optimization problem

The cost function in Eq. 4.5 is non-quadratic resulting in a challenging minimization problem. The quasi-Newton optimization method developed in (Çetin and Karl, 2001) is adapted to solve the minimization problem. The gradient of the cost function is

expressed as:

$$\nabla \tilde{J}(\mathbf{f}) = \tilde{H}(\mathbf{f}) \mathbf{f} - 2 \sum_{j=1}^N H^{jT} \mathbf{g}^j, \quad (4.6)$$

where

$$\tilde{H}(\mathbf{f}) \triangleq 2 \sum_{j=1}^N H^{jT} H^j + \lambda_1 D^T W_1(\mathbf{f}) D + \lambda_2 W_2(\mathbf{f}), \quad (4.7)$$

$$\begin{aligned} W_1(\mathbf{f}) &\triangleq \text{diag} \left\{ \frac{1}{((D\mathbf{f})_i^2 + \beta)^{1/2}} \right\}, \\ W_2(\mathbf{f}) &\triangleq \text{diag} \left\{ \frac{1}{((f)_i^2 + \beta)^{1/2}} \right\}, \end{aligned} \quad (4.8)$$

where  $\text{diag}\{\cdot\}$  is a diagonal matrix, and  $\tilde{\mathbf{H}}(\mathbf{f})$  is an approximation for the Hessian used in the quasi-Newton method. Each iteration of the quasi-Newton method is as follows:

$$\hat{\mathbf{f}}^{(n+1)} = \hat{\mathbf{f}}^{(n)} - \left[ \tilde{\mathbf{H}}(\hat{\mathbf{f}}^{(n)}) \right]^{-1} \nabla \tilde{J}(\hat{\mathbf{f}}^{(n)}). \quad (4.9)$$

Substituting the cost function given in Eq. 4.5, the following fixed-point iterative algorithm can be obtained:

$$\tilde{\mathbf{H}}(\hat{\mathbf{f}}^{(n)}) \hat{\mathbf{f}}^{(n+1)} = 2 \sum_{j=1}^N H^{jT} \mathbf{g}^j. \quad (4.10)$$

The iterations are terminated when  $\|\hat{\mathbf{f}}^{(n+1)} - \hat{\mathbf{f}}^{(n)}\|_2^2 / \|\hat{\mathbf{f}}^{(n)}\|_2^2 < \delta$ , where  $\delta$  is a small positive constant. Inside this iterative algorithm, another iterative algorithm, preconditioned conjugate gradient (CG) algorithm (Barrett et al., 1994), is employed in order to solve the set of linear equations (4.10) to calculate the updated estimate  $\hat{\mathbf{f}}^{(n+1)}$  for a given  $\tilde{\mathbf{H}}(\hat{\mathbf{f}}^{(n)})$ . The CG iterations are terminated when the  $\ell_2$ -norm of the relative residual becomes smaller than a threshold  $\delta_{CG} > 0$ .

The solution is initialized with the observation data at one polarization direction in the beginning of iterations. However, we also tried initialization with "all zeros" vector and that also converged to the same solution.

The convolution operation requires the domain of the output signal to be larger than the domain of the input signal by the support of the PSF. In convolutional reconstruction methods, the observed data is usually expanded by the size of the PSF so that the estimated underlying object has the same support as the original observed data. One approach for estimating the expanded area is to mirror the boundary region in the original observed data. However, since in our formulation the imaged structures are small compared to the support of the PSF, this results in significant errors in the estimated expanded area thus degrading the reconstruction performance. Another approach is to keep the observed data size the unchanged and only reconstruct a cropped region in the center with a smaller support than the observed data. However, this assumes that the underlying object image does not have any structure outside that region. Both of these methods rely on assumptions which cause large errors in the reconstruction in our problem since the support of the PSF is large compared to the size of the structures of interest in the underlying object. For this reason, we modified the forward model so that the domain of the underlying object intensity is larger than the domain of the observed intensity by half of the support of the PSF in each direction. This new forward model can be described by the following equation,

$$g^j(x, y) = (h^j(x, y) * f(x, y))w(x, y), \quad (4.11)$$

where  $w(x, y)$  is a window function which is zero outside the field of view. This approach acknowledges the fact that the observation data near an edge depends on the physical scene outside of the field of view. A comparison of this new forward model with the two aforementioned methods is presented in Section 4.4 using simulated and experimental data.

## 4.2 Simulated-data experiments

In order to assess the performance of the proposed image reconstruction algorithm in a controlled environment, we have simulated our experimental configuration. This configuration uses backside confocal imaging incorporating an aSIL under linearly-polarized light. We first simulated a theoretical PSF based on this configuration using the first approach explained in Section 3.2.1. We assumed an NA of 3.18 and a laser wavelength of 1300 nm. Fig. 3.1 shows the simulated PSF for  $x$ -polarized input light and for  $y$ -polarized input light.

We used the observation model in Eq. 4.11 and the theoretical PSF shown in Fig. 3.1 to create simulated observed images  $\mathbf{g}^j$  and we performed reconstruction from the simulated data. In Section 4.3, we also use the PSF shown in Fig. 3.1 to perform reconstruction from images acquired experimentally under linearly-polarized light.

The simulated data were created using a phantom which has the dimensions of a sample employed in our real data experiments. Fig. 4.1a shows the simulated object image using a pixel size of  $50nm$ , while Figs. 4.1b and 4.1c show simulated observation images for  $x$ - and  $y$ -polarized input light, respectively.

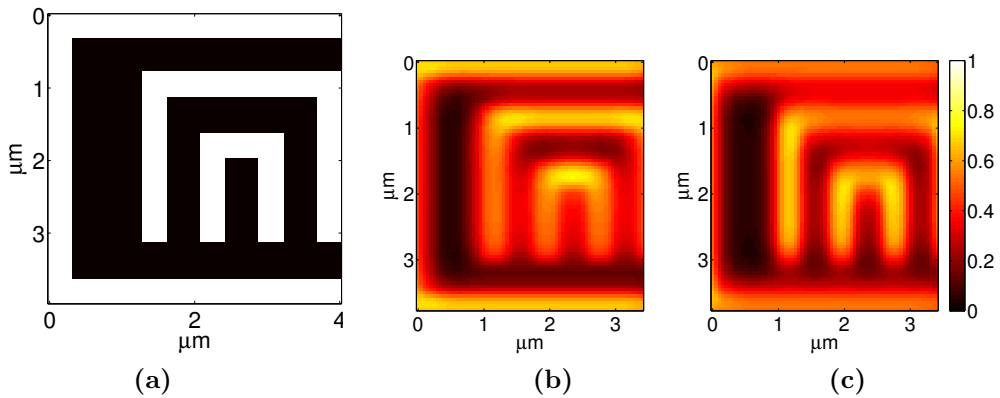


**Figure 4.1:** (a) Simulated object image and observed images under polarization in (b)  $x$  direction and (c)  $y$  direction.

First, we performed reconstruction using the observed images in Fig. 4.1 with no regularization terms using CG algorithm. We performed separate reconstructions from the observed image under  $x$ -polarization (Fig. 4.2a), and under  $y$ -polarization (Fig. 4.2b). Then, we performed reconstruction jointly under both polarizations (Fig. 4.2c). Our goal here is to show the improved reconstruction quality when multiple-polarization data are employed. It is clear from Fig. 4.2 that using multiple-polarization data leads to a visually improved reconstruction quality. We will also evaluate reconstruction performance quantitatively later in this section.

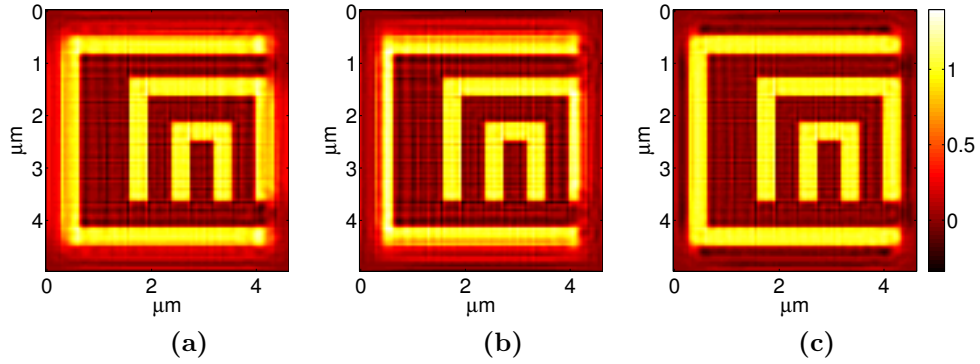


**Figure 4.2:** Image reconstruction results on simulated data with no regularization: (a) only from an observation image under  $x$ -polarized light, (b) only from an observation image under  $y$ -polarized light, (c) from observation images under both  $x$ - and  $y$ -polarized light.

In the second set of experiments, we performed reconstruction with both regularization terms (Eq. 4.2). The images reconstructed from observation under  $x$  and  $y$  polarization separately are shown in Figs. 4.3a and 4.3b. The regularization parameters were chosen as  $\lambda_1 = 0.0025$  and  $\lambda_2 = 0.0002$  for both  $x$ -polarization only reconstruction and  $y$ -polarization only reconstruction. These choices were obtained through an exhaustive search where the regularization parameters minimizing the MSE are chosen. The reconstruction obtained by using both polarizations jointly is shown in Fig. 4.3c. The regularization parameters were chosen as  $\lambda_1 = 0.005$  and  $\lambda_2 = 0.0004$ . These results indicate that using data taken under light which is linearly-

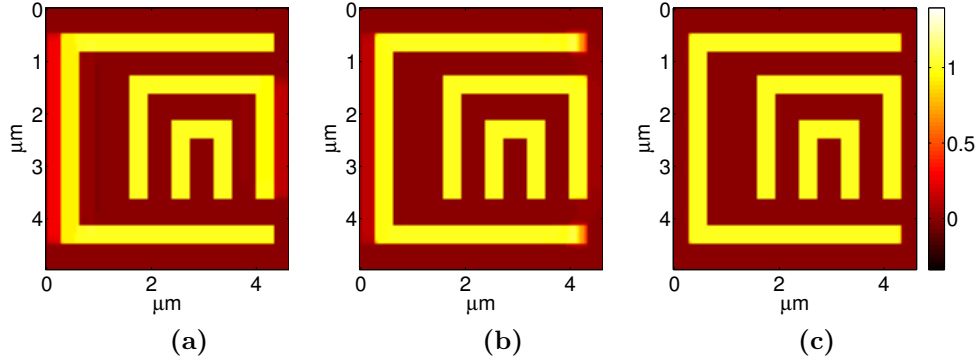


**Figure 4.3:** Regularized image reconstruction results on simulated data with=: (a) only from an observation image under  $x$ -polarized light for  $\lambda_1 = 0.0025$   $\lambda_2 = 0.0002$ , (b) only from an observation image under  $y$ -polarized light for  $\lambda_1 = 0.0025$   $\lambda_2 = 0.0002$ , (c) from observation images under both  $x$ - and  $y$ -polarized light for  $\lambda_1 = 0.005$   $\lambda_2 = 0.0004$ .

polarized in multiple directions is more advantageous than using data obtained under a single polarization direction. Also, it is clear that regularization terms help preserve sparsity of the edge field of the reconstructed image. We note that these simulated observed images are noiseless, while in any actual experimental scenario the observed images will likely be noisy. This along with the fact that in real conditions the linear forward model may not be accurate, the reconstruction performance may degrade. The reconstructions for single polarization are not perfect even though no noise is added to observation data because we are estimating a larger regions than field of view and this results in an underdetermined system. To quantify the reconstruction performance, we calculated the mean square error (MSE) between the underlying object image and the reconstructed image as follows:

$$MSE = \frac{\sum_{k=1}^{LS} (\hat{\mathbf{f}}_k - \mathbf{f}_k)^2}{LS} \quad (4.12)$$

where  $\hat{\mathbf{f}}$  is the reconstruction result,  $\mathbf{f}$  is the vectorized discrete underlying object intensity, and  $L$  and  $S$  are the number of pixels in horizontal and vertical directions, respectively. The bar plot in Fig. 4.4 presents MSE values for different types of

reconstructions. They show that the reconstruction performance increases, when we employ reconstruction from observed images under both polarization directions jointly compared with image reconstruction from an observed image under single polarization. They also demonstrate the increase in reconstruction performance by incorporating regularization terms in image reconstruction. The MSE for regularized image reconstruction employing both polarization data is sufficiently small that it does not appear in the plot.

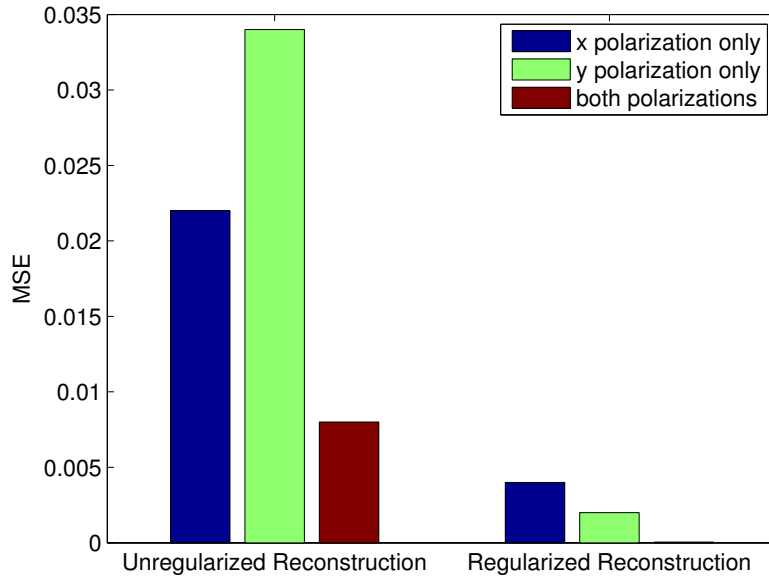


**Figure 4.4:** MSE between reconstructed images and underlying object image

We also performed experiments where we used a phantom which can be used as a resolution target. This phantom is shown in Fig.4.5. It consists of lines with varying width and varying separation. For this experiment, observation data is created convolving the phantom with the PSF that is simulated using the Green's function approach explained in Section 3.2.2. The lines are assumed to be aluminum metal lines because this is the case for the resolution target used in real data experiments



shown later. For the simulation of the PSF, an aluminum spherical particle of radius  $25nm$  is assumed to be placed on the silicon-air interface and the image is calculated using Eq. 3.4 with  $\alpha = 2.5^3$ . The simulated PSF is shown in Fig.3.5b. The pixel size for the PSF and the phantom is  $46nm$ . In this experiment, we also added additive Gaussian noise to the observation data and we study how reconstruction performance changes with different levels of noise. Although the signal-to-noise ratio (SNR) is not very low for experimental aSIL images in the next section, there are image modalities such as LVI that we study in Chapter 6 that have very low SNR levels. Therefore, it is useful to compare the performance of different sparse reconstruction approaches for different levels of noise. In this experiment, in addition to studying reconstruction performance for different levels of noise, we also study the resolution limit in the reconstructed image since the phantom has lines with varying width and varying separation. Observation data with different levels of noise are shown in Fig. 4.6. The intensity range for the resolution target phantom is  $[0,1]$ , but observation data in Fig. 4.5 have negative values. The reason for that is that reflection from the interface has higher intensity than the scattered light from the structures and the intensity of reflection from the interface has been subtracted from the total intensity in the PSF model in Eq. 3.4. In other words, the simulated PSF have negative intensity values and this results in negative values in the observation data.

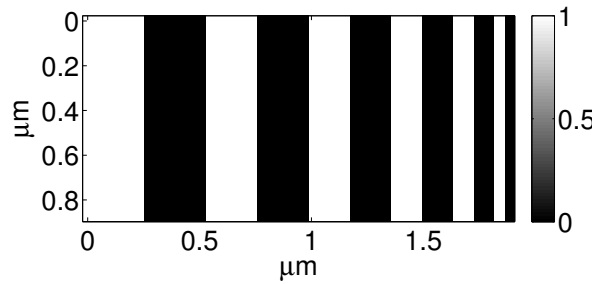


**Figure 4.5:** The resolution target phantom

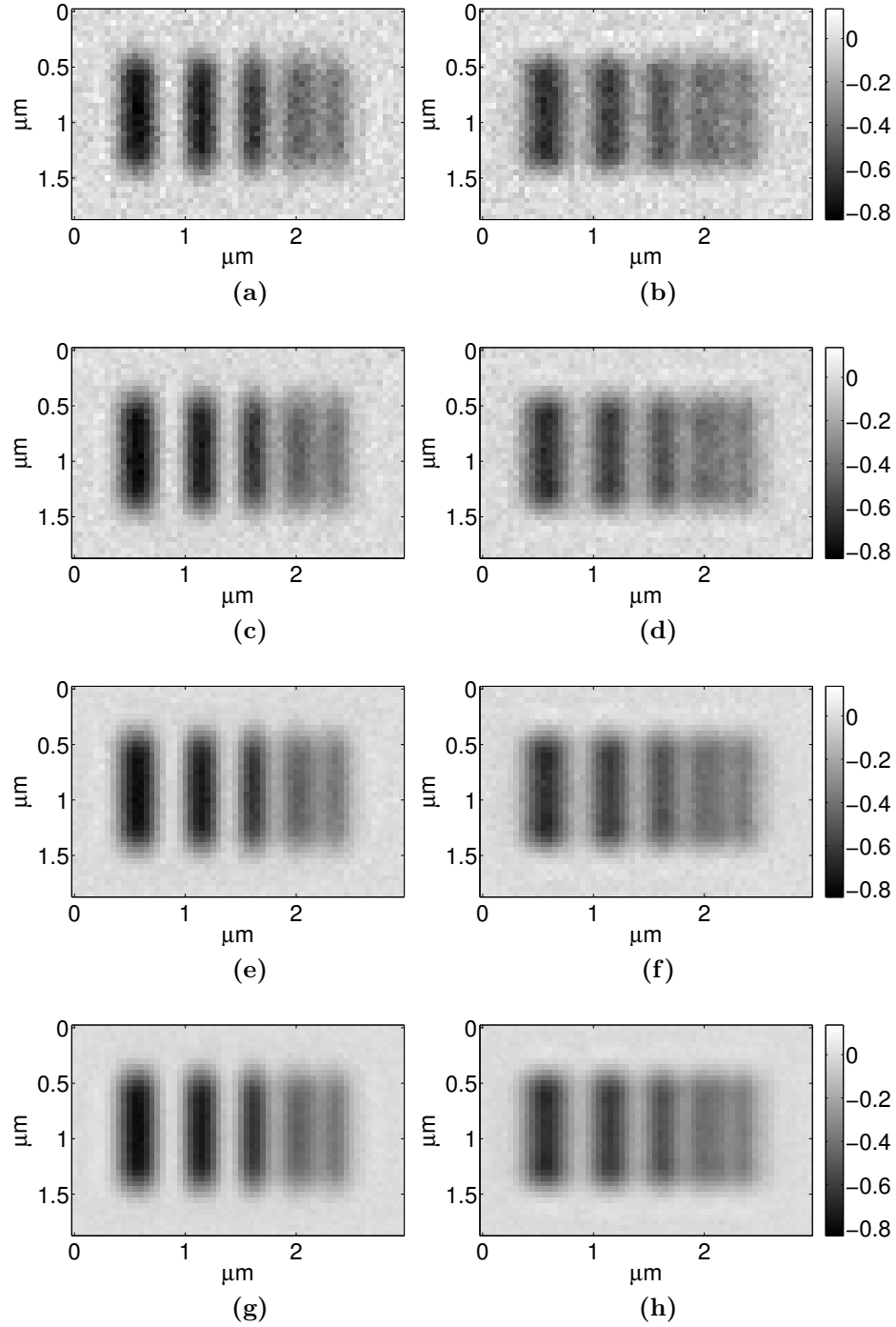


**Figure 4-6:** Simulated observation images of the resolution phantom of Fig. 4-5 for  $x$ -polarized input light (a) SNR=16dB, (c) SNR=20dB, (e) SNR=25dB, (g) SNR=30dB, and for  $y$ -polarized input light (b) SNR=16dB, (d) SNR=20dB, (f) SNR=25dB, (h) SNR=30dB

The results of the multiple polarization reconstruction framework are shown in Fig. 4-7. One of the resolution metrics used for IC imaging is the Sparrow resolution criterion. The Sparrow criterion defines the resolution as the distance between the peaks of the two PSFs when the midpoint just becomes visible. Similarly, we can evaluate if a resolution structure is resolved or not, in other words, if a structure is localized or not, depending on whether we observe a peak. The thinnest line of width  $56nm$  can only be localized for noise levels of 25 dB and 30 dB. For higher levels of noise the localization accuracy decreases. Also a quantitative comparison of the reconstruction performance for different levels of noise is shown in the MSE plot in Fig. 4-8. The error bars are calculated using the standard error given by  $\sigma/\sqrt{n}$ , where  $\sigma$  is the standard deviation of the MSE values over all realizations and  $n$  is the number of realizations. We have used 10 realizations in this experiment.

### 4.3 Real-data experiments

In order to test the proposed reconstruction method in a real-data scenario, we acquired experimentally three sets of images. The first data set was acquired using linearly-polarized light focused on passive polysilicon structures at the silicon-silicon dioxide interface in a test sample. The second dataset was acquired using circularly-polarized light focused on passive aluminum structures at the silicon-air interface. Under circularly polarized light, the PSF has a circular support having the same width in all directions, thus image reconstruction was performed using a single observed image. The third data set, acquired using linearly-polarized light, also contains images of passive aluminum structures at the silicon-air interface. However, the structures in the third set are smaller and their separation is also smaller. Hence, this data set is important for showing a super-resolution-like behavior of the proposed image reconstruction framework.

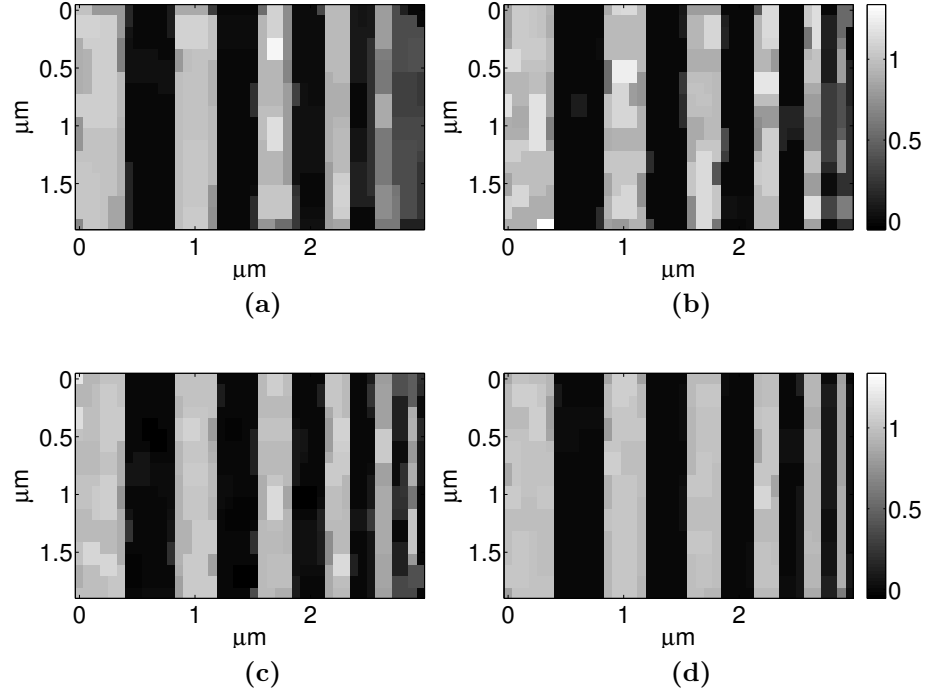


**Figure 4.7:** Results of regularized image reconstruction combining both polarization data (a) SNR=16dB  $\lambda_1 = 0.0025$   $\lambda_2 = 0.005$ , (b) SNR=20dB  $\lambda_1 = 0.0005$   $\lambda_2 = 0.005$ , (c) SNR=25dB  $\lambda_1 = 0.00025$   $\lambda_2 = 0.00025$ , (d) SNR=30dB  $\lambda_1 = 0.00025$   $\lambda_2 = 0.005$

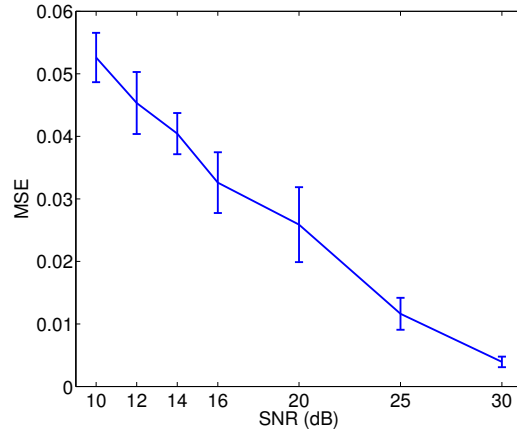


**Figure 4.8:** MSE between underlying object image and reconstructed images from observation data with different levels of noise

The experimental images for the first set of data are shown in Figs. 4.9a and 4.9b for the  $x$  and  $y$  directions, respectively. The image reconstruction results for this data set are presented in Figs. 4.10a, 4.10b, and 4.10c. The regularization parameters were chosen as  $\lambda_1 = 0.75$  and  $\lambda_2 = 0.5$  for  $x$ -polarization only reconstruction and as  $\lambda_1 = 0.5$  and  $\lambda_2 = 0.35$  for  $y$ -polarization only reconstruction. These choices were obtained through an exhaustive search where the regularization parameters giving the best qualitative result were chosen. The regularization parameters were chosen as  $\lambda_1 = 1$  and  $\lambda_2 = 0.5$  for both polarizations reconstruction. The pixel size for this data set is  $18.5nm$ . In the reconstruction framework, we employed the theoretical PSF shown in Fig. 3.1. Reconstruction results on experimental data indicate that performing

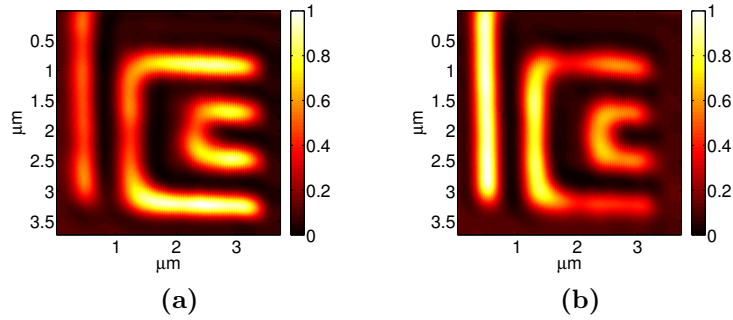


**Figure 4.9:** Experimental observation images under polarization in (a)  $x$  direction and (b)  $y$  direction.

reconstruction on multiple-polarization images increases the reconstruction quality - reconstructed images exhibit homogeneous regions, accentuated edges and shaper structures in all directions. In particular, the reconstruction obtained using only  $x$ -polarized data is of higher contrast and better resolution for horizontal structures than for vertical structures. A corresponding observation holds for the reconstruction from  $y$ -polarized data. The reconstruction obtained using both polarization data preserves the intensity of both vertical lines and horizontal lines. One metric of resolution for optical images is the Houston resolution criterion. The Houston criterion defines the

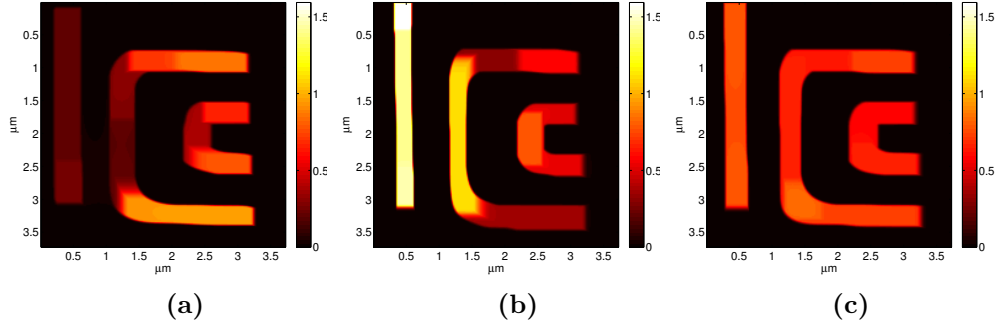


**Figure 4.10:** Regularized image reconstruction results on experimental data (a) only from an observation image under  $x$ -polarized light for  $\lambda_1 = 0.75$   $\lambda_2 = 0.5$ , (b) only from an observation image under  $y$ -polarized light for  $\lambda_1 = 0.5$   $\lambda_2 = 0.35$ , (c) from observation images under both  $x$ - and  $y$ -polarized light for  $\lambda_1 = 1$   $\lambda_2 = 0.5$ .

resolution as the Full Width at Half Maximum (FWHM) of the PSF. Relating the width of the PSF to the sharpness of the edges, the Houston criterion can be used to judge the resolution performance by the sharpness of the edges in the reconstructed image. For this purpose, we compare cross sections from the reconstructed images and the observation images. Comparing cross sections from the image reconstruction results with the cross sections from the experimental observed images in Fig. 4.11, it is clear that one can achieve edge resolution improvement with the proposed reconstruction framework for IC images acquired with high-NA systems employing linearly-polarized light.

The next experiment demonstrates the performance of the proposed methods when samples of different material properties are observed under circularly polarized light. The simulated theoretical PSF for the second set of data is presented in Fig. 4.12. We have used the reflected field approach explained in Section 3.2.1 in order to simulate this PSF. The microscope used to acquire these data had an NA of 3.2, and the wavelength of light used was 1300 nm. We imaged two different regions with resolution targets of different size. The experimental observations are shown in Figs. 4.13a and

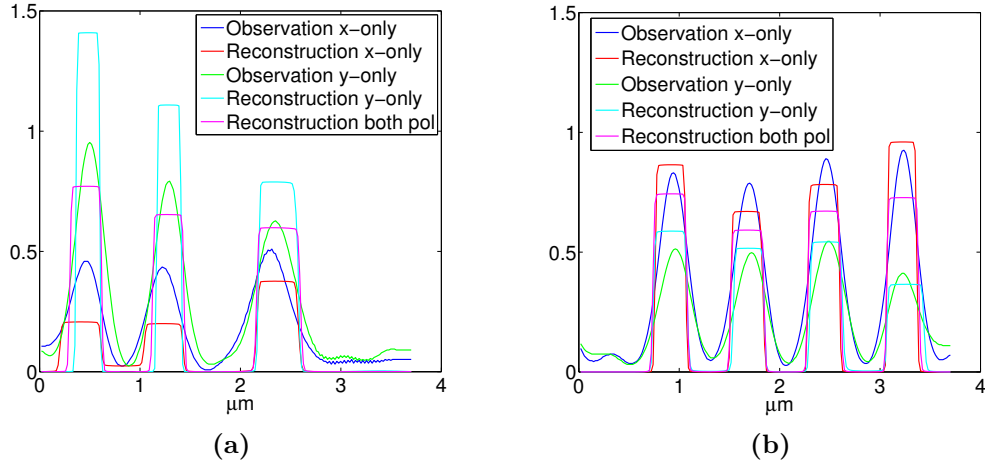


**Figure 4-11:** Cross sections from the observation data and reconstructed images: (a) horizontal (b) vertical

4-13b. Unlike the observation images shown in Fig. 4-9, the images of these structures show a black outline effect where there is an apparent dip in the intensity at the edges of the structures. We believe these are caused by destructive interference effects because of the change from a pure dielectric interface to a metal interface as the laser spot scans through the transition region. The reconstruction results for this data set are presented in Figs. 4-14a and 4-14b. The improvement for this data set is not as obvious as the improvement for the previous data set because of the greater mismatch between the assumed forward model and the actual system; the black outlines along the edges are not predicted by the PSF. This study demonstrated that depending on the size of the structures and on their material properties, the PSF needs to be modified. This is why, the second approach to PSF simulation was proposed in Section 3.2.2. For this reason, for the third set of data, which contains images of aluminum structures, we will use the PSF simulated with the second approach.

The third data set contains aSIL images of horizontal and vertical resolution lines with different pitches:  $282nm$ ,  $252nm$ , and  $224nm$ . They are made of metal aluminum lines deposited on a double-sided polished silicon wafer, hence they lie on silicon-air

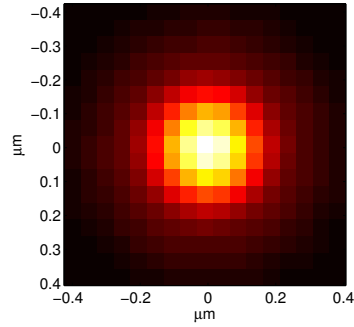


**Figure 4.12:** Simulated theoretical PSF for circularly-polarized input light source.

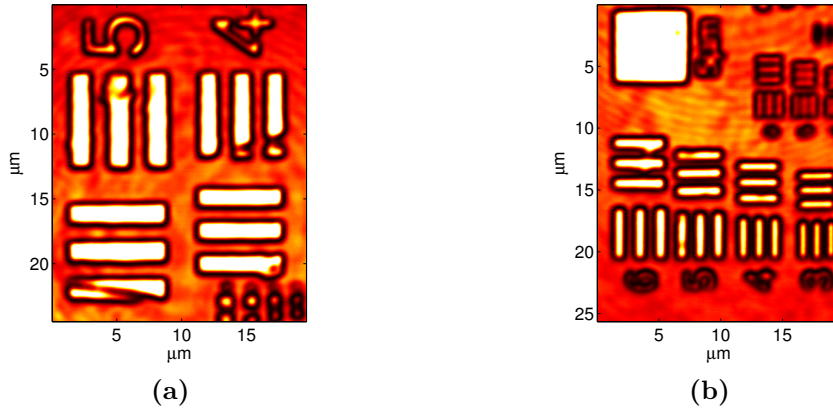


**Figure 4.13:** Experimental observation images

interface. The Scanning Electron Microscope (SEM) images of the aluminum lines are shown in Fig. 4.15. The aSIL microscopy data with  $x$ -polarized and  $y$ -polarized input light of the resolution target are shown in Figs. 4.16a and 4.16b for  $282nm$  pitch lines, in Figs. 4.17a and 4.17b for  $252nm$  pitch lines, and in Figs. 4.18a and 4.18b for  $224nm$  pitch lines. The regularization parameters were chosen as  $\lambda_1 = 0.0005$  and  $\lambda_2 = 0.05$  for the case of  $282nm$ , as  $\lambda_1 = 0.0005$  and  $\lambda_2 = 0.05$  for the case of  $252nm$  and as  $\lambda_1 = 0.00005$  and  $\lambda_2 = 0.001$  for the case of  $224nm$ . These choices were obtained through an exhaustive search where the regularization parameters giving the best qualitative result were chosen. Clearly, the  $252nm$  and  $224nm$  pitch lines



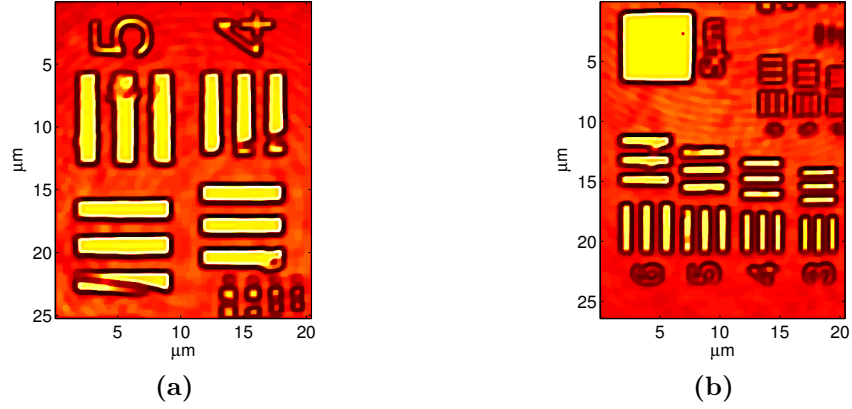


**Figure 4.14:** Regularized image reconstruction results (a)  $\lambda_1 = 0.1$ ,  $\lambda_2 = 0.01$ , (b)  $\lambda_1 = 0.1$ ,  $\lambda_2 = 0.01$

cannot be localized in the observation data. In the reconstruction framework, we have used the PSF shown in Fig. 3.5b with  $\alpha = 2.5^3$  for the  $282nm$  and  $252nm$  pitch lines. However, for the  $224nm$  pitch lines we have to account for the decrease in the width of the lines and used the PSF with  $\alpha = 2.4^3$ . The reconstructions are shown in Fig. 5.18a, 5.19a and 5.20a. There are some oscillations in the background, but the number of lines and the thickness of the lines for  $282nm$  and  $252nm$  pitch lines match the SEM data. The reconstruction for  $224nm$  pitch vertical lines is at the limit of localization, and some of the horizontal lines cannot be localized. The reason for this is the defect in the fabrication of the horizontal lines; it can be seen in the SEM image in Fig. 4.15c. The resolution of the optical system was  $282nm$  according to the Sparrow criterion, since we can localize lines with  $224nm$  separation in the reconstructed image; the equivalent resolution was improved to  $224nm$  by the reconstruction framework.

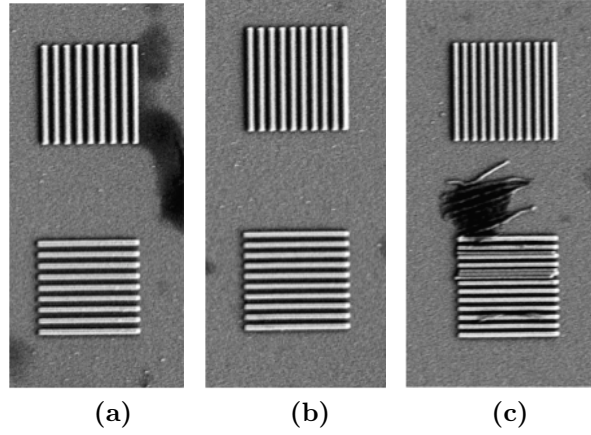


**Figure 4-15:** SEM images for lines resolution target with (a)  $282nm$  (b)  $252nm$  (c)  $224nm$  separation

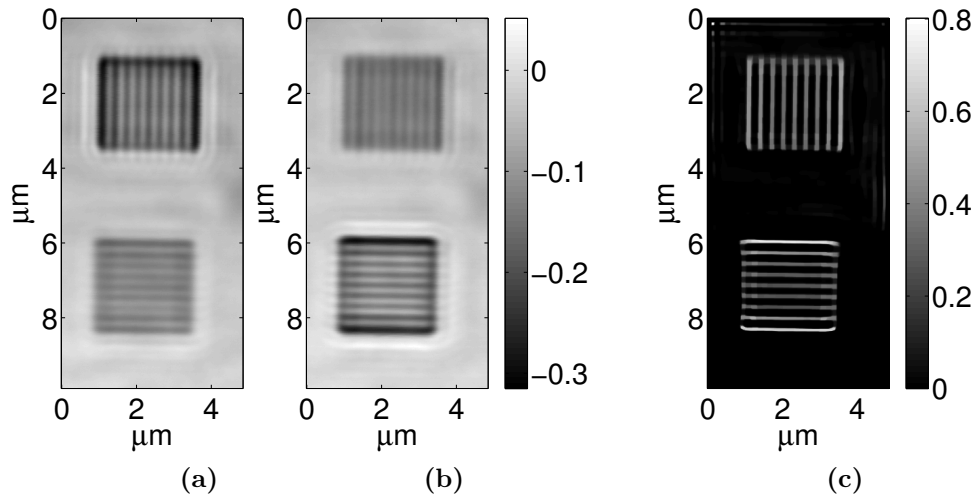


**Figure 4-16:** Observation data of resolution target of aluminum lines with  $282nm$  pitch (a)  $x$ -polarized input light (b)  $y$ -polarized input light, (c) regularized reconstruction results for  $\lambda_1 = 0.0005$ ,  $\lambda_2 = 0.05$ .

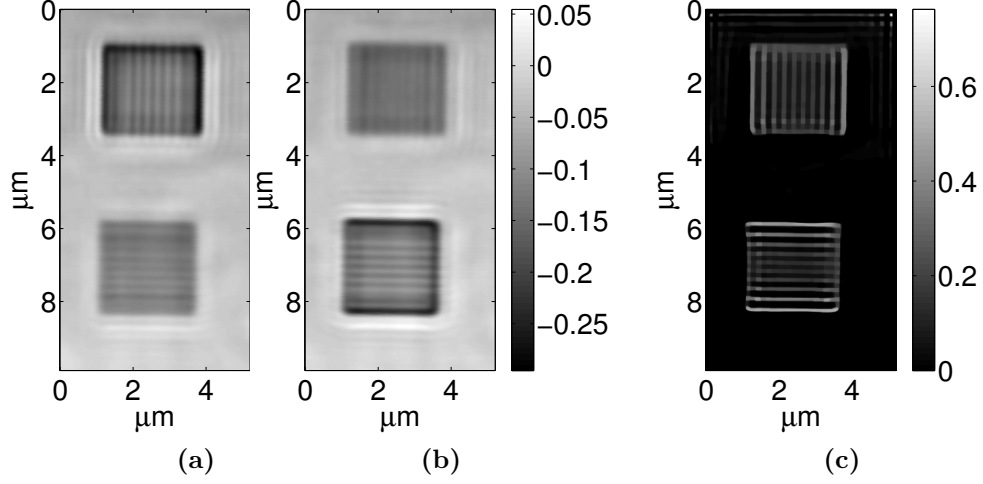


**Figure 4-17:** Observation data of resolution target of aluminum lines with 252nm pitch (a)  $x$ -polarized input light (b)  $y$ -polarized input light, (c) regularized reconstruction results for  $\lambda_1 = 0.0005$ ,  $\lambda_2 = 0.05$ .

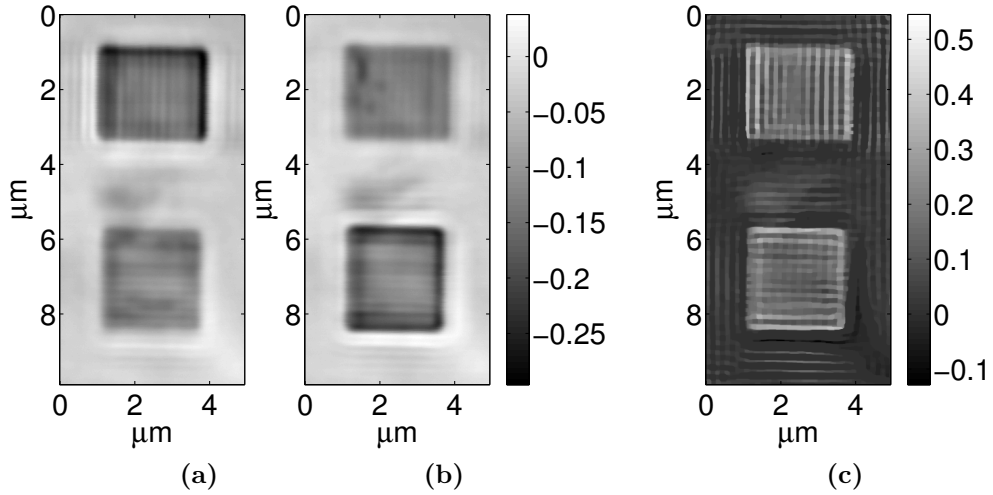


**Figure 4-18:** Observation data of resolution target of aluminum lines with 224nm pitch (a)  $x$ -polarized input light (b)  $y$ -polarized input light, (c) regularized reconstruction results for  $\lambda_1 = 0.00005$ ,  $\lambda_2 = 0.001$ .

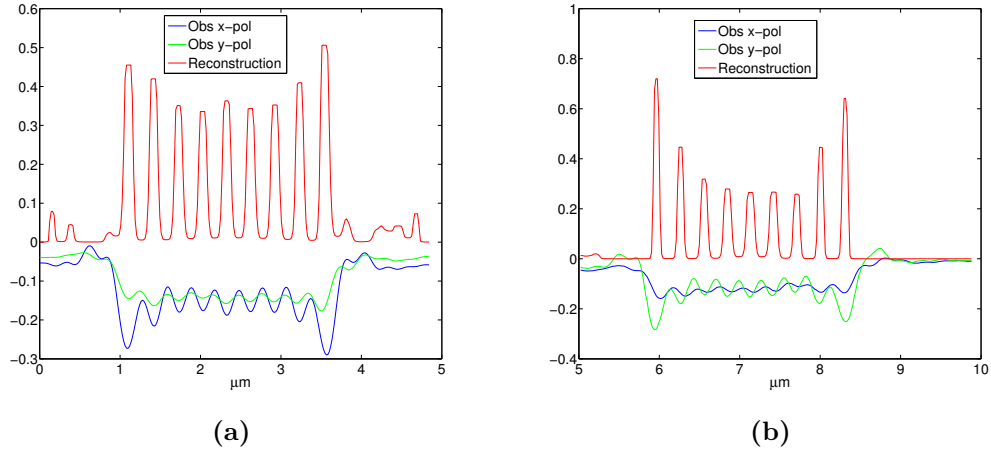


**Figure 4-19:** Cross sections from the observation and reconstructions for aluminum lines with 284nm separation (a) horizontal, (b) vertical.

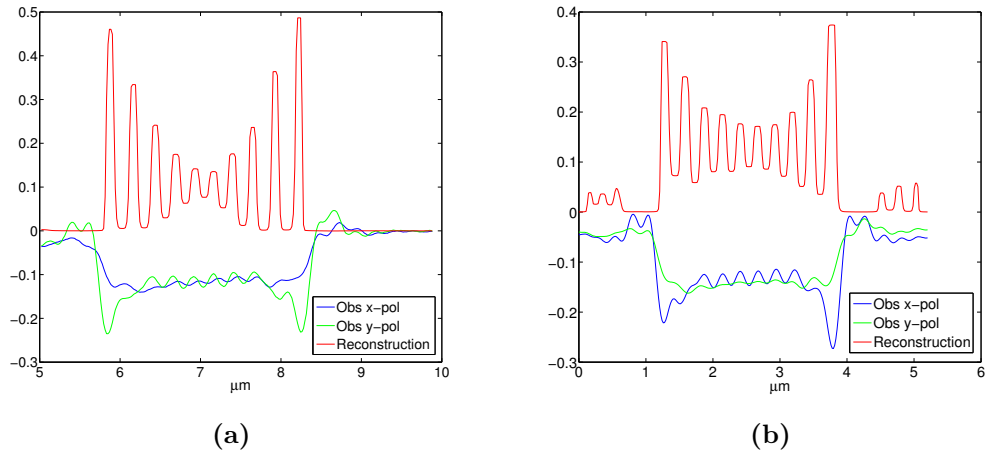


**Figure 4-20:** Cross sections from the observation and reconstructions for aluminum lines with 252nm separation (a) horizontal, (b) vertical.

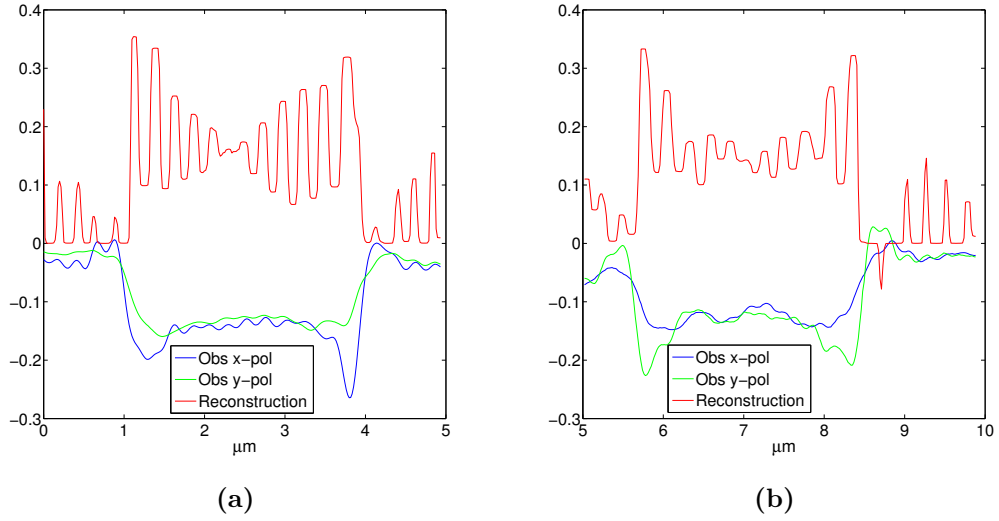


**Figure 4.21:** Cross sections from the observation and reconstructions for aluminum lines with  $224\text{nm}$  separation (a) horizontal, (b) vertical.

#### 4.4 Comparison of different boundary condition settings

We are modeling our system with a linear convolutional model. When we calculate the convolution of two discrete signals, one with size  $L$ , the other with size  $P$ , the size of the output signal is equal to  $L + P - 1$ . Modeling the system as in Eq. 3.1 requires that the observed image be larger than the underlying object image. Conventional image reconstruction techniques will set particular boundary conditions to handle this problem. We first employed two different boundary condition assumptions to handle this problem, but realized that since the size of the PSF is fairly large compared to the size of the observed image, conventional boundary conditions degraded the reconstruction performance. For this reason, we modified the forward model in order to avoid approximations that conventional boundary conditions make about the boundary pixels. These three different methods of handling boundary pixels are explained in the following subsections.

#### 4.4.1 Mirroring the boundary pixels

Before reconstruction, the observed image is padded with size of the PSF minus 1 pixels by mirroring the pixels at the boundary. In other words, the observed image will be in the center of a new padded image, and the boundary pixels of the padded image will be the first and last pixels of the observed image. Then, this new padded image will be employed to reconstruct an image of the same size as the observed image. When the size of the PSF is not large or we do not have structures along the boundary of the observed image, this method can be employed. However, in our case, as we can see in Fig. 4-22, a large number of pixels were padded and structures, which are not present in the underlying object, were created along the boundary of the padded image.

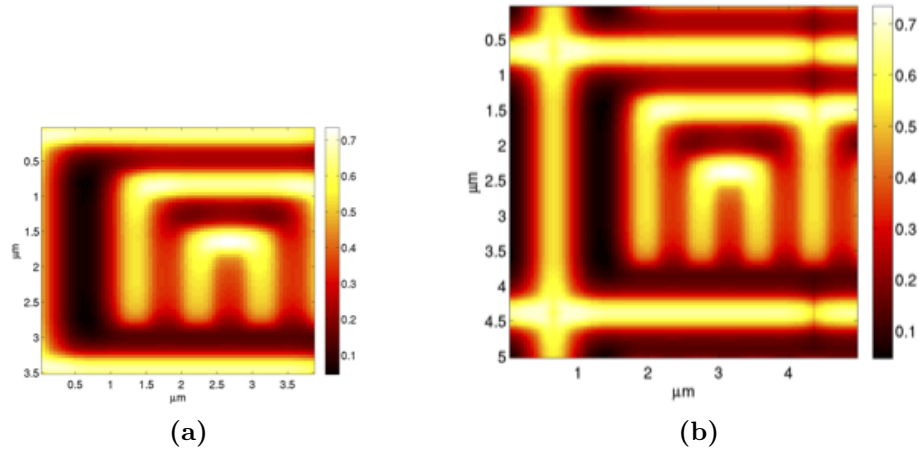


**Figure 4-22:** (a)observation (b)observation after mirror-image padding

#### 4.4.2 Reconstructing a cropped image

In this method, we do not modify the observed image but reconstruct an image corresponding to the center area in the observed image with pixel size equal to the number of pixels in observed image minus size of PSF plus 1. We basically perform

a reconstruction for a cropped center area in the observed image. The issue with this method is that it assumes the area outside of the cropped area in the underlying object to be zero-valued. It assumes that there are no structures outside this cropped region in the underlying object. For large PSFs, this method disregards fairly large structures.

#### 4.4.3 Modifying the forward model

The forward convolutional model is modified to account for the fact that we are observing a smaller area compared with the area of the underlying object we are reconstructing. In other words, we assume a convolutional model relating the area we are reconstructing with a larger observation image and we assume that we are cropping the center part, and only observing that part. This is expressed in Eq. 4.11. This is also shown in Fig. 4-23. The window function  $w(x, y)$  corresponds to the purple box in Fig. 4-23; in the new forward model the windowing function is added to the convolution operation. With this model, the linear forward system becomes underdetermined. We are trying to reconstruct a larger region than we are observing, but we still have information contained in the boundary pixels of the observed image about the region which is not in the field of view, because the pixels in the enlarged reconstruction affect the pixels in the boundary of observation.

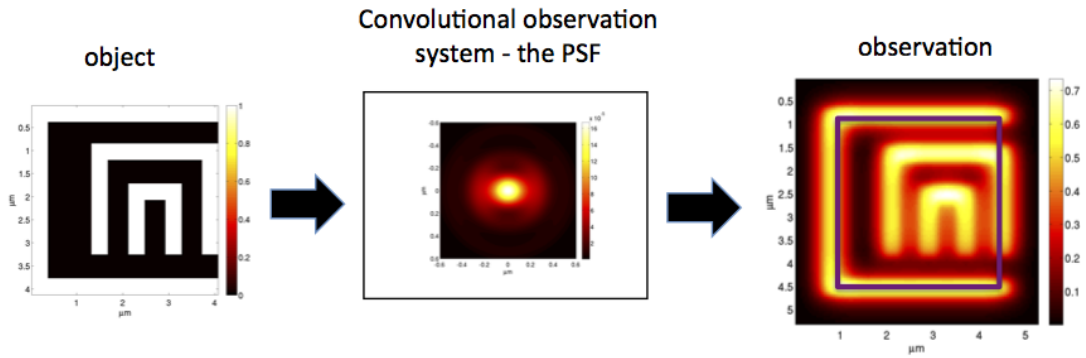


**Figure 4-23:** Diagram showing modification of the forward model

#### 4.4.4 Reconstruction results with different boundary condition settings

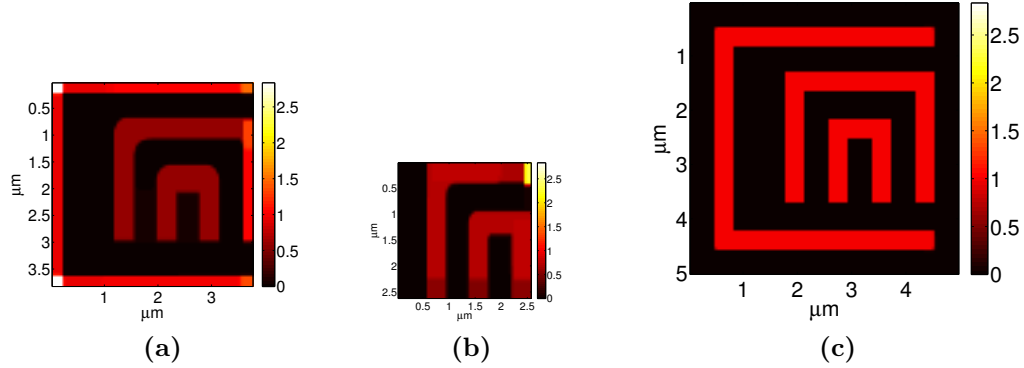


**Figure 4-24:** Image reconstruction results on simulated data comparing different boundary condition settings: (a) mirroring the boundary pixels for  $\lambda_1 = 0.5$ ,  $\lambda_2 = 0.75$ , (b) reconstructing a cropped center area for  $\lambda_1 = 0.375$ ,  $\lambda_2 = 0.59$ , (c) modifying the forward model for  $\lambda_1 = 0.0025$ ,  $\lambda_2 = 0.001$ .

In order to compare the reconstruction performance with these three different boundary condition settings, we performed reconstruction on the simulated data presented in Section 4.2 and on the experimental data under linearly-polarized light presented in Section 4.3. The results for the simulated data are shown in Fig. 4-24a, 4-24b, 4-24c and results on experimental data are shown in Fig. 4-25a, 4-25b, 4-25c. We also calculated MSE values for simulated data reconstructions for each of the boundary condition settings, (Fig. 4-26). These results show that modifying the forward model outperforms the other two boundary condition settings.

## 4.5 Conclusions

In this Chapter, we proposed a framework for resolution improvement for backside aSIL images of integrated circuits. Modification of the polarization direction of linearly-polarized light sources in high NA systems improves the resolution in selected directions. We applied a regularized image reconstruction algorithm to a set



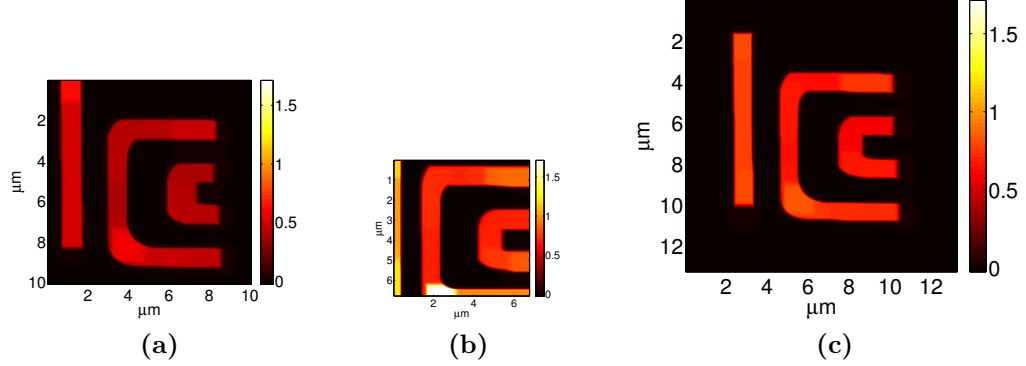


**Figure 4.25:** Image reconstruction results on experimental data comparing different boundary condition settings: (a) mirroring the boundary pixels for  $\lambda_1 = 1.25$ ,  $\lambda_2 = 0.75$ , (b) reconstructing a cropped center area for  $\lambda_1 = 1$ ,  $\lambda_2 = 0.25$ , (c) modifying the forward model for  $\lambda_1 = 1$ ,  $\lambda_2 = 0.5$ .

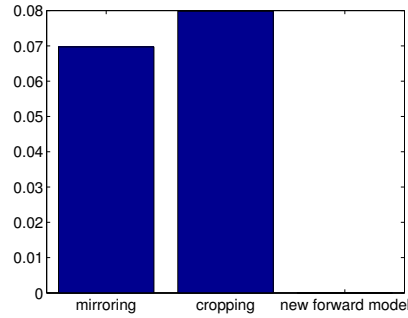


**Figure 4.26:** MSE between reconstructed images and underlying object image with different boundary condition settings.

of images collected with linearly-polarized light with different polarization directions and obtained a single higher-resolution reconstructed image benefiting from the best resolution in each observation image. The proposed method benefits from the preliminary knowledge about the structure of the underlying object by incorporating non-quadratic regularization functionals into the image reconstruction framework. We showed the advantage of this type of regularization over unregularized reconstruction in simulated data. Combining multiple images under input light with different

polarization directions increases the robustness of the reconstruction to noise in experimental data and increases robustness to mismatches between the actual system and the assumed forward model. Additionally, we compared different techniques for handling boundary pixels in a convolution model for an aSIL IC imaging system. This study is critical for this application because the PSF is fairly large compared to the size of objects of interest and conventional assumptions about boundary pixels might cause large errors in the reconstructed image.

## Chapter 5

# Dictionary-based image reconstruction for resolution enhancement in integrated circuit imaging

In this Chapter, we propose a synthesis-based image reconstruction framework which couples overcomplete dictionary-based representation with physics-based forward model to improve resolution and localization accuracy in high-NA confocal microscopy images of ICs.

Altering the polarization direction of linearly-polarized illumination in high-NA systems provides polarization diversity enabling collection of multiple observations with varying spatial resolution in different directions (Köklü et al., 2009). In Chapter 4, we proposed a novel image fusion framework that benefits from this polarization diversity and prior knowledge about the structures in ICs in order to achieve resolution improvement. In this fusion framework, prior knowledge about the structures in ICs, the fact that small features in ICs are composed of lines and rectangular structures resulting in piecewise-constant images, is incorporated into the reconstruction framework by using non-quadratic regularization functionals, in other words by an analysis-based sparsity paradigm. These non-quadratic functionals preserve the sparsity and the edges of the underlying features. Although resolution improvement can be achieved by these generic sparsifying priors, an additional improvement is possible by further exploiting the nature of the data. Therefore, we propose another framework which is based on overcomplete dictionaries and which exploits further the

highly structured nature of IC features.

The domain of IC imaging is particularly suitable for the application of overcomplete dictionaries in an image reconstruction framework. Predefined overcomplete dictionaries can be easily built using a limited set of building blocks derivable from computer aided design layouts (CADs). Specifically, ICs are mostly composed of horizontal or vertical lines of varying, constrained and known widths and lengths. Therefore, the scene in the field of view can be sparsely represented using these predetermined overcomplete dictionaries and this sparse representation will provide increased robustness to model mismatches, noise and resolution limits since dictionary elements pose strong priors for the structures in ICs. In this chapter, we present an image reconstruction framework to improve the resolution in high-NA IC imaging which couples a representation based on overcomplete dictionary with the extended PSF model from Section 3.2.2.

This Chapter is organized as follows. In Section 5.1, we provide details of the proposed framework. The observation model is described in Section 5.1.1. The sparse representation framework is presented in Section 5.1.2, while the corresponding construction of the dictionaries is described in Section 5.1.3. We present results on simulated and experimental data in Section 5.2. In Section 5.4, we provide summary and conclusions.

## 5.1 Dictionary-based image reconstruction framework for IC imaging

### 5.1.1 Observation model

Given the PSF modeled by the Green's function approach from Section 3.2.2, the assumed linear convolution model is expressed as:

$$\mathbf{g}^j = H^j \mathbf{f}, \quad (5.1)$$

where  $j$  indicates the polarization direction of linearly-polarized input light source,  $\mathbf{g}^j$  is the vectorized discrete observation data,  $\mathbf{f}$  is the discrete vectorized underlying object image,  $H^j$  is the Toeplitz matrix that implements convolution as a matrix operation based on the PSF in polarization direction  $j$ .

### 5.1.2 Sparse representation framework for resolution-enhanced IC imaging

Our goal is to obtain high-resolution images through sparse image reconstruction by using the information in CAD layouts. Additionally, we combine the information coming from high-resolution orientation information in each observation by incorporating the multiple observations from Section 5.1.1 into the sparse representation framework. The unknown underlying scene  $\mathbf{f}$  can be represented as:

$$\mathbf{f} = \Phi\boldsymbol{\eta}, \quad (5.2)$$

where  $\Phi$  is an overcomplete dictionary composed of building blocks of the structures in the IC and  $\boldsymbol{\eta}$  is the vector of representation coefficients. The dictionary  $\Phi$  can be predetermined by using the CAD layouts, since we know the dimensions of structures in ICs under consideration *a priori*. These structures are composed of lines of specified width and varying length. Combining this sparse representation with the observation model in Eq. 5.1, the overall model can be rewritten in the presence of noise  $\mathbf{w}_j$  as:

$$\mathbf{g}^j = H^j\Phi\boldsymbol{\eta} + \mathbf{w}_j. \quad (5.3)$$

We now create an estimate of the underlying IC scene by posing the problem as an  $\ell_p$  regularization problem, i.e., a sparse reconstruction problem with respect to the

given circuit dictionary  $\Phi$ :

$$\hat{\boldsymbol{\eta}} = \arg \min_{\boldsymbol{\eta}} J(\boldsymbol{\eta}) = \sum_{j=1}^N \| H^j \Phi \boldsymbol{\eta} - \mathbf{g}^j \|_2^2 + \lambda \| \boldsymbol{\eta} \|_p^p, \quad (5.4)$$

where  $p \leq 1$ ,  $N$  is the total number of observed images at various polarizations and  $\lambda$  is a regularization parameter that adjusts the overall level of problem sparsity. It has been shown in spectral analysis that higher-resolution spectral estimates can be obtained using the  $\ell_p$ -norm, where  $p < 2$  rather than the  $\ell_2$ -norm (Ciuciu et al., 1999). Previous studies show that  $\ell_p$ -regularization with  $p < 1$  can produce sparser solutions than  $\ell_1$ -regularization (Chartrand, 2007; Xu et al., 2012). However, in the case of  $p < 1$  the objective function in the minimization problem in Eq. 5.4 is non-convex, whereas it is convex for the case of  $p = 1$ . The minimization problem with  $p = 1$  is solved with the  $\ell_1$ -ls solver provided by the authors of the interior-point method for  $\ell_1$ -regularized least squares in (Kim et al., 2007). For the case of  $p \leq 1$ , the  $p$ -Shrinkage algorithm in (Voronin and Chartrand, 2013) has been used.

### 5.1.3 Construction of dictionaries

The structures in ICs consist of flat regions consisting of horizontal and vertical lines of constrained and varying width and length as can be seen in the CAD layout in Fig. 5-1. To construct our dictionary, we divided the structures into rectangles and included all possible locations of different size rectangles into the dictionary. For example if we want to sparsely represent the design shown in Fig. 5-2, we would construct the dictionary consisting of the elements shown in Fig. 5-3. The columns of the dictionary  $\Phi$  would consist of vectorized versions of all these images shown in Fig. 5-3 where every third element of the dictionary is shown. Fig. 5-3 is a mosaic of sub images of equal sizes and each sub image is a dictionary element. The size of the dictionary depends on the number of dictionary elements, on pixel size and on the

field of view.

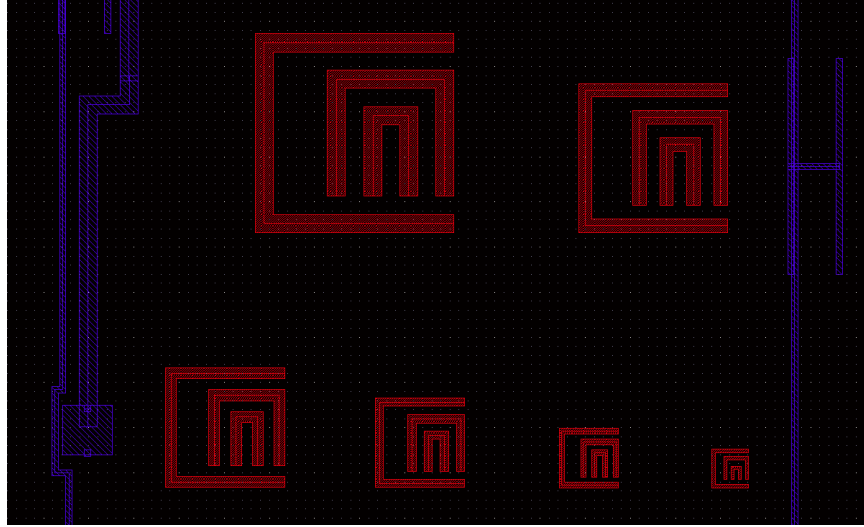


**Figure 5.1:** CAD layout example

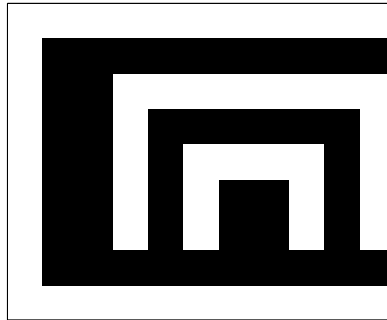


**Figure 5.2:** Design example

Ideally, we would specify the minimum and maximum width and length of the rectangles, since these are set by design rules of ICs and then we would include all rectangles within these limits to be in the dictionary.

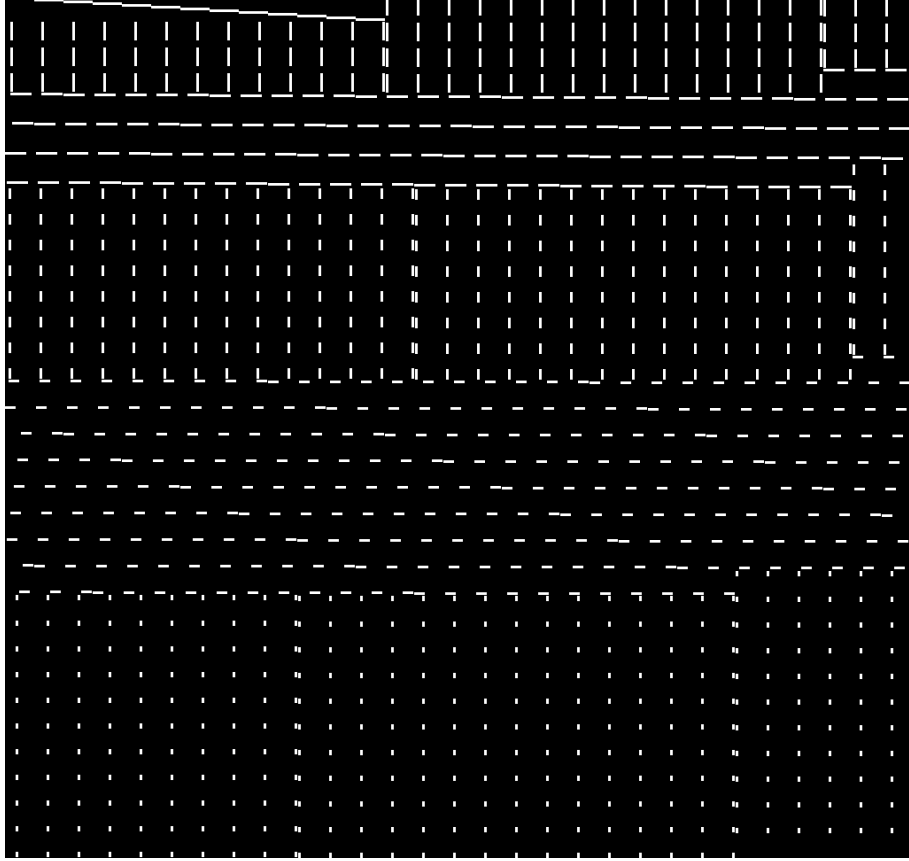


**Figure 5-3:** Dictionary elements for the design example from Fig. 5-2

## 5.2 Experimental results

### 5.2.1 Comparison of sparse reconstruction approaches through simulated data

Our goal in this section is to compare different sparse reconstruction techniques on simulated data with different levels of noise. Although the SNR is not very low for experimental reflectivity images, there are image modalities such as the LVI that have very low SNR levels. Therefore, it is useful to compare the performance of different sparse reconstruction approaches for different levels of noise. The phantoms for res-



olution targets used in the simulated experiments are shown in Fig. 5.4. In Figs. 5.5 and 5.6, simulated observation images of Phantom 1 and Phantom 2 are shown. For each phantom, 8 observations are created using linearly-polarized incident light with  $x$ - and  $y$ -polarization and 4 levels of additive Gaussian noise, with SNR given by 10 dB, 16 dB, 20 dB and 25 dB. The simulated observation images are created using convolution with the PSF presented in Section 3.2.2 for aluminum structures and with  $\alpha = 2.5^3$ . Figs. 5.7 and 5.8 compare different image reconstruction approaches; non-quadratic regularization that we studied in Chapter 4, dictionary-based  $\ell_1$ -regularization, and dictionary-based  $\ell_p$ -regularization with  $p = 1/2$  for the observations presented in Figs. 5.5 and 5.6. The reconstruction results show that when there are different-size structures, the dictionary-based  $\ell_p$ -regularization achieves better localization accuracy than the non-quadratic regularization. One of the resolution metrics used for IC Imaging is the Sparrow resolution criterion. The Sparrow criterion defines the resolution as the distance between the peaks of the two PSFs when the midpoint just becomes visible. Using this idea, we can evaluate if a resolution structure is resolved or not, in other words, if a structure is localized or not, depending on whether we observe a peak. Even the smallest structures are recovered in Figs. 5.7b, 5.7c, 5.7e and 5.7f, whereas they cannot be localized in Figs. 5.7a and 5.7d. The plots in Figs. 5.9 and 5.10 compare mean square error (MSE) values for different reconstruction approaches with respect to noise level. The MSE values are calculated using 10 realizations and the sample mean of the MSE values is used in the plot. The error bars are calculated using the standard error given by  $\sigma/\sqrt{n}$ , where  $\sigma$  is the standard deviation of the MSE values over all realizations and  $n$  is the number of realizations. The MSE plots show that reconstruction performance for dictionary-based  $\ell_p$ -regularization is higher than for non-quadratic regularization, and also that the dictionary-based  $\ell_{1/2}$ -regularization has the best reconstruction

performance and robustness to noise. The MSE values for Phantom 2 are lower than the ones for Phantom 1, this is because Phantom 1 has smaller structures which are closer to resolution limit. For this reason, it is more challenging. In terms of computation time, non-quadratic regularization is the faster than the dictionary-based approach. As the dictionary size increases, the computation time and the memory requirements also increase. The computation time is slowest for dictionary-based  $\ell_{1/2}$ -regularization but it can be decreased by initializing the result of dictionary-based  $\ell_1$ -regularization.

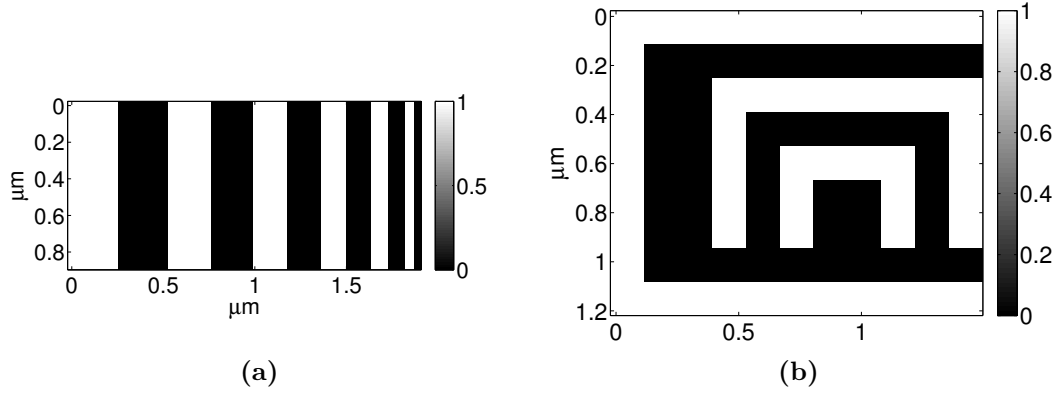


**Figure 5-4:** Phantoms for resolution structures used in simulated experiments (a) Phantom 1 (b) Phantom 2

### 5.2.2 Reconstruction results for aSIL microscopy data

We have 2 sets of experimental aSIL data. The first set contains linear polarization observations of a resolution structure made of  $0.35\mu m$  polysilicon lines fabricated on silicon-silicon dioxide interface. The second set contains images of horizontal and vertical resolution lines with different pitches;  $282nm$ ,  $252nm$ , and  $224nm$ . They are made of metal aluminum lines deposited on a double-sided polished silicon wafer, hence they lie on a silicon-air interface. The structure design for the first resolution target and the SEM images of the aluminum lines are shown in Fig. 5-11. The

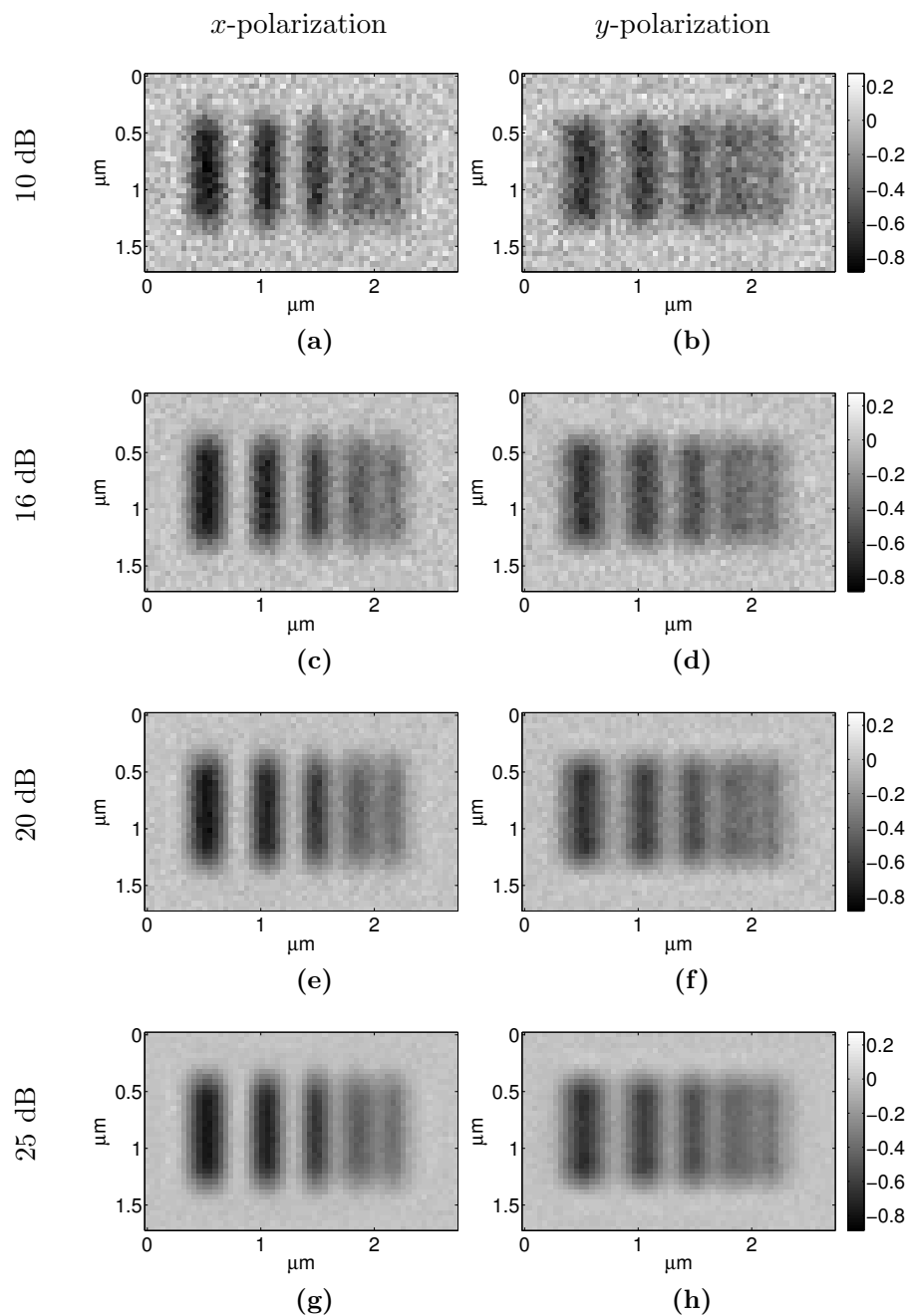


**Figure 5-5:** Simulated observation images for Phantom 1 for *x*-polarized input light: (a) SNR=10dB, (c) SNR=16dB, (e) SNR=20dB, (g) SNR=25dB, and for *y*-polarized input light : (b) SNR=10dB, (d) SNR=16dB, (f) SNR=20dB, (h) SNR=25dB.

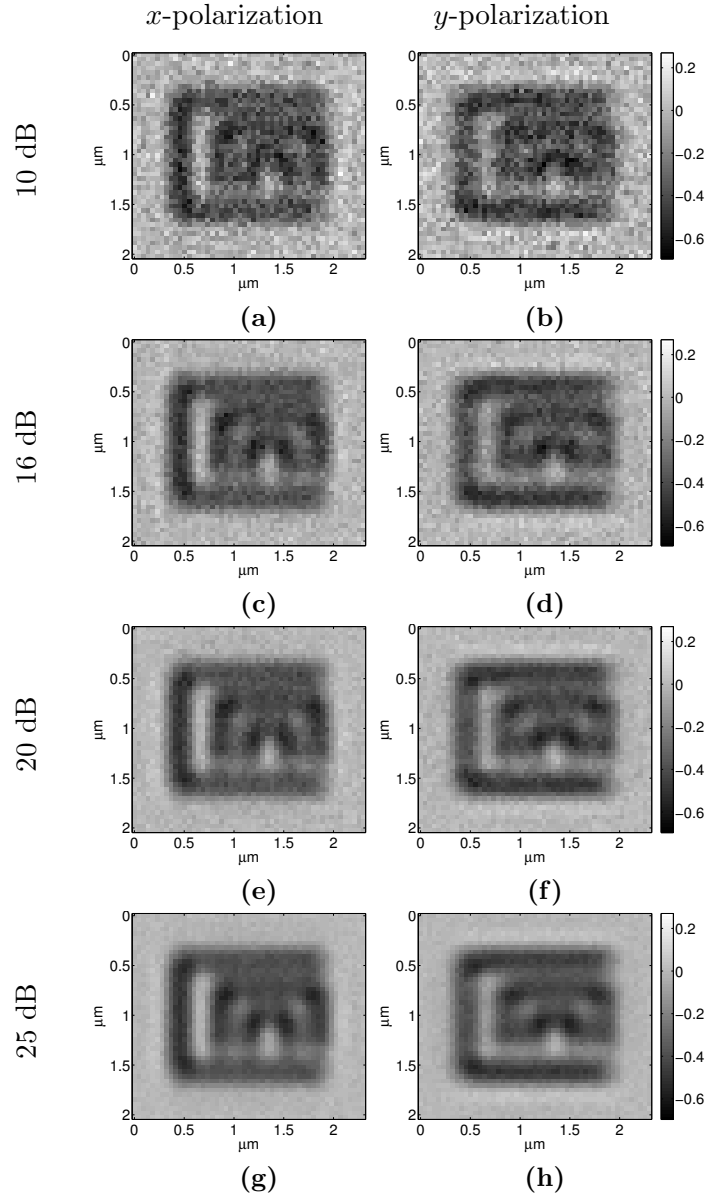


**Figure 5-6:** Simulated observation images for Phantom 2 for  $x$ -polarized input light: (a) SNR=10dB, (c) SNR=16dB, (e) SNR=20dB, (g) SNR=25dB, and for  $y$ -polarized input light: (b) SNR=10dB, (d) SNR=16dB, (f) SNR=20dB, (h) SNR=25dB.

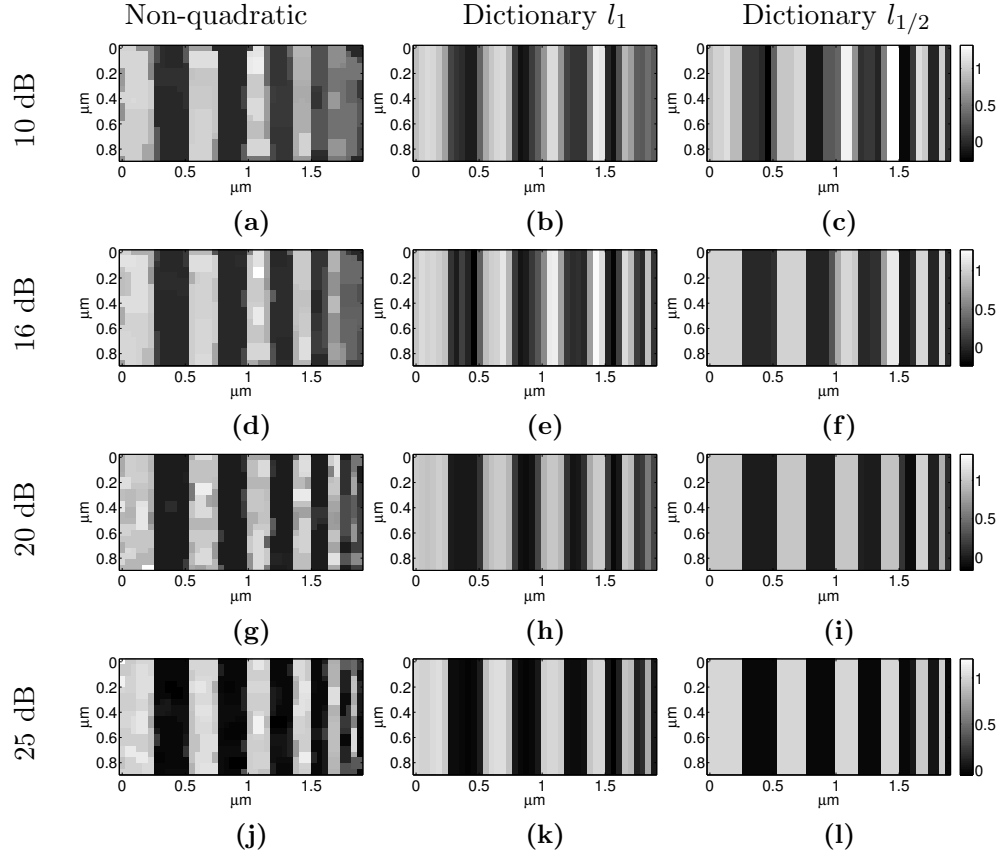


**Figure 5.7:** Sparse image reconstruction results for Phantom 1, non-quadratic regularization (a) SNR=10dB (d) SNR=16dB (g) SNR=20dB (j) SNR=25dB, dictionary-based  $\ell_1$ -regularization (b) SNR=10dB (e) SNR=16dB (h) SNR=20dB (k) SNR=25dB, dictionary-based  $\ell_{1/2}$ -regularization (c) SNR=10dB (f) SNR=16dB (i) SNR=20dB (l) SNR=25dB

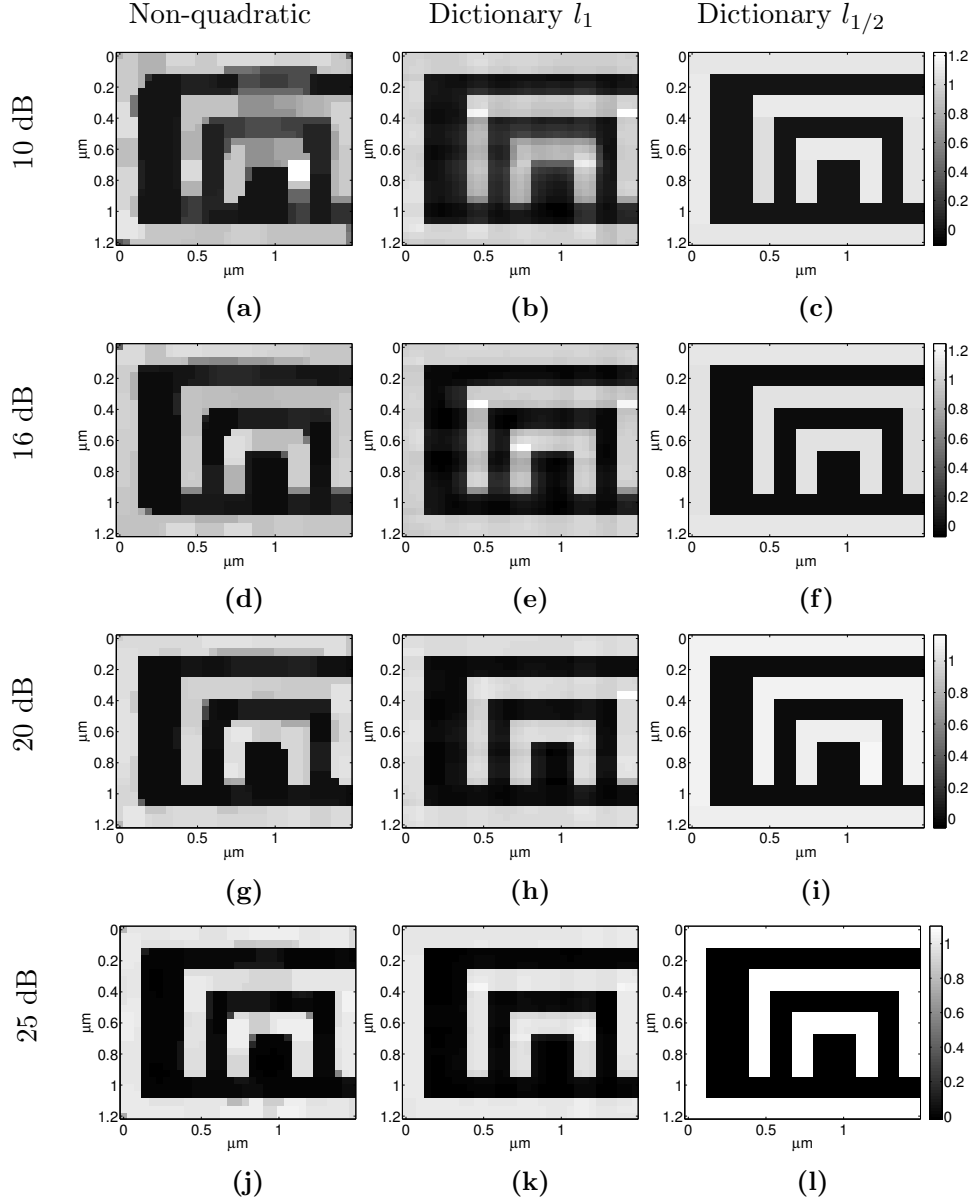


**Figure 5-8:** Sparse image reconstruction results for Phantom 2, non-quadratic regularization (a) SNR=10dB (d) SNR=16dB (g) SNR=20dB (j) SNR=25dB, dictionary-based  $\ell_1$ -regularization (b) SNR=10dB (e) SNR=16dB (h) SNR=20dB (k) SNR=25dB, dictionary-based  $\ell_{1/2}$ -regularization (c) SNR=10dB (f) SNR=16dB (i) SNR=20dB (l) SNR=25dB

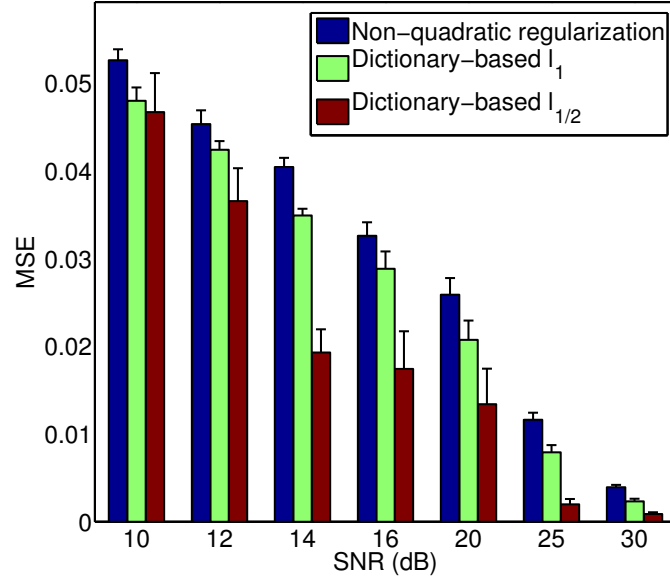


**Figure 5.9:** MSE plot for reconstructions of Phantom 1

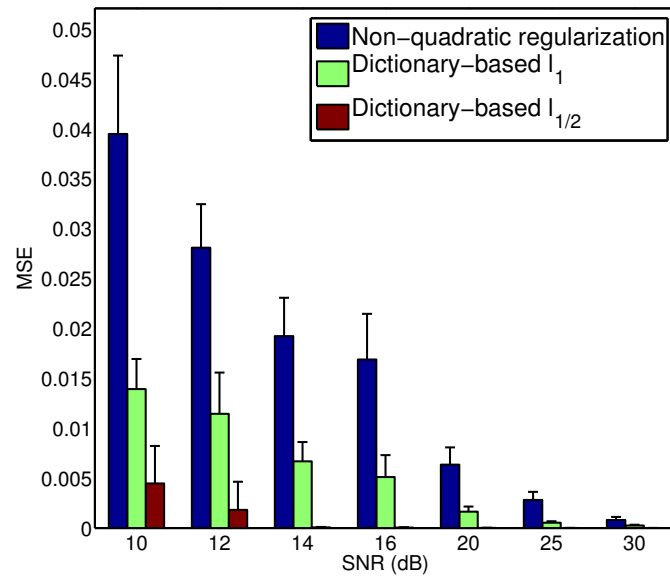


**Figure 5.10:** MSE plot for reconstructions of Phantom 2

CNN-shaped resolution target is large enough that all lines can be localized in aSIL microscopy data. However, for the second resolution target with aluminum lines, the lines are not localized, since the separation between the lines is smaller than the spot size of the laser beam. We can relate the edge thickness to the Houston resolution criterion since the width of the edge can be used to estimate FWHM of the PSF in an optical system. The reconstruction of the first resolution target shows an overall image enhancement and a better edge resolution. Moreover, according to the Sparrow criterion, we can define the equivalent resolution of the reconstruction framework as the distance between the peaks of two resolution lines when they just become visible. The reconstruction of the aluminum line resolution data shows image enhancement, improvement of edge resolution and improvement in localization accuracy.

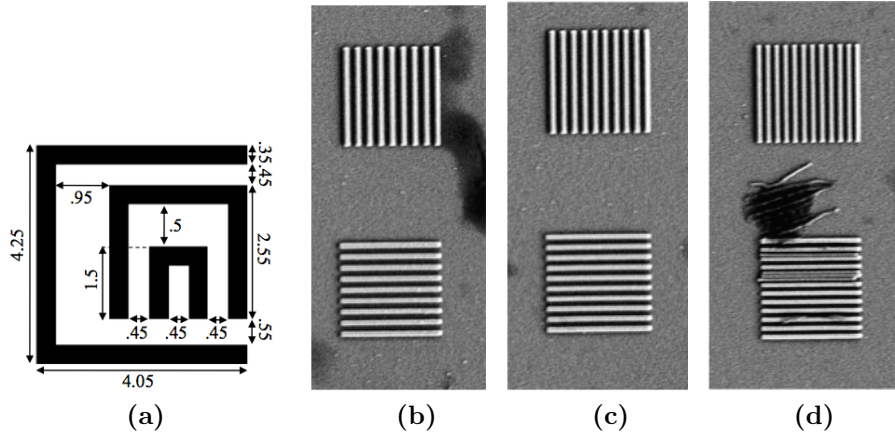


**Figure 5.11:** (a) CNN structure design and SEM images for lines resolution targets with (b)  $282nm$  (c)  $252nm$  (d)  $224nm$  line separation.

The aSIL microscopy images with linearly  $x$ -polarized and  $y$ -polarized light are shown in Figs. 5.12a and 5.12b for the CNN-shaped polysilicon resolution target. The results of various sparse reconstruction techniques for these observations are given in Figs. 5.13a, 5.13b, and 5.13c for non-quadratic regularization, dictionary-based  $\ell_1$ -regularization and dictionary-based  $\ell_{1/2}$ -regularization, respectively. The



PSF for polysilicon structures with  $\alpha = 2.5^3$  from Section 3.2.2 was used in the reconstruction framework. Both observation data and all the reconstructions are shown with the same amplitude scale. Horizontal and vertical cross sections from the middle section are plotted in Fig. 5-14 to compare reconstruction techniques and to show resolution improvement with respect to the observation. All reconstruction techniques provided enhancement in terms of edge resolution; the cross sections show that the edges became sharper. The dictionary-based technique shows a smoothness loss around the corners. The reason for this is the rounding around the corners in the fabrication process. The highest contrast is provided by the dictionary-based  $\ell_{1/2}$ -regularization.

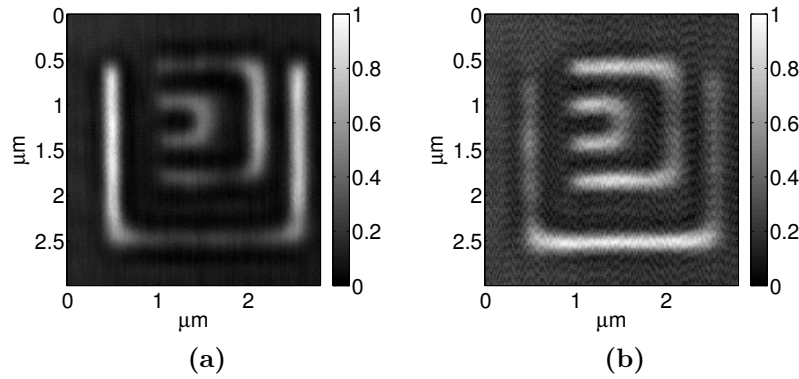


**Figure 5-12:** CNN-shaped polysilicon resolution target observation data with (a)  $x$ -polarized input light (b)  $y$ -polarized input

The aSIL data with  $x$ -polarized and  $y$ -polarized input light are shown in Figs. 5-15a and 5-15b for  $282\text{nm}$  pitch lines, in Figs. 5-16a and 5-16b for  $252\text{nm}$  pitch lines, and in Figs. 5-17a and 5-17b for  $224\text{nm}$  pitch lines. Clearly, the  $252\text{nm}$  and  $224\text{nm}$  pitch lines are not localized in the observation data. The non-quadratic regularization reconstructions are shown in Figs. 5-18a, 5-19a and 5-20a. There are some oscillations in the background, but the number of lines and the thickness of the lines for  $282\text{nm}$  and  $252\text{nm}$  pitch lines match the SEM data. The non-quadratic regularization reconstruction for  $224\text{nm}$  pitch vertical lines is at the limit of local-

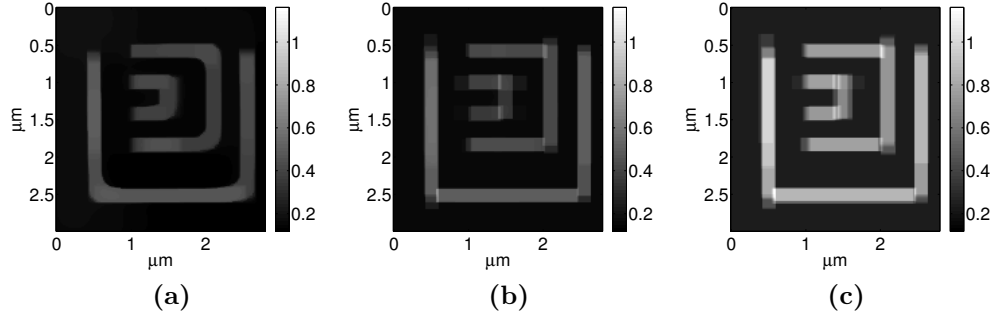
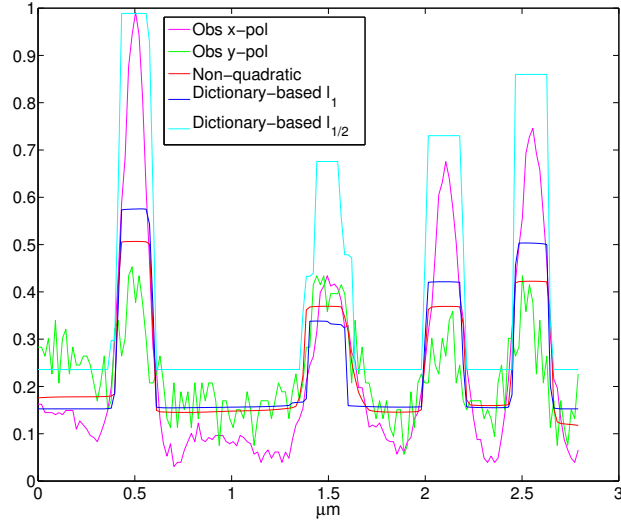
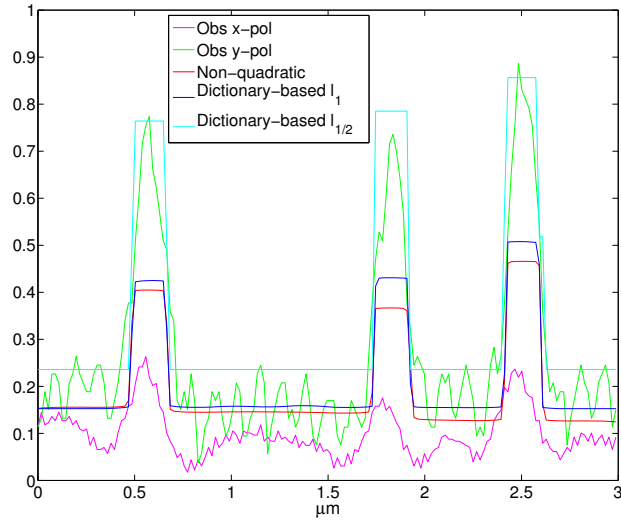


**Figure 5.13:** CNN-shaped polysilicon resolution target reconstruction results with (a) non-quadratic regularization (b) dictionary-based  $\ell_1$ -regularization (c) dictionary-based  $\ell_{1/2}$ -regularization.

ization, and some of the horizontal lines cannot be localized. The reason for this is the defect in fabrication of horizontal lines. This defect can be seen in the SEM image in Fig. 5.11d. The localization accuracy and resolution are improved by the dictionary-based reconstruction techniques compared to the non-quadratic regularization reconstruction. The results for dictionary-based  $\ell_1$ -regularization are shown in Figs. 5.18b, 5.19b and 5.20b and the ones for dictionary-based  $\ell_{1/2}$ -regularization are shown in Figs. 5.18c, 5.19c and 5.20c. For all reconstruction techniques a PSF with  $\alpha = 2.5^3$  from Section 3.2.2 was used for the  $282nm$  and  $252nm$  pitch lines and PSF with  $\alpha = 2.4^3$  was used for the  $224nm$  pitch lines. Imperfections in the defect regions started to appear in the dictionary-based  $\ell_{1/2}$ -regularization for horizontal lines of  $224nm$  pitch. The comparison of horizontal and vertical cross sections from the observation data and all reconstructions techniques is shown in Figs. 5.21, 5.22 and 5.23. The cross sections show that the best resolution is achieved by the dictionary-based  $\ell_{1/2}$ -regularization for all the lines data. However, we need to note that the computation time and the memory requirements are much higher for dictionary-based regularization than for non-quadratic regularization.



(a)



(b)

**Figure 5.14:** Cross sections from the observation and reconstructions for CNN-shaped polysilicon resolution target (a) horizontal (b) vertical

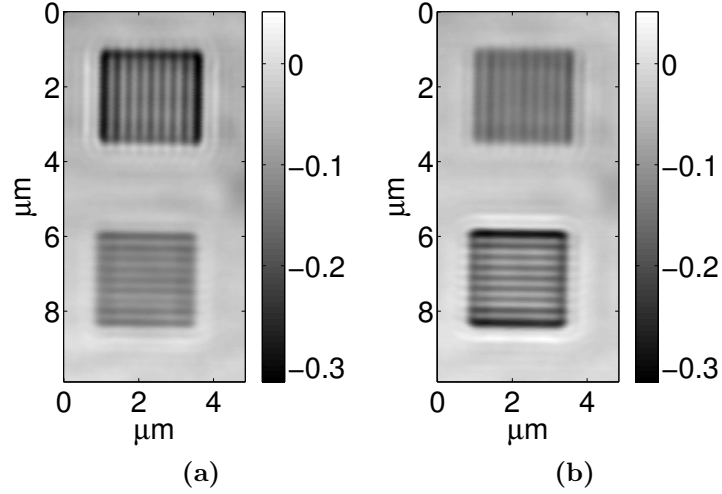


**Figure 5-15:** Observation data of resolution target of aluminum lines with 282nm pitch (a)  $x$ -polarized input light (b)  $y$ -polarized input light

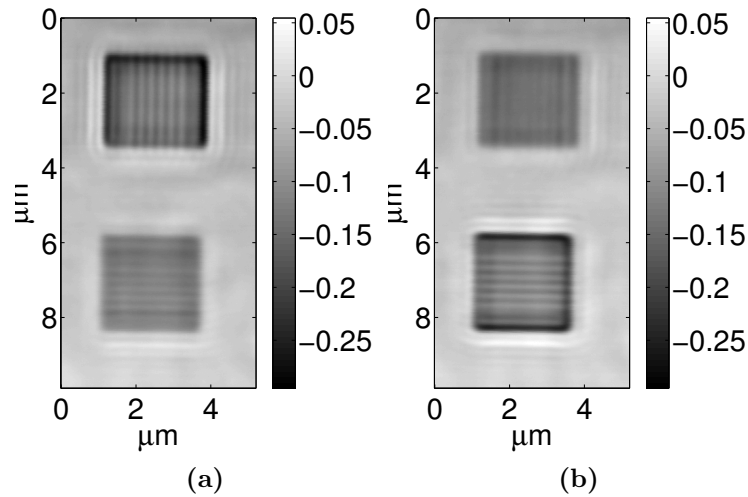


**Figure 5-16:** Observation data of resolution target of aluminum lines with 252nm pitch (a)  $x$ -polarized input light (b)  $y$ -polarized input light

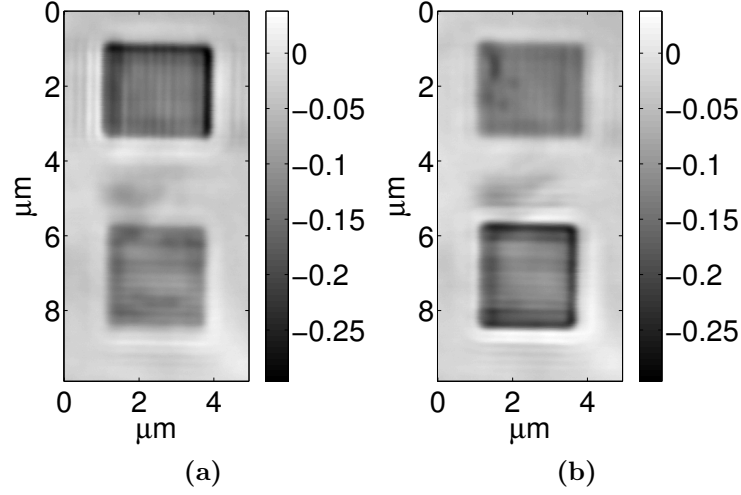


**Figure 5-17:** Observation data of resolution target of aluminum lines with  $224\text{nm}$  pitch (a)  $x$ -polarized input light (b)  $y$ -polarized input light

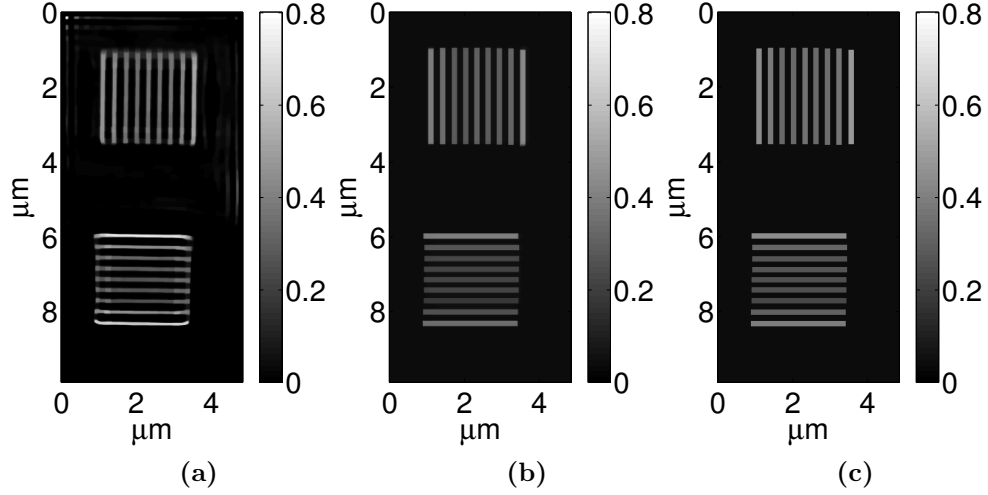


**Figure 5-18:** Reconstruction results of the resolution target of aluminum lines with  $282\text{nm}$  separation (a) non-quadratic regularization, (b) dictionary-based  $\ell_1$ -regularization, (c) dictionary-based  $\ell_{1/2}$ -regularization.

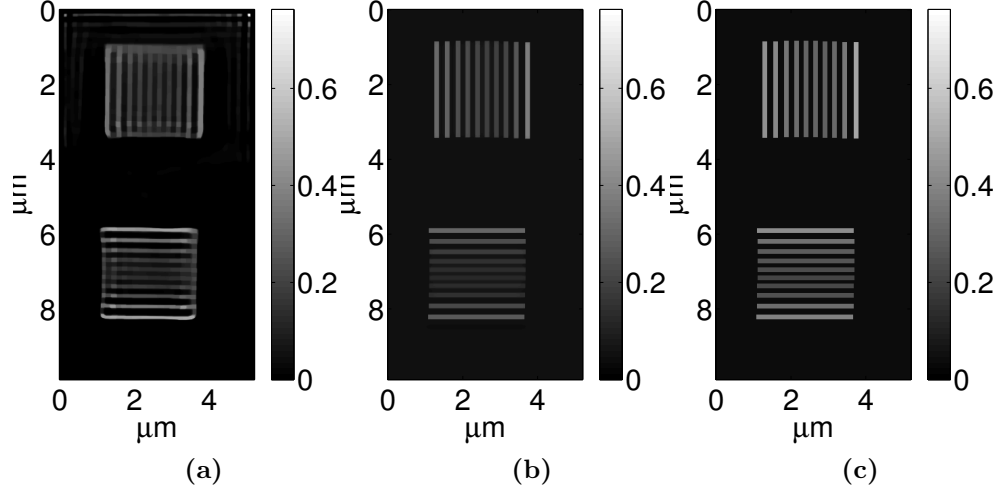


**Figure 5-19:** Reconstruction results of the resolution target of aluminum lines with  $252nm$  separation (a) non-quadratic regularization, (b) dictionary-based  $\ell_1$ -regularization, (c) dictionary-based  $\ell_{1/2}$ -regularization.

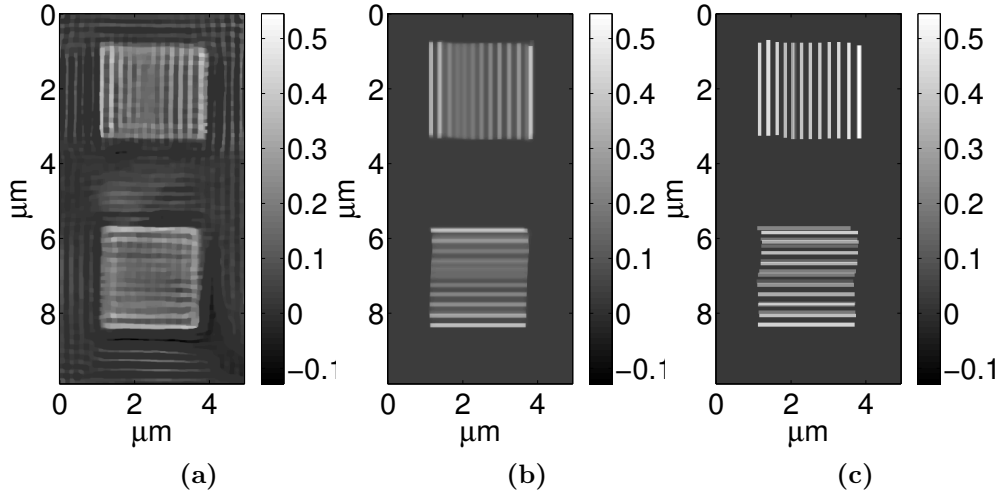


**Figure 5-20:** Reconstruction results of the resolution target of aluminum lines with  $224nm$  separation (a) non-quadratic regularization, (b) dictionary-based  $\ell_1$ -regularization, (c) dictionary-based  $\ell_{1/2}$ -regularization.

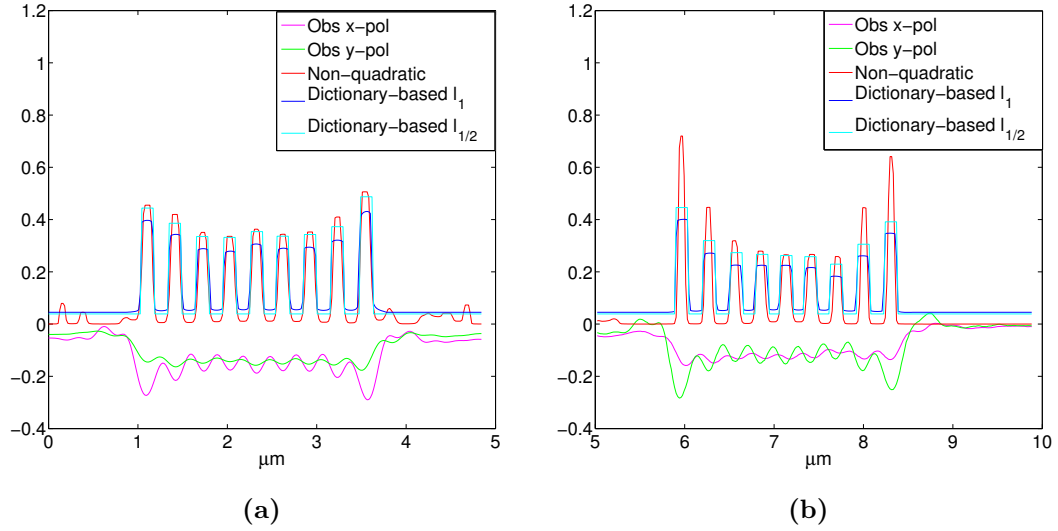


**Figure 5.21:** Cross sections from observation data and reconstructions for aluminum lines resolution target for 282nm pitch (a) horizontal (b) vertical

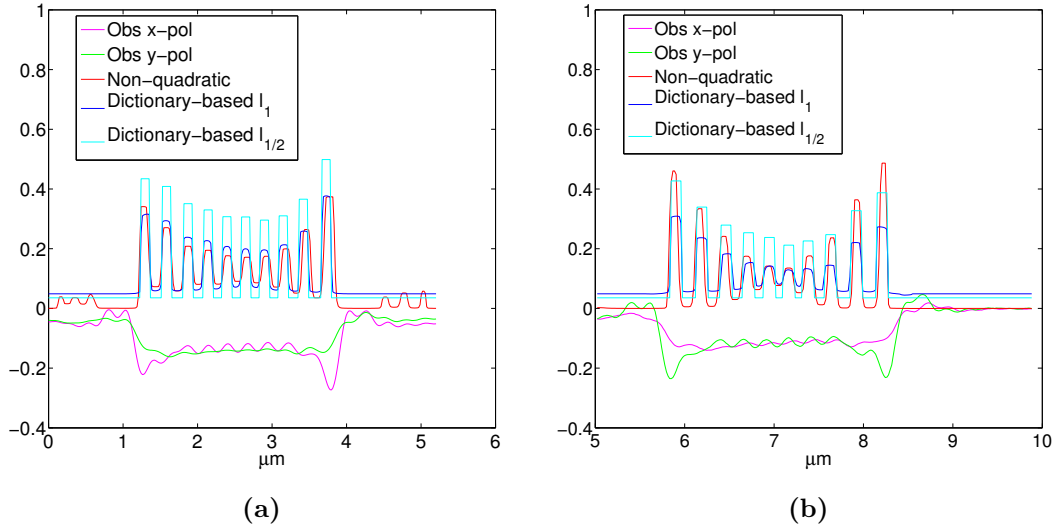


**Figure 5.22:** Cross sections from observation data and reconstructions for aluminum lines resolution target for 252nm pitch (a) horizontal (b) vertical

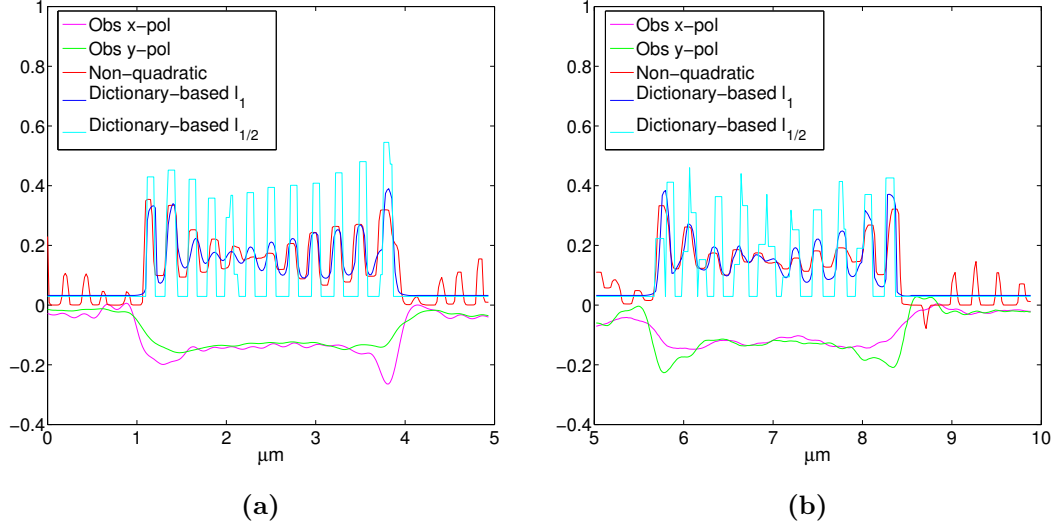


**Figure 5.23:** Cross sections from observation data and reconstructions for aluminum lines resolution target for 224nm pitch (a) horizontal (b) vertical

### 5.3 Initialization of dictionary-based $\ell_{1/2}$ -regularization

The sparse dictionary-based reconstruction problem, which is an  $l_p$ -regularization problem, given in Eq. 5.4 has a non-convex cost function for  $p < 1$ . This means that there is no guarantee of reaching a global minimum. For this reason, it is beneficial to compare reconstruction results for different initializations. In this section, we compare reconstruction results of dictionary-based  $l_{1/2}$ -regularization for two different initialization cases: the initialization with the result of  $l_1$ -regularization and the initialization with "all ones" coefficient vector,  $\boldsymbol{\eta}_0 = \mathbf{1}$ . We used the simulated observation from Section 5.2.1 and the experimental data of aluminum lines resolution target from Section 5.2.2. The reconstructions from simulated observations of Phantom 1 are shown in Fig. 5.25 and the reconstructions from simulated observations of Phantom 2 are shown in Fig. 5.24. The MSE plots in Figs. 5.27 and 5.26 show a quantitative comparison of reconstructions resulting from the two initializations for a single realization. The reconstruction results with different initializations



from experimental data are given in Figs. 5-28, 5-29 and 5-30. We observe that the initialization does not have a significant impact on the reconstruction performance for simulated data. The initialization with the result of  $l_1$ -regularization produces slightly better results. For experimental data, different initializations result in similar reconstruction results for lines with  $282nm$  separation.

## 5.4 Conclusions

In this chapter, we proposed a synthesis-based sparse representation framework using overcomplete dictionaries for image enhancement and resolution improvement of backside aSIL imaging of integrated circuits. The predetermined overcomplete dictionary-based sparse signal representation framework poses strong priors for underlying IC structures and subsequently improves resolution in image reconstruction. The framework incorporates polarization properties of high-NA optical systems using vectorial optics and electromagnetic analysis for PSF modeling and enables fusion of multiple polarization observations to benefit from improved resolution in each set of observation data. Dictionary-based image reconstruction techniques are particularly suitable for IC imaging because predetermined dictionaries can be built using the information stored in CAD layouts. Additionally, since the building blocks of structures in ICs come from a limited set, mostly line segments of varying width and length, dictionary blocks pose strong priors for the reconstructed scene. Hence, enforcing sparsity on the dictionary coefficients, the resolution can be significantly improved. The proposed framework was validated on simulated data and different sparse reconstruction approaches have been compared for different levels of noise. This study is crucial to evaluate the robustness of the framework to noise level since some modalities in IC imaging have higher levels of noise, such as LVI. We have also shown resolution improvement in experimental aSIL data. One disadvantage of the

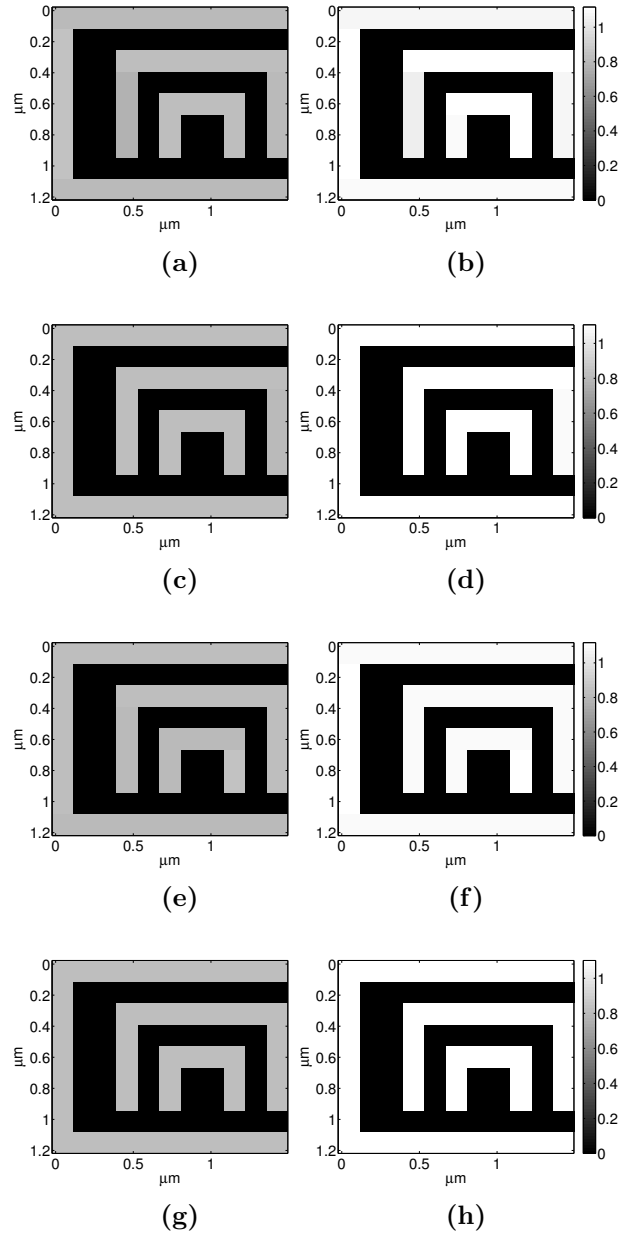


**Figure 5.24:**  $l_{1/2}$ -regularization reconstruction results of Phantom 2 observations with different initializations: "all ones" initialization (a) 10 dB (c) 16 dB (e) 20 dB (g) 25 dB, initialization with the result of  $l_1$ -regularization (b) 10 dB (d) 16 dB (f) 20 dB (h) 25 dB.

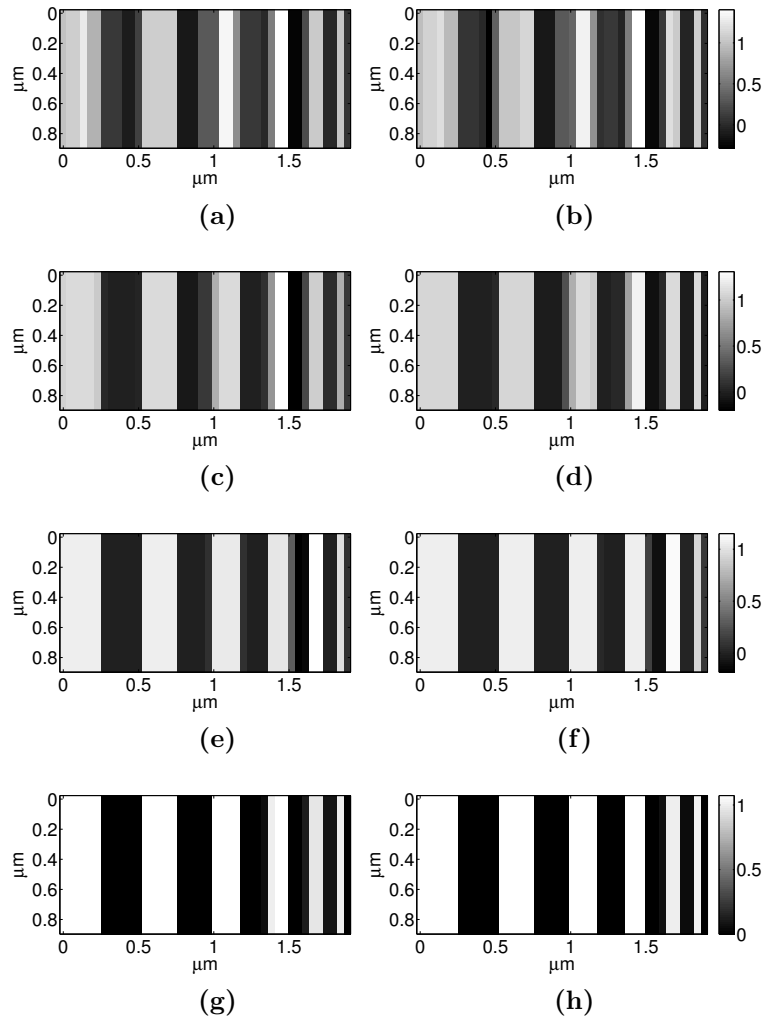


**Figure 5.25:**  $l_{1/2}$ -regularization reconstruction results of Phantom 1 observations with different initializations: "all ones" initialization (a) 10 dB (c) 16 dB (e) 20 dB (g) 25 dB, initialization with the result of  $l_1$ -regularization (b) 10 dB (d) 16 dB (f) 20 dB (h) 25 dB

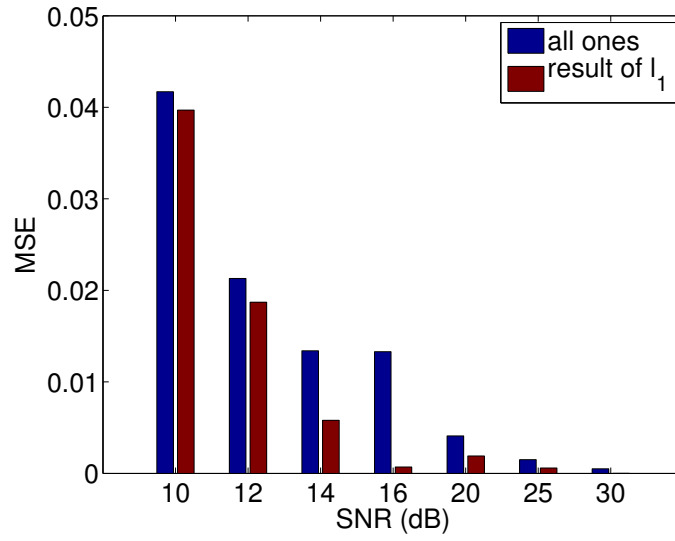


**Figure 5-26:** Comparison of MSE values for reconstructions from Phantom 1 observations for a single realization

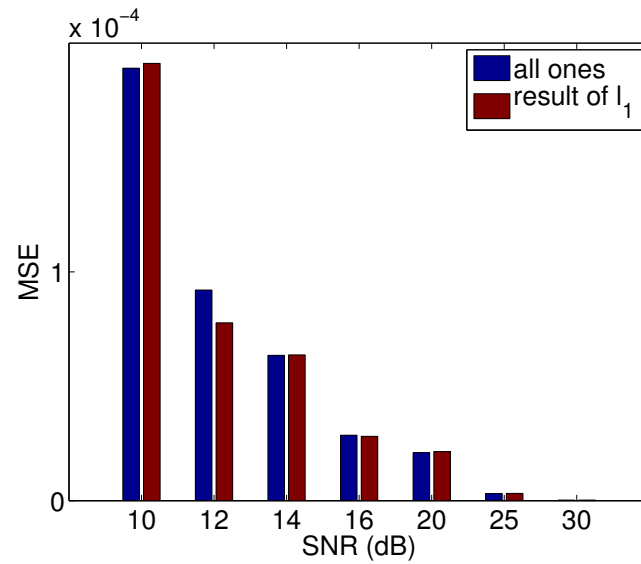


**Figure 5-27:** Comparison of MSE values for reconstructions from Phantom 2 observations for a single realization

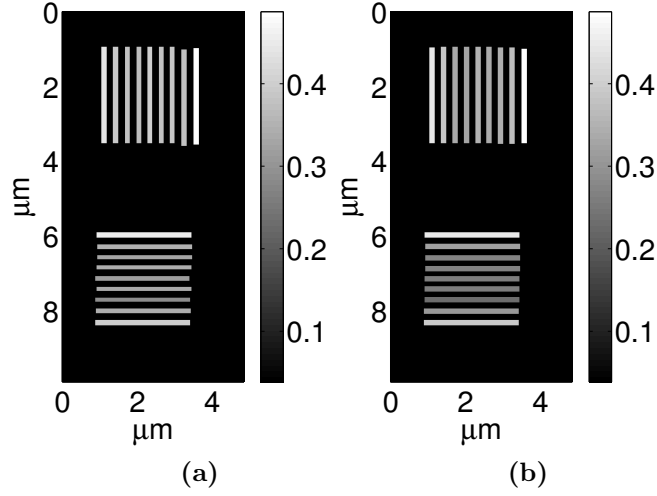


**Figure 5.28:**  $l_{1/2}$ -regularization reconstruction results of 282nm separation lines data with different initializations: (a) all ones initialization (b) initialization with the result of  $l_1$ -regularization

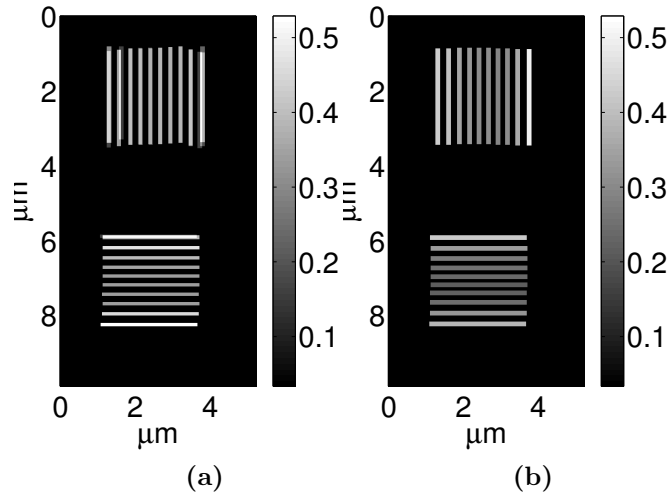


**Figure 5.29:**  $l_{1/2}$ -regularization reconstruction results of 252nm separation lines data with different initializations: (a) all ones initialization (b) initialization with the result of  $l_1$ -regularization

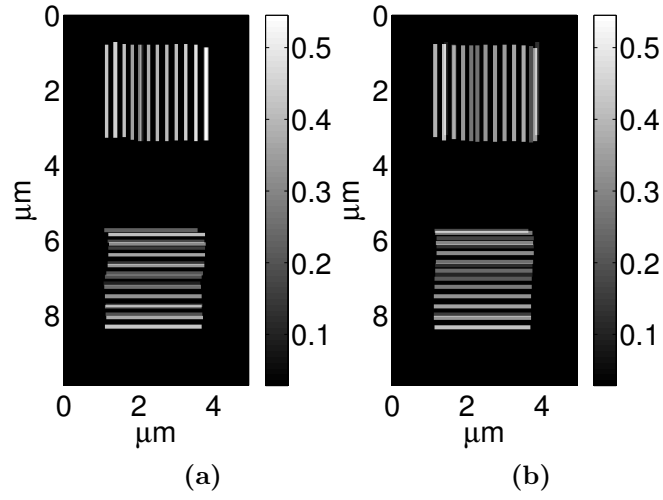


**Figure 5-30:**  $l_{1/2}$ -regularization reconstruction results of  $224nm$  separation lines data with different initializations: (a) all ones initialization (b) initialization with the result of  $l_1$ -regularization

technique compared to analysis-based approach in Chapter 4 is the computation time and memory requirements, especially when the scene gets more complex.

## Chapter 6

# Imaging active integrated circuits with 3D dictionaries for laser voltage imaging

Laser voltage imaging (LVI) (Yurt et al., 2012; Ng et al., 2010) is an optical backside FA technique that produces images of active regions in ICs. It is derived from the LVP measurement technique (Heinrich et al., 1986; Kindereit et al., 2008; Kindereit et al., 2007) that measures the modulations at a single location of the IC over time. These modulations are caused by the change in carrier densities below the gate and drain as the applied voltage varies over time. A review of these techniques was provided in Sections 2.2.1 and 2.2.2. Since the LVP signal is very noisy, multiple cycles are collected and averaged in order to increase SNR. This significantly increases the measurement time. On the other hand, LVI is a frequency-domain measurement and it records the amplitude and the phase of the first harmonic. Since the noise is white and spread to all frequencies, there is no requirement for averaging. Only the first harmonic is collected because the applied voltage is a periodic square wave with a known frequency. Therefore, the laser beam can be raster scanned in order to collect measurements from an area, producing images of the amplitude of the first harmonic and of the phase of the first harmonic. In order to create an image, where active regions are indicated, single harmonic is enough. On the other hand, there is also the second harmonic technique through which duty cycle degradation faults are detected by collecting the magnitude and the phase of the second harmonic (Celi et al., 2012). The experimental setup for LVI measurements is shown in Fig. 2-3. For each scan

point, a laser beam is focused by a high-NA optical system and the reflected light can be expressed as  $R(x, y, t) = R_0(x, y) + \Delta R(x, y, t)$ , where  $R_0(x, y)$  is the measured reflection from the static parts and  $\Delta R(x, y, t)$  is the modulated part of the reflected light coming from active regions. The first harmonic of the modulating part gives the LVI data for each scan position whereas the constant part (DC component) gives the reflection from static components. Therefore, LVI data is registered with optical images of the static components. It also has the same resolution properties as the images of static components.

In this chapter, our goal is to formulate a synthesis-based sparse representation framework for LVI. For this purpose, we first propose collecting measurements at multiple harmonics. Most of the energy is in the first harmonic because the applied voltage is a periodic square wave. However, energy in other harmonics is required in order to determine time signature of active regions, such as duty cycle, phase shift. We design overcomplete 3D dictionaries, one in space-time and one in space-frequency, in order to sparsely represent the multiple harmonics LVI data. These dictionaries are built according to properties of the modulation which depend on the applied voltage and the dimensions of the gate and drain regions obtained from CAD layouts. We propose a reconstruction framework based on this sparse representation in order to increase the spatial resolution of LVI data and to recover the switching behavior over time in different regions in the field of view. The PSF model based on Green's approach from Section 3.2.2 is used in order to model the spatial blur because LVI measurements are taken with the same high-NA system with linearly-polarized input light.

In Section 6.1, we introduce two different sparse representations based on two different 3D dictionaries, one in space-time and the other in space-frequency. In Section 6.2 we explain how we have built these 3D dictionaries. In Section 6.3,



we present simulated-data experiments. Section 6.4 summarizes and concludes this chapter.

## 6.1 Sparse representation framework for multiple-harmonics LVI

The voltage applied to the IC is periodic and results in periodic modulations in active regions. The blurry and noisy modulations in space and time can be expressed as:

$$\tau^j(x, y, t) = m_b^j(x, y, t) + w^j(x, y, t), \quad (6.1)$$

where

$$m_b^j(x, y, t) = h^j(x, y) * m(x, y, t), \quad (6.2)$$

$$w^j(x, y, t) \sim \mathcal{N}(0, m_b^j(x, y, t)), \quad (6.3)$$

$m(x, y, t)$  is the underlying modulation,  $h^j(x, y)$  is the PSF of the high NA imaging system illuminated by linearly polarized input light with polarization direction  $j$  and  $w^j(x, y, t)$  is the noise in the system. LVI measures the modulation in the frequency domain. The complex-valued harmonics can be expressed as:

$$\mathbf{d}_{k,l}^j = \frac{1}{T} \int_{\langle T \rangle} \tau_k^j(t) e^{-ilw_0 t} dt, \quad (6.4)$$

where  $k$  indicates the scan position in space where the laser beam is focused,  $T$  is the period of the periodic modulation and  $w_0$  is the fundamental frequency. Then, the observed harmonics LVI data can be collected in vector  $\mathbf{d}^j$  whose amplitude and phase can be expressed as  $|\mathbf{d}^j|$  and  $\angle \mathbf{d}^j$ , respectively. We have two different sparse representations: one in space-frequency and one in space-time. In space-frequency, we represent the Fourier series coefficients of the underlying modulation  $m(x, y, t)$  in

terms of an overcomplete 3D space-frequency dictionary. In space-time, the underlying modulation  $m(x, y, t)$  is represented in terms of an overcomplete 3D space-time dictionary. Details of these representations and the reconstruction framework are explained in the following sections.

### 6.1.1 Frequency-domain sparse representation

The Fourier series coefficients of the underlying modulation  $m(x, y, t)$  can be expressed as follows:

$$\mathbf{c}_{k,l} = \frac{1}{T} \int_{\langle T \rangle} m_k(t) e^{-ilw_0 t} dt, \quad (6.5)$$

where  $k$  indicates the scan position and  $l$  is the harmonic number. The overcomplete dictionary-based representation in space-frequency is expressed as:

$$\mathbf{c} = \Phi_w \boldsymbol{\eta}_w, \quad (6.6)$$

where  $\Phi_w$  is the predetermined space-frequency dictionary and  $\boldsymbol{\eta}_w$  is the vector of representation coefficients.

Then the sparse space-frequency dictionary-based reconstruction problem becomes:

$$\hat{\boldsymbol{\eta}}_w = \arg \min_{\boldsymbol{\eta}_w} \sum_{j=1}^N \|\mathbf{d}^j - H^j \Phi_w \boldsymbol{\eta}_w\|_2^2 + \lambda \|\boldsymbol{\eta}_w\|_1, \quad (6.7)$$

where  $N$  is the number of polarization directions,  $j$  indicates the polarization direction,  $H^j$  is the Toeplitz matrix that implements the convolution as a matrix operation. The estimated Fourier series coefficients for the underlying modulation become:

$$\hat{\mathbf{c}} = \Phi_w \hat{\boldsymbol{\eta}}_w. \quad (6.8)$$

Note that since the variables in the optimization problem in Eq. 6.7 are complex, the interior-point algorithm that we used in Chapter 5 to solve dictionary-based

reconstruction for real-valued problems does not apply here. Therefore, we used the quasi-Newton method (Çetin and Karl, 2001) explained in detail in Chapter 4 to solve the minimization problem.

### 6.1.2 Time-domain sparse representation

In order to use a space-time dictionary-based representation, the Fourier series expansion of the observed harmonics is used in order to generate the corresponding time domain observations:

$$\hat{\tau}_k^j(t) = \sum_{l=1}^L 2|\mathbf{d}_{k,l}^j| \cos(lw_0 t + \angle \mathbf{d}_{k,l}^j) \quad (6.9)$$

These time domain observations contain the effects of the noise and the blurring since the spectrum observations also do. For computations, this signal is discretized in time to obtain a vector of discrete estimated noisy and blurry modulations in space and time:  $\hat{\boldsymbol{\tau}}^j$ . The sparse representation in space-time can be expressed as:

$$\mathbf{m} = \Phi_t \boldsymbol{\eta}_t, \quad (6.10)$$

where  $\mathbf{m}$  contains the vectorized discrete underlying modulations. Then, the sparse space-time dictionary-based reconstruction problem becomes:

$$\hat{\boldsymbol{\eta}}_t = \arg \min_{\boldsymbol{\eta}_t} \sum_{j=1}^N \|\hat{\boldsymbol{\tau}}^j - H^j \Phi_t \boldsymbol{\eta}_t\|_2^2 + \lambda \|\boldsymbol{\eta}_t\|_1, \quad (6.11)$$

The estimated underlying modulation is the obtained from  $\hat{\boldsymbol{\eta}}_t$  as follows:

$$\hat{\mathbf{m}} = \Phi_t \hat{\boldsymbol{\eta}}_t. \quad (6.12)$$

## 6.2 Constructions of dictionaries

Spatially, the dictionaries are constructed by the same procedure as the dictionaries are constructed in Section 5.1.3. The spatial regions where the modulations are observed are flat regions consisting of horizontal and vertical lines of constrained and varying width and length. These regions can be obtained from the CAD layouts. Spatially, all possible locations of different-size rectangles are included into the dictionary. Fig. 6.1 shows an example of a CAD layout from an inverter. Fig.6.2 shows the gate and drain regions where the modulations are observed.

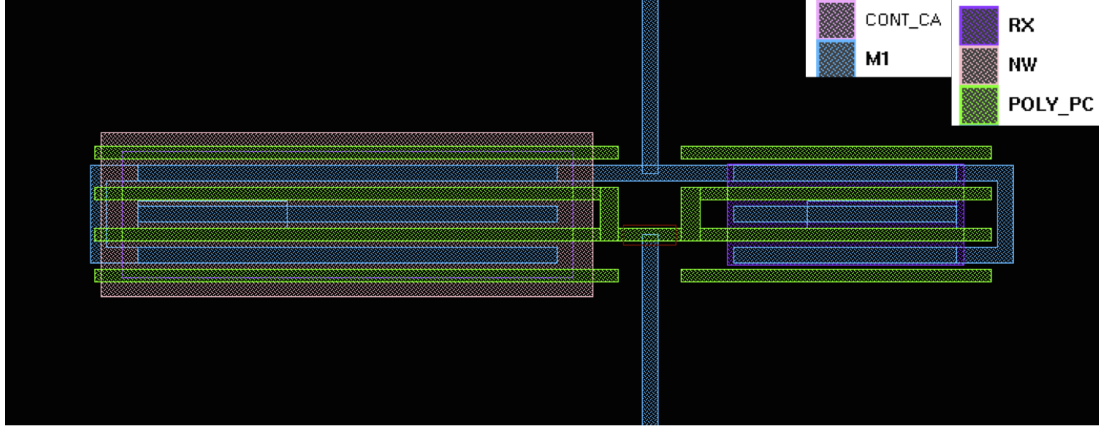


**Figure 6.1:** CAD layout of an inverter

We also need to include all possible time signatures or frequency signatures of the modulations. The applied voltage is a periodic square wave. Therefore, the modulations in time can be approximated as a periodic square wave ignoring the rise time and fall time. Depending on the circuit element of interest, the modulations will have the same period as the applied voltage or the period of the modulations will be a multiple of the period of the applied voltage. Additionally, depending on the circuit element, the modulations can be in phase with the applied voltage or there might be time shift. All possible periods and all possible time shifts should also be included in the dictionary. For the time dictionary, each region with different width

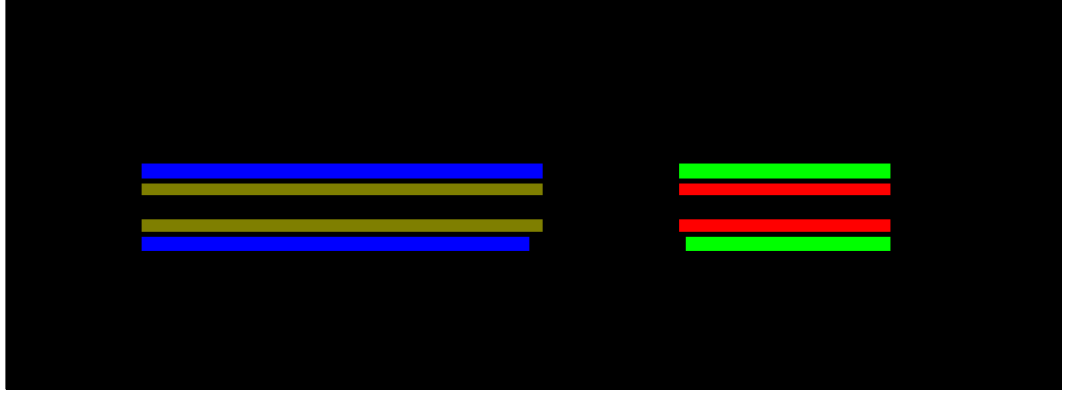


**Figure 6.2:** Active regions of the inverter, red: n-gate, dark green: p-gate, light green: n-drain, blue: p-drain

and height will also have a third dimension with all possible time signatures, in other words all possible periods and time shifts. Then, each column of the overcomplete time dictionary is the vectorized version of a 3D space-time behavior block where a region with fixed width and height has the same rectangular pulse with a given period and a given time shift. For the frequency dictionary, the Fourier series coefficients of all possible rectangular pulses are used to determine the third dimension of the dictionary elements. The Fourier series coefficients of the rectangular pulse train in Fig. 6.3 can be expressed as:

$$c_l = \frac{AT_1}{T_0} \text{sinc}(lw_0T_1)e^{-i\pi lw_0T_1}. \quad (6.13)$$

We use this expression in order to calculate the third dimension of space-frequency dictionaries.

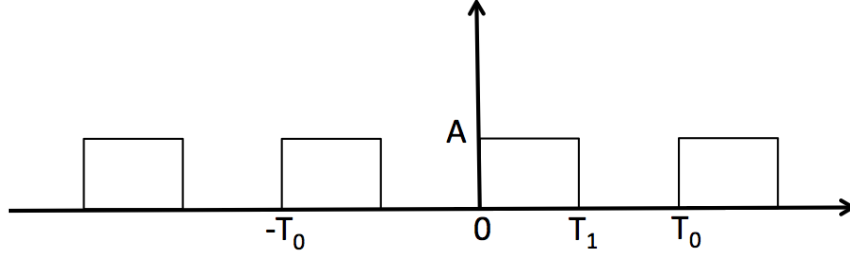


**Figure 6.3:** A rectangular pulse

### 6.3 Simulated-data experiments

Our goal in this section is to test the performance of the proposed framework in a controlled experiment. Therefore, we designed an experiment where simulated LVI data of an inverter is created using the modeled PSF from Section 3.2.2 and the CAD layout of a  $32nm$  process node device. The CAD layout for this inverter is shown in Fig. 6.1. There are 8 different rectangular regions where modulations are observed when the device is operational corresponding to the gate and drain regions. The modulations in the gate regions are stronger than the modulations in the drain regions because of the differences in free carrier densities. Amplitudes of modulations for all scan positions for two time points are shown in Figs 6.4 and 6.5 and modulations in time for 4 different scan positions are shown in Figs. 6.6. These 4 different scan positions are marked with colored dots in Fig. 6.4. We simulated LVI data using the observation model from Eq. 6.3. The amplitude and phase of the first 5 harmonics are shown in Figs. 6.7, 6.8, 6.9, 6.10, 6.11 for linearly-polarized illumination with  $x$ -polarization and in Figs. 6.12, 6.13, 6.14, 6.15, 6.16 for linearly-polarized illumination with  $y$ -polarization. The PSF in Fig. 3.5e is used in all simulations. All the amplitude data are shown in the same scale and all the phase data are shown on the same scale. The noise level is simulated according to characteristics of the experimental system. The variance of the noise scales with the amplitude of the total reflected light as given in Eq. 6.3 and the modulated part is 600 parts per million

compared to the total reflected light.

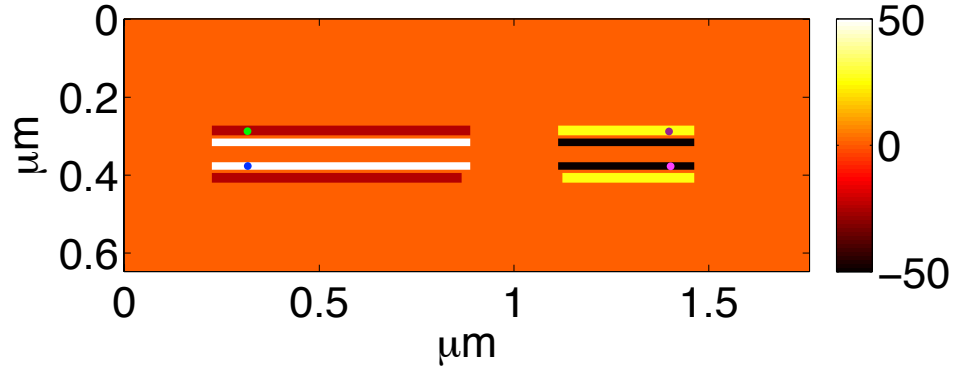


**Figure 6.4:** Amplitude of modulation for all scan positions at time  $t = 0.02$ ; colored dots mark scan position of the time plots: green p-type drain, blue p-type gate, purple n-type drain, pink n-type gate

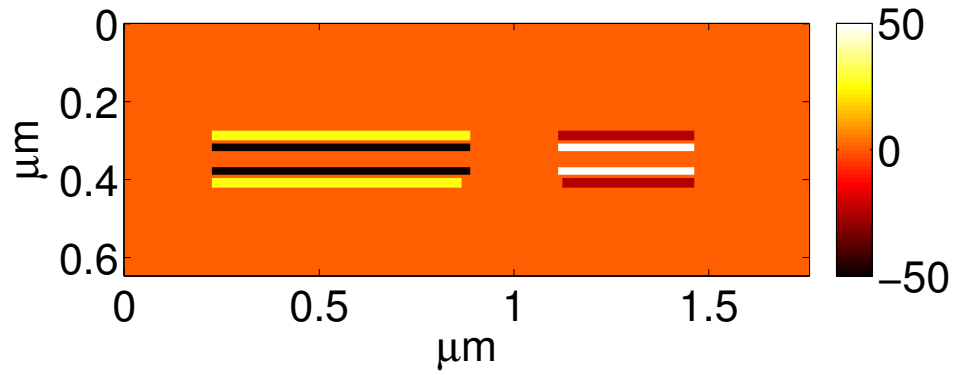


**Figure 6.5:** Amplitude of modulation for all scan positions at time  $t = 0.07$

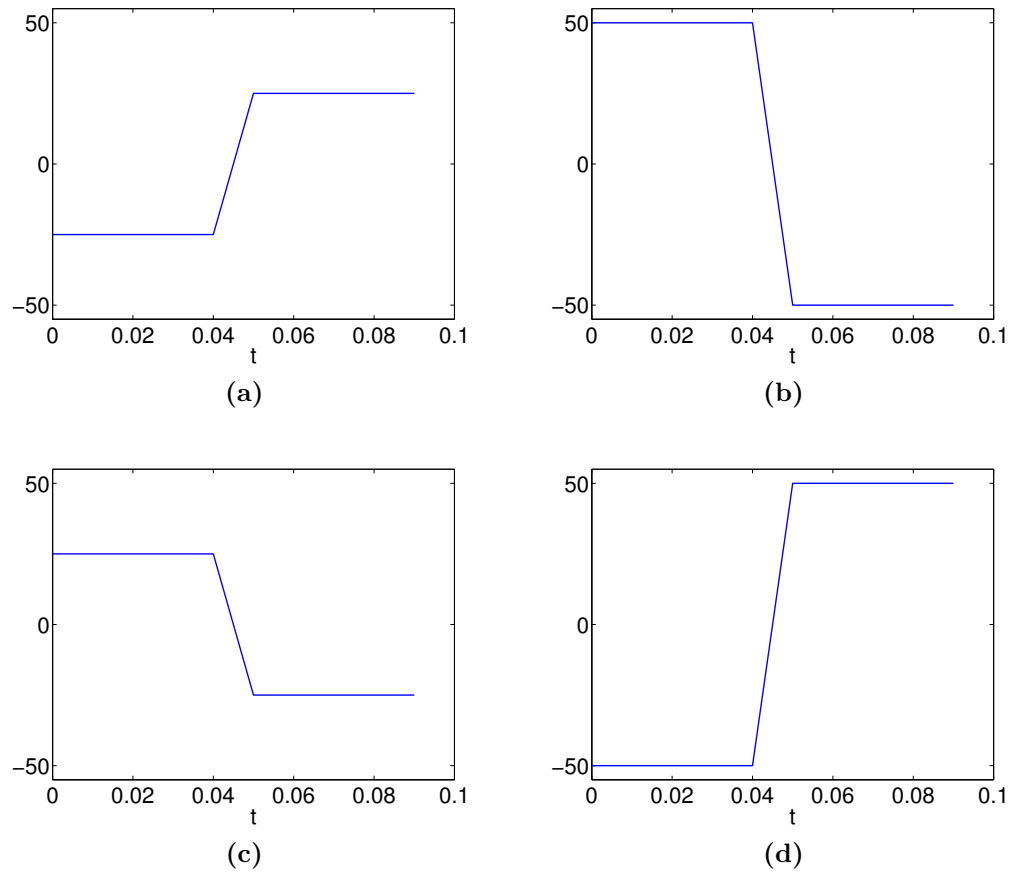
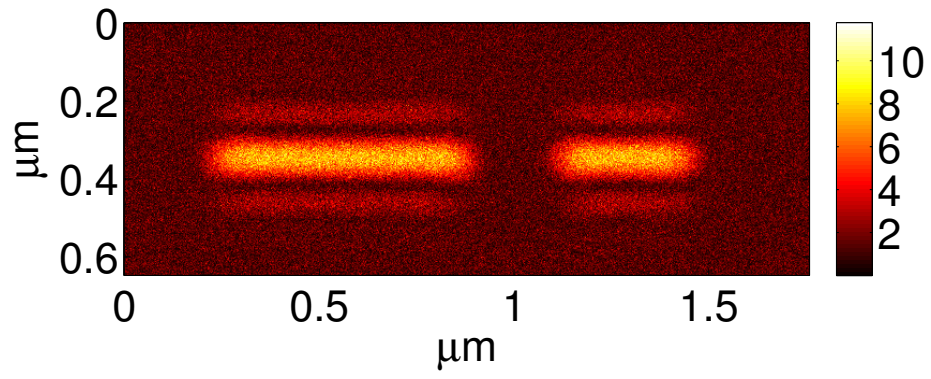
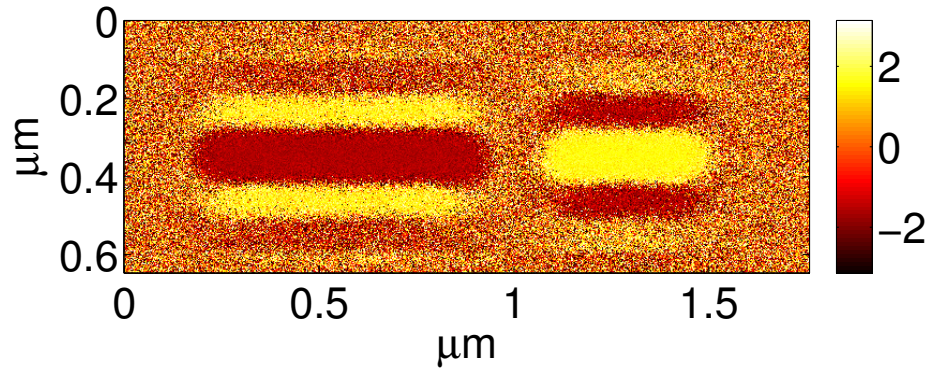


**Figure 6-6:** Modulations over time at single scan position, (a) p-type drain, (b) p-type gate, (c) n-type drain, (d) n-type gate.



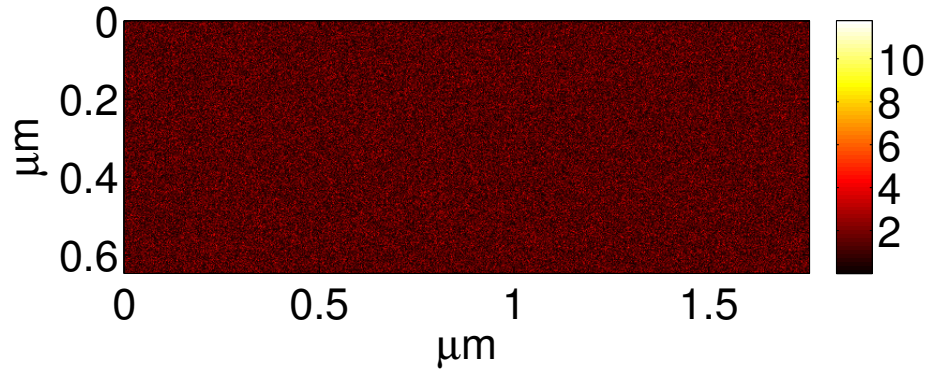


(a)

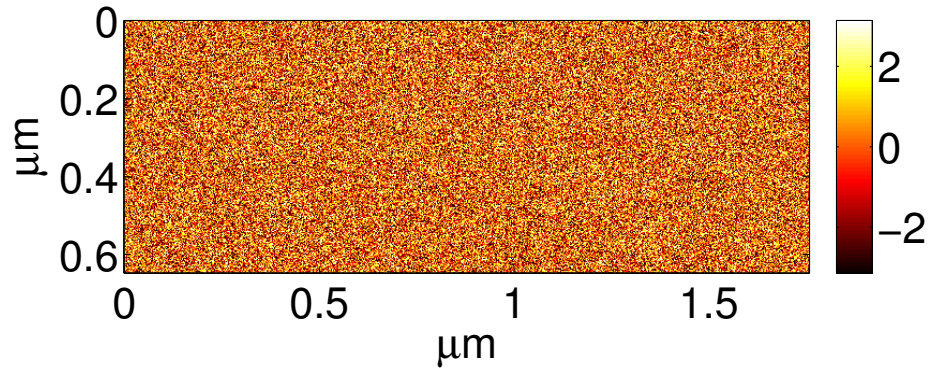


(b)

**Figure 6.7:** (a) Amplitude and (b) phase of the 1st harmonic for linearly-polarized input light in  $x$ -direction.

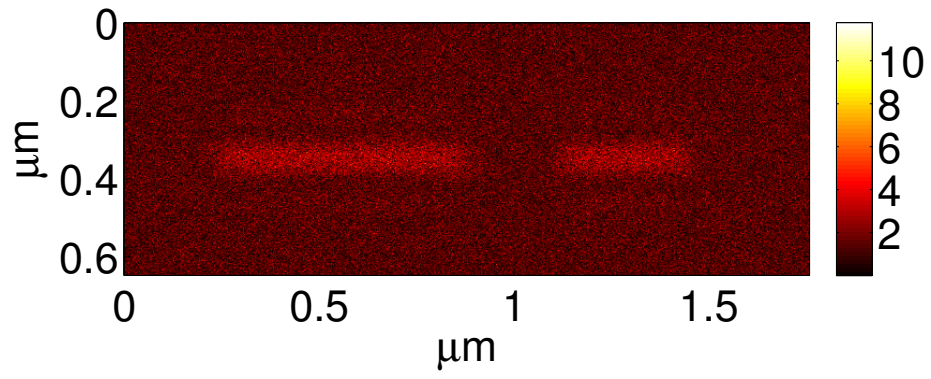


(a)

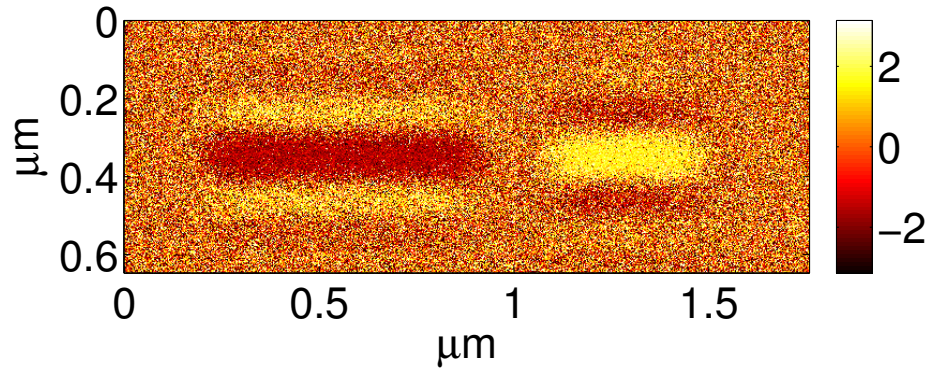


(b)

**Figure 6.8:** (a) Amplitude and (b) Phase of the 2nd harmonic for linearly-polarized input light in  $x$ -direction.

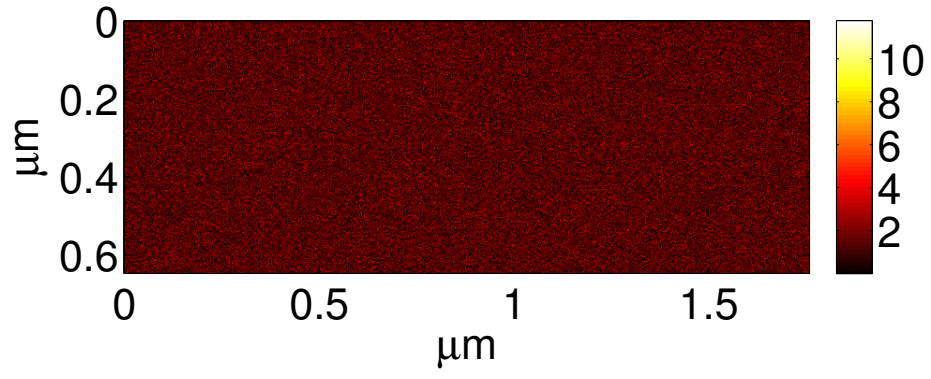


(a)

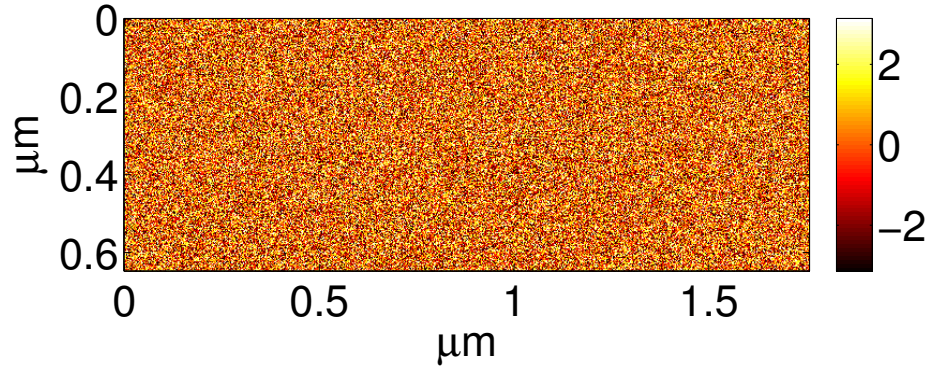


(b)

**Figure 6·9:** (a) Amplitude and (b) phase of the 3rd harmonic for linearly-polarized input light in  $x$ -direction.

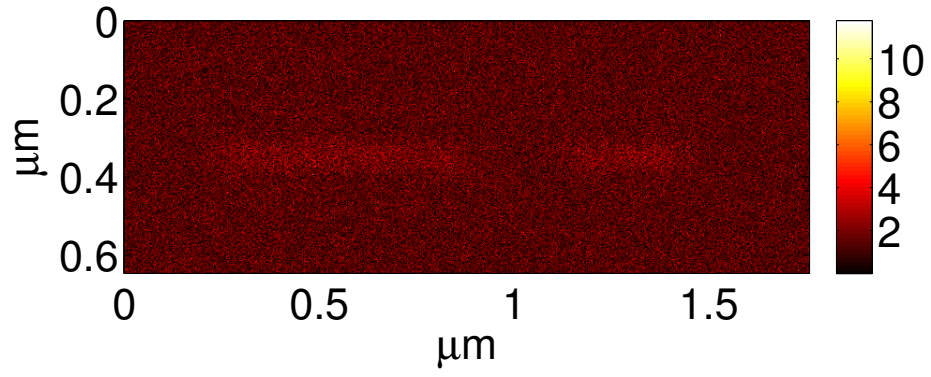


(a)

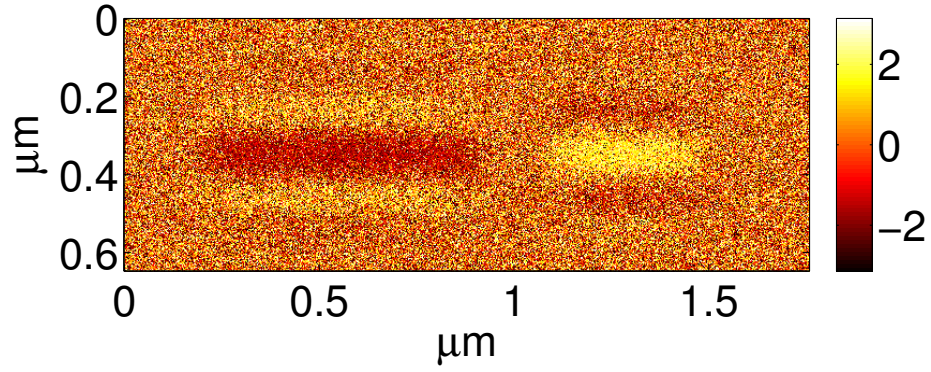


(b)

**Figure 6·10:** (a) Amplitude and (b) phase of the 4th harmonic for linearly-polarized input light in  $x$ -direction.



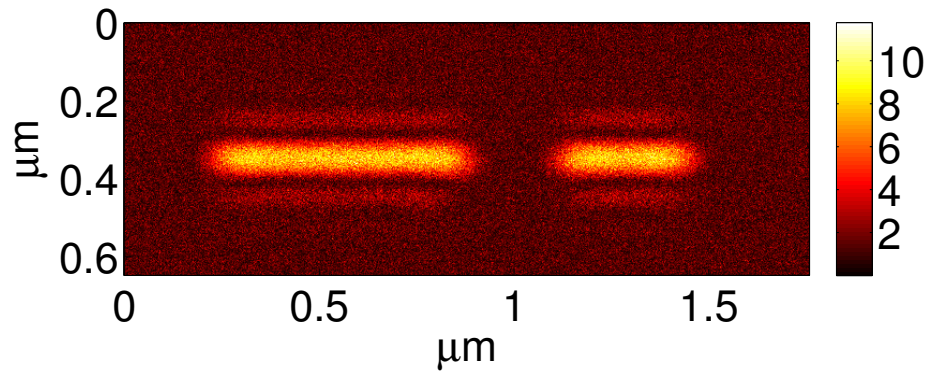
(a)



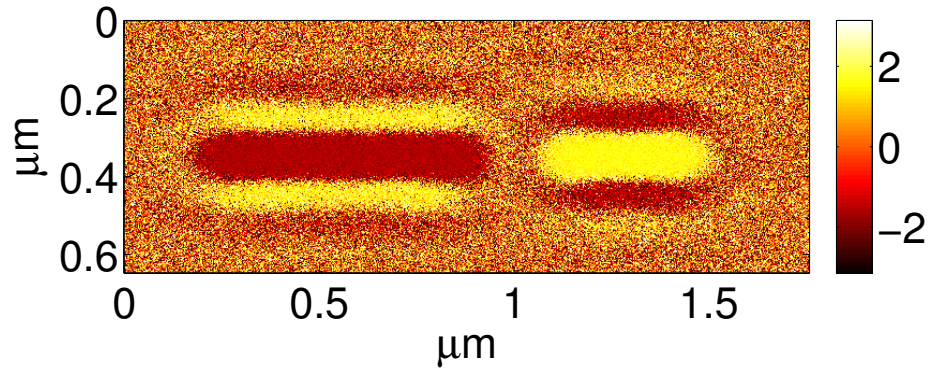
(b)

**Figure 6.11:** (a) Amplitude and (b) phase of the 5th harmonic for linearly-polarized input light in  $x$ -direction.



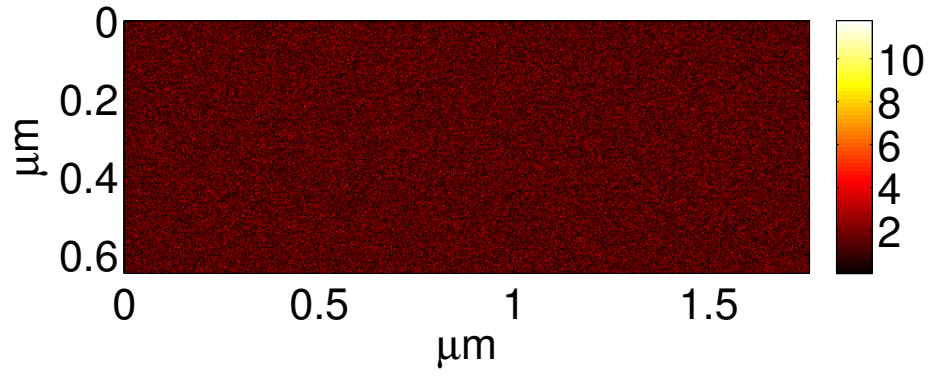


(a)

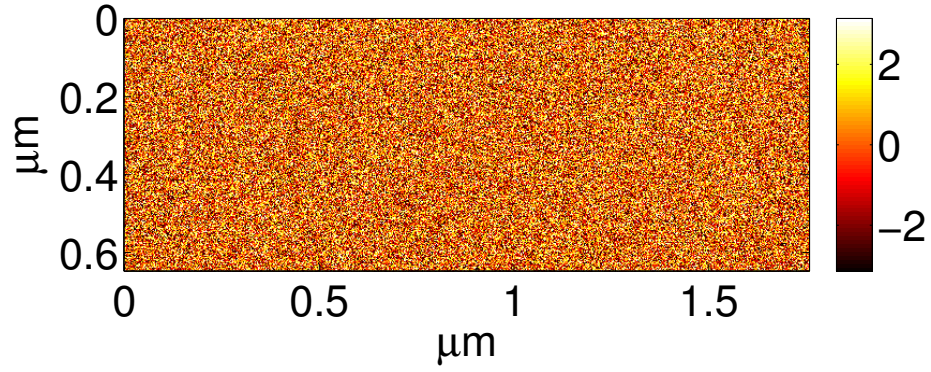


(b)

**Figure 6.12:** (a) Amplitude and (b) phase of the 1st harmonic for linearly-polarized input light in  $y$ -direction.

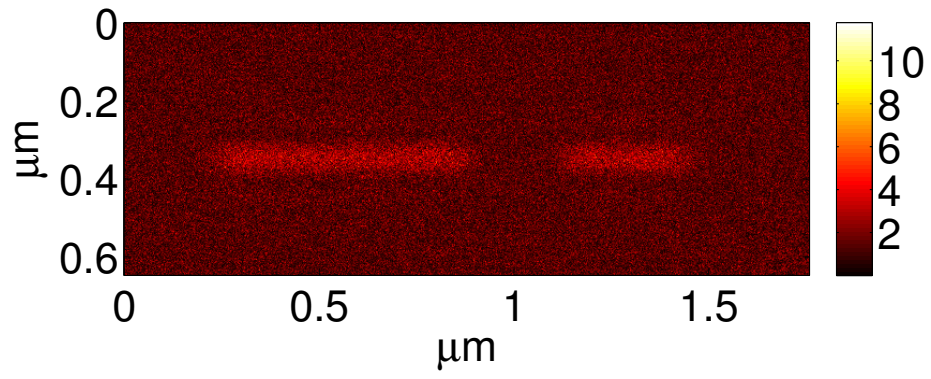


(a)

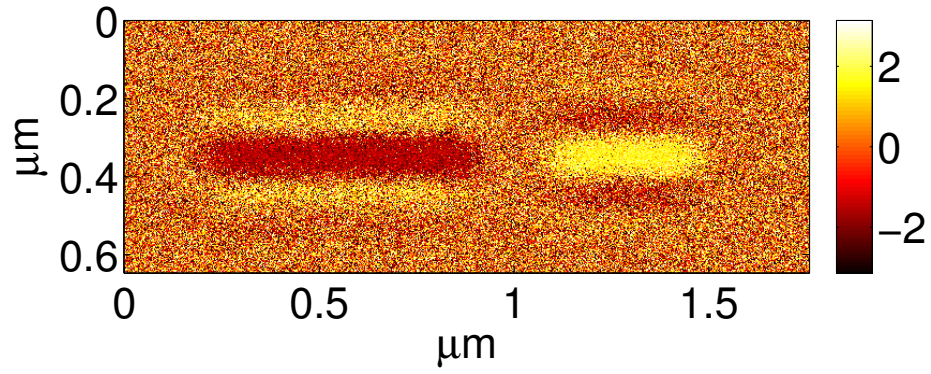


(b)

**Figure 6.13:** (a) Amplitude and (b) phase of the 2nd harmonic for linearly-polarized input light in  $y$ -direction.



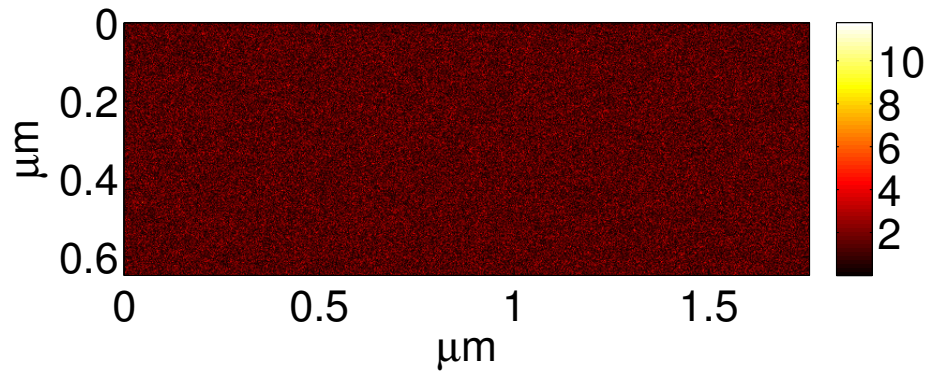
(a)



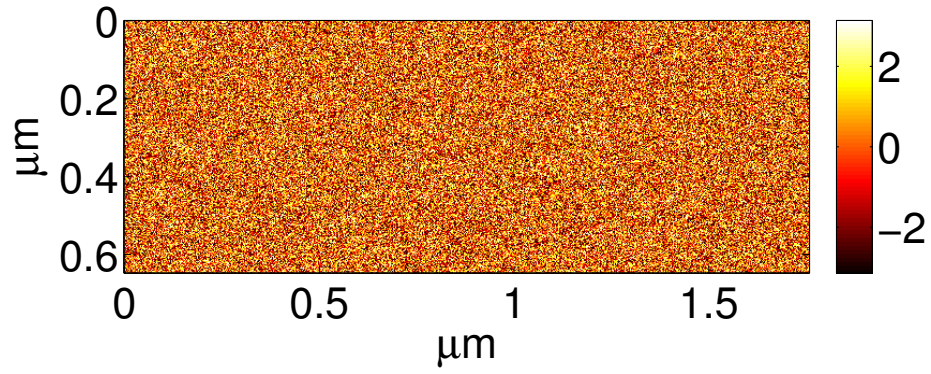
(b)

**Figure 6.14:** (a) Amplitude and (b) phase of the 3rd harmonic for linearly-polarized input light in  $y$ -direction



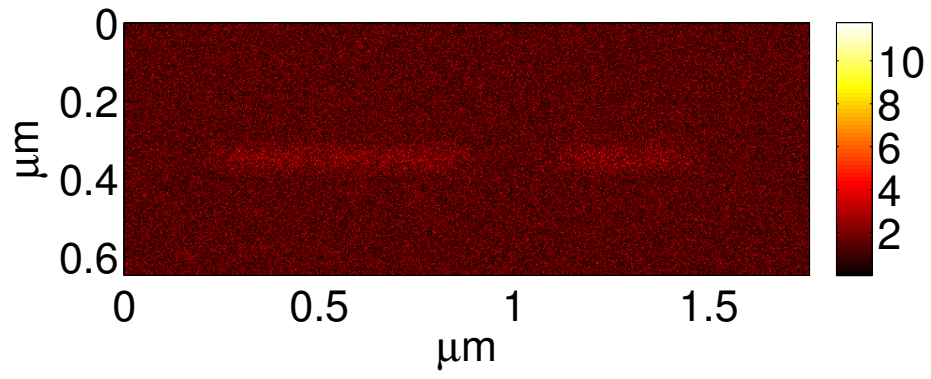


(a)

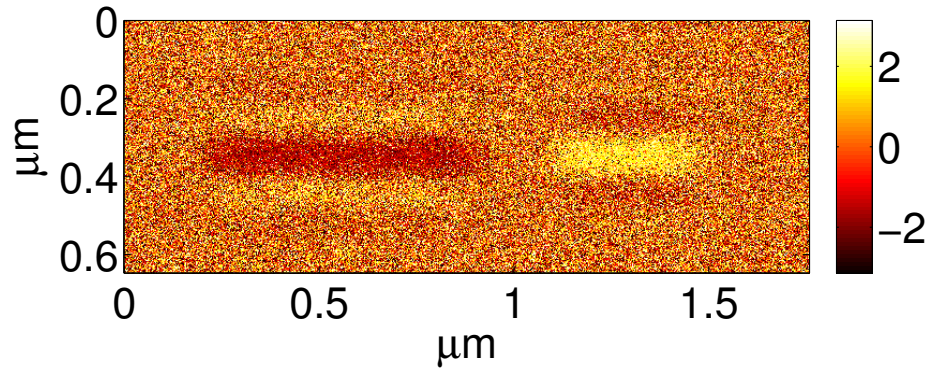


(b)

**Figure 6.15:** (a) Amplitude and (b) phase of the 4th harmonic for linearly-polarized input light in  $y$ -direction



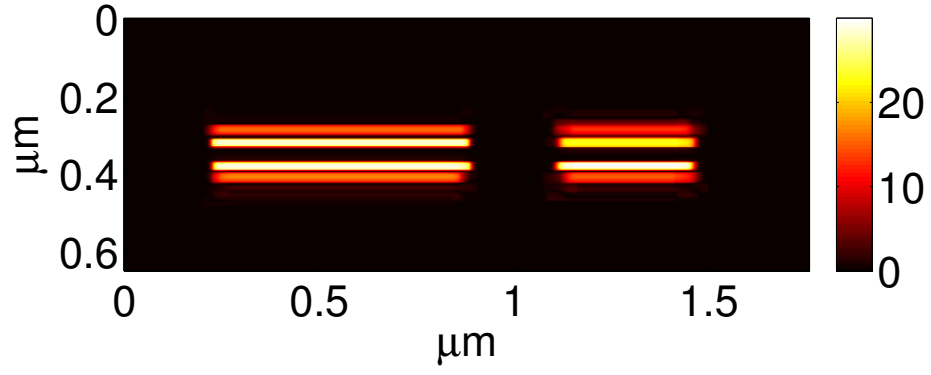
(a)



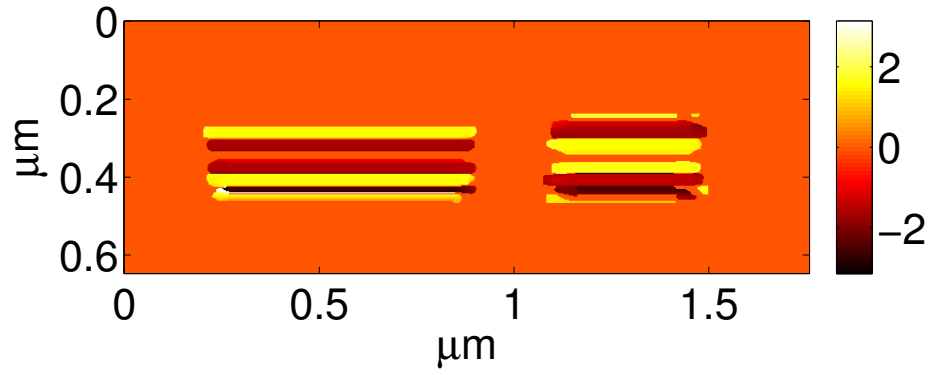
(b)

**Figure 6.16:** (a) Amplitude and (b) phase of the 5th harmonic for linearly-polarized input light in  $y$ -direction

We performed reconstructions with both space-frequency dictionaries and space-time dictionaries using all 5 harmonics, only 3 harmonics and only the first harmonic. Reconstruction results with space-frequency sparse representation using all 5 harmonics are shown in Figs. 6-17, 6-18, 6-19, 6-20 and 6-21. Figs. 6-22, 6-23 and 6-24 present results using only the first 3 harmonics and results only using the first harmonic are shown in Fig. 6-25. In order to assess the performance of the sparse representation, the ground truth LVI data of a system with no noise and no blur is simulated and it is shown in Figs. 6-26, 6-27, 6-28, 6-29 and 6-30. Fig. 6-31 compares vertical cross sections from reconstructions, observations and the ground truth data. The sparse reconstruction was able to recover gate drain regions which were blurred and merged in the observations. Hence, the sparse representation framework increases the resolution and localization accuracy according to Sparrow criterion. Using fewer harmonics did not decrease the reconstruction performance significantly. The reconstruction results using all 5 harmonics and only 3 harmonics are almost equivalent. In Fig. 6-32, the MSE for the first harmonic of the reconstructions is plotted. The error bars are calculated over 10 realizations. The MSE values are very similar. Using fewer harmonics does not decrease the reconstruction performance. However, in the case of an inverter the modulations come from a limited set, for a more complex circuit element, there might be different periods and more phase shift. In such a scenario, the number of harmonics used can affect the reconstruction performance.

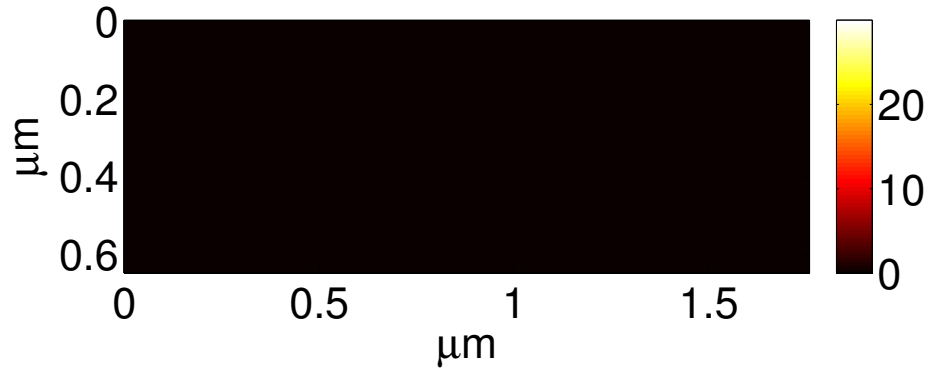


(a)

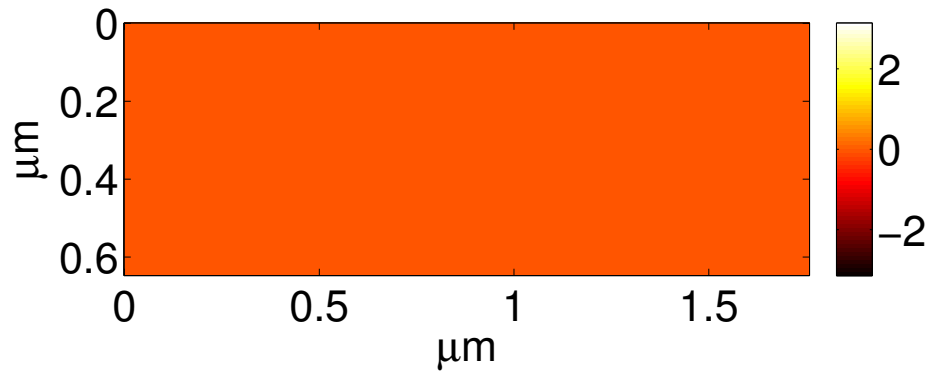


(b)

**Figure 6-17:** (a) Amplitude and (b) phase of the 1st harmonic of the reconstruction result of space-frequency sparse representation using all 5 harmonics. Phase values corresponding to amplitudes lower than 1 are set to 0.

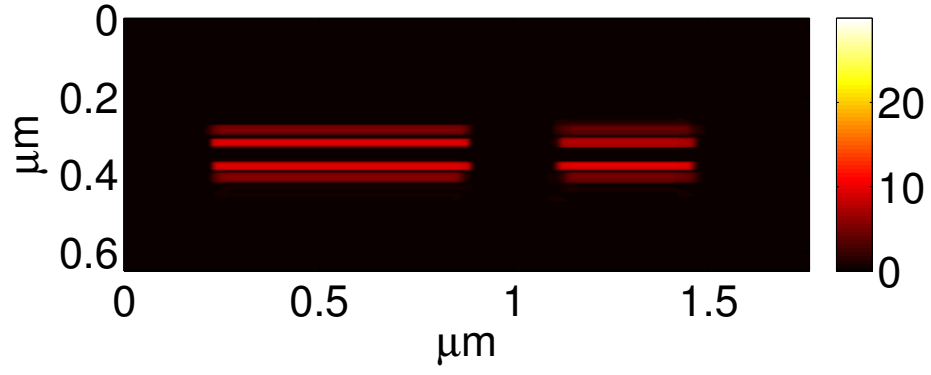


(a)

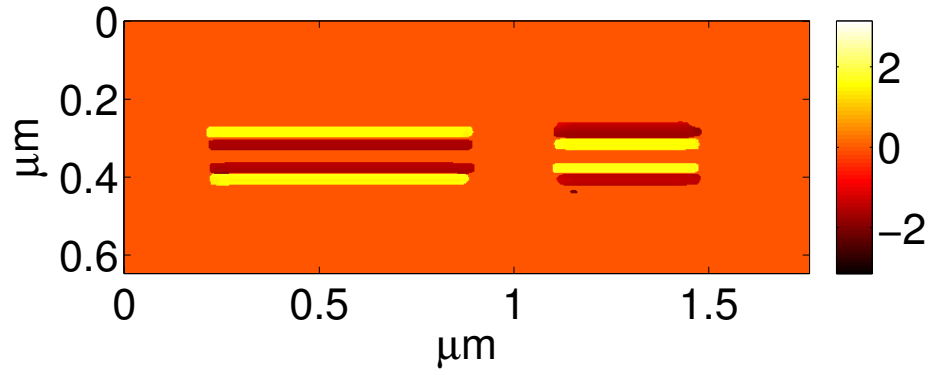


(b)

**Figure 6-18:** (a) Amplitude and (b) phase of the 2nd harmonic of the reconstruction result of space-frequency sparse representation using all 5 harmonics. Phase values corresponding to amplitudes lower than 1 are set to 0.

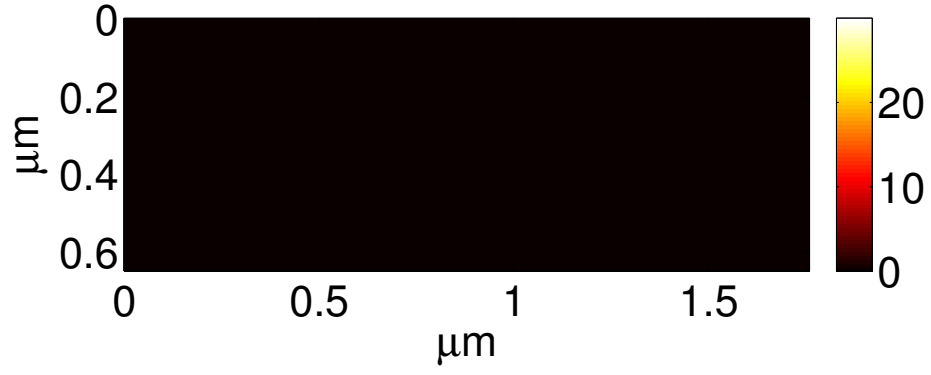


(a)

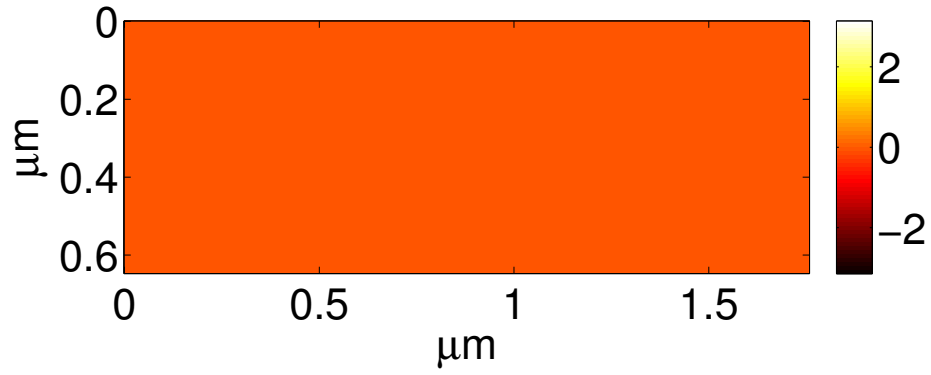


(b)

**Figure 6-19:** (a) Amplitude and (b) phase of the 3rd harmonic of the reconstruction result of space-frequency sparse representation using all 5 harmonics. Phase values corresponding to amplitudes lower than 1 are set to 0.

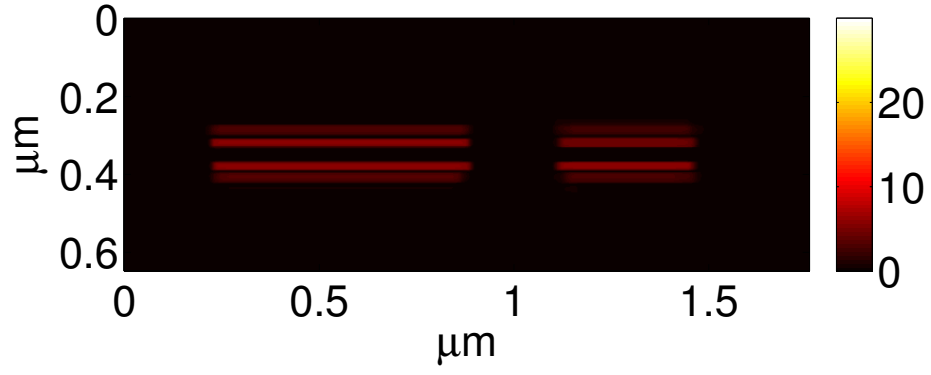


(a)

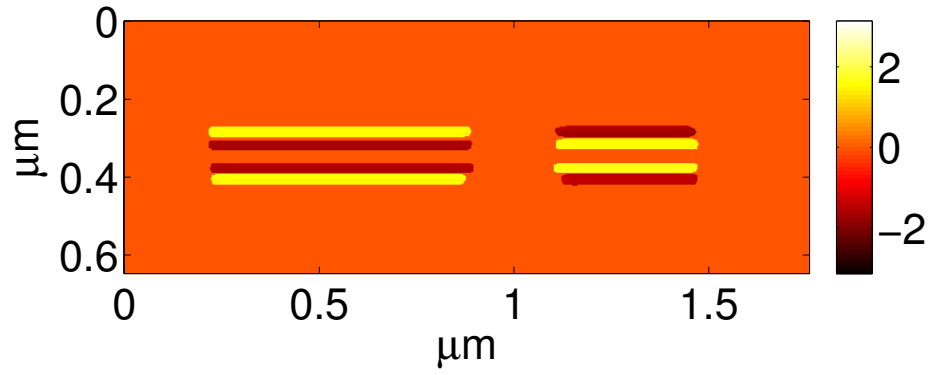


(b)

**Figure 6·20:** (a) Amplitude and (b) phase of the 4th harmonic of the reconstruction result of space-frequency sparse representation using all 5 harmonics. Phase values corresponding to amplitudes lower than 1 are set to 0.



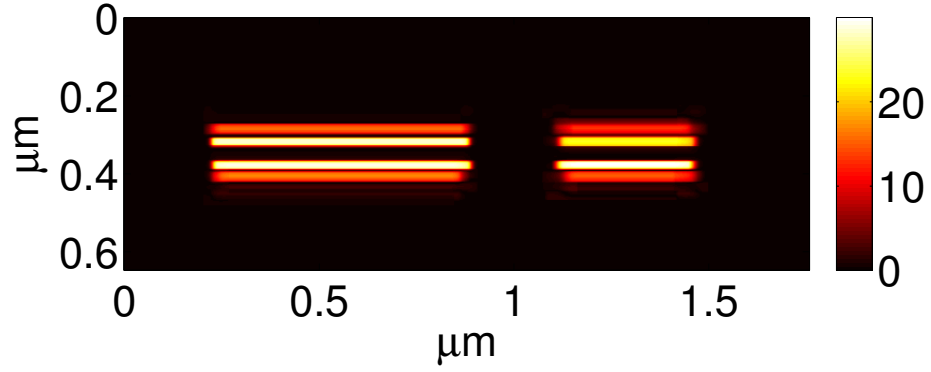
(a)



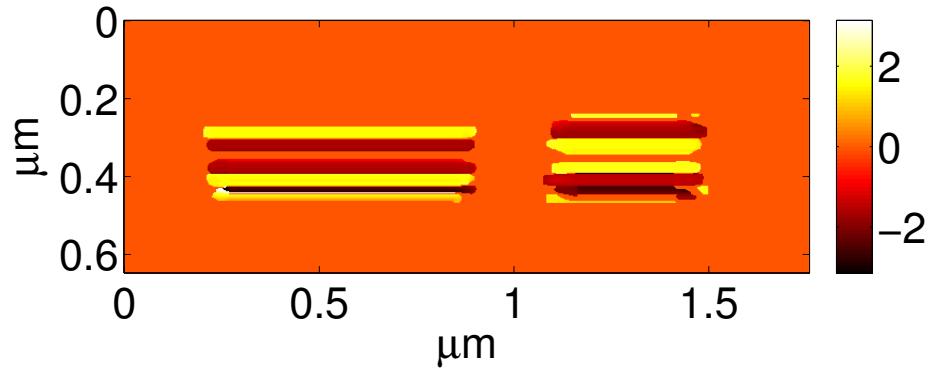
(b)

**Figure 6·21:** (a) Amplitude and (b) phase of the 5th harmonic of the reconstruction result of space-frequency sparse representation using all 5 harmonics. Phase values corresponding to amplitudes lower than 1 are set to 0.



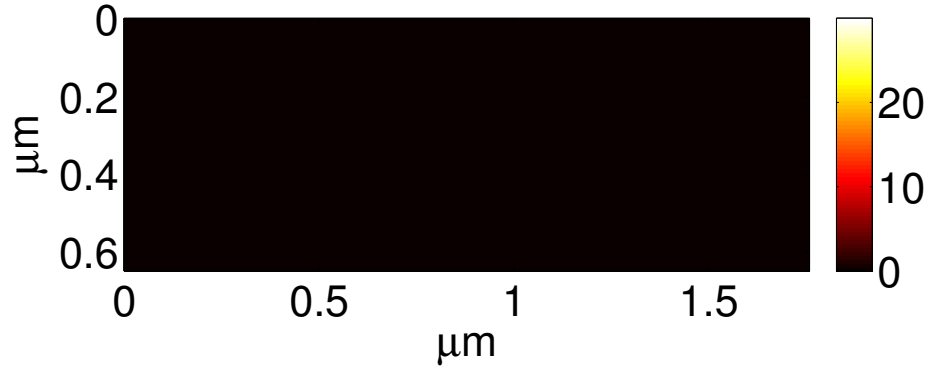


(a)

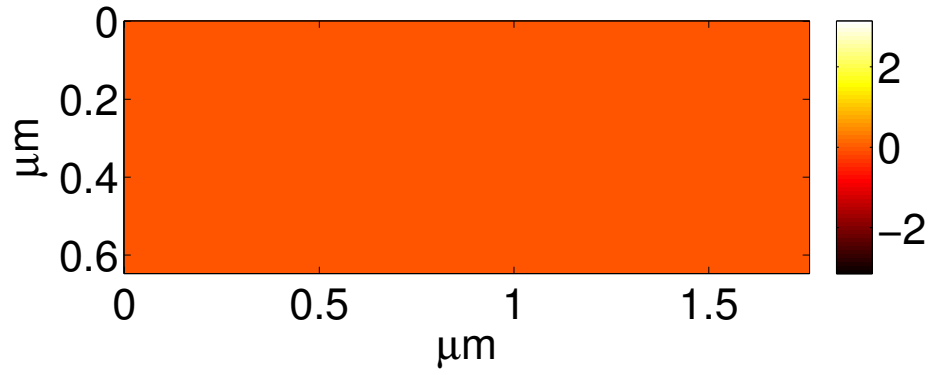


(b)

**Figure 6·22:** (a) Amplitude and (b) phase of the 1st harmonic of the reconstruction result of space-frequency sparse representation using 3 harmonics. Phase values corresponding to amplitudes lower than 1 are set to 0.

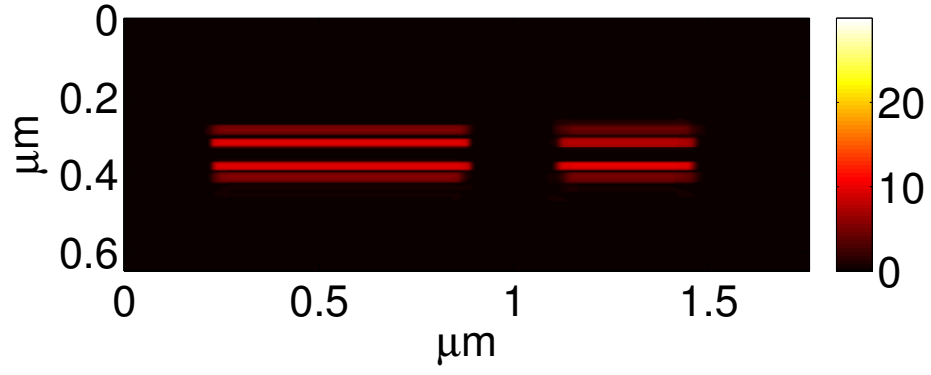


(a)

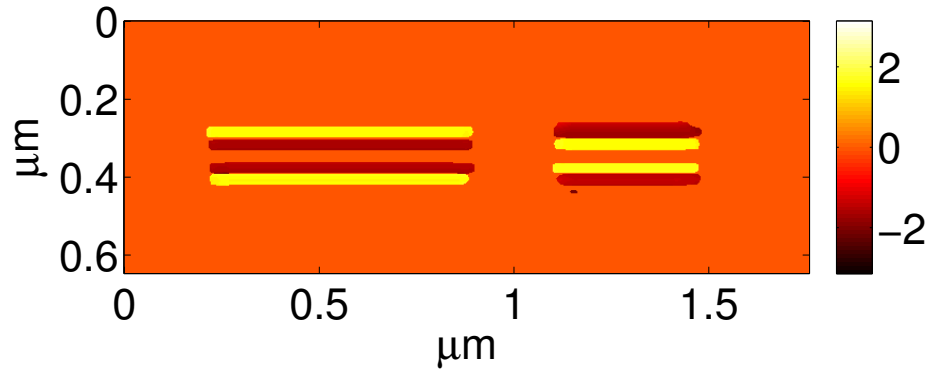


(b)

**Figure 6·23:** (a) Amplitude and (b) phase of the 2nd harmonic of the reconstruction result of space-frequency sparse representation using 3 harmonics. Phase values corresponding to amplitudes lower than 1 are set to 0.

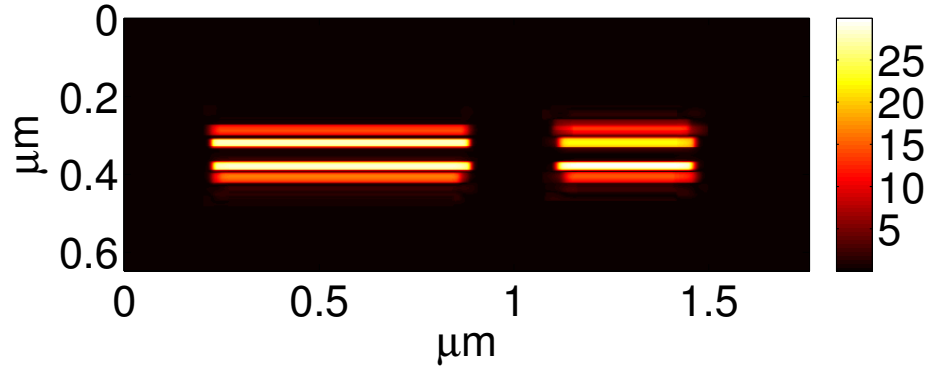


(a)

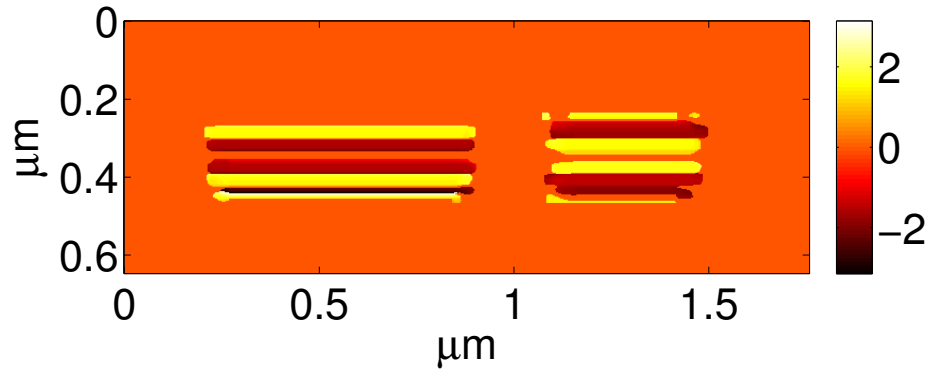


(b)

**Figure 6·24:** (a) Amplitude and (b) phase of the 3rd harmonic of the reconstruction result of space-frequency sparse representation using 3 harmonics. Phase values corresponding to amplitudes lower than 1 are set to 0.

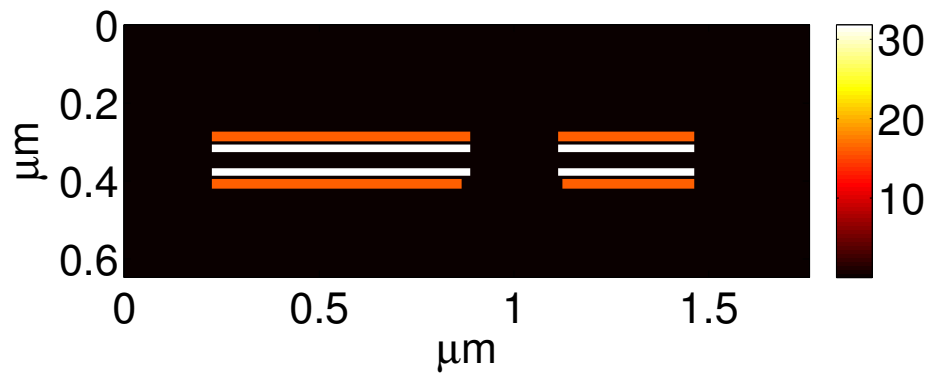


(a)

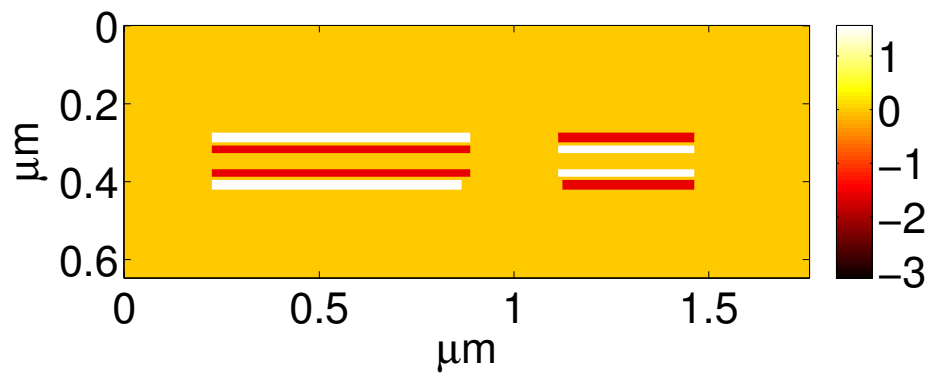


(b)

**Figure 6-25:** (a) Amplitude and (b) phase of the 1st harmonic of the reconstruction result of space-frequency sparse representation using only 1st harmonic. Phase values corresponding to amplitudes lower than 1 are set to 0.

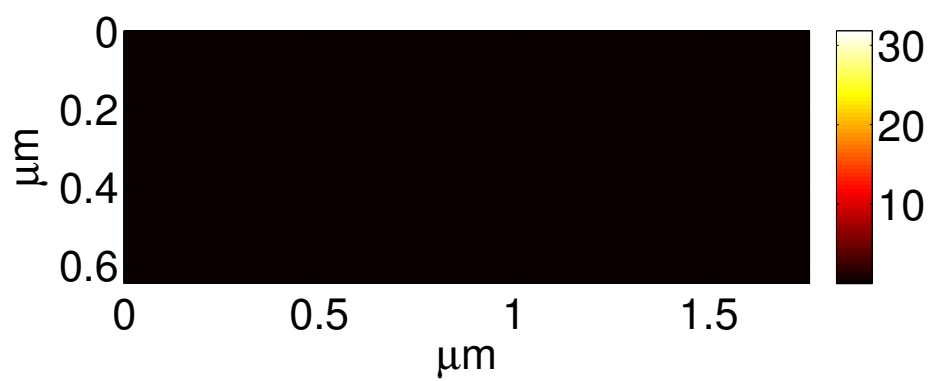


(a)

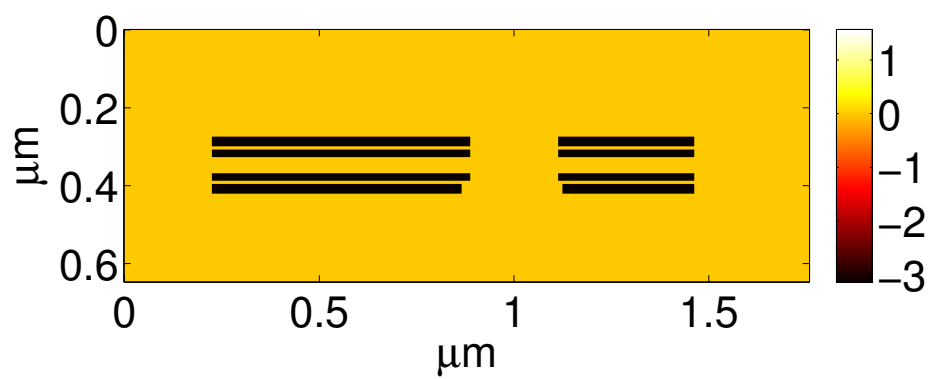


(b)

**Figure 6·26:** (a) Amplitude and (b) phase of the 1st harmonic of the ground truth

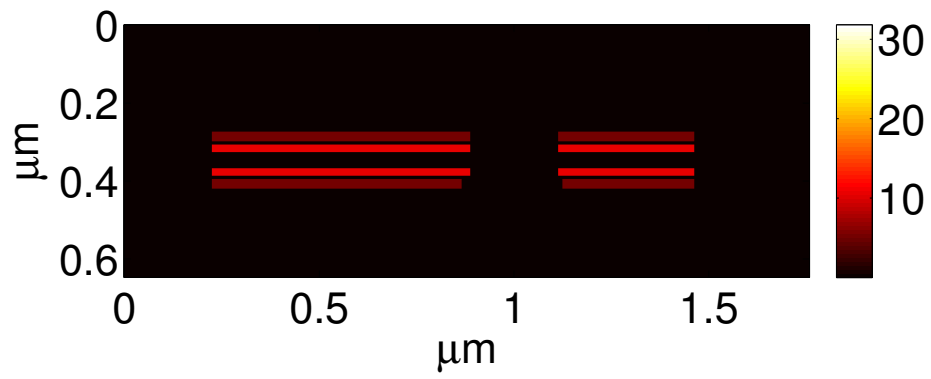


(a)

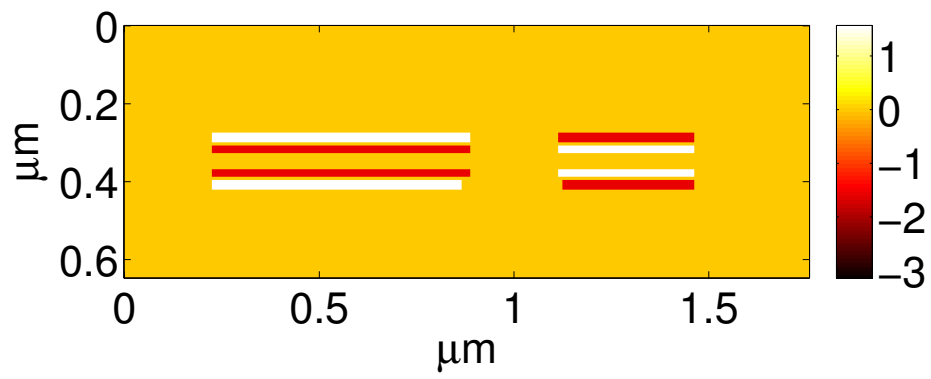


(b)

**Figure 6-27:** (a) Amplitude and (b) phase of the 2nd harmonic of the ground truth

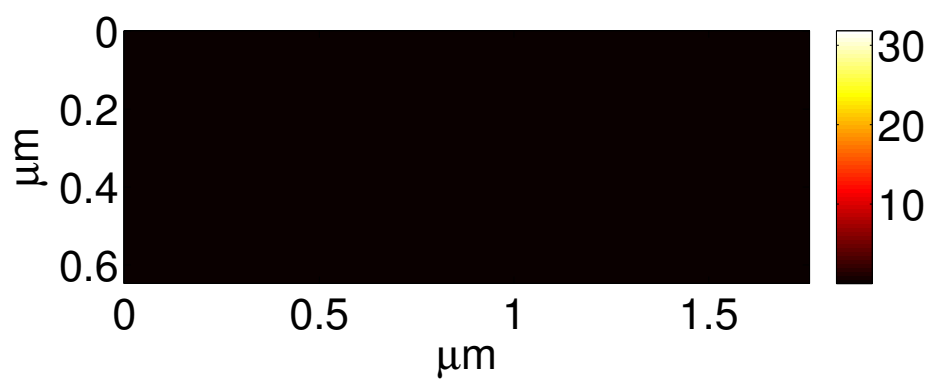


(a)

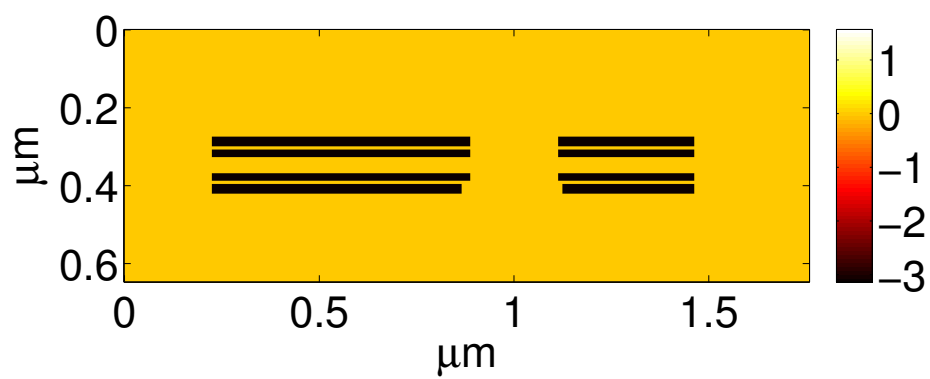


(b)

**Figure 6.28:** (a) Amplitude and (b) phase of the 3rd harmonic of the ground truth



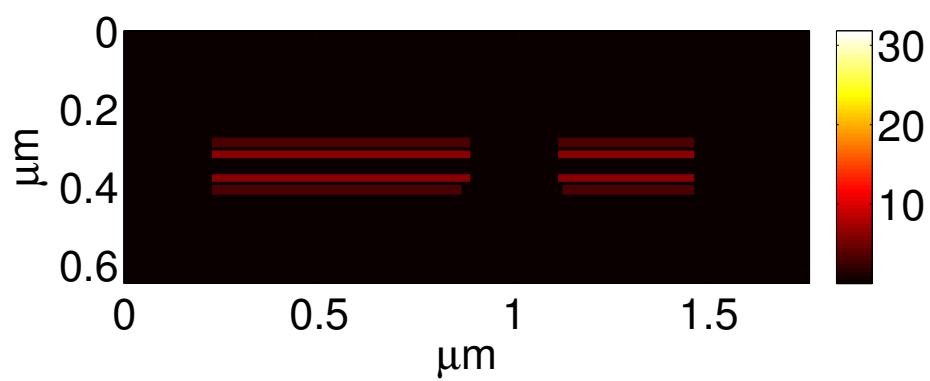
(a)



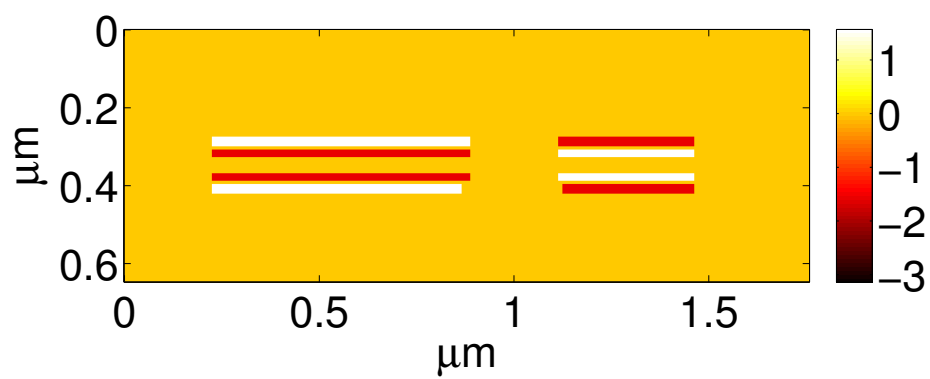
(b)

**Figure 6.29:** (a) Amplitude and (b) phase of the 4th harmonic of the ground truth





(a)



(b)

**Figure 6.30:** (a) Amplitude and (b) phase of the 5th harmonic of the ground truth

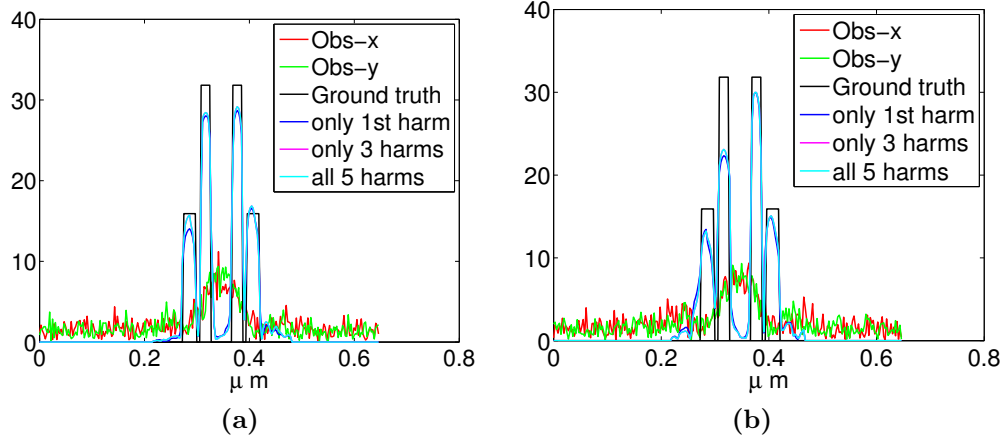


**Figure 6-31:** Comparison of the vertical cross sections of the amplitude of the first harmonic: (a) p-type transistor, (b) n-type transistor. The cross sections for all 5 harmonics reconstruction and only 3 harmonics reconstruction overlap.

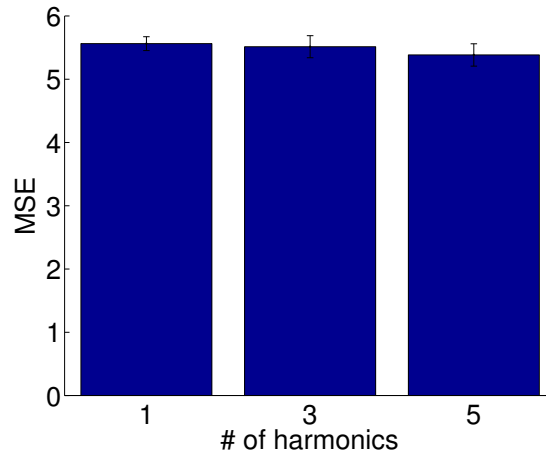
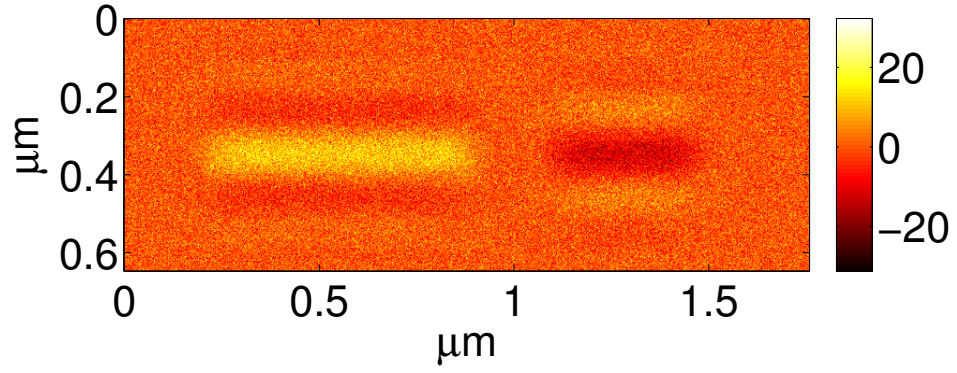
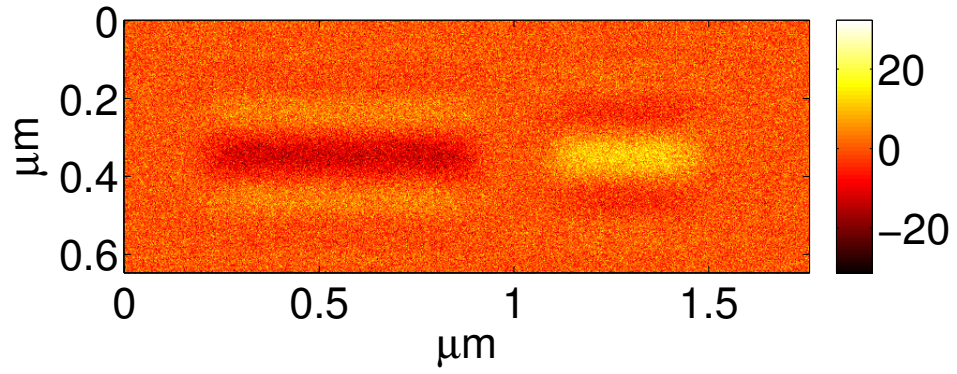


**Figure 6-32:** The MSE for the first harmonic of the reconstructions

We also performed reconstructions with a space-time representation. Eq. 6.9 is used in order to represent the original observation data in time with Fourier series expansion. The time domain is discretized to produce 10 samples both for time-domain representation of the LVI observation and for the elements of the space-time dictionary. Three different estimations of time-domain modulation are calculated: using all 5 harmonics, using only the first 3 harmonics and using only the first harmonic. The observations for all scan positions at two different times are shown in Figs. 6-33, 6-34, 6-35, 6-36, 6-37 and 6-38. Modulation over time for scan positions specified in Fig. 6-4 are shown in Figs. 6-39, 6-40, 6-41, 6-42, 6-43 and 6-44. The results for sparse space-time representation using all 5 harmonics for all scan positions at two different time points are shown in Fig. 6-45 and the reconstructed modulation over time at 4 different scan positions is shown in Fig. 6-46. The results of reconstruction using only 3 harmonics are shown in Fig. 6-47 for all scan positions at two different times and in Fig. 6-48 over time at 4 different scan positions. Similarly, the results of the sparse space-time representation using only the first harmonic are presented in Figs. 6-49 and 6-50. The gate and drain regions are not localized in the observation data whereas they are localized in sparse space-time representation results. In addition to resolution improvement in space, the reconstructed modulation is also sharp in time because the space-time dictionary elements are composed of square waves in the time. Fig. 6-51 compares vertical cross sections from reconstructions, observations and the ground truth data. In Fig. 6-52, the mean of MSE values for the space slice at time  $t = 0.02$  and for the space slice at time  $t = 0.07$  of the reconstructions is plotted.

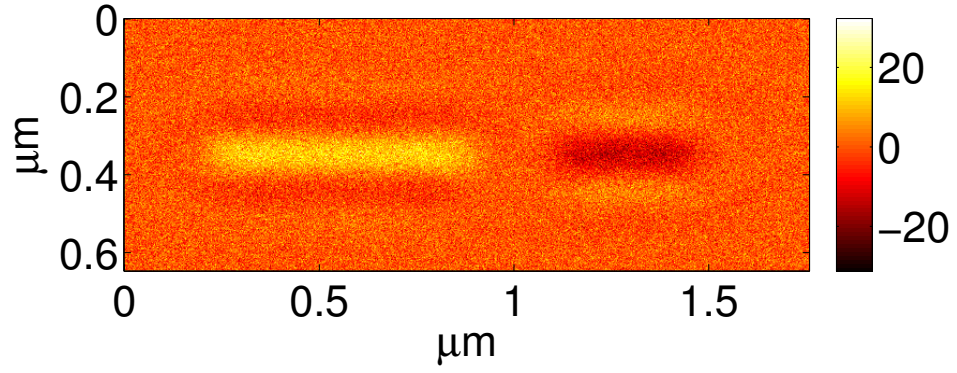


(a)

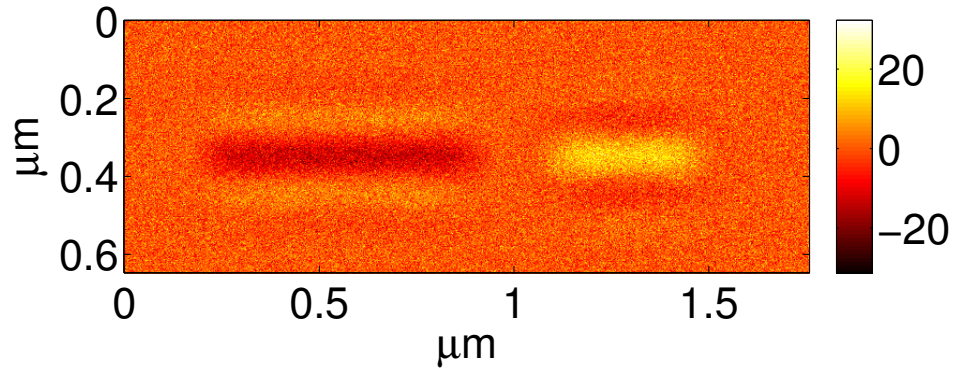


(b)

**Figure 6-33:** Amplitude of observed modulation (Fourier series expansion of 5 harmonics) in all scan positions for  $x$ -polarized input light (a) at time point  $t = 0.02$  (a) at time point  $t = 0.07$

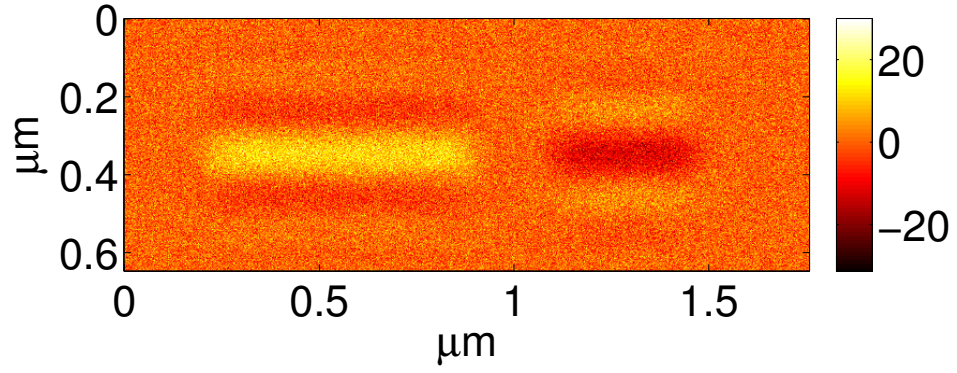


(a)

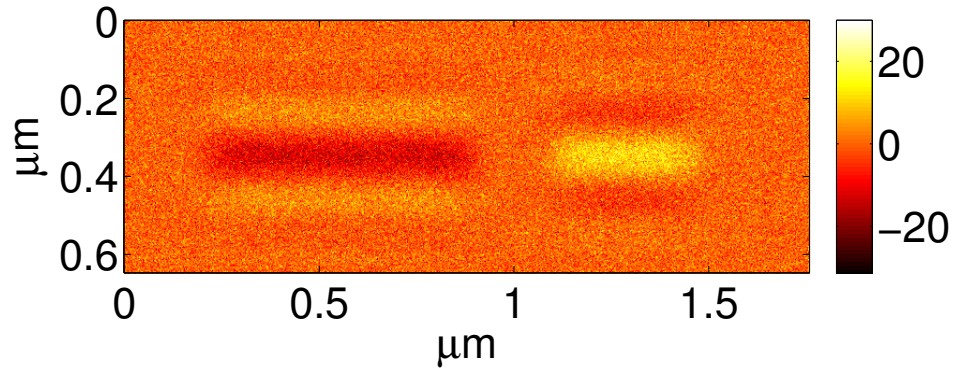


(b)

**Figure 6.34:** Amplitude of the observed modulation (Fourier series expansion of 5 harmonics) at all scan positions for  $y$ -polarized input light (a) at time  $t = 0.02$ , (b) at time  $t = 0.07$ .

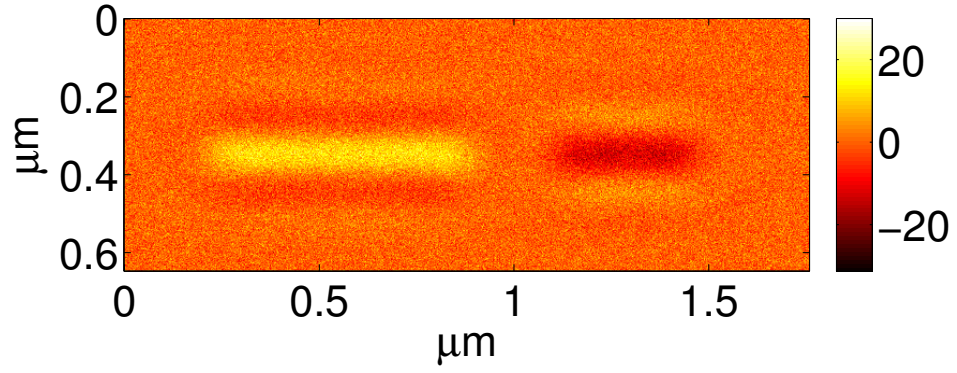


(a)

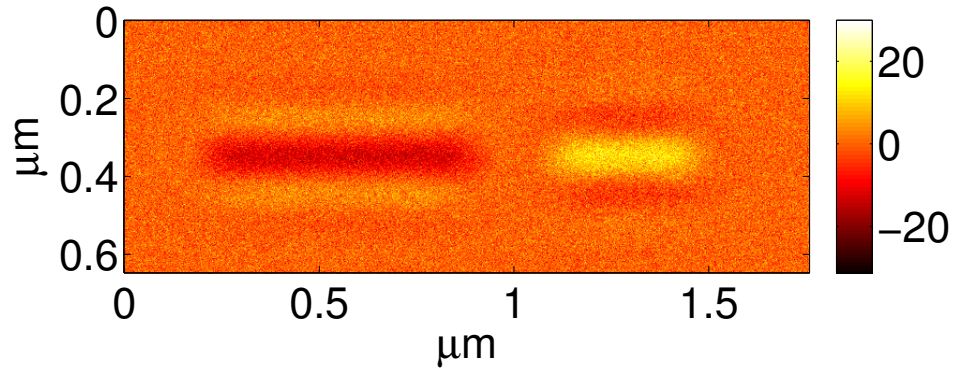


(b)

**Figure 6·35:** Amplitude of the observed modulation (Fourier series expansion of 3 harmonics) at all scan positions for  $x$ -polarized input light (a) at time  $t = 0.02$ , (b) at time  $t = 0.07$ .

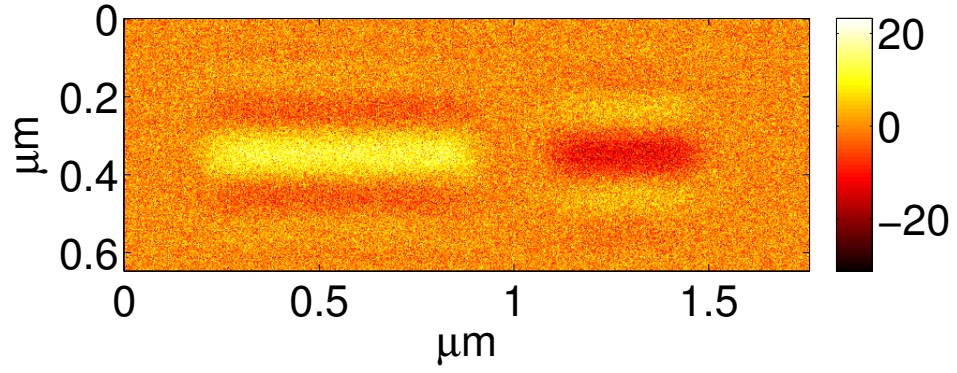


(a)

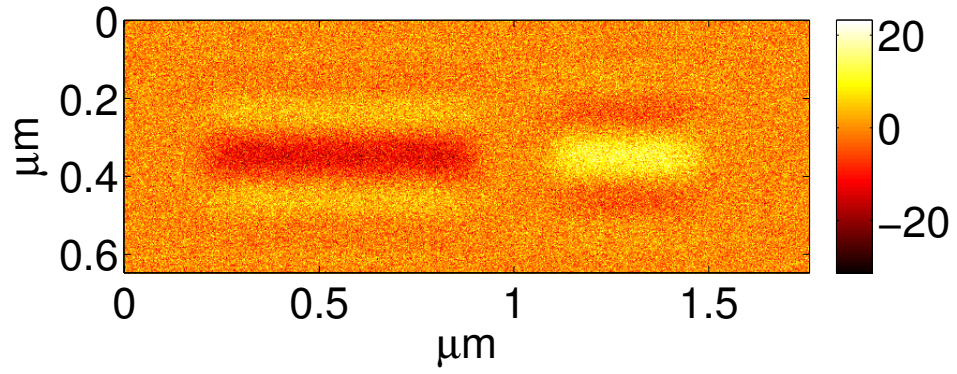


(b)

**Figure 6·36:** Amplitude of the observed modulation (Fourier series expansion of 3 harmonics) at all scan positions for  $y$ -polarized input light (a) at time  $t = 0.02$ , (b) at time  $t = 0.07$ .



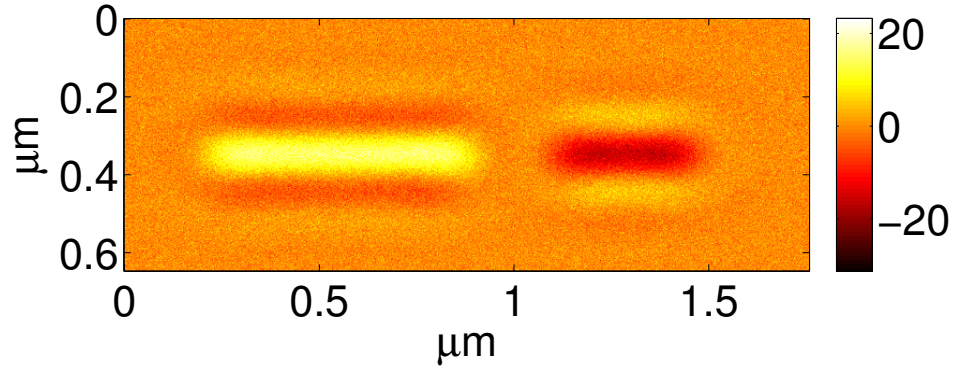
(a)



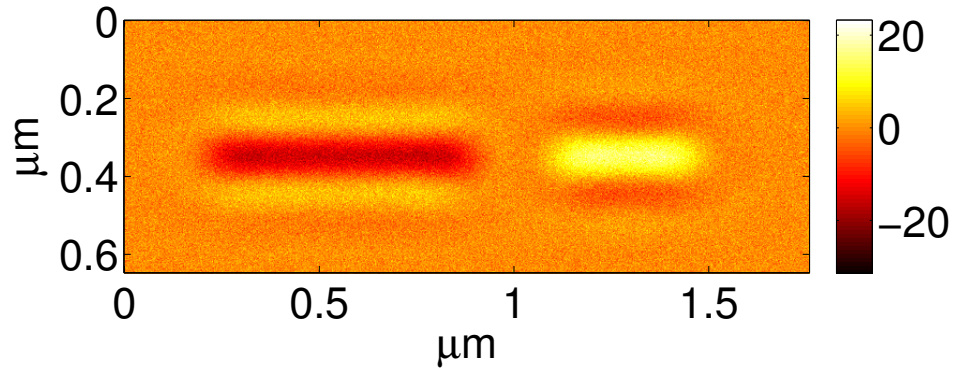
(b)

**Figure 6·37:** Amplitude of the observed modulation (Fourier series expansion of 1 harmonic) at all scan positions for  $x$ -polarized input light (a) at time  $t = 0.02$ , (b) at time  $t = 0.07$ .





(a)



(b)

**Figure 6·38:** Amplitude of the observed modulation (Fourier series expansion of 1 harmonic) at all scan positions for  $y$ -polarized input light (a) at time  $t = 0.02$ , (b) at time  $t = 0.07$ .

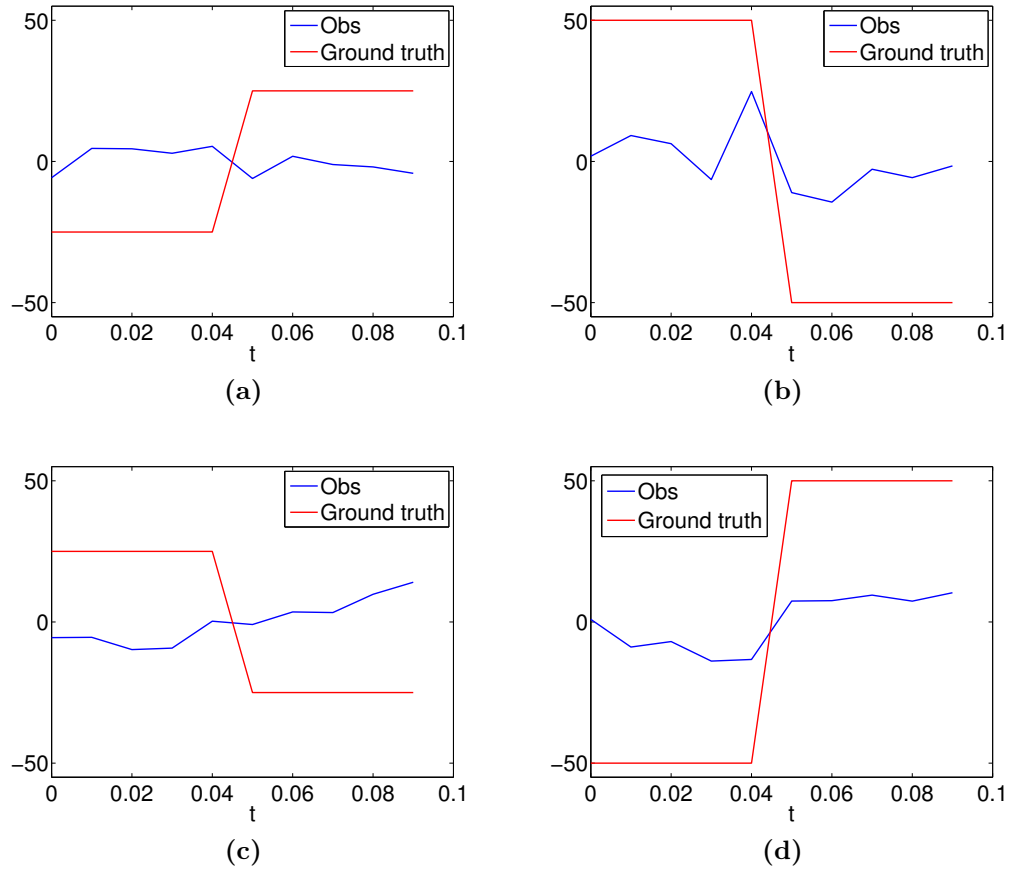


**Figure 6-39:** Observed modulations (Fourier series expansion of 5 harmonics) over time at a single scan position: (a) p-type drain, (b) p-type gate, (c) n-type drain, (d) n-type gate for  $x$ -polarized input light.

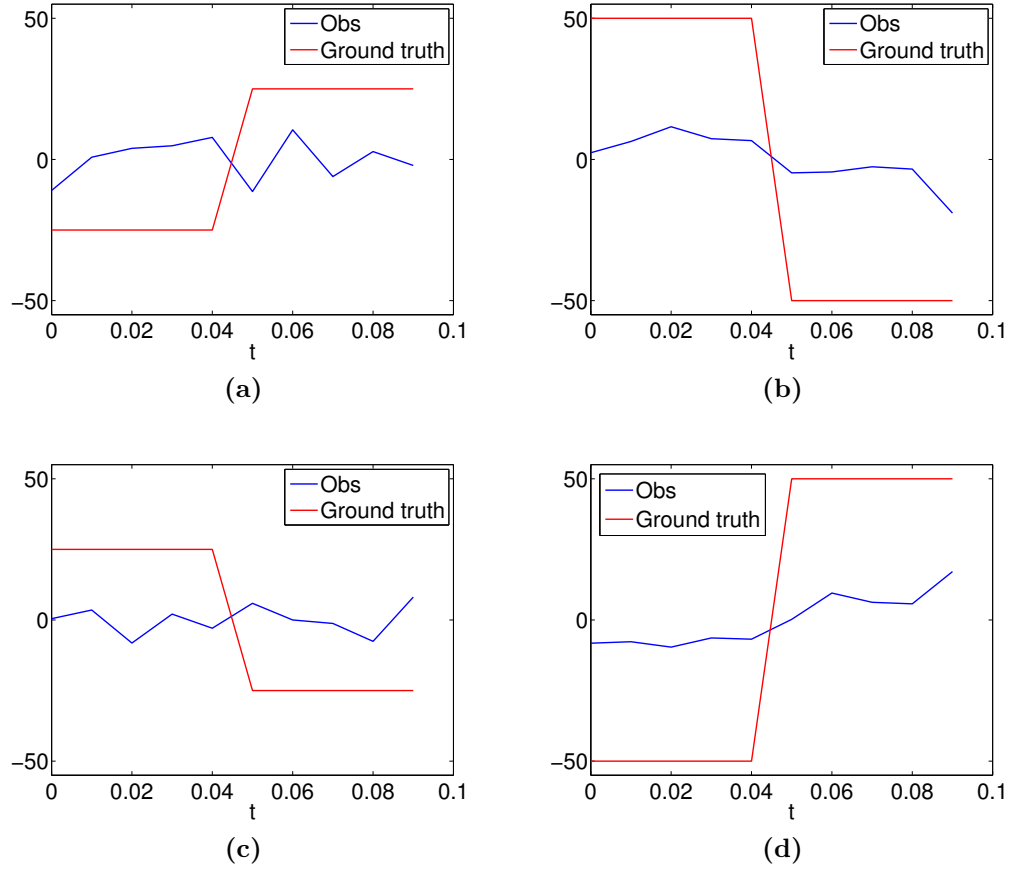


**Figure 6-40:** Observed modulations (Fourier series expansion of 5 harmonics) over time at a single scan position: (a) p-type drain, (b) p-type gate, (c) n-type drain, (d) n-type gate for  $y$ -polarized input light.

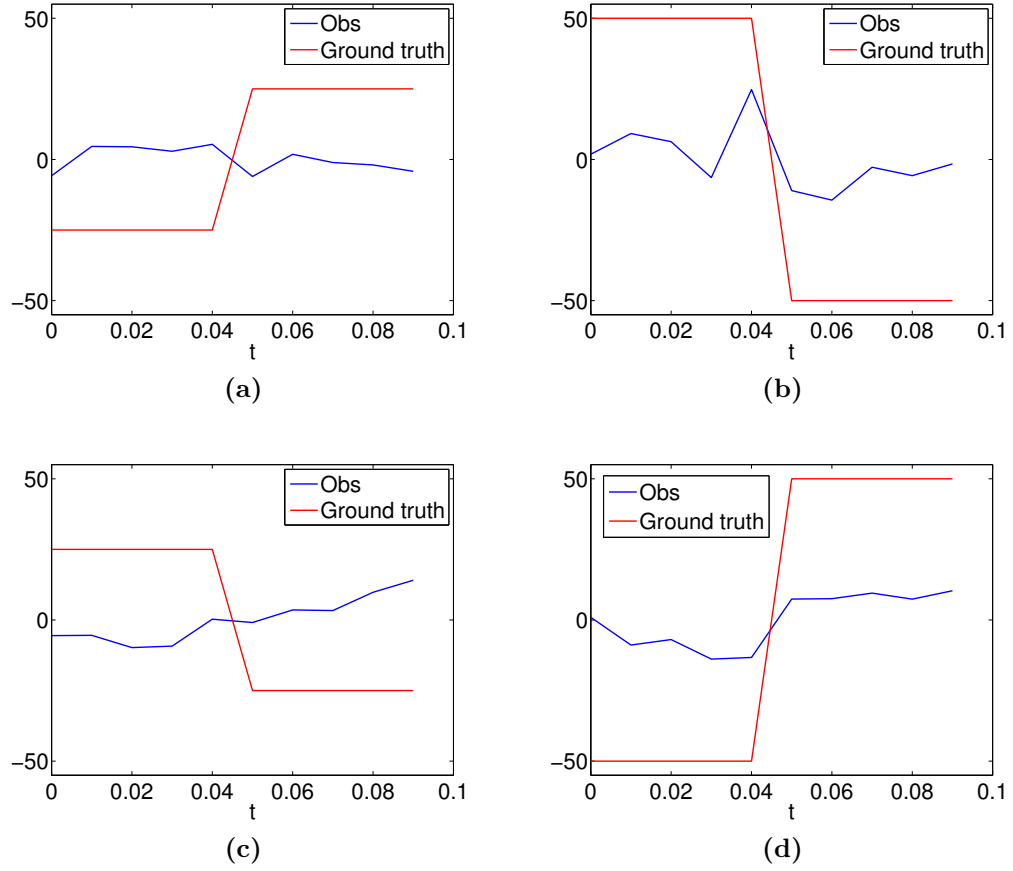


**Figure 6-41:** Observed modulations (Fourier series expansion of 3 harmonics) over time at a single scan position: (a) p-type drain, (b) p-type gate, (c) n-type drain, (d) n-type gate for  $x$ -polarized input light.

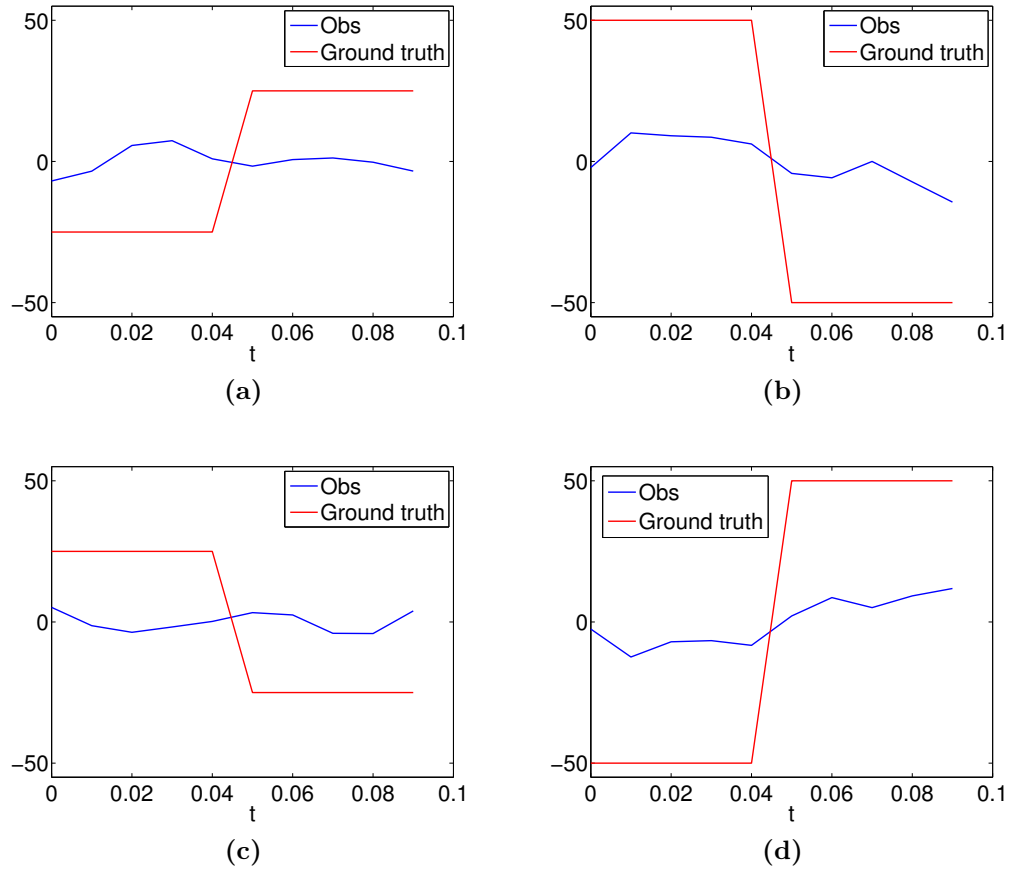


**Figure 6-42:** Observed modulations (Fourier series expansion of 3 harmonics) over time at a single scan position: (a) p-type drain, (b) p-type gate, (c) n-type drain, (d) n-type gate for  $y$ -polarized input light.

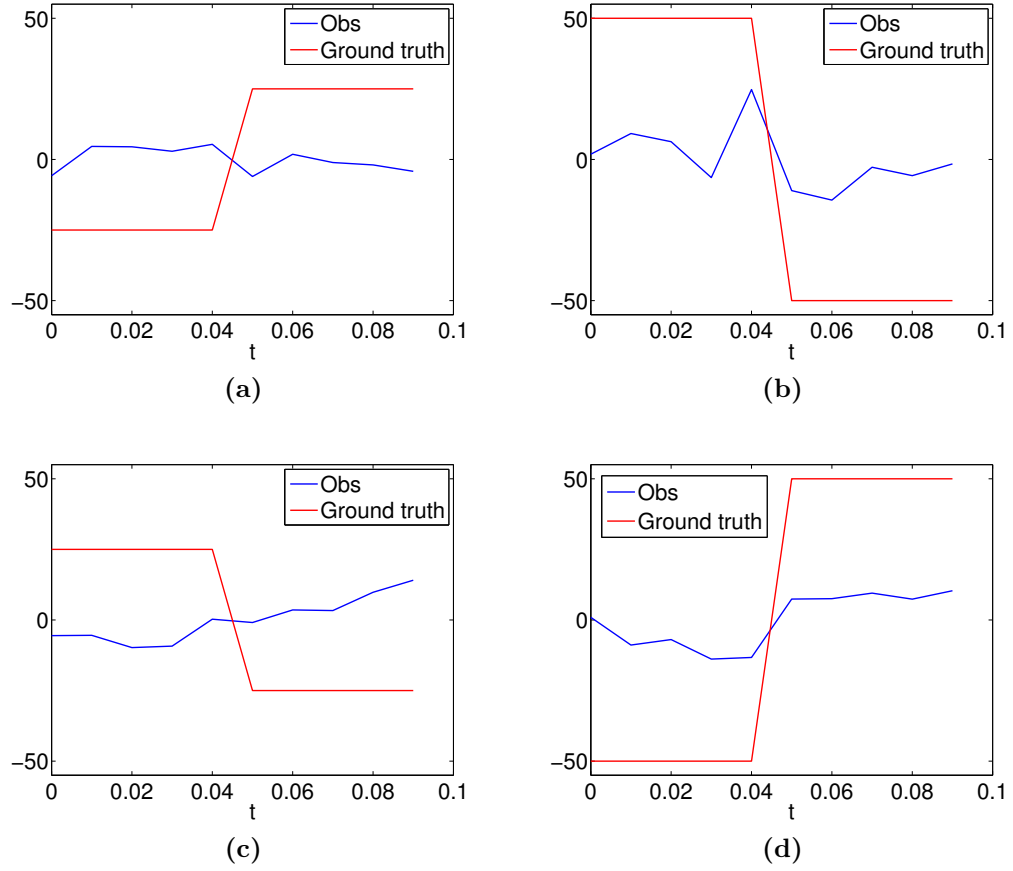


**Figure 6-43:** Observed modulations (Fourier series expansion of 1 harmonic) over time at a single scan position: (a) p-type drain, (b) p-type gate, (c) n-type drain, (d) n-type gate for  $x$ -polarized input light.

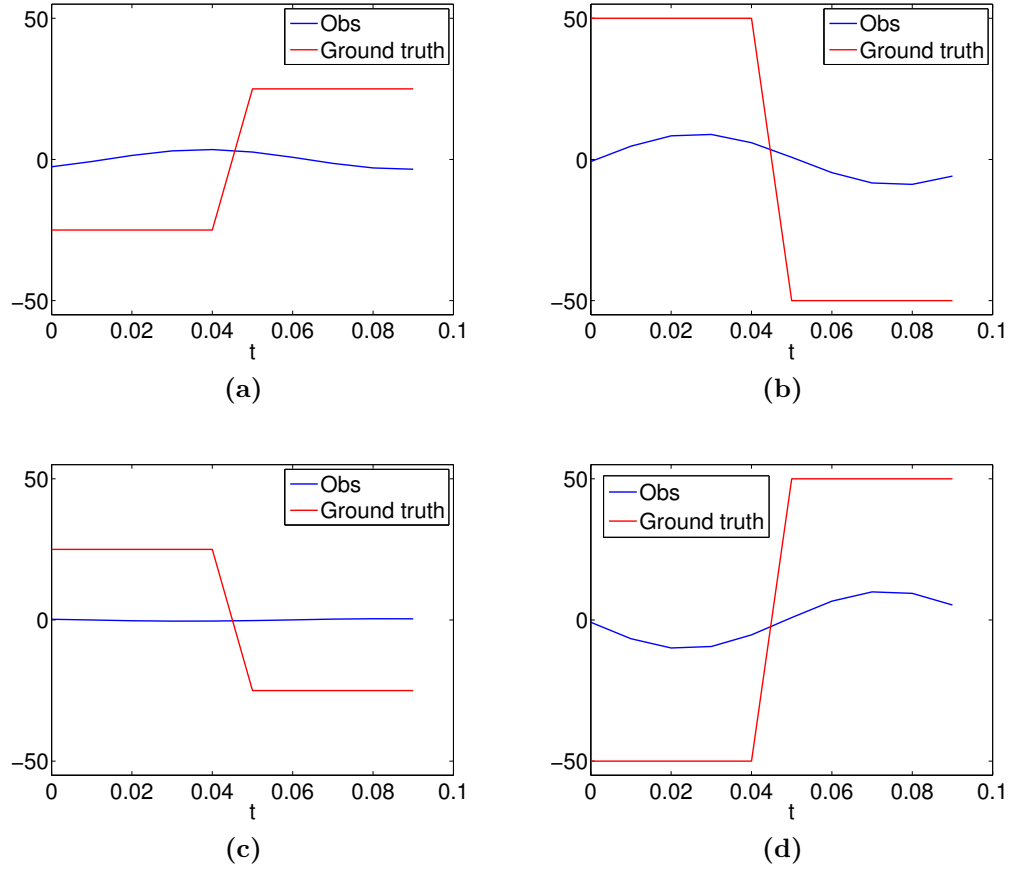
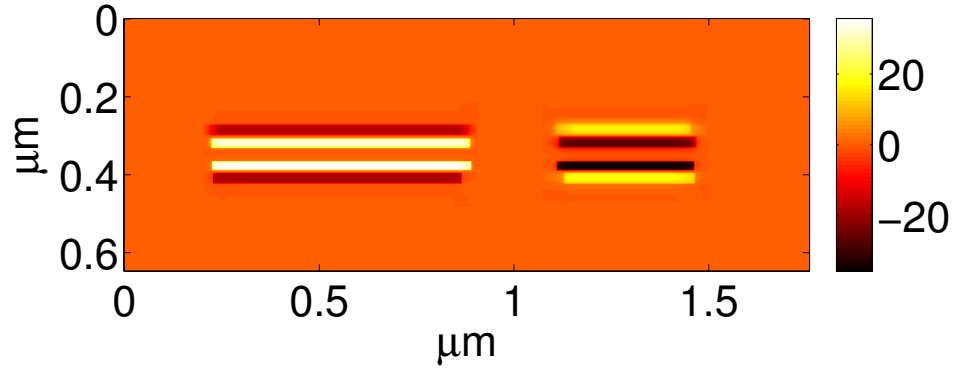
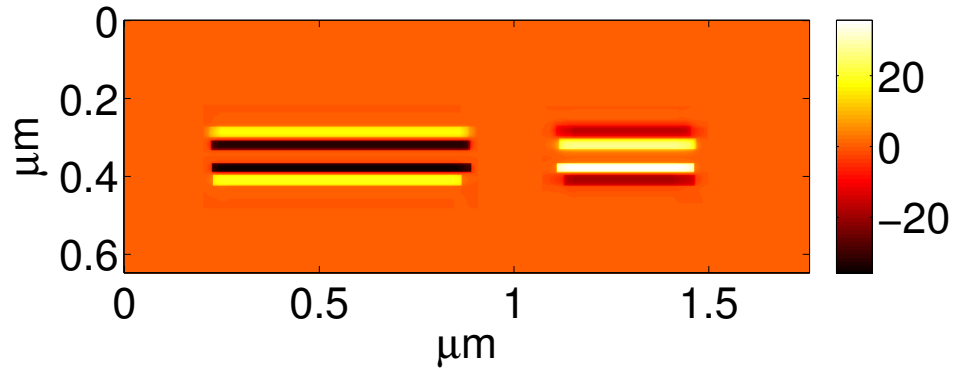


**Figure 6-44:** Observed modulations (Fourier series expansion of 1 harmonic) over time at a single scan position: (a) p-type drain, (b) p-type gate, (c) n-type drain, (d) n-type gate for  $y$ -polarized input light.



(a)



(b)

**Figure 6.45:** Amplitude of the reconstructed modulation (using all 5 harmonics) for all scan positions (a) at time  $t = 0.02$  (b) at time  $t = 0.07$ .



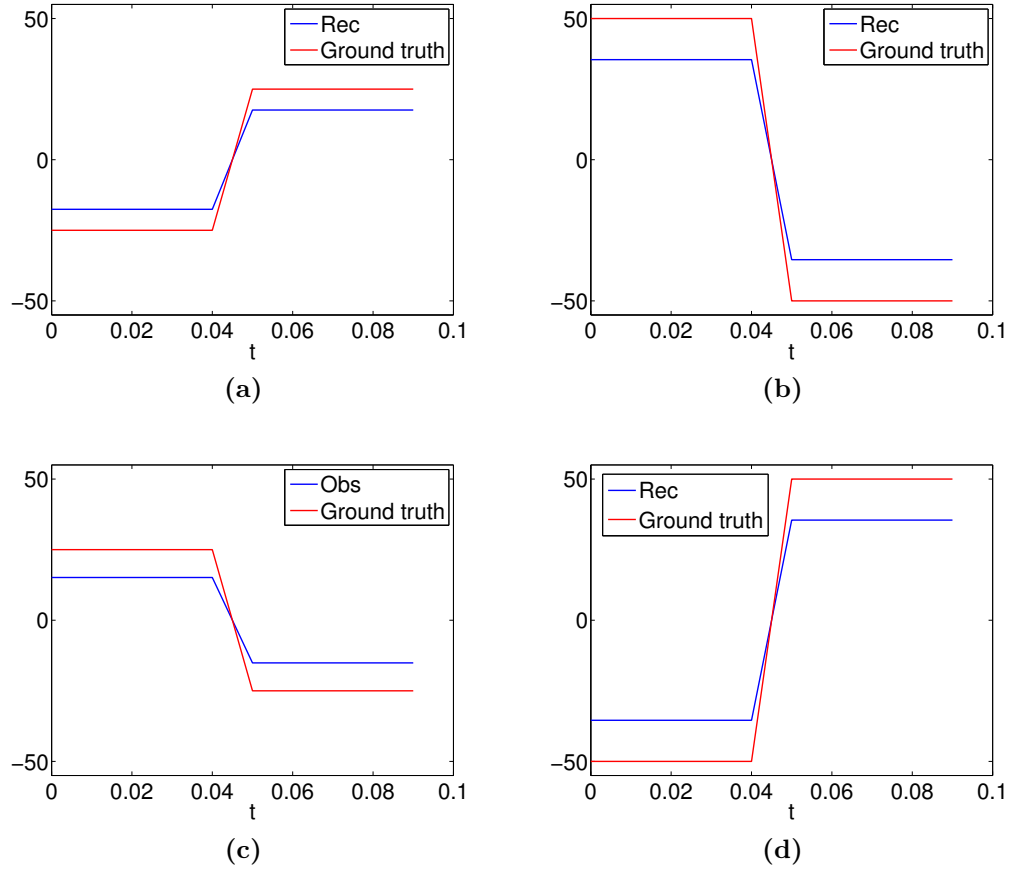
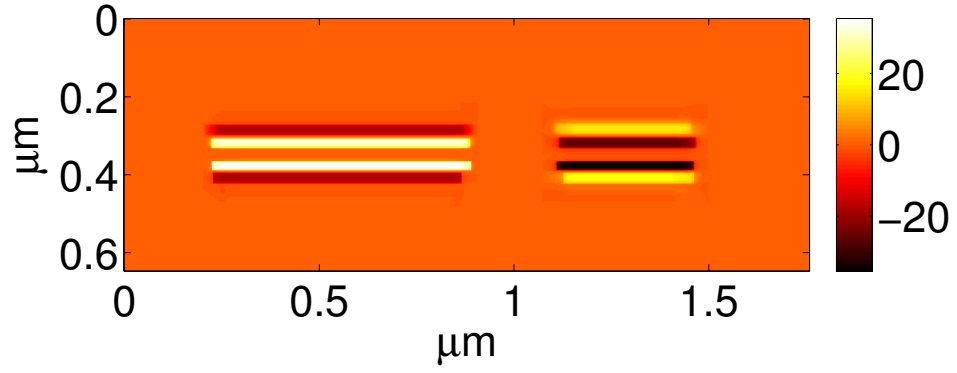
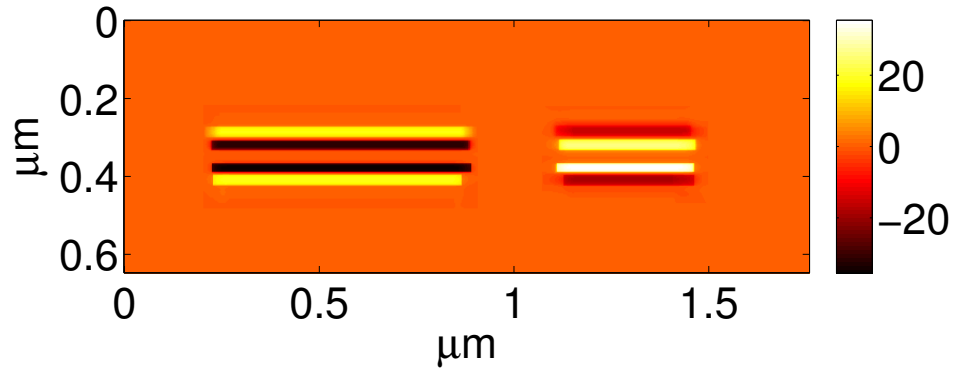


**Figure 6-46:** Reconstructed modulation (using all 5 harmonics) over time at a single scan position: (a) p-type drain, (b) p-type gate, (c) n-type drain, (d) n-type gate.



(a)



(b)

**Figure 6-47:** Amplitude of the reconstructed modulation (using only first 3 harmonics) for all scan positions (a) at time  $t = 0.02$ , (b) at time  $t = 0.07$ .

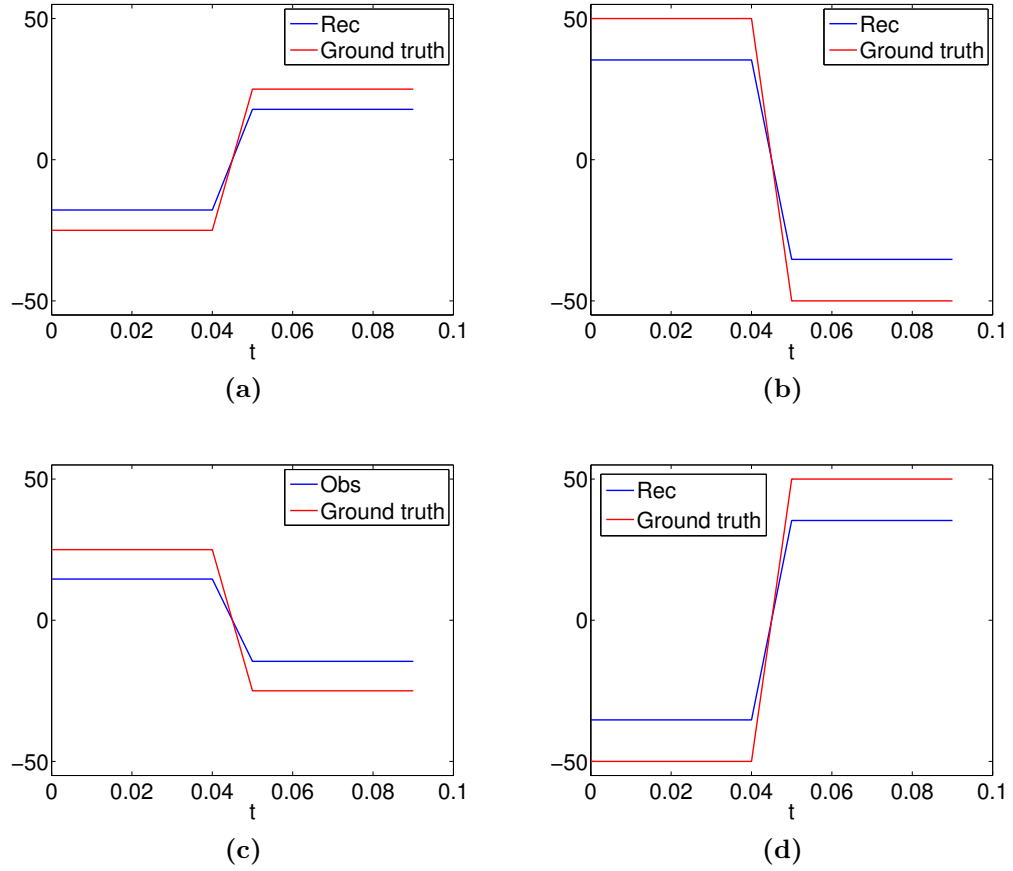
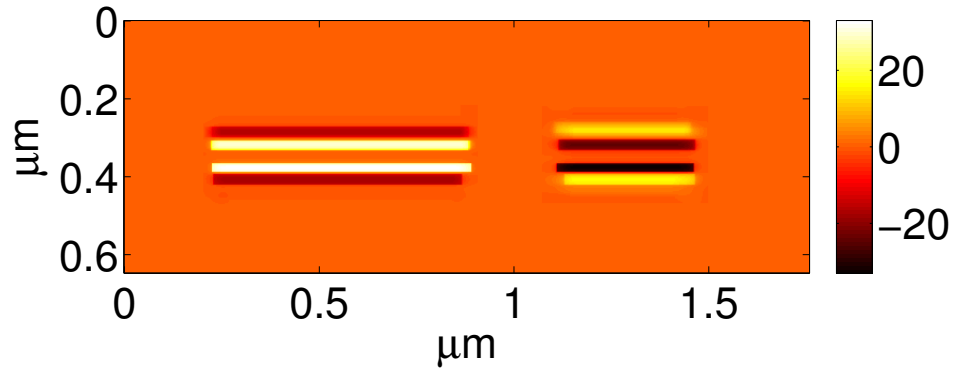
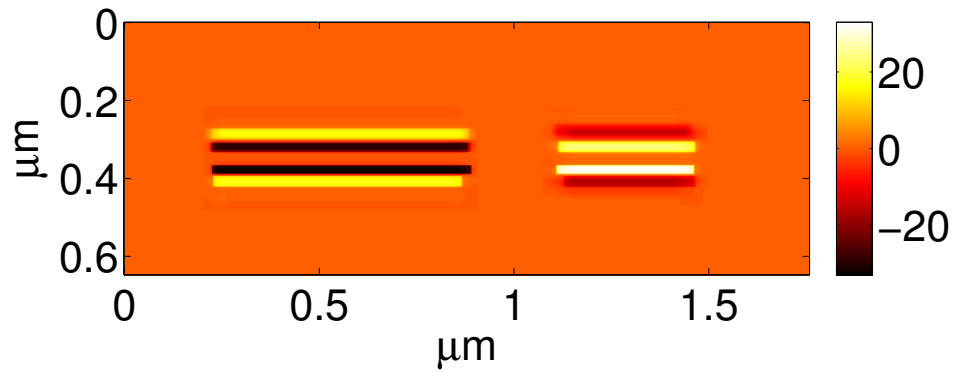


**Figure 6-48:** Reconstructed modulation (using only first 3 harmonics) over time at a single scan position: (a) p-type drain, (b) p-type gate, (c) n-type drain, (d) n-type gate.



(a)



(b)

**Figure 6-49:** Amplitude of the reconstructed modulation (using only first harmonic) for all scan positions (a) at time  $t = 0.02$ , (b) at time  $t = 0.07$ .

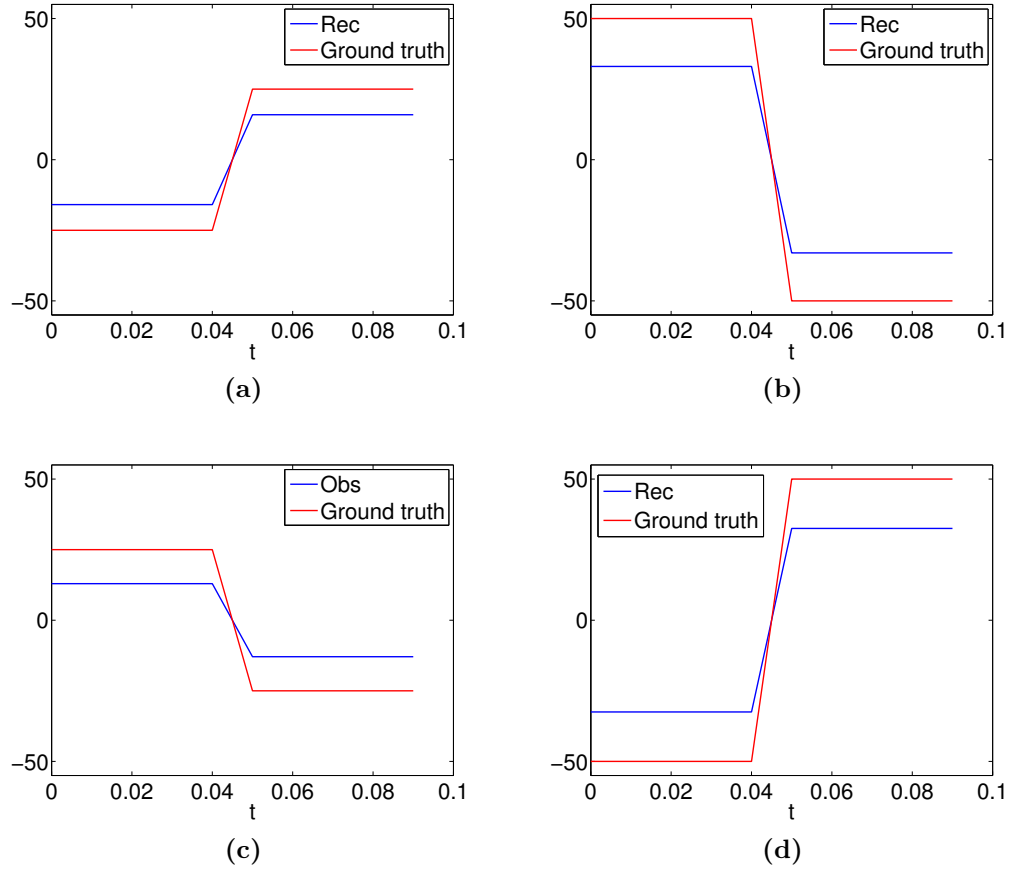


**Figure 6.50:** Reconstructed modulation (using only first harmonic) over time at a single scan position: (a) p-type drain, (b) p-type gate, (c) n-type drain, (d) n-type gate.

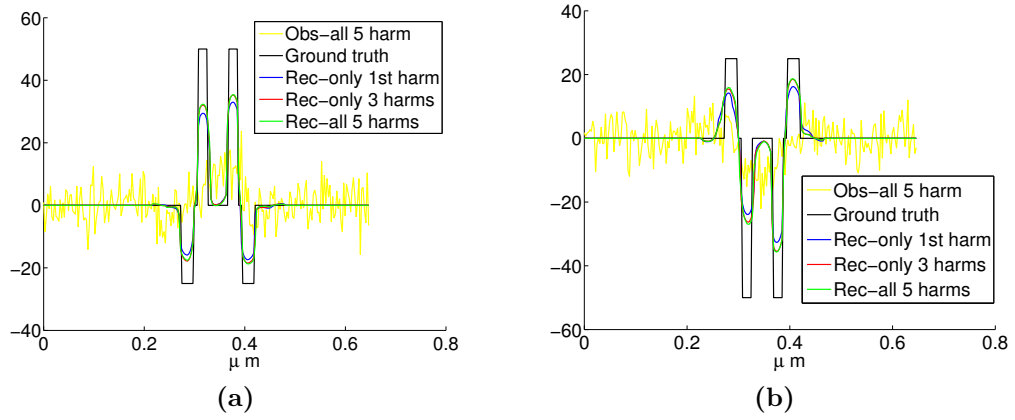


**Figure 6.51:** Comparison of vertical cross sections of all scan positions data at time point  $t = 0.02$  (a) from p-type transistor (b) from n-type transistor. The cross sections for all 5 harmonics reconstruction and only 3 harmonics reconstruction almost overlap.

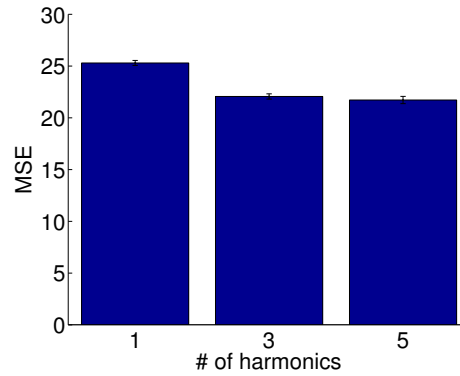
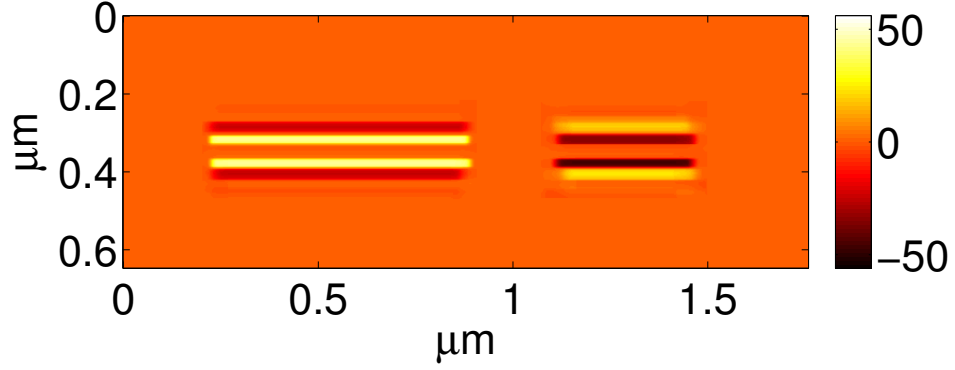


**Figure 6.52:** The mean MSE for the reconstruction amplitude at all scan positions at time point  $t = 0.02$  and  $t = 0.07$

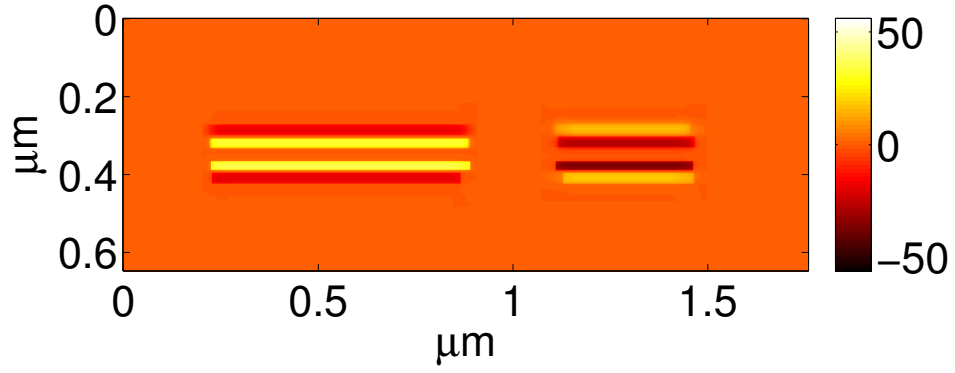
### 6.3.1 Comparison of space-frequency representation and space-time representation results

In this section, we compare the performance of space-frequency representation and space-time representation. However, the reconstructions are in two different domains and the MSE values are not comparable since the amplitude ranges are different and space-frequency representations are complex-valued. Therefore, we used Fourier series expansion in order to represent the results of space-frequency representation in time domain. Figs. 6-53 and 6-54 compare the amplitudes for all scan positions at times  $t = 0.02$  and  $t = 0.07$  for the reconstructions using all 5 harmonics. Fig. 6-55 compares reconstructed modulations in time at 4 different scan positions. Additionally, vertical cross sections from at  $t = 0.02$  are compared in Fig. 6-56.

Both the sparse space-time representation and the sparse space-frequency representation were able to recover spatial regions where modulations were observed. They are also able to changes in behavior over time. For both methods, the regularization parameter is chosen by an exhaustive search. The best parameter is chosen as the one giving the best best resolution qualitatively. In order to assess localization accuracy of time modulation, we clustered scan positions into 3 different regions with different time behavior: no modulation (non-active regions), rectangular pulse with phase 0 and rectangular pulse with phase  $\pi$ . We used k-means clustering technique (Späth, 1985). We also clustered the raw simulated LVI data in order to show the increase in localization accuracy through the proposed sparse representation. The underlying true clusters are shown in Fig. 6-57. The clustering results for LVI data are shown in Figs. 6-58. The clustering results for sparse representations are given in Fig. 6-59. We also calculated a localization accuracy metric defined as the percentage of the number of scan positions with the wrong cluster label divided by the total number of scan positions. The bar plot in Fig. 6-60 compares the localization error for



(a)

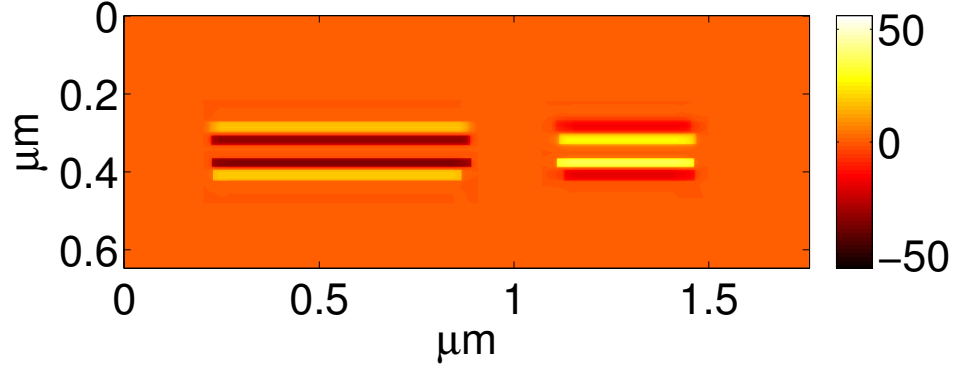


(b)

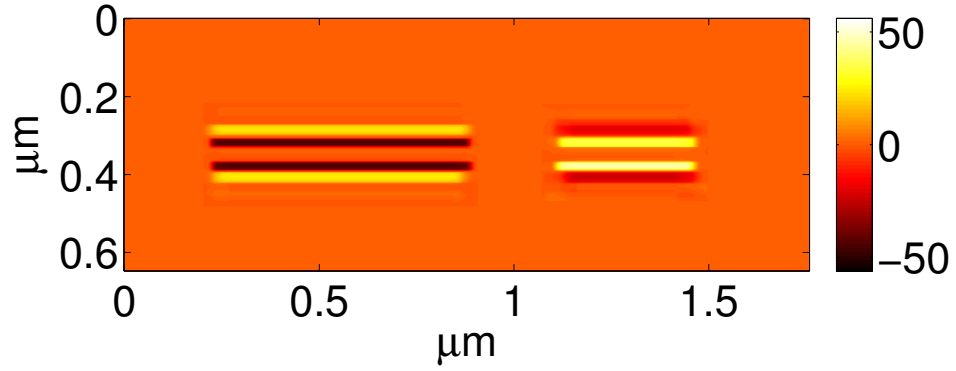
**Figure 6-53:** Comparison of amplitudes of the reconstructed modulation for all scan positions at time  $t = 0.02$  (a) space-time representation (b) space-frequency representation

raw LVI observation data, sparse space-time representation results and sparse space-frequency representation results. The error bars are calculated over 10 realizations. The localization accuracy of the both representations are on the same level showing a significant increase in localization accuracy compared to LVI observation data. For an inverter, there are only 3 clusters for modulation behavior in time. However, for more complex circuit element, the number of clusters can be higher. Even though increasing the number of harmonics does not have higher localization accuracy for the inverter, for a more complex elements increasing number of harmonics might be





(a)



(b)

**Figure 6-54:** Comparison of amplitudes of the reconstructed modulation for all scan positions at time  $t = 0.07$  (a) space-time representation (b) space-frequency representation

required to increase localization accuracy.

We should also point out that the computation time and memory requirements is independent of number of harmonics used for space-time representation. However, using fewer number of harmonics in space-frequency representation also decreases the computation time and the memory requirement, because the size of the observation data and the overcomplete dictionary decreases.

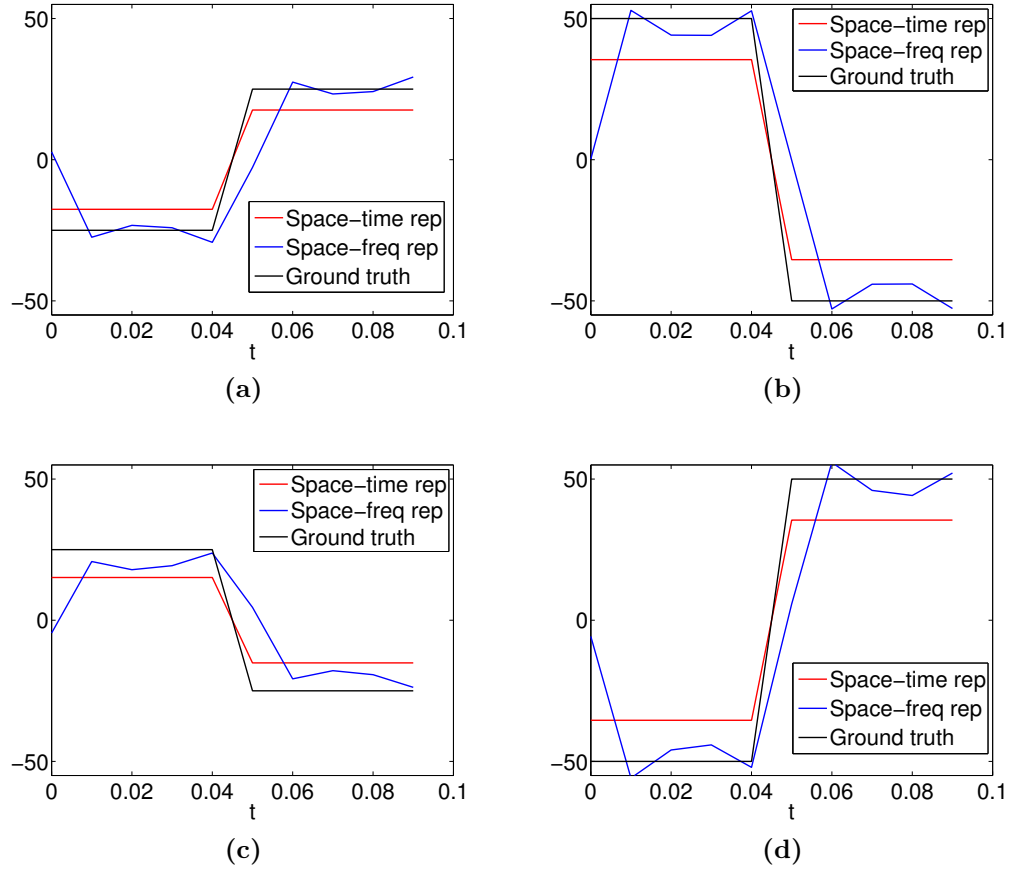


**Figure 6.55:** Comparison of the reconstructed modulations over time at a single scan position: (a) p-type drain, (b) p-type gate, (c) n-type drain, (d) n-type gate.

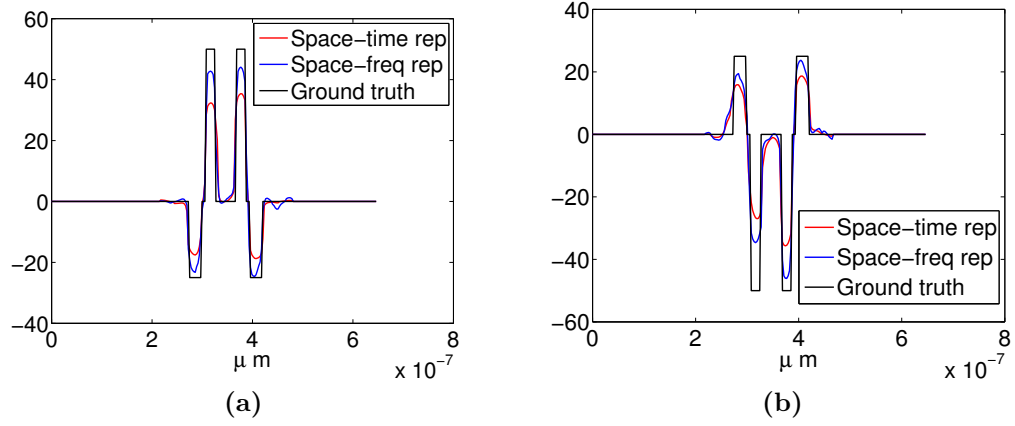


**Figure 6-56:** Comparison of vertical cross sections of all scan positions at time  $t = 0.02$ : (a) p-type transistor, (b) n-type transistor.

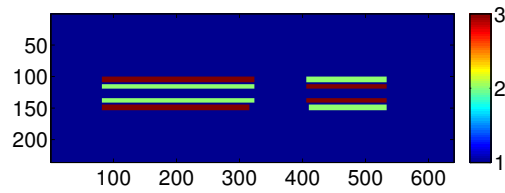


**Figure 6-57:** True cluster labels for the underlying modulation

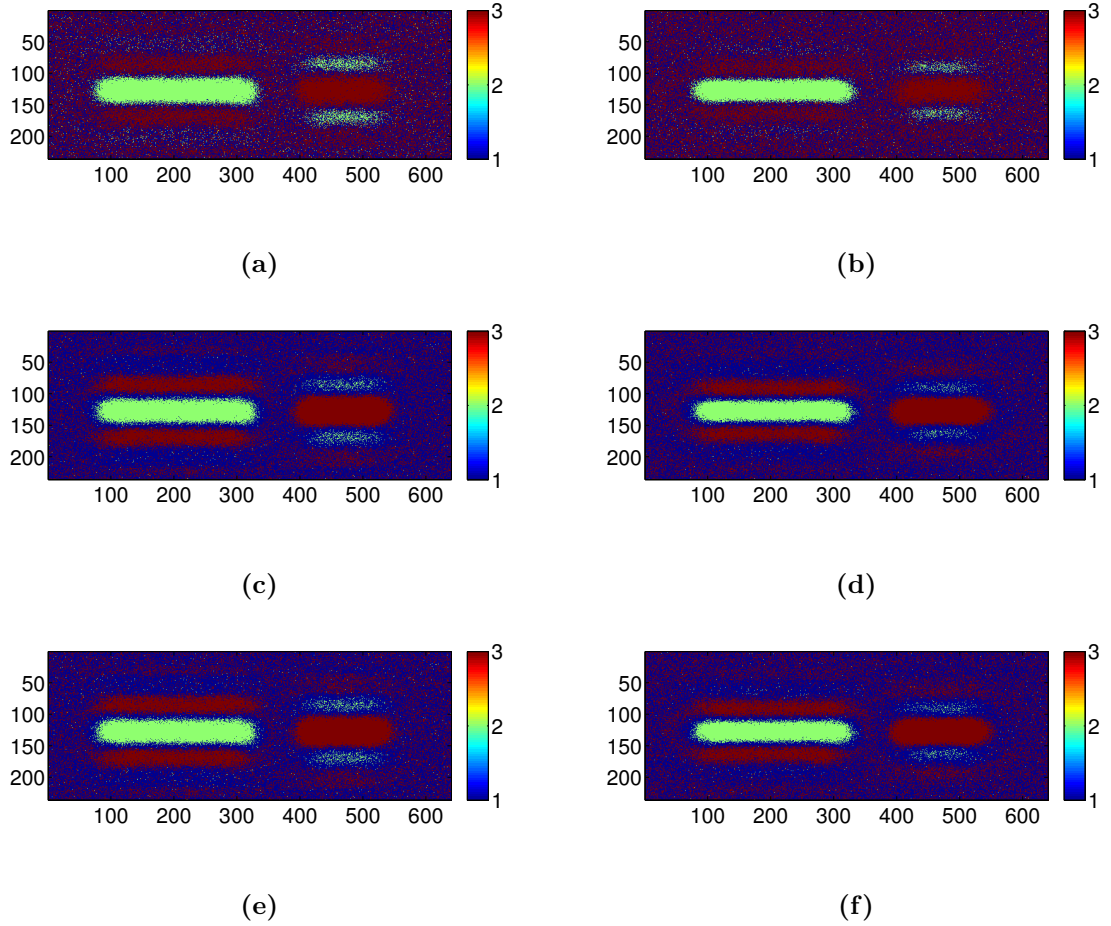


**Figure 6.58:** Cluster labels of LVI data under linearly-polarized light in  $x$ -direction: (a) 5 harmonics (c) 3 harmonics (e) 1 harmonic, under linearly-polarized light in  $y$ -direction: (b) 5 harmonics (d) 3 harmonics (f) 1 harmonic

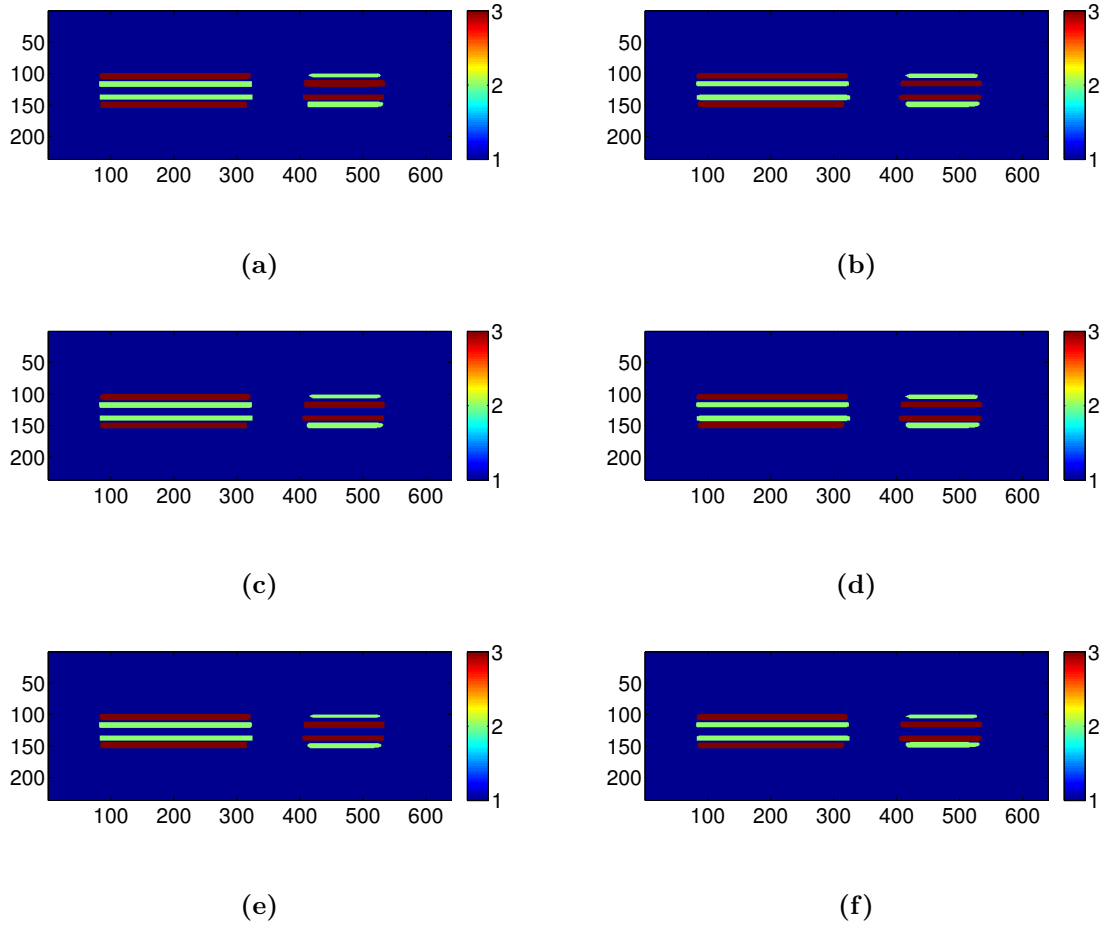


**Figure 6.59:** Cluster labels for sparse space-time representation: (a) 5 harmonics (c) 3 harmonics (e) 1 harmonic, sparse space-frequency representation: (b) 5 harmonics (d) 3 harmonics (f) 1 harmonic.

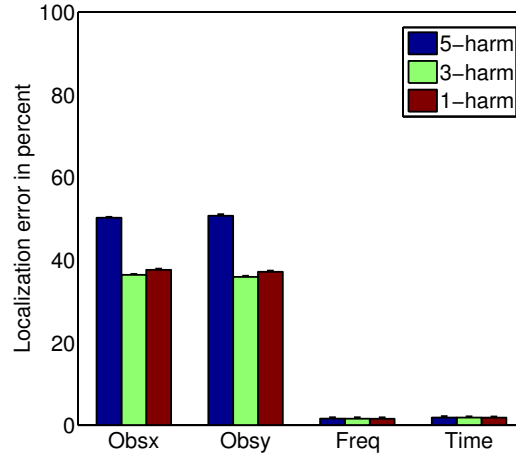


**Figure 6-60:** Comparison of localization accuracy

## 6.4 Conclusion

In this chapter, sparse space-frequency and space-time representations based on over-complete dictionaries were proposed in order to increase spatial resolution and localization accuracy of optical measurements of device activity, specifically LVI measurements. The proposed framework was validated on simulated data. The sparse representation enables recovery of different regions with different time signatures. Scan positions can be clustered into regions with different time behavior using the reconstruction results of sparse representation whereas clustering results using LVI measurements without sparse representation does not produce accurate cluster labels. Localization accuracy for the two sparse representations, space-time and space-frequency, was almost equivalent.

## Chapter 7

# Application of resolution enhancement techniques to dark-field subsurface microscopy of integrated circuits

The highest possible resolution is achieved by imaging through the silicon substrate using aSILs with effective NA approaching the index of the substrate ( $NA \cong 3.5$ ) (Köklü et al., 2008). One important property at high NA is that the reflected light from the silicon-dielectric interface is comparable in magnitude to the scattered light from small objects in the dielectric medium, resulting in low-contrast images. In order to increase the contrast of images, a polarization-sensitive dark-field microscopy has been proposed and modeled that successfully suppresses the strong background reflection and increases both contrast and resolution (Yurt et al., prep).

We can use sparse image reconstruction techniques to recover spatial high-frequency information from low-resolution observations. We proposed frameworks applying these techniques to high-NA microscopy images in Chapters 4 and 5. These frameworks combine prior knowledge about ICs with physics-based optical forward model and recover spatial high-frequency information, which is typically lost in low-resolution observations. In this chapter, we propose a signal processing framework in order to estimate the PSF of dark-field subsurface microscopy system from observation data because for dark-field subsurface microscopy the PSF model is different than regular subsurface microscopy. We incorporate this PSF into an image reconstruction framework, which can be formulated using two different image reconstruction techniques,

an analysis-based sparsity paradigm from Chapter 4 and a synthesis-based sparsity paradigm using overcomplete dictionaries from Chapter 5. Both of these techniques take advantage of the prior knowledge about ICs. We demonstrate on experimental data that the synthesis-based image reconstruction provides better image enhancement and higher resolution than the analysis-based based image reconstruction.

## 7.1 Dark-field subsurface microscopy for integrated circuits

The goal of dark-field subsurface microscopy is to increase resolution and contrast by suppressing the strong background reflection. An aSIL confocal microscope is modified by adding a linear polarizer and a quarter wave plate prior to the objective lens to allow us to selectively filter the background light that has specularly reflected from the dielectric interface of silicon and the low-index medium (see Fig. 7.1). This simple implementation of the polarization-sensitive optics allows one to virtually eliminate the background signal creating a dark-field image. Fig. 7.2 shows a comparison of a typical confocal and corresponding dark-field subsurface confocal microscope image of aluminum lines fabricated on a double-side polished silicon wafer. In the typical case, there is a strong reflection from the background, which significantly diminishes the visibility of features as shown in Fig. 7.2a . In the dark-field case, the specularly-reflected circularly-polarized light is filtered after traversing the quarter wave plate and linear polarizer. The resulting image is largely free of background and the visibility of the small features is enhanced significantly. We advance this technique by applying image reconstruction algorithms developed earlier in this thesis to background-suppressed subsurface images.



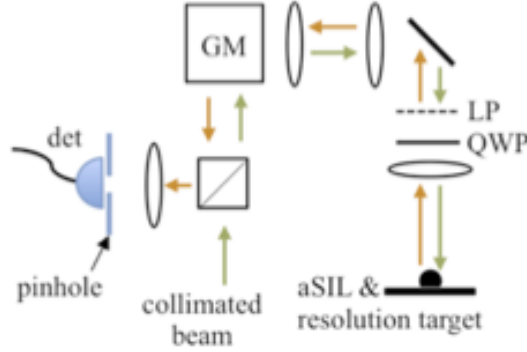


**Figure 7.1:** Confocal microscope setup. (Collimated beam from  $1310nm$  laser; GM galvanometric mirror; LP linear polarizer; QWP quarter-wave plate; aSIL aplanatic solid immersion lens; pinhole is  $10nm$ )

## 7.2 Image reconstruction framework

The image reconstruction framework is composed of two steps. The first step involves the estimation of the PSF of the system from observed images since the PSF for dark-field subsurface microscopy is different from the one for regular subsurface microscopy. In the second step, we formulate an image reconstruction formulation using the estimated PSF in a linear forward model together with regularizers that incorporate prior information about the features of interest.

Two different formulations are proposed according to how prior knowledge about the integrated circuits is incorporated into image reconstruction. The first formulation, used in Chapter 4, assumes that IC images are sparse and they are composed of piecewise-constant regions. This assumption relies on ICs being composed of small lines and small rectangular structures. We can incorporate this information into the reconstruction by means of non-quadratic regularization functionals in the image reconstruction formulation. Therefore, we can preserve the sparsity and the edges of the underlying features.

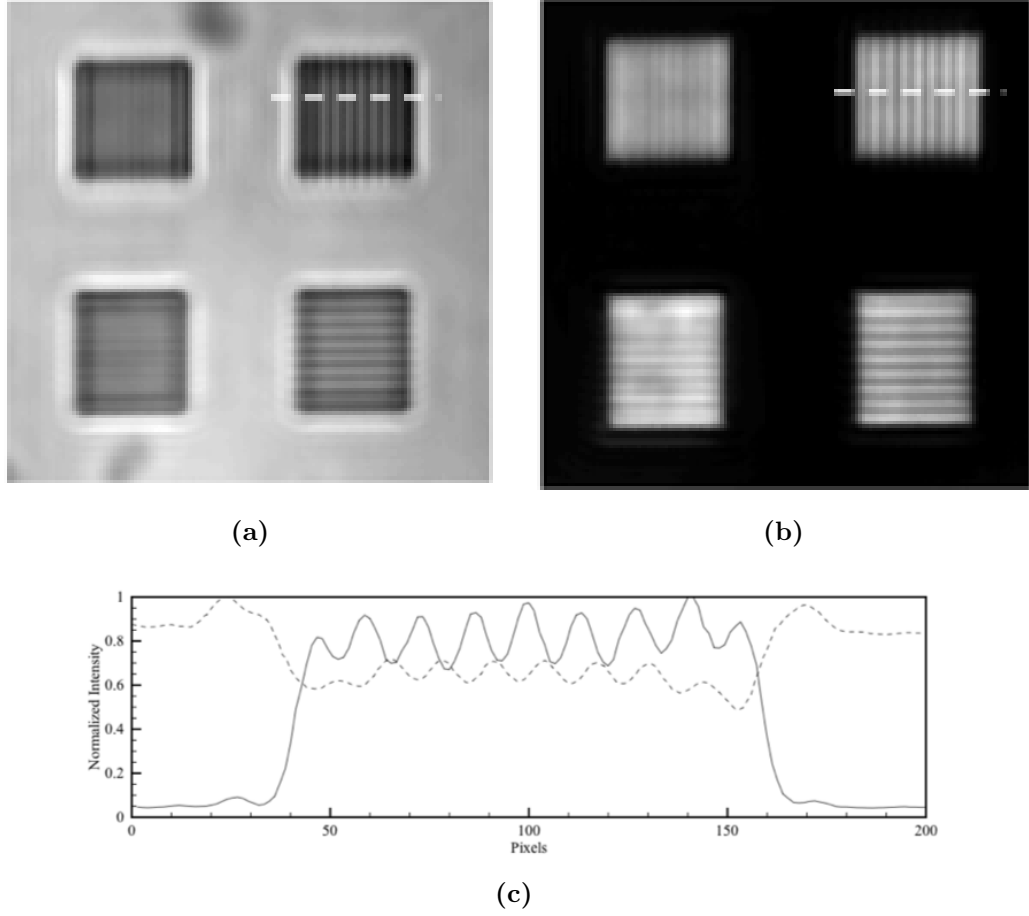


**Figure 7.2:** (a) Metal lines separated by  $252nm$ ,  $282nm$  on a resolution target, imaged using  $1310nm$  circular polarization without linear polarizer in the return path. (b) The same set of metal lines imaged with a linear polarizer and quarter wave plate in place. (c) The intensity profile corresponding to dashed lines in (a) and (b). The dashed line is for circularly-polarized illumination, and the solid line is for the case of linear polarizer and quarter wave plate inserted (b).

Our second approach uses CAD layouts in order to build an overcomplete dictionary of rectangular building blocks, which vary in their size and in location. This dictionary can be incorporated into a sparse image reconstruction as proposed in Chapter 5.

### 7.2.1 PSF Estimation and Observation Model



**Figure 7-3:** Locations of cross sections used to estimate the LSF of the system.

In this section, we explain how we estimate the PSF of the optical system and how we employ this PSF in order to formulate an optical forward model. The cross sections, as seen in Fig. 7-3, along the lines from the center part can be used in order to estimate the Line Spread Function (LSF) of the system. We collect multiple cross sections from different lines in the observation and we fit a spline to the average of these cross sections using a least squares spline approximation. The derivative of this estimated function will give us the estimated Line Spread Function of the system. However, since the lines are thin, boundary effects result in spurious artifacts in the waist of the estimated LSF. In order to filter these imperfections out, we approximate the LSF with an Airy disk. We use this as is the estimated 1D PSF and since the system can be assumed to be isotropic, this airy disk can be rotated to obtain the 2D PSF of the system.

The assumed linear observation model of the system becomes:

$$g(x, y) = \hat{h}(x, y) * f(x, y), \quad (7.1)$$

where  $g(x, y)$  is the observed intensity,  $f(x, y)$  is the intensity of the underlying object,  $*$  denotes the convolution operation, and  $\hat{h}(x, y)$  is the estimated PSF of the optical system.

In practice, the data we collect is discretized in spatial coordinates on a uniformly-spaced grid and Eq. 7.1 becomes:

$$\mathbf{g} = \hat{H}\mathbf{f}, \quad (7.2)$$

where  $\mathbf{g}$  is a vector of discretized observation data,  $\mathbf{f}$  is the discrete underlying object image,  $\hat{H}$  is the Toeplitz matrix that implements convolution as a matrix operation based on the estimated PSF.

### 7.2.2 Image reconstruction based on non-quadratic regularization

The underlying features in ICs have smooth, homogeneous and sparse structure. This preliminary knowledge can be incorporated into the reconstruction by employing non-quadratic regularization functionals. The image reconstruction based on non-quadratic regularization can be formulated as the following optimization problem:

$$\mathbf{f} = \arg \min_{\mathbf{f}} J(\mathbf{f}), \quad (7.3)$$

where

$$J(\mathbf{f}) = \|\hat{H}\mathbf{f} - \mathbf{g}\|_2^2 + \lambda_1 \|D\mathbf{f}\|_1 + \lambda_2 \|\mathbf{f}\|_1, \quad (7.4)$$

where  $D$  is the discrete approximation to the gradient operator that computes first-order image differences in horizontal and vertical directions. The second and third terms in Eq. 4 are regularizers that favor sparsity in the edge field of the reconstructed image and the recovery of small scatterers, respectively. The optimization problem in

Eq. 4 is solved using the quasi-Newton method developed in (Çetin and Karl, 2001) and explained more detail in Chapter 4.

### 7.2.3 Dictionary-based image reconstruction

The structures in ICs consist of flat regions consisting of horizontal and vertical lines of constrained and varying width and length. The width and length of these lines are easily derivable from CAD layouts. Therefore, the application of overcomplete dictionaries in an image reconstruction framework becomes particularly suitable for IC imaging domain. We can construct an overcomplete dictionary from building blocks derived from CAD layouts. These building blocks are rectangles of varying width and length and all possible locations of these rectangles are included into the dictionary. More detail about how to build this dictionary is explained in Section 5.1.3.

Given such a scene dictionary  $\Phi$ , the unknown underlying scene  $\mathbf{f}$  can be represented as:

$$\mathbf{f} = \Phi\boldsymbol{\eta}, \quad (7.5)$$

where  $\Phi$  is the appropriate overcomplete dictionary and  $\boldsymbol{\eta}$  is the vector of representation coefficients. Now, we can estimate the underlying IC scene by solving the following optimization problem:

$$\hat{\boldsymbol{\eta}} = \arg \min_{\boldsymbol{\eta}} \|\hat{H}\Phi\boldsymbol{\eta} - \mathbf{g}\|_2^2 + \lambda\|\boldsymbol{\eta}\|_1, \quad (7.6)$$

where  $\lambda$  is a regularization parameter that determines the overall level of problem sparsity. We are using the interior point algorithm (Kim et al., 2007) in order to solve the optimization problem. The estimated underlying scene will then be:

$$\hat{\mathbf{f}} = \Phi\hat{\boldsymbol{\eta}}. \quad (7.7)$$

### 7.3 Experimental results

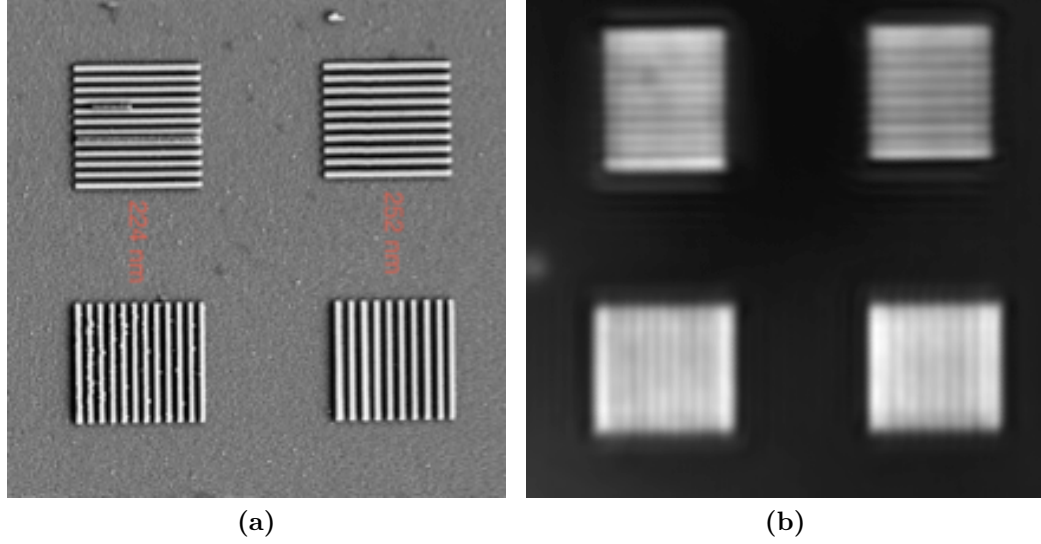


**Figure 7.4:** (a) SEM image of metal aluminum lines separated by  $252nm$  (right) and  $224nm$  (left), and fabricated on a double-side polished silicon wafer, (b) dark-field subsurface microscopy image.

In Fig. 7.4, the dark field subsurface microscopy image of a resolution target and its corresponding SEM image are shown. The resolution target is composed of metal aluminum lines separated by  $252nm$  and  $224nm$ , and fabricated on a double-side polished silicon wafer. The average of cross sections from center parts of lines and the least-squares spline approximation of this average are shown in Fig. 7.5a. The derivative of this spline approximation gives us the estimated LSF of the system, which is shown in Fig. 7.5b. However, since the lines are thin, at the end of the lines we observe boundary effects and this causes errors at the waist of the LSF. Therefore, we fit an Airy disk to this estimated LSF (Fig. 7.5b). We also note that, we make the estimated LSF symmetric by averaging right and left sides. The estimated PSF of the system, which is obtained by rotating this 1D Airy disk, is shown in Fig. 7.6.

The next step is to incorporate this PSF into our two image reconstruction frameworks in order to improve the resolution and quality of the observed image. In Figs.

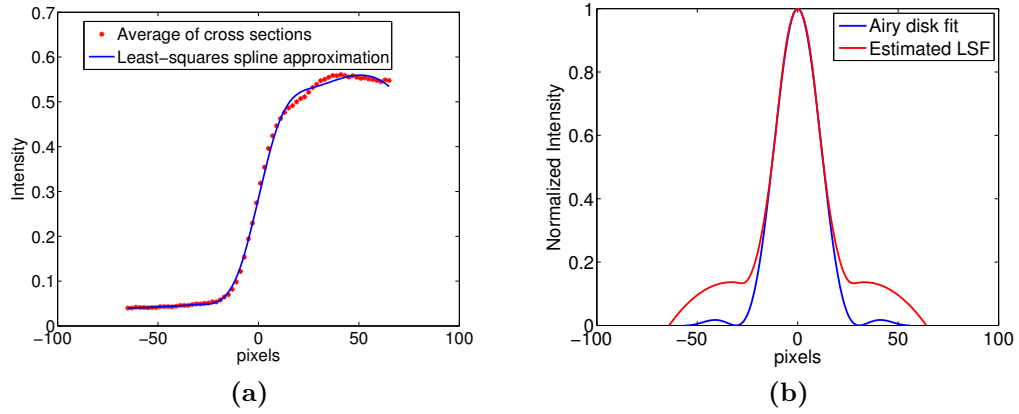


**Figure 7.5:** (a) Average of cross sections from the center of lines and a least-squares spline approximation to this average (b) The estimated LSF which is the derivative of the least-squares spline approximation and the airy disk fit to this estimated LSF

7.7, 7.8 and 7.9, we show the observation and the results of two image reconstruction techniques for  $252nm$  spaced vertical lines, for  $224nm$  spaced vertical lines and for  $224nm$  spaced horizontal lines, respectively. Both techniques appear to improve the resolution of observation data. For the  $252nm$  case, there are 10 lines. Though these lines are sharper and clearer in the reconstruction results. For the  $224nm$  case, there are 12 lines but we cannot see them all in the observation. In the reconstruction results of the  $224nm$  spaced vertical lines, we can clearly count 12 separate lines. This shows that we improve not only edge resolution, but we also improve localization accuracy. We can see in the SEM data that there are some fabrication imperfections in  $224nm$  spaced horizontal lines. For this reason, we could not recover all 12 lines after image reconstruction of  $224nm$  spaced horizontal lines. However, the location of the fabrication default actually corresponds to the blurred region in the dictionary-based image reconstruction of  $224nm$  spaced horizontal lines. One of the resolution metrics used for IC Imaging is a Sparrow resolution criterion. The Sparrow criterion defines the resolution as the distance between the peaks of the two point sources when the

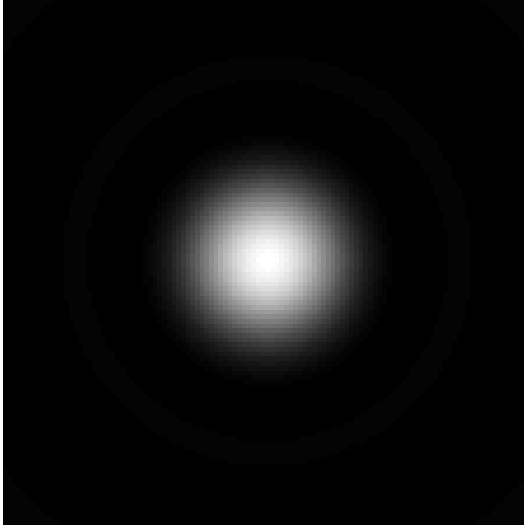


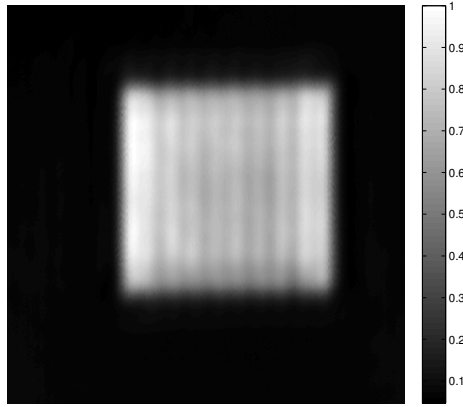
**Figure 7-6:** The estimated PSF of the system

midpoint just becomes visible. Similarly, we can evaluate if a resolution structure is resolved or not, in other words, if a structure is localized or not, depending on whether we observe a peak. We are able to observe exact number of peaks in lines with  $224nm$  spacing after resolution improvement while exact number of peaks was observed in lines with  $252nm$  spacing for experimental data. This shows at least 12 % resolution improvement.

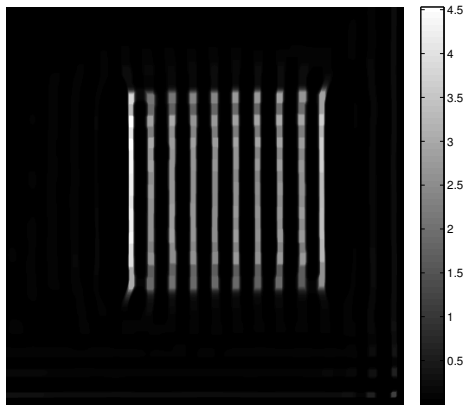
## 7.4 Conclusions

In this chapter, we applied image reconstruction to improve the resolution of dark-field subsurface microscopy. We applied two different sparse image reconstruction techniques with different levels of assumed prior knowledge - an image reconstruction based on non-quadratic regularization and a dictionary-based image reconstruction. Both techniques provide at least 12 % resolution improvement; we are able to localize lines with  $224nm$  spacing after resolution improvement while lines with  $252nm$  spacing

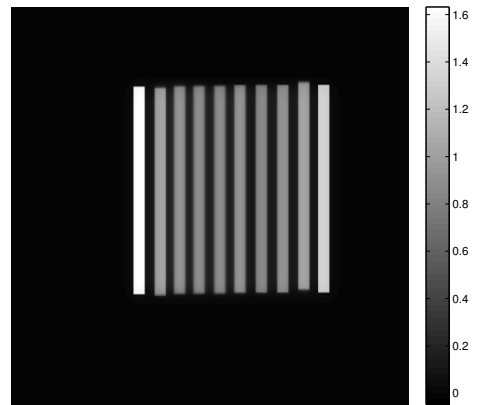




(a)

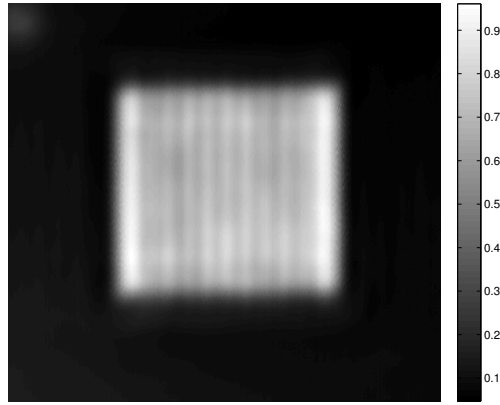


(b)

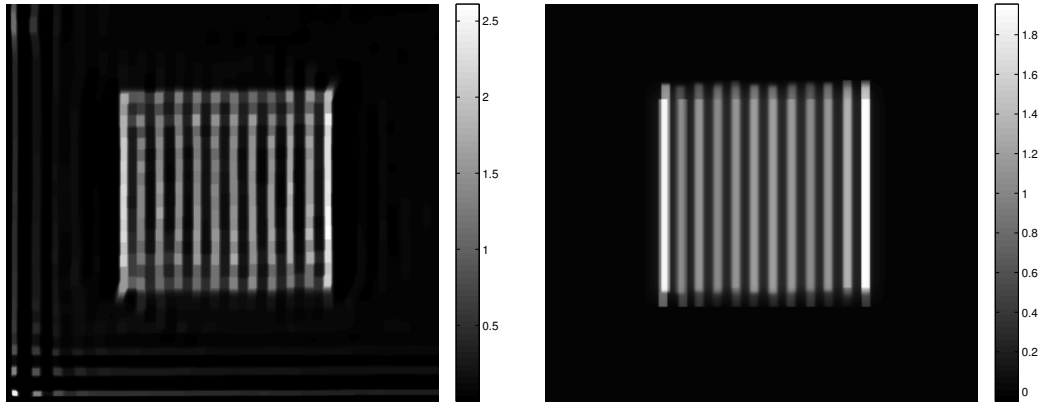


(c)

**Figure 7.7:** 252nm spacing vertical lines: (a) observation, (b) image reconstruction result based on non-quadratic regularization, (c) dictionary-based image reconstruction result.



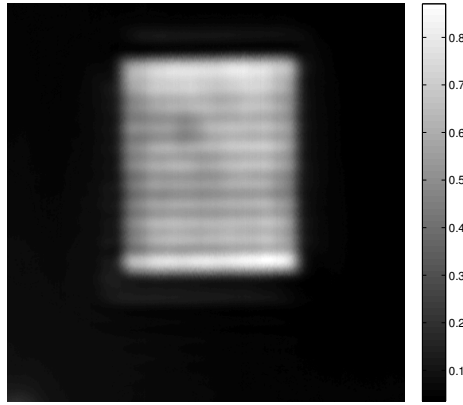
(a)



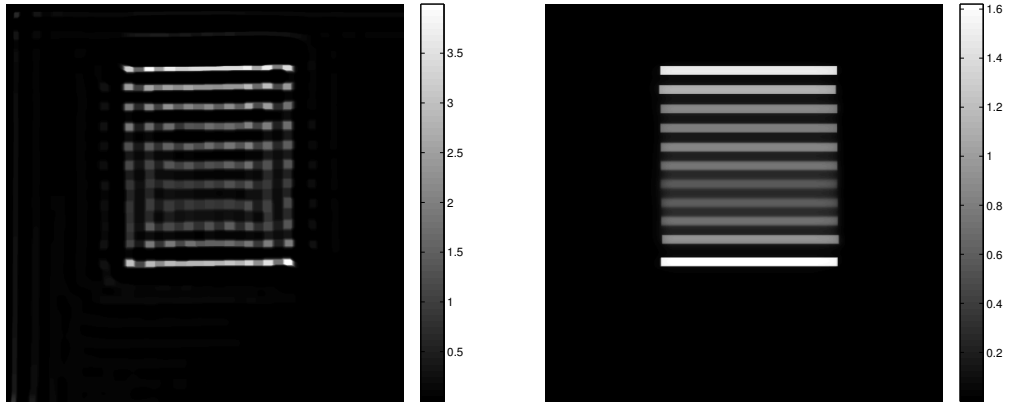
(b)

(c)

**Figure 7.8:** 224nm spacing vertical lines: (a) observation, (b) image reconstruction result based on non-quadratic regularization, (c) dictionary-based image reconstruction result.



(a)



(b)

(c)

**Figure 7.9:** 224nm spacing horizontal lines: (a) observation, (b) image reconstruction result based on non-quadratic regularization, (c) dictionary-based image reconstruction result.

are at the limit of localization in experimental data. However, dictionary-based image reconstruction provides higher edge resolution and maintains the homogeneity of the intensity within the structures.

## Chapter 8

# Focus determination for high NA subsurface imaging of integrated circuits

The interface effects in high-NA focusing of linearly-polarized light has been studied in (Koklu and Unlu, 2009) and it have been shown theoretically and experimentally that the tightest focus on the interface happens at two different longitudinal focuses for two orthogonal polarization directions. When the focus point is changed near the interface along the longitudinal axis, the shape and the support of the focal spot changes. Therefore, the observation images and their resolution also change. Collecting data at multiple-polarization and multiple longitudinal focuses, we can estimate the focus point of collected observation data. In this chapter, we formulate a method in order to identify the focus point of the each data and to identify the point of best focus. In Section 8.1, we explain the focus identification procedure and in Section 8.2 we present preliminary experiments for focus identification.

### 8.1 Focus identification

Using the linear convolutional model, the observations collected at different longitudinal focuses and under linearly-polarized input light with different polarization directions can be expressed as follows:

$$g_{z_0}^j(x, y) = h_{z_0}^j(x, y) * f(x, y), \quad (8.1)$$

where  $g_{z_0}^j(x, y)$  is the observed intensity under linearly-polarized light at polarization direction  $j$  and at longitudinal focus  $z_0$ ,  $f(x, y)$  is the intensity of the underlying object,  $*$  denotes the convolution operation, and  $h_{z_0}^j(x, y)$  is the PSF of the optical system with linearly-polarized input light of polarization direction  $j$  and focused at longitudinal point  $z_0$ .

In practice, when the data are collected, it is discretized in spatial coordinates on a uniformly spaced grid, Eq. 8.1 can be expressed as follows;

$$\mathbf{g}_{z_0}^j = H_{z_0}^j \mathbf{f}, \quad (8.2)$$

where  $\mathbf{g}_{z_0}^j$  is a vector of discretized observation data under linearly-polarized light at polarization direction  $j$  and at longitudinal focus  $z_0$ ,  $\mathbf{f}$  is the discrete underlying object image,  $H_{z_0}^j$  is the Toeplitz matrix that implements convolution as a matrix operation.

Given a set of observation data collected under linearly-polarized light with different polarization direction and at different longitudinal focuses  $\left\{ \{\mathbf{g}_z^j\}_{j=1}^N \right\}_{i=1}^Z$ , we first need to estimate  $z_0$  independently for each set  $\{\mathbf{g}_z^j\}_{j=1}^N$ , in other words we need to register each data set of multiple polarizations at a specific longitudinal focus to one of the theoretically-simulated PSFs corresponding to focuses at different longitudinal points. This can be achieved in two steps. Firstly, the underlying objects corresponding to every simulated PSF for each data set of multiple polarizations  $\{\mathbf{g}_z^j\}_{j=1}^N$  can be estimated by solving the following optimization problem;

$$\forall z, z_0 : \hat{\mathbf{f}}_{z, z_0} = \arg \min_{\mathbf{f}} \sum_{j=1}^N \|\mathbf{g}_z^j - H_{z_0}^j \mathbf{f}\|_2^2 + \|\mathbf{f}\|_2^2, \quad (8.3)$$

where  $z$  is the label of the focus point for the experimental data.

Secondly, the estimated underlying objects will be used to calculate the data fitting error and to register the data to the PSF which gives the least data fitting

error through the following minimization;

$$\forall z : \hat{z}_0 = \arg \min_{z_0} \sum_{j=1}^N \left\| \mathbf{g}_z^j - H_{z_0}^j \hat{\mathbf{f}}_{z,z_0} \right\|_2^2. \quad (8.4)$$

In the following section, we show preliminary focus registration results on experimental aSIL data.

## 8.2 Preliminary focus identification experiment

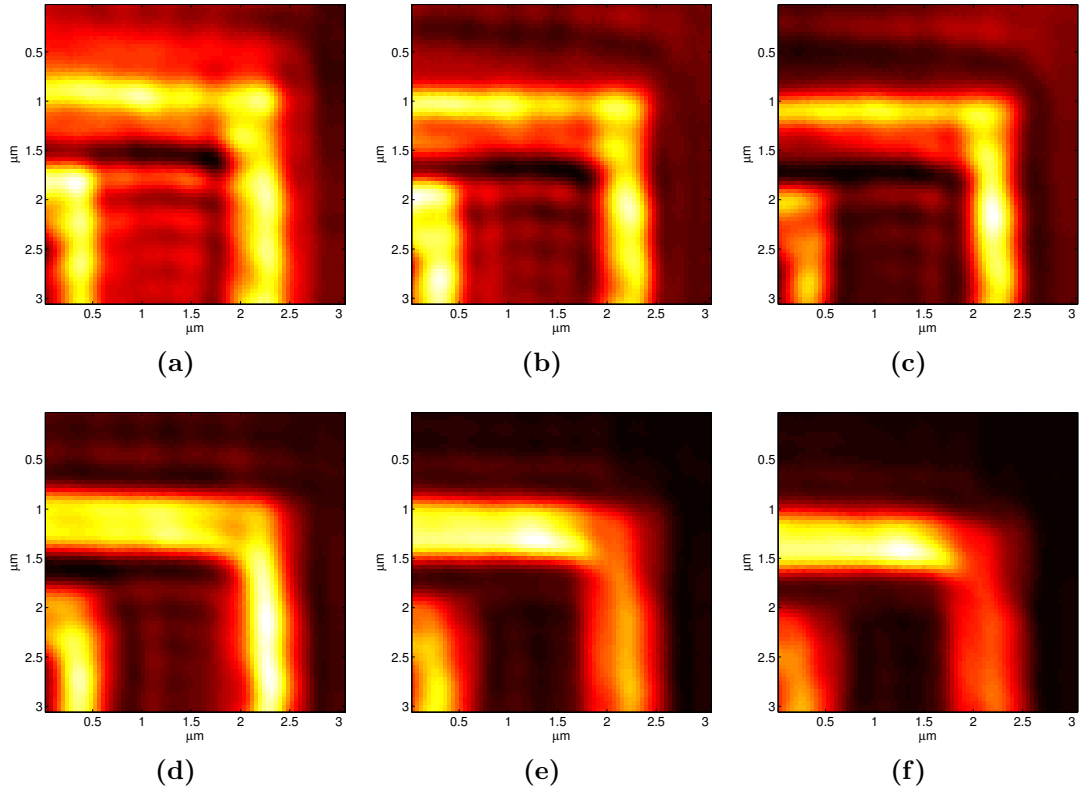


**Figure 8-1:** Examples of experimental observation data under linearly polarized input light with polarization in  $x$ -direction with longitudinal focus point label: (a) 1, (b) 7, (c) 10, (d) 22, (e) 28, (f) 30.

Multiple-polarization and multiple-longitudinal focus data were collected experimentally by moving a sample in longitudinal direction and illuminating it with

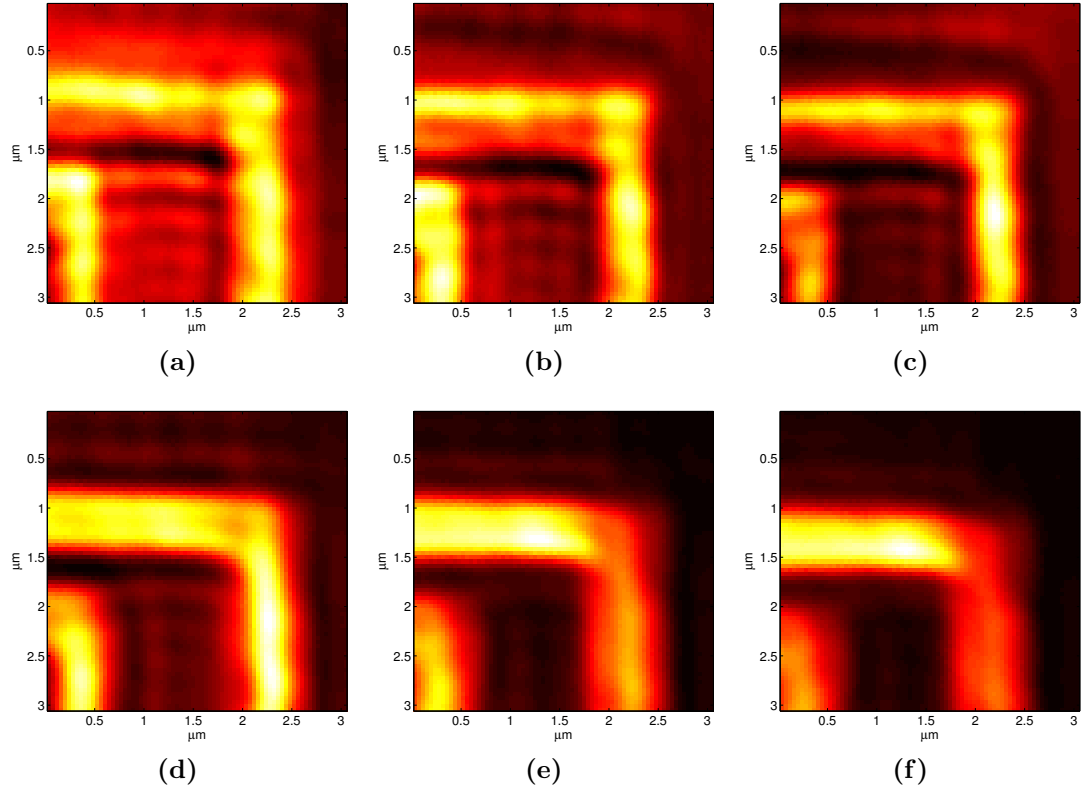


**Figure 8.2:** Examples of experimental observation data under linearly polarized input light with polarization in  $y$ -direction with longitudinal focus point label: (a) 1, (b) 7, (c) 10, (d) 22, (e) 28, (f) 30.

linearly-polarized input light source in  $x$  and  $y$  polarization directions. The structures of interest, where we focus the light, are polysilicon and they are fabricated at a silicon-silicon dioxide interface. Examples of experimental observation images under linearly-polarized light with polarization in  $x$ -direction and  $y$ -direction are shown in Fig. 8.1 and Fig. 8.2, respectively.

PSFs with different longitudinal focuses along the dielectric interface were simulated as explained in Section 3.2.1. The variable  $z_0$  in Eq. 2.45 determines the longitudinal point on the sample where the light is focused. Examples of simulated PSFs for linearly polarized input light in the  $x$ -direction are shown in Fig. 8.3.

The experimental data is registered to simulated PSFs using the procedure ex-



plained in Section 8.1. Fig. 8.4 shows registration results computed by solving the minimization in Eq. 8.4. The  $x$ -axis shows the label for the experimental data and the  $y$ -axis shows the corresponding estimated longitudinal point. We expect a linear behavior in the plot in Fig. 8.4 because the data are collected by varying the focus equally and monotonically along the longitudinal axis. Similarly, the simulated PSFs were calculated by changing  $z_0$  uniformly. Although there are some deviations for certain points, the expected linear behavior can be observed.

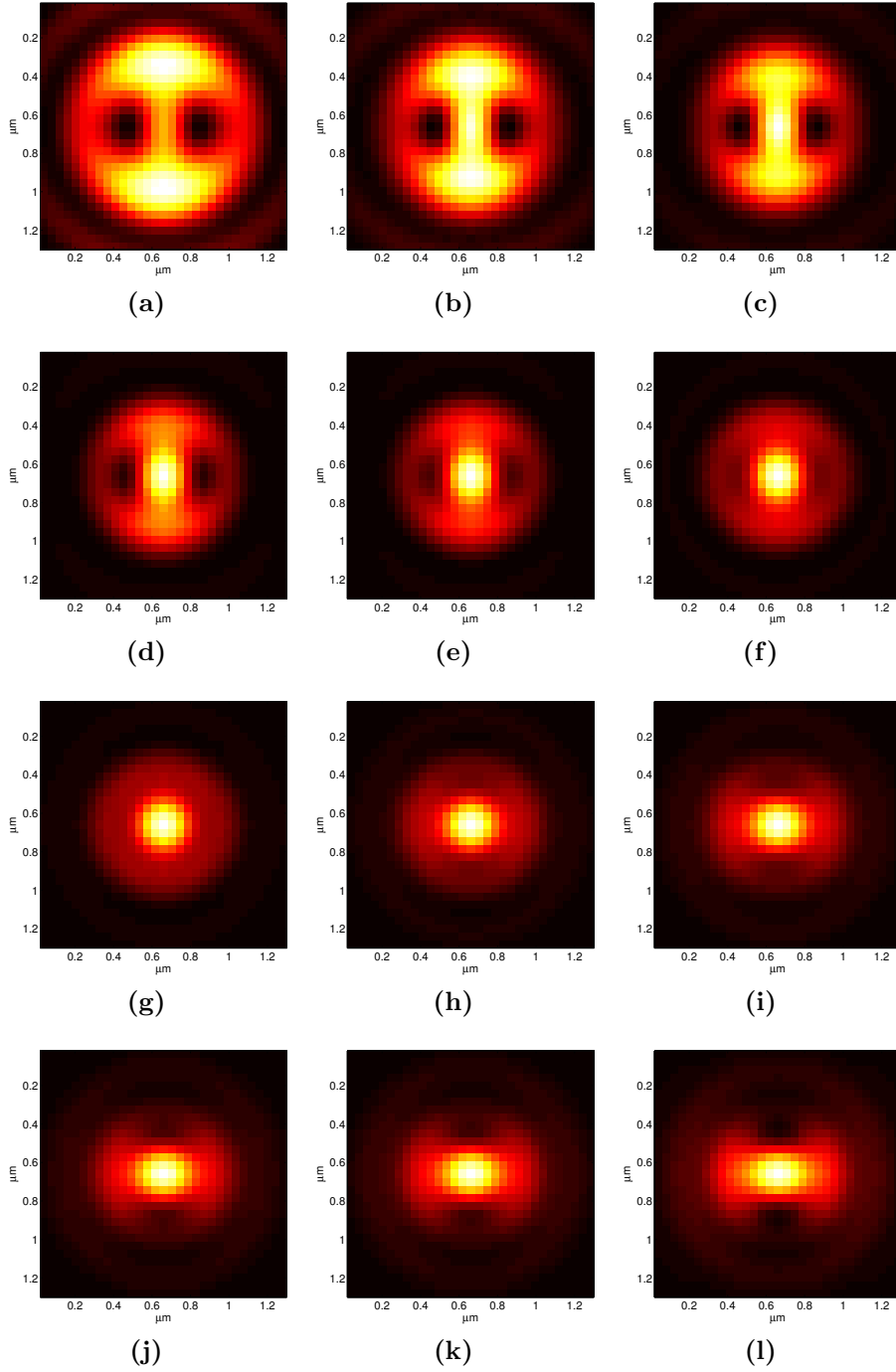


**Figure 8-3:** Examples of PSFs under linearly-polarized input light with polarization in the  $x$ -direction with longitudinal focus point  $z_0 =$  (a)  $-340 \mu m$ , (b)  $-280 \mu m$ , (c)  $-240 \mu m$ , (d)  $-180 \mu m$ , (e)  $-140 \mu m$ , (f)  $-100 \mu m$ , (g)  $-60 \mu m$ , (h)  $-20 \mu m$ , (i)  $0 \mu m$ , (j)  $15 \mu m$ , (k)  $25 \mu m$ , (l)  $55 \mu m$ .

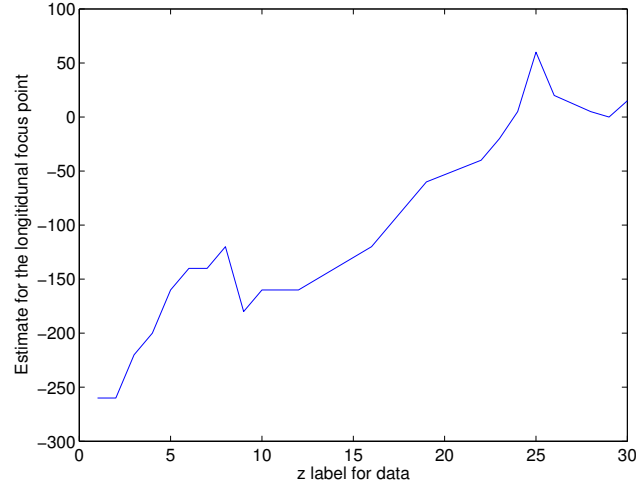


**Figure 8-4:** Estimated longitudinal focus point vs experimental data  $z$  label.

### 8.3 Conclusion

In this chapter, we proposed a procedure for focus identification of high-NA subsurface imaging. The procedure determines the focus of multiple-focus data by matching the data to simulated PSFs with different longitudinal focus points near the interface along the longitudinal axis. The results of this focus identification can also be used in a multiple-focus, multiple-polarization image reconstruction framework. The focus registration results of this framework can be used in a multiple-polarization multiple-focus image reconstruction formulation in order to obtain one single image with higher resolution.

## Chapter 9

# Conclusions

### 9.1 Summary and conclusions

This dissertation makes contributions to the area of optical fault analysis of ICs, addressing resolution challenges that arise because of the increasing density and smaller length scales in ICs. In particular, we formulate a sparse reconstruction framework to improve the resolution of static IC images and dynamic optical measurements of device activity.

In Chapter 3, we proposed two different approaches to model a PSF for the high-NA aSIL subsurface imaging. An accurate PSF is necessary for the success of sparse image reconstruction proposed in this thesis. Both of these PSF models use vectorial optics to account for polarization effects in high-NA subsurface imaging. The Green's function approach in Section 3.2.2 extends the first approach from Section 3.2.1 in order to provide a more accurate model suitable for a wider range of materials. It also models the dependence of the PSF on the size of the object of interest.

In Chapter 4, we proposed a novel sparse reconstruction framework that benefits from polarization diversity of high-NA systems. The output of this approach is a single image, with improved resolution, obtained from a set of images collected using linearly-polarized light with different polarization directions. The proposed framework is an example of an analysis-based sparsity paradigm formulated as a linear inverse problem enforcing sparsity through non-quadratic regularization functionals appropriate to IC features. The advantage of this type of regularization over unreg-

ularized reconstruction is demonstrated on simulated data. Also, benefits of sparse reconstruction utilizing polarization diversity are shown on simulated and experimental data. Combining multiple images under input light with different polarization directions increases the robustness of the reconstruction to noise and to mismatches between the actual system and the assumed forward model. Additionally, Section 4.4 focused on a practical problem of boundary conditions. It presents a comparison of different techniques for handling boundary pixels in a convolution model for an aSIL IC imaging system. This comparison is critical for aSIL IC imaging. The PSF of the system is fairly large compared to the size of structures in ICs, and therefore, large errors in the reconstruction can occur due to a conventional handling of boundary pixels. We have showed that modifying the forward model in order to remove any assumptions on the boundary pixels produced the best performance.

In Chapter 5, we proposed a synthesis-based sparse reconstruction framework using overcomplete dictionaries to increase the resolution and localization accuracy of IC imaging. Overcomplete dictionary-based representation is especially suitable for IC imaging. The structures in ICs come from a limited set, mostly line segments of varying widths and lengths. The overcomplete dictionary for the sparse representation of an IC scene was built a-priori using CAD layouts containing the design for the device of interest. The proposed framework was validated on both simulated data and experimental data. We also compared the performance of analysis- and synthesis-based sparsity paradigms on both simulated data and experimental data. The synthesis-based approach produces higher resolution and has better performance in terms preserving the intensity smoothness within the structures and eliminating any background oscillations. We should note that this increased performance comes with a memory and computation time tradeoff because the dictionary-based approach requires higher memory and higher computation time.

In Chapter 6, an extension of the synthesis-based sparsity paradigm was formulated in order to improve the resolution and localization accuracy of optical measurements of device activity, specifically LVI measurements. Spatial regions of active areas with the same signature over time or over frequency were coupled by an overcomplete dictionary consisting of space-time or space-frequency blocks. These dictionaries were predetermined according to the properties of modulation, which depends on the applied voltage and on the dimensions of gate, and drain regions obtained from CAD layouts. The sparse representation increases the spatial resolution of LVI measurements and enables localization of different regions with different time signatures. We have showed that the localization error can be decreased significantly through the sparse representation approach.

Applications of the proposed analysis- and synthesis-based sparsity paradigms to dark-field subsurface microscopy of ICs were provided in Chapter 7. We have showed that both techniques provide at least 12 % resolution improvement by enabling the localization of structures, which were not localized in observation data. We also proposed a signal processing approach in order to estimate the PSF of a dark-field subsurface microscopy system from the observation data. Finally, a focus determination procedure using a stack of observation data with different longitudinal focus points was presented in Chapter 8.

## 9.2 Topics for future research

### **Applications to high-NA systems with higher-order laser beams and apodization**

The resolution of high-NA subsurface imaging systems can be also increased through optical microscopy techniques such as by using of higher-order laser beams for illumination and through apodization of the laser beam. A decrease in the spot size of the

focused illumination can be achieved when the system is illuminated with radially-polarized light where the central part is blocked. The proposed sparsity paradigms can be also used for such systems. However, this requires the simulation of a PSF for radially-polarized illumination. Additionally, multiple observation data with different apodization masks can be collected and combined through sparse reconstruction framework.

### **Apodization control for determining a PSF for better reconstruction performance**

The support of the focused light can be modified by designing phase and amplitude masks which are placed to the back of the objective on the pupil plane. The goal of the design is to reduce the width of the focused light in order to increase the resolution. However, decreasing the main lobe width of the focused light can result in an increase in the amplitude of the second lobe or in a decrease of the collection efficiency. The design of the phase and amplitude masks can be formulated as an optimization problem which aims at finding the optimum PSF that will produce higher resolution in the reconstructed images while it might not improve the resolution of observation data.

### **$l_p$ -regularization with $p < 1$ in synthesis-based sparsity paradigm for LVI data**

In Chapter 5, we showed that in synthesis-based sparsity paradigm using  $l_p$ -regularization with  $p < 1$  is more robust than with  $p = 1$  approach in the presence of noise. Since LVI data are noisy, sparsity paradigm proposed in Chapter 6 for LVI measurement should be also extended to  $l_p$ -regularization with  $p < 1$ .

### **Pseudo-nonlinear forward model based on overcomplete dictionaries**

The forward model of high-NA microscope is a nonlinear model where images depend on the shape and alignment of the object of interest. In this dissertation, we proposed a PSF model in order to approximate the nonlinear forward model as a convolution with a PSF. The reason for this is that the calculation of the full vectorial response of the system to any random structure is computationally expensive since it requires rigorous numerical methods. Therefore, an inverse problem formulation that uses the full vectorial model would also be computationally expensive. It will be more efficient, in terms of computation time, to use a pseudo-nonlinear approximation in the reconstruction framework where a linear combination of pre-calculated nonlinear responses of dictionary elements is used as an approximation to the forward model. In other words, the predetermined overcomplete dictionary can be composed of nonlinear responses of different structures in the CAD layout. Then, a sparse representation framework can be used in order to determine the representation coefficients for scene reconstruction.

### **Localization of faults in LVI measurements through synthesis-based sparsity paradigm**

The synthesis-based sparsity paradigm proposed in Chapter 6 can be extended so that the faults can be localized. This can be achieved by building the overcomplete dictionary in such a way that it includes the frequency or the time signature for expected faults. This requires a forward model for LVI measurements incorporating the changes in modulation in the presence of expected faults.



## References

- Abbe, E. (1873). Beiträge zur Theorie des Mikroskops und der mikroskopischen Wahrnehmung. *Archiv für Mikroskopische Anatomie*, 9:413–468.
- Aharon, M., Elad, M., and Bruckstein, A. (2006). k-svd: An algorithm for designing overcomplete dictionaries for sparse representation. *IEEE Transactions on Signal Processing*, 54(11):4311–4322.
- Barrett, R., Berry, M., Chan, T. F., Demmel, J., Donato, J., Dongarra, J., Eijkhout, V., Pozo, R., Romine, C., and der Vorst, H. V. (1994). *Templates for the Solution of Linear Systems: Building Blocks for Iterative Methods, 2nd Edition*. SIAM, Philadelphia, PA.
- Bruce, M., Dabney, G., and McBride, S. (1999). Waveform acquisition from the backside of silicon using electro-optic probing. In *International Symposium for Testing and Failure Analysis (ISTFA)*. ASM International.
- Çetin, M. and Karl, W. (2001). Feature-enhanced synthetic aperture radar image formation based on nonquadratic regularization. *IEEE Transactions on Image Processing*, 10(4):623–631.
- Celi, G., Dudit, S., Parrassin, T., Vallet, M., Perdu, P., Reverdy, A., and Lewis, D. (2012). Laser voltage imaging: New perspective using second harmonic detection on submicron technology. In *International Symposium for Testing and Failure Analysis (ISTFA)*. ASM International.
- Cetin, M., Stojanovic, I., Onhon, N., Varshney, K., Samadi, S., Karl, W., and Willsky, A. (2014). Sparsity-driven synthetic aperture radar imaging: Reconstruction, autofocusing, moving targets, and compressed sensing. *IEEE Signal Processing Magazine*, 31(4):27–40.
- Chartrand, R. (2007). Exact reconstruction of sparse signals via nonconvex minimization. *IEEE Signal Processing Letters*, 14(10):707–710.

- Chen, R., Agarwal, K., Zhong, Y., Sheppard, C. J. R., Phang, J. C. H., and Chen, X. (2012). Complete modeling of subsurface microscopy system based on aplanatic solid immersion lens. *Journal of the Optical Society of America A*, 29(11):2350–2359.
- Chen, S. S., Donoho, D. L., and Saunders, M. A. (2001). Atomic decomposition by basis pursuit. *SIAM Review*, 43(1):129–159.
- Chim, W. K. (2000). *Semiconductor Device and Failure Analysis : Using Photon Emission Microscopy*. Wiley.
- Ciuciu, P., Idier, J., and Giovannelli, J. F. (1999). Markovian high resolution spectral analysis. In *IEEE International Conference on Acoustics, Speech, and Signal Processing*.
- Demoment, G. (1989). Image reconstruction and restoration: overview of common estimation structures and problems. *IEEE Transactions on Acoustics, Speech and Signal Processing*, 37(12):2024–2036.
- Donoho, D., Elad, M., and Temlyakov, V. (2006). Stable recovery of sparse overcomplete representations in the presence of noise. *IEEE Transactions on Information Theory*, 52(1):6–18.
- Donoho, D., Johnstone, I., Hoch, J., and Stern, A. (1992). Maximum entropy and the nearly black object. *Journal of the Royal Statistical Society. Series B*, 54(1):41–81.
- Donoho, D. L. and Johnstone, I. M. (1994). Ideal spatial adaptation by wavelet shrinkage. *Biometrika*, 81:425–455.
- Elad, M. and Aharon, M. (2006). Image denoising via sparse and redundant representations over learned dictionaries. *IEEE Transactions on Image Processing*, 15(12):3736–3745.
- Foreman, M. R. and Török, P. (2011). Computational methods in vectorial imaging. *Journal of Modern Optics*, 58(5-6):339–364.
- Gazit, S., Szameit, A., Eldar, Y. C., and Segev, M. (2009). Super-resolution and reconstruction of sparse sub-wavelength images. *Optics Express*, 17(26):23920–23946.

- Goldstein, M., Solkner, G., and Gornik, E. (1993). Heterodyn interferometer for the detection of electric and thermal signals in integrated circuits through the substrate. *Review of Scientific Instruments*, 64(10):3009–3013.
- Heinrich, H. K., Bloom, D. M., and Hemenway, B. R. (1986). Noninvasive sheet charge density probe for integrated silicon devices. *Applied Physics Letters*, 48(16):1066 – 1068.
- Hu, L., Chen, R., Agarwal, K., Sheppard, C. J. R., Phang, J. C. H., and Chen, X. (2011). Dyadic green’s function for aplanatic solid immersion lens based sub-surface microscopy. *Optics Express*, 19(20):19280–19295.
- Ippolito, S. B., Goldberg, B. B., and Unlu, M. S. (2001). High spatial resolution subsurface microscopy. *Applied Physics Letters*, 78(26):4071–4073.
- Jin, J. (2014). *The Finite Element Method in Electromagnetics*. Wiley Interscience, 3 edition.
- Karl, W. C. (2000). *Handbook of Image and Video Processing*, chapter Regularization in image restoration and reconstruction, pages 141 – 160. Academic Press.
- Kim, S.-J., Koh, K., Lustig, M., Boyd, S., and Gorinevsky, D. (2007). An interior-point method for large-scale l1-regularized least squares. *IEEE Journal of Selected Topics in Signal Processing*, 1(4):606–617.
- Kindereit, U. (2009). *Investigation of laser-beam modulations induced by the operation of electronic devices*. PhD thesis, Berlin Institute of Technology, Berlin, Germany.
- Kindereit, U., Boit, C., Kerst, U., Kasapi, S., Ispasoiu, R., Ng, R., and Lo, W. (2008). Comparison of laser voltage probing and mapping results in oversized and minimum size devices of 120 nm and 65 nm technology. *Microelectronics Reliability*, 48(8-9):1322–1326.
- Kindereit, U., Woods, G., Tian, J., Kerst, U., Leihkauf, R., and Boit, C. (2007). Quantitative investigation of laser beam modulation in electrically active devices as used in laser voltage probing. *IEEE Transactions on Device and Materials Reliability*, 7(1):19 –30.

- Koklu, F. and Unlu, M. (2009). Focusing anomalies in the vicinity of dielectric interfaces. In *Proceedings of IEEE Photonics Society 2009 Annual Meeting*, pages 359–360.
- Köklü, F. H., Ippolito, S. B., Goldberg, B. B., and Ünlü, M. S. (2009). Subsurface microscopy of integrated circuits with angular spectrum and polarization control. *Optics Letters*, 34(8):1261–1263.
- Köklü, F. H., Quesnel, J. I., Vamivakas, A. N., Ippolito, S. B., Goldberg, B. B., and Ünlü, M. S. (2008). Widefield subsurface microscopy of integrated circuits. *Optics Express*, 16(13):9501–9506.
- Kolachina, S. (2011). Introduction to laser voltage probing (lvp) of integrated circuits. In Committee, E. D. R., editor, *Microelectronics Failure Analysis, Desk Reference Sixth Edition*. ASM International.
- Liao, J. Y., Kasapi, S., Cory, B., Marks, H. L., and Ng, Y. S. (2010). Scan chain failure analysis using laser voltage imaging. *Microelectronics Reliability*, 50(911):1422–1426. 21st European Symposium on the Reliability of Electron Devices, Failure Physics and Analysis.
- Moore, G. E. (1998). Cramming more components onto integrated circuits (reprinted from electronics, pg 114-117, april 19, 1965). *Proceedings of the IEEE*, 86(1):82–85.
- Munro, P. R. T. and Török, P. (2007). Calculation of the image of an arbitrary vectorial electromagnetic field. *Optics Express*, 15(15):9293–9307.
- Ng, Y. S., Lundquist, T., Skvortsov, D., Liao, J., Kasapi, S., and Marks, H. (2010). Laser voltage imaging: A new perspective of laser voltage probing. In *International Symposium for Testing and Failure Analysis (ISTFA)*. ASM International.
- Nikawa, K., Saiki, T., Inoue, S., and Ohtsu, M. (1999). Imaging of current paths and defects in al and tisi interconnects on very-large-scale integrated-circuit chips using near-field optical-probe stimulation and resulting resistance change. *Applied Physics Letters*, 74(7):1048–1050.
- Novotny, L. and Hecht, B. (2006). *Principles of Nano-Optics*. Cambridge University Press.

- Pocklington, H. (1897). Electrical oscillations in wires. *Proceedings of the Cambridge Philosophical Society*, 9:324–332.
- Richards, B. and Wolf, E. (1959). Electromagnetic diffraction in optical systems. ii. structure of the image field in an aplanatic system. *Proceedings of the Royal Society of London. Series A. Mathematical and Physical Sciences*, 253(1274):358–379.
- Ring, W. (2000). Structural properties of solutions to total variation regularization problems. *ESAIM: Mathematical Modelling and Numerical Analysis*, 34:799–810.
- Samadi, S., Çetin, M., and Masnadi-Shirazi, M. A. (2009). Multiple feature-enhanced synthetic aperture radar imagery. In *Algorithms for Synthetic Aperture Radar Imagery*, volume 7337, pages 733701–10. SPIE.
- Serrels, K. A., Ramsay, E., Warburton, R. J., and Reid, D. T. (2008). Nanoscale optical microscopy in the vectorial focusing regime. *Nature Photonics*, 2(5):311–314.
- Soden, J. and Anderson, R. E. (1993). Ic failure analysis: techniques and tools for quality reliability improvement. *Proceedings of the IEEE*, 81(5):703–715.
- Soref, R. and Bennett, B. (1987). Electrooptical effects in silicon. *IEEE Journal of Quantum Electronics*, 23(1):123 – 129.
- Späth, H. (1985). *Cluster dissection and analysis: theory, FORTRAN programs, examples*. Computers and their applications. Horwood.
- Starck, J.-L., Elad, M., and Donoho, D. (2005). Image decomposition via the combination of sparse representations and a variational approach. *IEEE Transactions on Image Processing*, 14(10):1570–1582.
- Tikhonov, A. N. (1963). Solution of incorrectly formulated problems and the regularization method. *Soviet Mathematics*, 4:1035–1038.
- Török, P., Munro, P. R. T., and Kriezis, E. E. (2008). High numerical aperture vectorial imaging in coherent optical microscopes. *Optics Express*, 16(2):507–523.
- Tuysuzoglu, A., Kracht, J. M., Cleveland, R. O., Cetin, M., and Karl, W. C. (2012). Sparsity driven ultrasound imaging. *The Journal of the Acoustical Society of America*, 131(2):1271–1281.

- Vigil, K., Lu, Y., Yurt, A., Cilingiroglu, T. B., Bifano, T. G., Ünlü, M. S., and Goldberg, B. B. (2014). Integrated circuit super-resolution failure analysis with solid immersion lenses. *Electronic Device Failure Analysis*, 16:26–33.
- Vogel, C. and Oman, M. (1998). Fast, robust total variation-based reconstruction of noisy, blurred images. *IEEE Transactions on Image Processing*, 7(6):813–824.
- Voronin, S. and Chartrand, R. (2013). A new generalized thresholding algorithm for inverse problems with sparsity constraints. In *IEEE International Conference on Acoustics, Speech, and Signal Processing*.
- Xu, C. and Denk, W. (1999). Comparison of one- and two-photon optical beam-induced current imaging. *Journal of Applied Physics*, 86(4):2226–2231.
- Xu, Z., Chang, X., Xu, F., and Zhang, H. (2012).  $l_{1/2}$  regularization: A thresholding representation theory and a fast solver. *IEEE Transactions on Neural Networks and Learning Systems*, 23(7):1013–1027.
- Yee, S. (1966). Numerical solution of initial boundary value problems involving maxwell’s equations in isotropic media. *IEEE Transactions on Antennas and Propagation*, 14:302–307.
- Yurt, A., Grogan, M. D. W., Goldberg, B. B., and Unlu, M. S. (in prep.). Polarization sensitive dark-field subsurface imaging of integrated circuits. *Optics Letters*.
- Yurt, A., Grogan, M. D. W., Ramachandran, S., Goldberg, B. B., and Ünlü, M. S. (2014a). Effect of vector asymmetry of radially polarized beams in solid immersion microscopy. *Optics Express*, 22(6):7320–7329.
- Yurt, A., Ramsay, E., Köklü, F., Stockbridge, C. R., Lu, Y., Ünlü, M., and Goldberg, B. B. (2012). Dual-phase interferometric confocal imaging for electrical signal modulation mapping in ics. In *International Symposium for Testing and Failure Analysis (ISTFA)*. ASM International.
- Yurt, A., Uyar, A., Cilingiroglu, T. B., Goldberg, B. B., and Ünlü, M. S. (2014b). Evanescent waves in high numerical aperture aplanatic solid immersion microscopy: Effects of forbidden light on subsurface imaging. *Optics Express*, 22(7):7422–7433.

## Tenzile Berkin (Abanoz) Cilingiroglu

924 Beacon St., Apt. 3  
 Boston, MA 02215  
 +1 (617) 955 1166  
 berkin@bu.edu

### Education

**Boston University**, Boston, MA

*Doctor of Philosophy*, Electrical Engineering **January 2015 (Expected)**  
 Dissertation: “A sparsity-based framework for resolution enhancement in optical fault analysis of integrated circuits”. Advisor: Prof. M. Selim Unlu, Prof. W. Clem Karl.

**Koc University**, Istanbul, TURKEY

*Master of Science*, Electrical Engineering **August 2008**  
 Dissertation: “Optimal selection of encoding configuration for scalable and multiple description video coding”. Advisor: Prof. A. Murat Tekalp.

**Koc University**, Istanbul, TURKEY

*Bachelor of Science*, Electrical and Computer Engineering **June 2006**  
 Merit Scholarship recipient

### Awards and Scholarship

- Merit Scholarship with full tuition waiver (2001-2006).
- Scholarship for graduate study in Turkey from Turkish National Science Foundation (2006-2008).
- Graduate Assistantship, Boston University, 2009-2014.
- Graduate Teaching Fellowship, Boston University, 2008.
- Outstanding poster award, ISTFA 2012.

### Research and Professional Experience

**Information Sciences and Systems Laboratory and Optical Characterization and Nanophotonics Laboratory**, Boston University, Boston, MA

*Graduate Research Assistant* **May 2009 - December 2014**

- Developed and implemented novel algorithms for resolution improvement and fault localization in optical microscopic data of integrated circuits.
- Implemented estimation algorithms for calculating biomass accumulation in high throughput interferometric microscopy.

- IConducted research on feature selection and classification for anomalous activity detection in surveillance videos.

**DCG Systems Inc.**, Fremont, CA

*Intern*

**June-August 2013**

- Developed and implemented algorithms for resolution improvement in optical fault localization data of integrated circuits.

**Electrical and Computer Engineering Department, Boston University,**  
Boston, MA

*Teaching Assistant*

**September 2008 - June 2009**

- Courses: Introduction to electronics, Digital Signal Processing, Signals and Systems.
- Gave recitation classes, prepared handouts, graded exams and homeworks.

**Multimedia Networking Laboratory, Koc University, Istanbul, TURKEY**

*Graduate Research Assistant*

**September 2006 - August 2008**

- Developed and implemented optimization algorithms for encoding configuration optimization of scalable and multi-view video coding.

**Electrical Engineering Department, Koc University, Istanbul, TURKEY**

*Teaching Assistant*

**September 2006 - August 2008**

- Courses: Signal Processing, Digital Signal Processing,
- Gave recitation classes, graded exams and homeworks.

## **Publications**

- Cilingiroglu, T. B, Uyar, A., Karl, W. C, Konrad, J., Tuysuzoglu, A., Goldberg, B. B., Unlu, M. S., Dictionary based Image Reconstruction for Superresolution in Integrated Circuit Imaging, in preparation for submission to Optics Express.
- Cilingiroglu, T. B, Zangeneh, M., Uyar, A., Karl, W. C, Konrad, J., Joshi, A., Goldberg, B. B., Unlu, M. S., Dictionary-based Sparse Representation for Resolution Improvement in Laser Voltage Imaging of CMOS Integrated Circuits accepted for Design, Test and Automation in Europe (DATE) 2015.



- Cilingiroglu, T. B., Karl, W. C., Konrad, J., Grogan, M. D. W., Yurt, A., Tuysuzoglu, A., Goldberg, B. B., Unlu, M. S., Resolution Improvement through Sparse Image Reconstruction Techniques for Darkfield Subsurface Microscopy of Integrated Circuits, International Symposium for Testing and Failure Analysis (ISTFA), 2014.
- Uyar. A., Yurt, A., Cilingiroglu, T. B., Unlu, M. S., Goldberg, B. B., Imaging Performance of aSIL Microscopy on Subsurface Imaging of SOI Chips International Symposium for Testing and Failure Analysis (ISTFA), 2014.
- Yurt. A., Uyar, A., Cilingiroglu, T. B., Unlu, M. S., Goldberg, B. B., Evanescent waves in high numerical aperture aplanatic solid immersion microscopy: Effects of forbidden light on subsurface imaging, Optics Express, vol. 22, issue 7, pp. 7422-7433, 2014
- Cilingiroglu, T. B., Tuysuzoglu, A., Karl, W. C., Konrad, J., Goldberg, B. B., Unlu, M. S., Dictionary-based Image Enhancement for Integrated Circuit Imaging, IEEE International Conference in Acoustics, Speech and Signal Processing (ICASSP), 2013.
- Cilingiroglu, T. B., Koklu, F. H., Ramsay, E., Lu, Y., Yurt, A., Karl, W. C., Konrad, J., Goldberg, B. B., Unlu, M. S., Image Reconstruction Techniques for High Numerical Aperture Integrated Circuit Imaging, International Symposium for Testing and Failure Analysis (ISTFA), 2012.
- Abanoz, T. B., Tekalp, A. M., SVC-based scalable multiple description video coding and optimization of encoding configuration, Elsevier Journal of Image Communication, vol. 24, October 2009.
- Abanoz, T. B., Tekalp, A. M., Optimization of encoding configuration in scalable multiple description coding for rate-adaptive P2P video multicasting, Proc. IEEE International Conference on Image Processing (ICIP), 2009.
- Abanoz, T. B., Tekalp, A. M., Optimal Selection of Encoding configuration for Scalable Video Coding, Proc. IEEE International Conference on Image Processing (ICIP), 2007.

## Related Course Projects

- Adaptive Methods for Computed Tomography, Image restoration and reconstruction, spring 2009.
- Scene Segmentation for Behavior Correlation, Statistical methods II, spring 2010.

- A review of high dynamic range imaging on static scenes, Digital Image Processing and Communication, fall 2008.
- Adaptive De-interlacing based on texture and motion vector analysis, Image and video processing, spring 2006.

## **Skills**

- Programming languages: Matlab, C, C++, Open CV, Python
- Operating Systems: Windows, Linux, OS X
- Software packages/frameworks: Latex, Lumerical FDTD Solutions
- Languages: Turkish, English, French